Magneto-microphotoluminescence spectroscopy as a tool for the study of disorder in semiconductor quantum wells

Dissertation
zur Erlangung des Doktorgrades
der Mathematisch-Naturwissenschaftlichen Fakultäten
der Georg-August-Universität Göttingen

vorgelegt von
Matthias Erdmann
aus Coesfeld

Göttingen, 2007

D7

Referent:	Prof. Dr. R.G. Ulbrich
Korreferent:	Prof. Dr. Th. Pruschke

Tag der mündlichen Prüfung: 07.05.2007

Contents

Chapter 1

Introduction

GaAs/$Al_xGa_{1-x}As$ quantum wells belong to the class of two-dimensional semiconductor heterostructures, where electrons and holes are confined to a nm-thin layer of semiconductor material with smaller bandgap sandwiched between barrier material with a larger bandgap. Due to the alloy composition fluctuations on the atomic scale in the $Al_xGa_{1-x}As$ alloy near the nominal interfaces, the GaAs/$Al_xGa_{1-x}As$ interface position can not be unambiguously defined on the atomic scale [Oga87, Sal93]. Rather, a some lattice constants wide region exists where it is impossible to decide if a Ga atom belongs to the GaAs layer or to the $Al_xGa_{1-x}As$ barrier. Concerning the distribution of the substitutional alloy atoms in the $Al_xGa_{1-x}As$ alloy on the group-III sublattice, a lot of studies have shown that the a priori assumption of a random, uncorrelated distribution of isovalent atoms in the $Al_xGa_{1-x}As$ alloy is not justified. From the interatomic distance up to several lattice constants, a correlation between neighbouring atoms has been found (short range ordering, SRO) [Hei98, Hei99]. In GaAs/$Al_xGa_{1-x}As$ quantum wells, it was observed that short-range ordering during growth of the interfacial layers contributes significantly to the observed interface disorder [Reu00]. On a larger scale, from nm up to μm, phase separation, clusters and long range ordering (LRO) have been observed [Kua85]. It is the aim of this thesis to explore the significance of short-range correlations between Al atoms for optical spectra of narrow GaAs/$Al_xGa_{1-x}As$ quantum wells, where a few atomic layers of GaAs are sandwiched between barriers of the substitutional $Al_xGa_{1-x}As$ alloy.

In the recent decades, two-dimensional semiconductor heterostructures composed of binary/ternary alloy combinations have served as model systems for the investigation of physical effects resulting from quantum confinement, and have found many applications in electronic and optoelectronic devices. Due to the reduced dimensionality, disorder in the heterointerfaces of narrow quantum wells has an important influence on device quality, e.g., on optical spectra. Early on, it has been recognized that deviations from in-plane translational symmetry cause lateral localization of Coulomb-correlated electron-hole pairs (excitons) in the QW plane and result in inhomogeneous broadening of spatially averaged QW exciton spectra [Wei81]. Subsequently, spatially averaging optical techniques like photoluminescence (PL) spectroscopy have been widely applied to the characterization of disorder of narrow quantum wells, using inhomogeneous broadening as a measure of interface quality [Her91]. Optical techniques have been found to complement data obtained by direct structural techniques like, e.g., transmission electron microscopy (TEM) [Pet77] and X-ray diffraction [Fle80]. However, as an indirect technique, the interpretation of QW exciton spectra obtained by spatially averaging PL in terms of interface structure requires some degree of modeling. In most models, the intrinsic short-range disorder on the atomic scale in GaAs/$\mathrm{Al}_x\mathrm{Ga}_{1-x}\mathrm{As}$ quantum wells, resulting from composition fluctuations in the $\mathrm{Al}_x\mathrm{Ga}_{1-x}\mathrm{As}$ barriers, has been considered to be irrelevant for exciton localization [Wei81], or at least of secondary importance [War92]. The study of Ogale *et al.* [Oga87] remained singular in that it pointed out the primary importance of composition fluctuations in the $\mathrm{Al}_x\mathrm{Ga}_{1-x}\mathrm{As}$ barriers for optical properties of GaAs/$\mathrm{Al}_x\mathrm{Ga}_{1-x}\mathrm{As}$ quantum wells.

Two developments do now enable a new approach to the study of exciton disorder-localization in narrow quantum wells, and of the relation between the atomistic configuration of the QW interfaces and optical spectra: On the experimental side, optical techniques with high spatial resolution ($< 1\ \mu$m) like microphotoluminescence (μPL) have opened up new possibilities to investigate exciton disorder-localization in that they allow to resolve the emission from individual exciton states localized by the fluctuating band edges in a narrow quantum well ("natural quantum dots") [Zre94, Bru94, Kop00]. High-spatial-resolution magnetoluminescence spectroscopy thereby gives access to diamagnetic shift and Zeeman splitting of single exciton states in the low-energy tail of the μPL spectra [Hes94]. The central motivation to study the diamagnetic shift is that it provides information about localization properties of individual quantum dot states [Hal92, Wal98, Bay98]. The idea is that the diamagnetic shift distribution as a function of transition energy in the low-energy tail of μPL spectra should give experimental access to the potential minimum statistics of the underlying QW interface disorder potential, and thereby to its statistical properties like the lateral correlation length.

On the theoretical side, the theory of exciton disorder-localization, that has been developed in the envelope function framework, allows a detailed description of exciton localization in narrow quantum wells. For sufficiently thin wells (QW width < exciton Bohr radius), the model of a three-dimensional exciton moving between the corrugated QW interfaces can be replaced by that of a quasi-two-dimensional exciton with lateral Bohr radius a_B. Its constituents, electron and hole, move in lateral disorder potentials, representing the fluctuations of the local band edges [Zim97]. The concept of band edge fluctuations replaces the concept of interface fluctuations, which is not applicable offhand in GaAs/$\mathrm{Al}_x\mathrm{Ga}_{1-x}\mathrm{As}$ quantum wells, due to the lack of an unambiguous definition of the heterointerface position on the atomic scale. In GaAs/$\mathrm{Al}_x\mathrm{Ga}_{1-x}\mathrm{As}$ quantum wells, the local band edges are determined by the distribution of Al atoms in a QW cross section weighted with the electron/hole envelope wave functions. [1] Localization of excitons in the QW plane is determined by the combination of the Coulomb interaction between electrons and holes and electron and hole confinement by fluctuations of the local band edges ("interface disorder"). The disorder potentials for electron and hole can, e.g., be characterized by their amplitude (standard deviation, "disorder strength") and correlation length. With respect to exciton localization, three length scales of lateral disorder can be distinguished: (i) disorder on the atomic scale, (ii) disorder on the length scale of the exciton Bohr radius, and (iii) long-range disorder. The theory of exciton localization gives detailed account of the effects of disorder on the full

---

[1] To be precise, the fluctuations of the local band edges relative to the bulk band edges are determined in this way. The question of the influence of composition fluctuations in $\mathrm{Al}_x\mathrm{Ga}_{1-x}\mathrm{As}$ on the bulk band edges remains.

two-particle motion of a Coulomb-correlated electron-hole pair, and on the diamagnetic shift of single exciton states [Gro05].

This thesis combines μPL and magneto-μPL experiments with the analysis of structural data obtained in a recent cross-sectional scanning tunneling microscopy (XSTM) study to investigate exciton localization in narrow (001) GaAs/Al$_x$Ga$_{1-x}$As quantum wells. The GaAs/Al$_x$Ga$_{1-x}$As quantum wells were grown by MBE without growth interruption at the interfaces. They are therefore especially well suited for the study of short-range disorder on the length scale between (i) and (ii). A special sample design has been chosen that – in addition to the optical measurements – allows the investigation of the interfaces of the same quantum well sample on the atomic scale with room-temperature XSTM. [2]

After this introduction, chapters 2 and 3 describe the basic concepts of excitons and exciton localization in narrow GaAs/Al$_x$Ga$_{1-x}$As QWs. The full three-dimensional problem of the Coulomb-correlated motion of electron and hole between corrugated quantum well barriers can be simplified in the case of narrow quantum wells with relatively weak disorder: The significant difference in strength of the vertical confinement (in growth direction) and lateral confinement (in the QW plane) allows a separation of the three-dimensional exciton motion into vertical and lateral motion [Zim97]. This reflects in the division into chapters 2 and 3: Chapter 2 describes excitons in quantum wells with in-plane translational symmetry. The effects of a magnetic field in growth direction on the lowest exciton state in the quantum well are described in detail, including the effect of the magnetic field on the exciton wave function. Based on this description of quantum well excitons, chapter 3 introduces the theory of exciton localization in narrow QWs. First, the example of a GaAs/Al$_x$Ga$_{1-x}$As QW with nominally perfectly flat interfaces and random, uncorrelated Al distribution in the barriers is described. Subsequently, the results of three decades of research on interface disorder in GaAs/Al$_x$Ga$_{1-x}$As quantum wells are reviewed. In the last section, the effect of a magnetic field in Faraday configuration on quantum dot exciton ground states is described (diamagnetic shift), with a focus on the relation between diamagnetic shift and lateral extension of the local confinement potential.

Chapter 4 describes the sample design that has been chosen to study the same QW heterostructure with structural (XSTM) as well as with optical (μPL) methods.

Principles of scanning tunneling microscopy (STM) are outlined in chapter 5, and the structural data of one of the GaAs/Al$_{0.3}$Ga$_{0.7}$As QWs are analyzed. The structural data obtained by XSTM give access to the atomic scale structure of the interfaces of a 4-nm GaAs/Al$_{0.3}$Ga$_{0.7}$As QW: Constant current topographs show a 160 nm long QW cross-section with atomic resolution and chemical sensitivity. In a study concomitant to the main part of this thesis, optical spectra of the 4-nm QW have been simulated on the basis of these structural data. This study was started by Claus Ropers [Rop03] and pursued in close collaboration with the semiconductor theory group at the Humboldt-Universität Berlin.

Chapter 6 describes basics of μPL spectroscopy and the experimental setup used in this study. Spatially averaged and spatially resolved PL spectra of the narrow quantum wells are shown. In the low-energy tail of μPL spectra obtained at 500 nm spatial resolu-

---

[2] Contrary to the common belief that only doped quantum wells can be studied by STM [Jah96].

tion, the spectrally narrow emission lines of localized exciton states are observed. The fine structure of single exciton states has been studied by polarization-dependent spectroscopy to obtain additional insight into their localization properties. The simulation of optical spectra on the basis of the XSTM data is described. Temperature-dependent μPL spectra have been obtained to study relaxation effects and the Stokes shift. Based on the insight that μPL spectra can be characterized by an effective carrier temperature that is higher than the lattice temperature, experimental and simulated μPL spectra of the 4-nm GaAs/$Al_{0.3}Ga_{0.7}As$ quantum well can be directly compared in the last section.

Chapter 7 describes the results of magneto-μPL experiments on the narrow GaAs/ $Al_{0.3}Ga_{0.7}As$ QWs. In the magneto-μPL experiments, a magnetic field is applied in growth direction (Faraday configuration), and the effect of the magnetic field on single exciton states is studied. By increasing the magnetic field in steps as small as 50 mT to a maximum field of 10 T, diamagnetic shift and Zeeman splitting of single exciton states in the low-energy tail of the μPL spectra can be determined. The positive slope observed in the diamagnetic shift distribution as a function of transition energy is discussed in detail as the consequence of exciton localization by short-range correlated interface disorder in the QW plane. Extending the comparison of structural and optical properties of the 4-nm QW, the experimental diamagnetic shift distribution is compared with a simulated distribution obtained on the basis of the XSTM data.

Chapter 8 presents the results of magneto-μPL experiments on the GaAs/AlAs double quantum well sample. In a several μm^2 large region showing signatures of strong disorder, transitions with negative diamagnetic coefficients are observed. Simultaneously to QD states with negative diamagnetic coefficients, we observe complicated B-field patterns at the low-energy end of the spectral emission region below the QW peak. The question is discussed if these rare observations are related to the combination of exciton localization by strong disorder and the shrinking of the exciton wave function by the magnetic field. Theoretical investigations that have been stimulated by our experimental observation of negative diamagnetic coefficients have recently excluded this possibility [Mul06]. At present, it is assumed that the complex shifts as well as the negative diamagnetic coefficients are related to charged exciton transitions in coupled quantum dots.

Finally, chapter 9 summarizes the results of this work. The appendix contains material related to the numerical simulations performed for this study.

References

[Bay98] M. Bayer, S. N. Walck, T. L. Reinecke, and A. Forchel, *Exciton binding energies and diamagnetic shifts in semiconductor quantum wires and quantum dots*, *Phys. Rev. B* 57, 6584 (1998).

[Bru94] K. Brunner, G. Abstreiter, G. Böhm, G. Tränkle, and G. Weimann, *Sharp-line photoluminescence and 2-photon absorption of zero-dimensional biexcitons in a GaAs/AlGaAss structure*, *Phys. Rev. Lett.* 73, 1138 (1994).

[Fle80] R. M. Fleming, D. B. Mcwhan, A. C. Gossard, W. Wiegmann, and R. A. Logan, *X-ray diffraction study of inter-diffusion and growth in* $(GaAs)_n(AlAs)_m$ *multilayers*, *J. Appl. Phys.* 51, 357 (1980).

[Gro05] M. Grochol, F. Grosse, and R. Zimmermann, *Exciton wave function properties probed by diamagnetic shift in disordered quantum wells*, *Phys. Rev. B* 71, 125339 (2005).

[Hal92] V. Halonen, T. Chakraborty, and P. Pietilainen, *Excitons in a parabolic quantum dot in magnetic fields*, *Phys. Rev. B* 45, 5980 (1992).

[Hei98] A. J. Heinrich, *Ordering in ternary compound semiconductors on the atomic scale*, Ph.D. thesis, Universität Göttingen, 1998.

[Hei99] A. J. Heinrich, M. Wenderoth, K. J. Engel, T. C. G. Reusch, K. Sauthoff, R. G. Ulbrich, and E. R. W. K. Uchida, *Short-range ordering in* $Al_xGa_{1-x}As$ *grown with metal-organic vapor phase epitaxy*, *Phys. Rev. B* 59, 10296 (1999).

[Her91] M. A. Herman, D. Bimberg, and J. Christen, *Heterointerfaces in quantum wells and epitaxial growth processes - Evaluation by luminescence techniques*, *J. Appl. Phys.* 70, R1 (1991).

[Hes94] H. F. Hess, E. Betzig, T. D. Harris, L. N. Pfeiffer, and K. W. West, *Near-field spectroscopy of the quantum constituents of a luminescent system*, *Science* 264, 1740 (1994).

[Jah96] U. Jahn, S. H. Kwok, M. Ramsteiner, R. Hey, H. T. Grahn, and E. Runge, *Exciton localization, photoluminescence spectra, and interface roughness in thin quantum wells*, *Phys. Rev. B* 54, 2733 (1996).

[Kop00] U. Kops, P. G. Blome, M. Wenderoth, R. G. Ulbrich, C. Geng, and F. Scholz, *Intrinsic quantum dots in partially ordered bulk (GaIn)P*, *Phys. Rev. B* 61, 1992 (2000).

[Kua85] S. T. Kuan, T. F. Kuech, W. I. Wang, and E. L. Wilkie, *Long-range order in* $Al_xGa_{1-x}As$, *Phys. Rev. Lett.* 54, 201 (1985).

[Mul06] E. Muljarov and R. Zimmermann, unpublished result. Private communication (2006).

[Oga87] S. B. Ogale, A. Madhukar, F. Voillot, M. Thomsen, W. C. Tang, T. C. Lee, J. Y. Kim, and P. Chen, *Atomistic nature of heterointerfaces in III-V semiconductor-based quantum well structures and its consequences for photoluminescence behavior*, *Phys. Rev. B* 36, 1662 (1987).

[Pet77] P. M. Petroff, *Transmission electron-microscopy of interfaces in III-V compound semiconductors*, *J. Vac. Sci. Technol.* 14, 973 (1977).

[Reu00] T. C. G. Reusch, M. Wenderoth, A. J. Heinrich, K. J. Engel, N. Quaas, K. Sauthoff, R. G. Ulbrich, E. R. Weber, K. Uchida, and W. Wegscheider, *Influence of short-range ordering on roughness of (AlGa)As interfaces studied with cross-sectional scanning tunnelingmicroscopy*, *Appl. Phys. Lett.* 76, 3882 (2000).

[Rop03] C. Ropers, *Exzitonlokalisierung in AlGaAs/GaAs-Quantenfilmen*, Diploma thesis, Universität Göttingen, 2003.

[Sal93] H. W. M. Salemink and O. Albrektsen, *Atomic-scale composition fluctuations in III-V semiconductor alloys*, *Phys. Rev. B* 47, 16044 (1993).

[Wal98] S. N. Walck and T. L. Reinecke, *Exciton diamagnetic shift in semiconductor nanostructures*, *Phys. Rev. B* 57, 9088 (1998).

[War92] C. A. Warwick and R. F. Kopf, *Microscopic thickness variation of macroscopically uniform quantum wells*, *Appl. Phys. Lett.* 60, 386 (1992).

[Wei81] C. Weisbuch, R. Dingle, A. C. Gossard, and W. Wiegmann, *Optical characterization of interface disorder in* $GaAs/Ga_{1-x}Al_xAs$ *multi-quantum well structures*, *Solid State Commun.* 38, 709 (1981).

[Zim97] R. Zimmermann, F. Grosse, and E. Runge, *Excitons in semiconductor nanostructures with disorder*, *Pure Appl. Chem.* 69, 1179 (1997).

[Zre94] A. Zrenner, L. V. Butov, M. Hagn, G. Abstreiter, G. Bohm, and G. Weimann, *Quantum dots formed by interface fluctuations in AlAs/GaAs coupled quantum well structures*, *Phys. Rev. Lett.* 72, 3382 (1994).

Chapter 2

Fundamentals: Excitons in narrow quantum wells

This chapter aims at the description of the magnetic-field dependence of the lowest exciton states in narrow GaAs/$\mathrm{Al}_x\mathrm{Ga}_{1-x}\mathrm{As}$ quantum wells with in-plane translational symmetry. The composition fluctuations in the $\mathrm{Al}_x\mathrm{Ga}_{1-x}\mathrm{As}$ alloy are neglected here by treating the alloy in the virtual crystal approximation [Nor31], assuming a perfect lattice and a compositionally averaged crystal potential.

Excitons in narrow quantum wells are commonly described in the envelope function approach [Bas88]. In this approach, wave functions of electronic states in nanostructures are considered, for each material separately, as product of the electronic (Bloch) states of the bulk material and envelope wave functions. In the envelope function approach, the description of the properties of quantum well excitons is based on properties of the bulk material (band structure), of the interface (band offsets), and on the geometry of the quantum well (well width).

Thus, the first section of this chapter introduces bulk properties of GaAs, $\mathrm{Al}_x\mathrm{Ga}_{1-x}\mathrm{As}$ ($0 < x < 1$) and AlAs. Then, the band offsets at GaAs/$\mathrm{Al}_x\mathrm{Ga}_{1-x}\mathrm{As}$ heterojunctions and the in-plane band structure of GaAs/$\mathrm{Al}_x\mathrm{Ga}_{1-x}\mathrm{As}$ quantum wells are described. This provides the basis for the description of single-particle (electron, hole) states in GaAs/$\mathrm{Al}_x\mathrm{Ga}_{1-x}\mathrm{As}$ quantum wells in a "particle-in-a-box" model. The single-particle wave functions in turn provide a basis for the description of exciton states in narrow quantum wells. Based on the exciton wave function properties, the effects of a perpendicular magnetic field on the lowest exciton state ("exciton ground state") in a narrow quantum well are described.

2.1 Band structure of bulk GaAs, $\mathrm{Al}_x\mathrm{Ga}_{1-x}\mathrm{As}$, and AlAs

The binary III-V compound semiconductors Gallium arsenide (GaAs) and Aluminum arsenide (AlAs) crystallize in the cubic zinc blende structure. The crystal lattice consists of two face-centered cubic (fcc) sublattices occupated by group-III and group-V atoms. The sublattices are translated by 1/4 of the space diagonal against each other. Each atom is surrounded by four atoms of the other species in a tetrahedral configuration. The lattice constants of GaAs and AlAs differ by only about 0.1 % at room

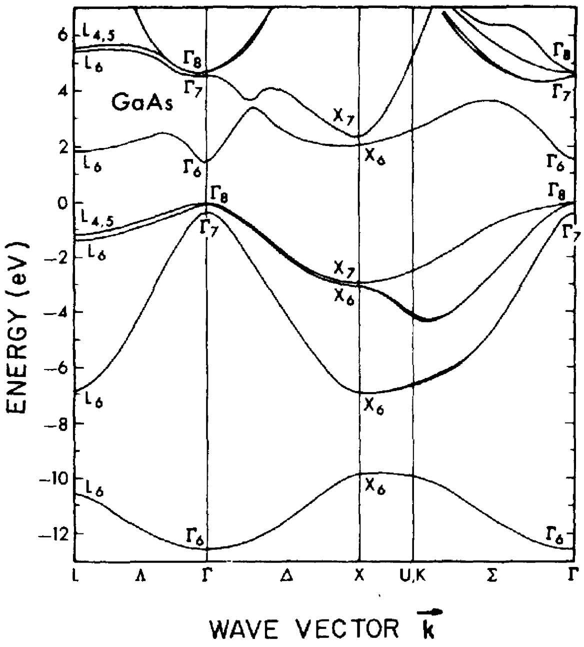

Figure 2.1: *[Che76] Electronic band structure of GaAs, calculated by a pseudopotential technique.*

temperature. The ternary $Al_xGa_{1-x}As$ $(0 < x < 1)$ alloy likewise crystallizes in the zincblende structure with respect to the anion and cation sublattices. The group-III sites in an $Al_xGa_{1-x}As$ crystal are occupied by Al or Ga atoms; a random, spatially uncorrelated distribution of Al atoms on the group-III lattice sites represents the simplest case. However, the tendency to form an ordered state of Ga and Al atoms has been observed in $Al_xGa_{1-x}As$ layers grown by metal-organic vapor phase epitaxy (MOVPE) [Kua85, Hei98, Hei99], as well as in MBE-grown $Al_xGa_{1-x}As$ layers [Kua85].

The band structure of GaAs, as calculated by a pseudopotential technique [Che76], is shown in Fig. 2.1. Near points of high symmetry, the bands are denoted by the corresponding point group symmetry, using the double group notation [Kos63]. The top of the highest valence band (Γ_8) is chosen as zero of energy. The fundamental band gap at the center of the Brillouin zone (Γ) is $E_G = 1.519$ eV at $T = 0$ K [Bas88]. With respect to optical transitions, only the band structure in the direct vicinity of the fundamental gap is of interest. The lowest conduction band (Γ_6) is two-fold spin-degenerate at the Γ point ($S = 1/2$, $S_z = \pm 1/2$). Near Γ, the conduction band is described by the isotropic dispersion relation

$$E_e(\boldsymbol{k}) = \frac{\hbar^2}{2m_e}\,\boldsymbol{k}^2\,, \qquad m_e = 0.067\,m_0\,, \tag{2.1}$$

where m_0 is the free electron mass. The spin-orbit interaction removes the spin degeneracy away from $\boldsymbol{k} = 0$ [Dre55]; the resulting very small k-linear terms are neglected here. Deviations from the parabolic dispersion due to interaction of the lowest conduction band with valence bands and higher conduction bands [Eke89] will be described later in this chapter.

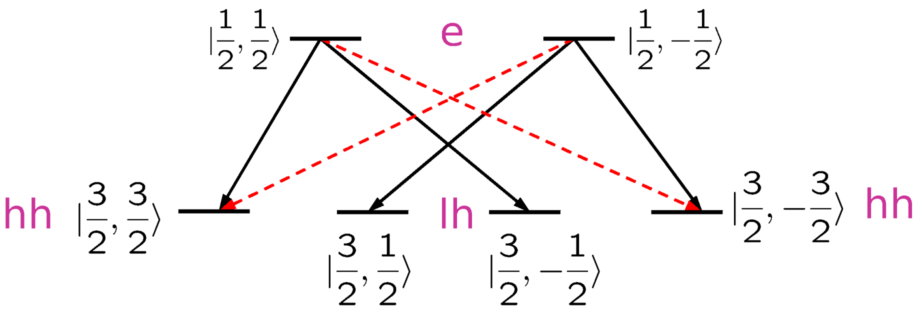

Figure 2.2: *Scheme of optical dipole transitions between conduction band edge and heavy-hole/light-hole band edges in a bulk III-V semiconductor. Dashed arrows mark dipole-forbidden transitions.*

Without inclusion of the spin-orbit interaction, the valence band would be six-fold degenerate at Γ [Kan57]. Spin-orbit interaction causes an energetic separation of the Γ_7 valence band from the Γ_8 bands; the spin-orbit splitting between Γ_7 and Γ_8 band edges in GaAs is $\Delta = 0.341$ eV [Bas88]. The Γ_7 valence band is denoted as split-off band; it will not be considered further here. The two highest Γ_8 valence bands are degenerate at Γ. In the effective-mass approximation, they are characterized by their different effective masses and denoted heavy-hole (hh) and light-hole (lh) band. Each band is two-fold spin-degenerate at Γ.

The symmetry properties of the zone-center wave functions are determined by the zincblende structure and inherited from the symmetry of the corresponding atomic orbitals. At Γ, the symmetry of the conduction band functions corresponds to the symmetry of atomic s-orbitals, and the symmetry of valence band functions at Γ corresponds to the symmetry of atomic p-orbitals [Kan57]. In this model, the zone-center wave functions of the Γ_8 valence bands have the total angular momentum $J = 3/2$. The corresponding magnetic quantum numbers of the zone-center wave functions take the values $J_z = \pm 3/2$ (heavy-hole band, hh) and $J_z = \pm 1/2$ (light-hole band, lh). The dipole selection rules

$$\Delta J = 1\,,\ \Delta M = \pm 1\,, \tag{2.2}$$

where M is the magnetic quantum number, $M = J_z$, describe the dipole-allowed optical transitions. Figure 2.2 shows allowed and forbidden direct optical transitions between conduction band edge and heavy-hole (hh) and light-hole (lh) band edges. Solid arrows mark dipole-allowed optical transitions, the dashed arrows mark dipole-forbidden transitions. The oscillator strength of e-hh transitions is three times larger than that of e-lh transitions due to the different Clebsch-Gordan coefficients of hh and lh zone-center states.

For a description of the dispersion relations of heavy- and light-hole bands, it is useful to introduce the general form of a Hamiltonian for the four $J = 3/2$ states degenerate at $\boldsymbol{k} = 0$ which respects the symmetry of the problem [Lut56]. The general form of a Hamiltonian which is quadratic in $\boldsymbol{k}$, invariant under rotations, and which can be constructed with the two vectors $\boldsymbol{k}$ and $\boldsymbol{J}$ is [Hau04]

$$H = \frac{\hbar^2}{2m_0}\left[\left(\gamma_1 + \frac{5\gamma_2}{2}\right)\boldsymbol{k}^2 - 2\gamma_2\,(\boldsymbol{k}\cdot\boldsymbol{J})^2\right]. \tag{2.3}$$

The real parameters γ_1, γ_2 are called Luttinger parameters [Lut56]. Experimental Luttinger parameters for GaAs are $\gamma_1 = 6.85$, $\gamma_2 = 2.1$ [Chu95, Hau04]. For $\boldsymbol{k}$ in [001] direction, the Hamiltonian Eq. (2.3) is already diagonal. Neglecting the negative sign, the [001] dispersion relations for the two spin-degenerate $J = 3/2$ bands are

$$\begin{aligned} E_{hh}(\boldsymbol{k}) &= (\gamma_1 - 2\gamma_2)\,\frac{\hbar^2\boldsymbol{k}^2}{2m_0}\,, \\ E_{lh}(\boldsymbol{k}) &= (\gamma_1 + 2\gamma_2)\,\frac{\hbar^2\boldsymbol{k}^2}{2m_0}\,. \end{aligned} \tag{2.4}$$

Using the experimental Luttinger parameters, the heavy-hole and light-hole effective [001] masses in GaAs are obtained as

$$m_{hh} = 0.377\,m_0\,, \quad m_{lh} = 0.09\,m_0\,. \tag{2.5}$$

Luttinger also considered a more general Hamiltonian for the four $J = 3/2$ states, which is invariant only under the symmetry operations of the cubic symmetry group [Lut56, Hau04]

$$H = \frac{\gamma_1}{2m_0}\hbar^2\boldsymbol{k}^2 - \frac{\hbar^2}{2m_0}\sum_{i,j=1}^{3}\left[\gamma_3 - (\gamma_3 - \gamma_2)\delta_{ij}\right]\boldsymbol{K}_{ij}\boldsymbol{J}_{ij}\,, \tag{2.6}$$

where

$$\boldsymbol{K}_{ij} = 3k_ik_j - \delta_{ij}k^2\,,\ \boldsymbol{J}_{ij} = \frac{3}{2}(J_iJ_j + J_jJ_i) - \delta_{ij}J^2\,. \tag{2.7}$$

The dispersion relations due to Eq. (2.6) are no longer isotropic. By diagonalizing the Luttinger Hamiltonian Eq. (2.6), direction-dependent effective masses can be calculated [Hou88]. For the heavy-hole band,

$$m_{hh} = m_0\begin{cases} (\gamma_1 - 2\gamma_2)^{-1} \\ (\gamma_1 - 2\gamma_3)^{-1} \\ [\gamma_1 - (\gamma_2^2 + 4\gamma_3^2)^{1/2}]^{-1} \end{cases} \text{in}\begin{cases} [001] \\ [111] \\ [110] \end{cases} \text{direction}\,. \tag{2.8}$$

The experimental value of the Luttinger parameter γ_3 for GaAs is $\gamma_3 = 2.9$ [Chu95, Hau04]. Neglecting the difference $\gamma_3 - \gamma_2$, Eq. (2.6) reduces to Eq. (2.3), which is called spherical approximation.

Band structure of $\mathrm{Al}_x\mathrm{Ga}_{1-x}\mathrm{As}$ and AlAs

With respect to the anion and cation sublattices, the crystal structure of $\mathrm{Al}_x\mathrm{Ga}_{1-x}\mathrm{As}$ $(0 < x < 1)$ and AlAs alloys is almost identical with that of GaAs. However, the ternary $\mathrm{Al}_x\mathrm{Ga}_{1-x}\mathrm{As}$ alloy does not possess the translational symmetry of the binary alloy crystal, since either Ga or Al atoms occupy the group-III lattice sites. Despite the lack of translational symmetry in substitutional alloys like $\mathrm{Al}_x\mathrm{Ga}_{1-x}\mathrm{As}$, their description in terms of single Bloch states has been used in many phenomenological models, e.g., by adopting the *virtual crystal approximation* [Nor31]. The virtual crystal approximation (VCA) assumes a perfect lattice and a compositionally averaged crystal potential, and therefore completely neglects effects due to chemical and positional disorder. The VCA treats the alloy as a pseudo-material, in which all anions are the same (As) as are all cations ($\mathrm{Al}_x\mathrm{Ga}_{1-x}$ pseudo-atoms). In the VCA, $\mathrm{Al}_x\mathrm{Ga}_{1-x}\mathrm{As}$ parameters are therefore calculated by linear interpolation between GaAs and AlAs parameters,

$$P_{\mathrm{AlGaAs}}(x) = x\,P_{\mathrm{AlAs}} + (1-x)\,P_{\mathrm{GaAs}}\,. \tag{2.9}$$

Only in recent years, it has become possible to calculate the band edge states of substitutional semiconductor alloys directly, using atomistic pseudopotentials and plane wave basis functions in supercells large enough to capture localization effects due to composition fluctuations [Wan98]. A new way of analyzing the alloy electronic structure has been proposed, based on a "majority representation" of the reciprocal space spectrum of the alloy eigenstates. A strong majority representation of valence and conduction band edge states with the single dominant point $\boldsymbol{k}_{\mathrm{MR}} = \Gamma$ was found for the random $\mathrm{Al}_{0.3}\mathrm{Ga}_{0.7}\mathrm{As}$ alloy. The spectral weight at $\boldsymbol{k} = \boldsymbol{k}_{\mathrm{MR}}$ was found to be $\sim 90\%$ of the total spectral weight for the conduction band edge states and $\sim 75\%$ for the valence band edge states [Wan98]. This implies that the band edge states in the random $\mathrm{Al}_{0.3}\mathrm{Ga}_{0.7}\mathrm{As}$ alloy can be classified in the language of Bloch states of the constituents. Very recently, a tight-binding supercell method, that incorporates randomness at an atomistic level, has been used to calculate approximate band structures of random $\mathrm{Al}_x\mathrm{Ga}_{1-x}\mathrm{As}$ alloys [Boy07].

The $\mathrm{Al}_x\mathrm{Ga}_{1-x}\mathrm{As}$ band structure is qualitatively similar to the GaAs band structure for $x < 0.45$. The fundamental bandgap is at Γ; two higher conduction band minima are at the X and L points on the surface of the first Brillouin zone [Fig. 2.3(a)]. For $x < 0.45$, the fundamental bandgap of $\mathrm{Al}_x\mathrm{Ga}_{1-x}\mathrm{As}$ increases approximately linearly with increasing Al content x. Table 2.1 gives an expression for the dependence of the $\mathrm{Al}_x\mathrm{Ga}_{1-x}\mathrm{As}$ bandgap at Γ on Al content x. For an accurate description above $x > 0.45$, a quadratic coefficient ("bowing parameter") is necessary, indicating the

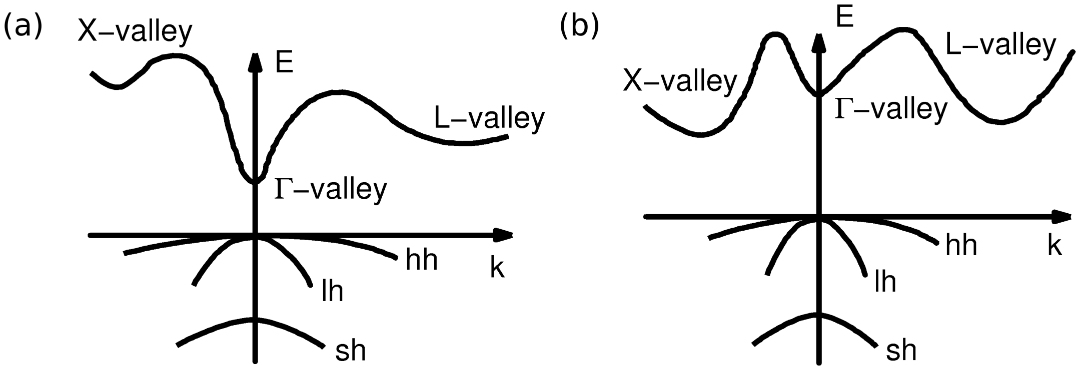

Figure 2.3: *(a) Qualitative band structure of GaAs and* $\mathrm{Al}_x\mathrm{Ga}_{1-x}\mathrm{As}$ *alloy* ($x < 0.45$) *in the vicinity of* Γ. *(b) Qualitative band structure of AlAs and* $\mathrm{Al}_x\mathrm{Ga}_{1-x}\mathrm{As}$ *alloy* ($x > 0.45$) *in the vicinity of* Γ.

failure of VCA to correctly describe the alloy bandgap. Figure 2.3(b) qualitatively shows the band structure of AlAs and the ternary $\mathrm{Al}_x\mathrm{Ga}_{1-x}\mathrm{As}$ alloy for $x > 0.45$. The fundamental band gap is indirect and corresponds to transitions between the valence band at Γ and the conduction band at X. The X conduction band minimum in AlAs is below the Γ conduction band edge in AlAs, which is at higher energy than in GaAs. The bandgaps are temperature-dependent; the values in Tab. 2.1 apply to $T = 2$ K [Ont74].

The conduction band effective mass in AlAs is more than double the GaAs effective mass, $m_{e,\mathrm{AlAs}} = 0.15\,m_0$. The valence band masses are determined by the AlAs Luttinger parameters $\gamma_1 = 3.45$, $\gamma_2 = 0.68$, $\gamma_3 = 1.29$ [And90]. Effective masses in $\mathrm{Al}_x\mathrm{Ga}_{1-x}\mathrm{As}$ alloys are obtained by linear interpolation between GaAs and AlAs masses. Effective electron and heavy-hole [001] masses in $\mathrm{Al}_x\mathrm{Ga}_{1-x}\mathrm{As}$ [Ada94] have been calculated using the GaAs Luttinger parameters of Binggeli and Baldereschi [Bin91] and averaged AlAs Luttinger parameters. Table 2.1 summarizes values for band gap and [001] electron and heavy-hole masses in $\mathrm{Al}_x\mathrm{Ga}_{1-x}\mathrm{As}$ alloys ($0 \leq x \leq 1$).

E_g/eV	$m_{\mathrm{e},[001]}/m_0$	$m_{\mathrm{hh},[001]}/m_0$
1.519 + 1.36 x + 0.22 x^2	0.067 + 0.083 x	0.33 + 0.18 x

Table 2.1: *Band gap ($T = 2$ K) and [001] effective electron and heavy-hole masses of* $\mathrm{Al}_x\mathrm{Ga}_{1-x}\mathrm{As}$ *alloys* ($0 \leq x \leq 1$) *[Ada94].*

Conduction band nonparabolicity

The interaction of the Γ_6 conduction band with higher conduction bands of symmetry Γ_7 and Γ_8 (see Fig. 2.1) causes a deviation of the conduction band dispersion in GaAs from the parabolic dispersion relation Eq. (2.1) [RoeU84]. The conduction band dispersion up to fourth order in $\boldsymbol{k}$ is [Eke89]

$$\begin{aligned} E(\boldsymbol{k}) = \frac{\hbar^2 k^2}{2m_e} &+ \alpha_0 k^4 + \beta_0 (k_x^2 k_y^2 + k_y^2 k_z^2 + k_z^2 k_x^2) \\ &\pm \gamma_0 \left[k^2 (k_x^2 k_y^2 + k_y^2 k_z^2 + k_z^2 k_x^2) - 9 k_x^2 k_y^2 k_z^2\right]^{1/2}, \end{aligned} \tag{2.10}$$

where $k = |\boldsymbol{k}|$, m_e is the effective electron mass, and the nonparabolicity parameters α_0, β_0, γ_0 are determined from numerically calculated band structures. The last term describes the spin splitting due to the lack of inversion symmetry in GaAs. The values for the nonparabolicity parameters α_0, β_0, γ_0 are all negative. Using a 14-band k·p model [Bra85], values for GaAs have been numerically determined: $\alpha_0 = -2107$ eV Å^4, $\beta_0 = -2208$ eV Å^4, $\gamma_0 = -27.57$ eV Å^3 [Mal86, Eke89]. The effects of nonparabolicity become important in quantum wells, where the lowest confined state lies well above the conduction band edge.

2.2 Quantum well band structure

2.2.1 GaAs/Al$_x$Ga$_{1-x}$ As heterojunctions and heterostructures

The fabrication of semiconductor heterointerfaces with controlled profiles (doping, chemical composition) on the nanometer scale was initiated by proposals for the realization of artificial semiconductor heterostructures [Kro57a, Kro57b, Esa70] and the development of molecular beam epitaxy (MBE) of III-V semiconductor materials [Cho70]. Two semiconductor materials grown on top of each other using heteroepitaxy form a heterointerface. Electronic properties change more or less abruptly at the interface, since band gaps and effective masses usually differ between the two materials. The band offsets at a GaAs/Al$_{0.3}$Ga$_{0.7}$As heterojunction are shown in Fig. 2.4(a). The conduction band edge in GaAs is at lower energy than the conduction band edge in Al$_{0.3}$Ga$_{0.7}$As, while the valence band edge in GaAs is at higher energy. Conduction and valence band offsets cause reflection of electrons and holes at the heterojunction. In a double heterojunction where, e.g., a thin GaAs film is sandwiched between Al$_{0.3}$Ga$_{0.7}$As barriers with larger bandgap, the quantum mechanical reflection of electrons at the nearby heterojunctions leads to discrete subbands of electron and hole states confined to the GaAs layer. The so-called quantum size effect (*quantum confinement*) has been first observed in low-temperature optical absorption spectra of an MBE-grown GaAs/Al$_{0.2}$Ga$_{0.8}$As multiple quantum well heterostructure with GaAs layer thickness down to 7 nm [Din74].

In a GaAs/Al$_{0.3}$Ga$_{0.7}$As quantum well, electrons and holes are confined to the same layer. This situation is denoted as type-I, i.e., a thin layer of GaAs between Al$_{0.3}$Ga$_{0.7}$As forms a type-I quantum well. The total band gap offset ΔE is distributed between conduction and valence band by the offset ratio f_e/f_h. For GaAs/Al$_{0.3}$Ga$_{0.7}$As heterojunctions, photoluminescence experiments suggest the value $f_e/f_h = 0.65/0.35$ [Dug85, Wol86, Kop92].

The band offsets at a GaAs/AlAs heterojunction are shown in Fig. 2.4(b). Since AlAs has an indirect bandgap with the conduction band minimum at the X-point, the band edges at the X-point are shown in addition to the conduction band edges at Γ. For electrons at the X-point, the band offsets at the GaAs/AlAs heterojunction are contravariant, i.e., the AlAs-GaAs conduction band offset at the X-point and the AlAs-GaAs valence band offset at the Γ-point are both negative. For Γ-electrons, the AlAs-GaAs band offsets are covariant. Therefore, depending on the growth sequence and on the widths of GaAs and AlAs layers, a sequence of GaAs and AlAs layers results in a type-I or a type-II heterostructure.

Since the GaAs conduction band minimum at Γ lies below the X-minimum in AlAs, the lowest confined Γ-electron state in not too narrow GaAs/AlAs quantum wells lies below the X-minimum in the AlAs barrier. In this case, the electron ground state of the heterostructure is localized in the well. Type-II ground states occur when the Γ electron ground state (E_0^Γ) in the well is pushed above the E_0^X ground state in the AlAs barrier. This happens in very narrow GaAs/AlAs wells ($d < 3.5$ nm) [Moo88].

Electron and hole states in idealized quantum wells are often described in the envelope function approximation (EFA) [Lut55, Bas88]. Using the EFA, the wave functions of electrons and holes in a semiconductor heterostructure are described by products of

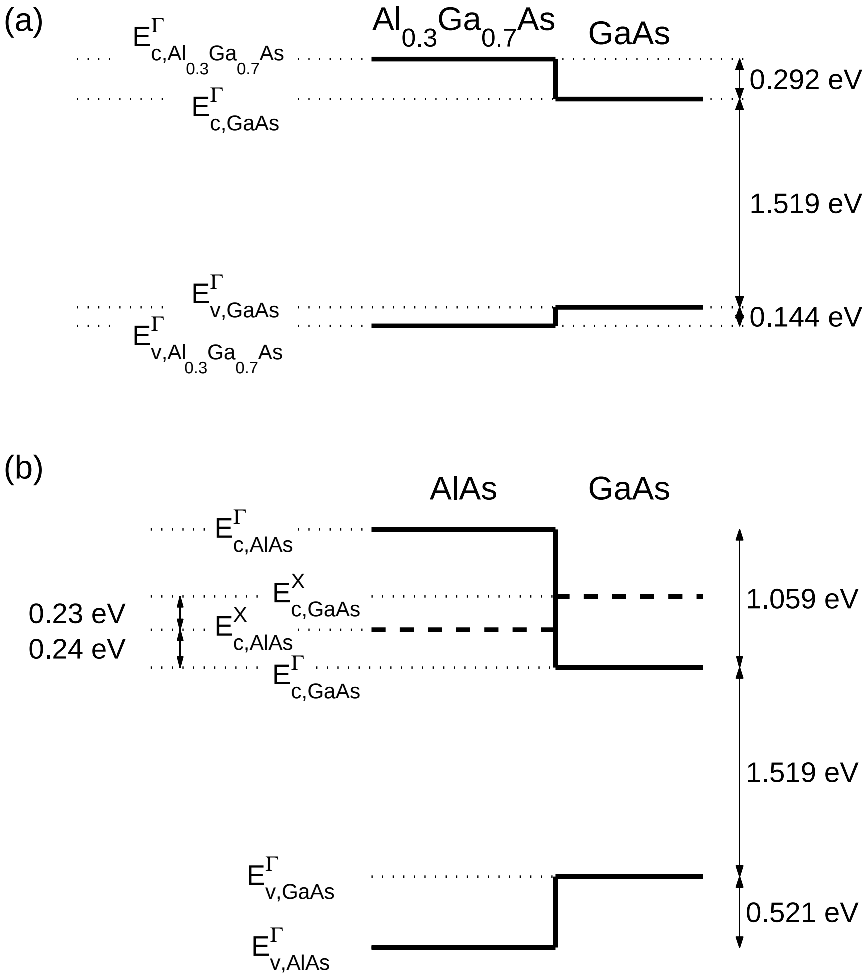

Figure 2.4: *Band alignment at (a) $Al_{0.3}Ga_{0.7}As/GaAs$ and (b) AlAs/GaAs heterojunctions. In (a), the conduction and valence band edges at Γ are shown (solid lines). In (b), also the valence band edges at the X point are shown (dashed lines). Band gaps and band offsets at $T = 2$ K are indicated.*

Bloch functions and envelope functions. While the Bloch functions reflect the atomistic structure of the semiconductor material, the envelope functions describe the spatial confinement of the quasiparticles (electron, hole) in the heterostructure on a nm scale. Due to the one-dimensional confinement in growth direction (z), the envelope functions of electron and hole states in a quantum well depend on the z-coordinate only. The QW envelope functions can therefore be calculated in a one-dimensional model, using the material-dependent band offsets in bulk [Bas88]. In the simplest case (assuming constant masses throughout the heterostructure), this model is analogous to the quantum mechanical model of a particle in a box. The energy of the lowest confined state is denoted as confinement energy.

In-plane band structure of GaAs/Al$_x$Ga$_{1-x}$ As quantum wells

Every confined level in the above-mentioned model corresponds to a subband, since electrons and holes are allowed to move freely in the QW plane (x, y) according to the in-plane band structure of the respective subband. Due to the breaking of the crystal symmetry in quantum wells, the QW in-plane band structure differs from the bulk crystal band structure normal to the (001) direction. The next two paragraphs describe the in-plane band structure of conduction and valence bands in narrow (001) GaAs/Al$_x$Ga$_{1-x}$ As quantum wells. With some caution, an effective-mass description of the in-plane band structure is possible. This requires the definition of in-plane and perpendicular effective masses ($m_{\|}$, $m_{\perp}$) for electrons and holes, that depend on the QW width.

Conduction band Using the bulk conduction band dispersion [Eq. (2.10)], including nonparabolicity effects in lowest order in k, and calculating confinement energies for a quantum well with infinite barriers, energy-dependent effective electron masses can be defined by [Eke89]

$$m_{e,\perp} = m_e\,(1+\alpha'\epsilon)\,, \quad m_{e,\|} = m_e\,[1+(2\alpha'+\beta']\epsilon\,, \tag{2.11}$$

where m_e is the bulk effective electron mass. The parameters α', β' are related to the nonparabolicity parameters α_0, β_0 in Eq. (2.10), and ϵ is the confinement energy of the lowest subband. The nonparabolicity parameters α', β' are related to α, β by

$$\alpha' = -(\frac{2m}{\hbar^2})^2\,\alpha\,, \quad \beta' = -(\frac{2m}{\hbar^2})^2\,\beta\,. \tag{2.12}$$

For GaAs, $\alpha' = 0.64$ eV^{-1} and $\beta' = 0.7$ eV^{-1} [Eke89]. Results obtained by Ekenberg for in-plane and perpendicular electron masses $m_{e,\|}$, $m_{e,\perp}$ in narrow GaAs/Al$_{0.3}$Ga$_{0.7}$As quantum wells are shown in Fig. 2.5. The bulk effective electron mass in GaAs is indicated by the dashed line. The enhancement of the in-plane effective mass $m_{e,\|}$ over the bulk mass value is 2-3 times larger than the enhancement of the perpendicular effective mass $m_{e,\perp}$.

Valence band Denoting the in-plane wave vector with $k_{\|}$, the quantum well confinement lifts the degeneracy of heavy-hole and light-hole bands at $k_{\|} = 0$ [Chu95].

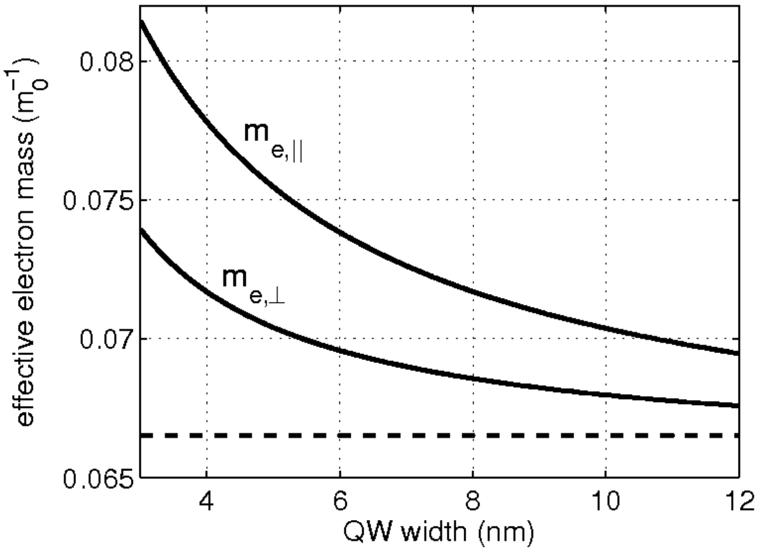

Figure 2.5: *[Eke89] Well-width dependence of effective electron masses in (001) GaAs/Al$_{0.3}$Ga$_{0.7}$As quantum wells in units of the free electron mass m_0. Values for perpendicular ($m_e^\Gamma(\perp)$) and parallel ($m_e^\Gamma(\|)$) electron masses are shown. The dashed line indicates the bulk GaAs value ($m_e^\Gamma = 0.067\ m_0$).*

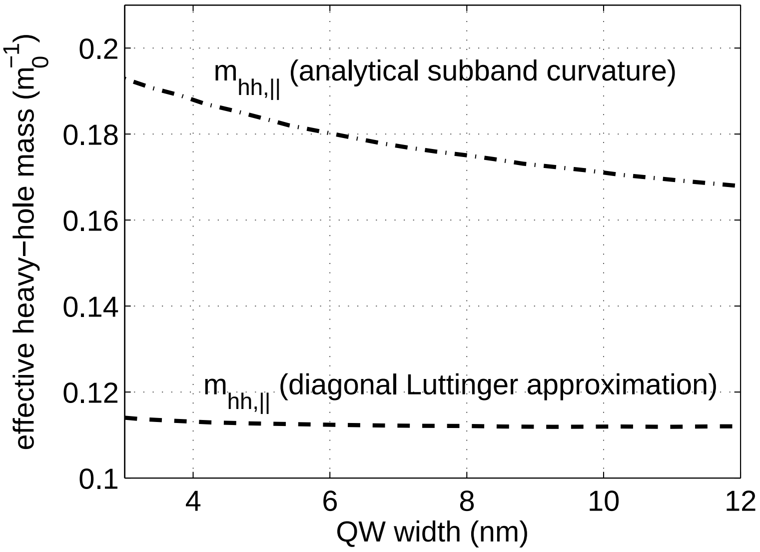

Figure 2.6: *[Sia00] Well-width dependence of the effective in-plane heavy-hole mass in (001) GaAs/Al$_{0.3}$Ga$_{0.7}$As quantum wells in units of the free electron mass m_0. Values have been calculated: (i) using the diagonal Luttinger approximation $1/m_h = P_w(\gamma_1^w + \gamma_2^w) + P_b(\gamma_1^b + \gamma_2^b)$, where $P_{w,b}$ denotes the probability that the hole is in the well and barrier material, respectively (dashed line); and (ii) taking as the hole mass the subband curvature at the Γ point that is known analytically [For94].*

Calculated QW valence band structures (see e.g. [Chu95]) show that heavy-hole and light-hole subband minima are split by several meV in narrow quantum wells. Within the Luttinger effective-mass approximation [Eq. (2.6)], a mass reversal of heavy and light hole bands occurs in the (110) plane. Using an average of light- and heavy-hole masses to determine the in-plane dispersion relations, a light mass is obtained in the heavy-hole subband and a heavier mass in the light-hole subband [Din74]. In this model the two subbands are considered decoupled for any $k_{\|}$ value, and, therefore, the bands cross at a certain value of $k_{\|}$. However, the interaction between both bands at finite $k_{\|}$ gives rise to an anticrossing behaviour between the bands, leading to a flattening of the in-plane dispersion relation of the heavy-hole subband [Maa84]. Figure 2.6 shows that the diagonal Luttinger approximation – where bulk masses for barrier and well are weighted with the portions of the wave function in barrier and well – predicts a too small in-plane heavy-hole effective mass (i) compared to the result that is obtained when the quantum well subband curvature at $k_{\|} = 0$, which is analytically known [For94], is taken as the heavy-hole mass (ii). The values shown in Figure 2.6 have been taken from [Sia00]. The heavy-hole in-plane mass, that is determined from the quantum well subband curvature, increases with decreasing QW width.

2.3 Electronic states in quantum wells

In the envelope function formalism (EFF), electronic states in a heterostructure consisting of materials A and B are *exactly* described by a product of an envelope function $u(\boldsymbol{r})$ and the cell periodic part of a zone-center Bloch function $f_\Gamma(\boldsymbol{r})$, separately for each material region,

$$\psi^X(\boldsymbol{r}) = u^X(\boldsymbol{r})\, f_\Gamma^X(\boldsymbol{r})\,, \quad \boldsymbol{r} \in X\,, \tag{2.13}$$

where $X = A, B$ represents the material, the $u^X(\boldsymbol{r})$ are envelope functions, and the zone-center states $f_\Gamma^X(\boldsymbol{r})$ are different in materials A and B. The derivation of the heterostructure effective-mass differential equations and boundary conditions have been thoroughly reviewed by Burt [Bur92]. In the flat band approximation and for a single band, one recovers Schrödinger-like equations of the form [Bar91], separately for electron and hole (a=e,h)

$$H_a(\boldsymbol{r})\, u_a(\boldsymbol{r}) = E_a\, u_a(\boldsymbol{r})\,, \tag{2.14}$$

where $H_a(\boldsymbol{r})$ represents an effective (electron, hole) Hamiltonian for the heterostructure, and $u_a(\boldsymbol{r})$ are envelope functions for electron and hole. The dependence of H_a on the position coordinate $\boldsymbol{r}$ covers the material dependence of band edges and effective masses. Due to the complexity of the exact heterostructure effective-mass equations derived in the envelope function formalism [Bur92], often approximate equations are used.

The simplest example is the one-dimensional particle-in-a-box model applied to electrons or holes in a quantum well. In this model, electronic states are calculated from effective Schrödinger equations

$$-\frac{\hbar^2}{2m_a}\frac{d^2u_a(z)}{dz^2} + V_a(z)u_a(z) = E_a\, u_a(z) \quad (a = e, h)\,, \tag{2.15}$$

where the position-dependent material potentials $V_e(z)$, $V_h(z)$, corresponding to the band offsets of conduction and valence band, are piecewise constant in barrier and

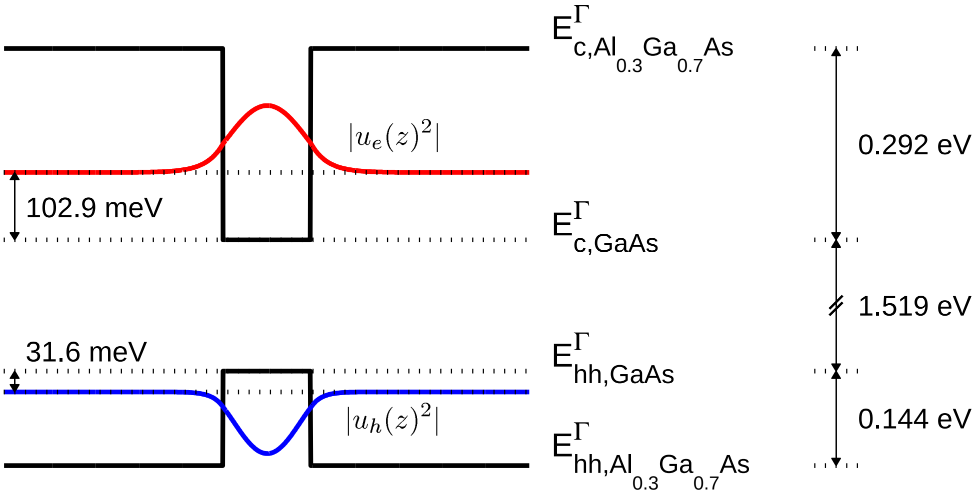

Figure 2.7: *Electron and heavy-hole ground states in a 4-nm GaAs/*$Al_{0.3}Ga_{0.7}As$ *square well. Confinement energies have been calculated in the EFA/VCA using a variable-mass finite-difference method.*

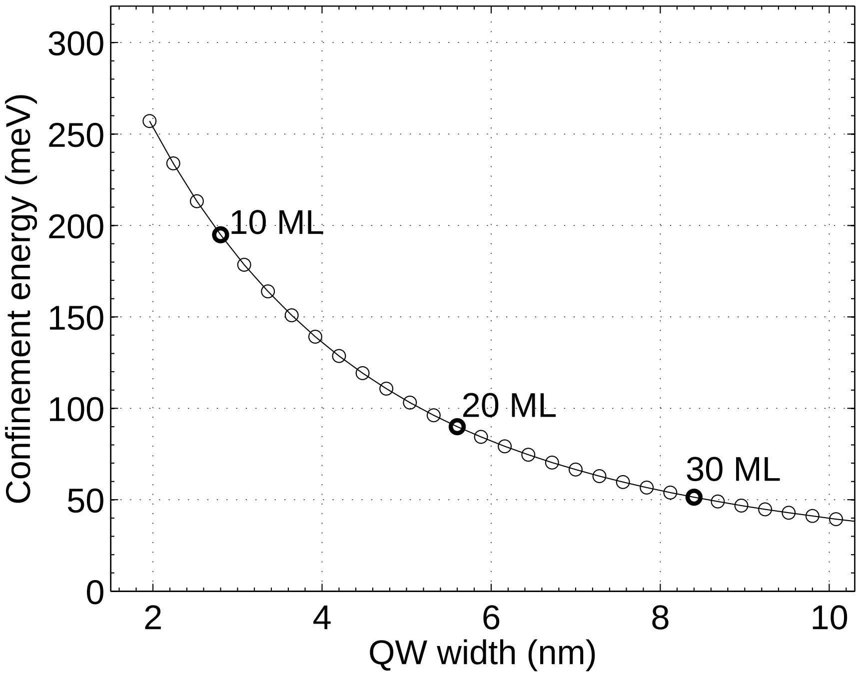

Figure 2.8: *Well-width dependence of the sum of electron and heavy-hole confinement energies in a square GaAs/*$Al_{0.3}Ga_{0.7}As$ *QW. Energies at integer monolayer widths are marked by the open circles. Values have been calculated in the EFA/VCA using a variable-mass finite-difference method.*

well. To distinguish such an approximate approach from the exact EFF, the term envelope function approximation (EFA) is used. An accurate determination of energy levels and single-particle wave functions in the EFA requires to include the different effective masses in barrier and well. It is usually assumed that the so-called current-conserving boundary conditions should be applied at an atomically abrupt interface [Ben66]. A modified kinetic-energy operator with position-dependent mass can be defined, resulting in the heterostructure differential equations

$$\left(-\frac{\hbar^2}{2}\frac{d}{dz}\frac{1}{m_a(z)}\frac{d}{dz} + V_a(z)\right) u_a(z) = E_a\, u_a(z) \quad (a = e, h)\,, \qquad (2.16)$$

where $V_e(z)$, $V_h(z)$ describe the material-dependent band offsets in the heterostructure. Integrating this equation across an interface gives the boundary condition $\frac{1}{m_a(z)} u_a'(z)$ continuous, which is consistent with current conservation [Ben66, Bur92]. A consequence of applying this condition is that the derivatives of the envelope functions u_a become discontinuous because of the change in the effective mass, and a kink in the envelope function results. Such a kink is not present in the exact wave function known from the EFF [Bur94]. This raises questions about the validity of the (variable-mass) particle-in-a-box model. A brief, general discussion of the validity and range of applicability of the EFA has been given by Burt [Bur94]. As general criterion for the applicability of the variable-mass particle-in-a-box-model, it was stated that the envelope function should be slowly varying over the range of a lattice constant. More precise statements about the validity of the EFA require a comparison with results of atomistic model calculations [DiC03].

In a GaAs/$\mathrm{Al_{0.3}Ga_{0.7}As}$ quantum well, the confinement in growth direction can be approximately described by applying the virtual crystal approximation to the $\mathrm{Al_{0.3}Ga_{0.7}As}$ barriers. The effect of composition fluctuations in the barriers is thereby neglected. The combination of envelope function approximation (EFA) and virtual crystal approximation (VCA) is used to calculate electron and hole ground state energies in a [001] GaAs/$\mathrm{Al_{0.3}Ga_{0.7}As}$ quantum well in a one-dimensional model. The band gap values ($T = 2$ K) from Table 2.1 have been used here, the [001] masses from Table 2.1 have been taken as quantization masses, and the band offset ratio $f_e/f_h = 0.65/0.35$ has been assumed.

Figure 2.7 shows valence and conduction band edges of a 4-nm GaAs/$\mathrm{Al_{0.3}Ga_{0.7}As}$ quantum well in the VCA. Ground state energies and envelope (z) wave functions $u_e(z)$, $u_h(z)$ for electron and heavy-hole have been calculated by numerically solving the variable-mass Schrödinger equation Eq. (2.16) using a finite-difference method (see Appendix A). In Fig. 2.7, probability densities $|u_e(z)|^2$, $|u_h(z)|^2$ of electron and heavy-hole z wave functions are shown. The confinement energy of the hole ground state is about one third of the confinement energy of the electron ground state. The total (electron plus hole) confinement energy in the 4-nm GaAs/$\mathrm{Al_{0.3}Ga_{0.7}As}$ QW is ~ 130 meV.

In Fig. 2.8, confinement energy values calculated in the EFA/VCA are shown down to well widths $d_{\mathrm{QW}} = 2$ nm. The open circles mark integer multiples of a monolayer ($d_{\mathrm{ML}} = 0.28$ nm). The confinement energy monotonically increases with shrinking well thickness. Roughly, the total confinement energy is 200 meV at a QW width of 10 monolayers, 100 meV at 20 ML, and 50 meV at 30 ML. Often, the EFA/VCA approximation has been used down to well widths of a few nm. To date, only few calculations of electron confinement energy in GaAs/$\mathrm{Al_{0.3}Ga_{0.7}As}$ quantum wells beyond the EFA/VCA approximation are available [Dar97, DiC03]. The results, obtained from empirical tight-binding calculations, indicate a deviation of confinement energies in thin wells with $d < 5$ nm from the predictions in the EFA/VCA framework. However, it seems difficult to assess the accuracy of the few available results obtained to date. Throughout this work, confinement energies and envelope wave functions calculated in the EFA/VCA framework are used.

2.4 Bulk and quantum well excitons

Wannier excitons in a bulk crystal

Optical properties of semiconductors in the vicinity of the band gap are determined by the Coulomb interaction between electrons and holes. A single Coulomb-correlated electron-hole pair constitutes a quasi-particle, the *exciton*, which can be seen as the elementary optical excitation of an intrinsic semiconductor crystal. The quantum theory for a single exciton has been originally formulated by Elliott [Ell57], using several approximations: A simple parabolic two-band model is used, the Hamiltonian for the exciton is formulated in envelope function approximation, screening of the Coulomb interaction is taken into account by the zero-frequency crystal dielectric constant ϵ, and the short-range exchange interaction is neglected. As a result, the eigenvalue equation ("Wannier equation") [Ell57]

$$\left(-\frac{\hbar^2}{2\mu}\triangle_{\boldsymbol{r}} - \frac{1}{4\pi\epsilon_0}\frac{e^2}{\epsilon|\boldsymbol{r}|}\right)\varphi(\boldsymbol{r}) = E\cdot\varphi(\boldsymbol{r})\,, \tag{2.17}$$

where μ is the effective reduced mass of the exciton and $\boldsymbol{r} = \boldsymbol{r_e} - \boldsymbol{r_h}$ is the electron-hole relative coordinate, is a mathematical analogon of the Schrödinger equation for the hydrogen atom. More accurate theories have been developed later, taking the valence band structure in III-V semiconductors into account [Bal70, Bal71]. In bulk semiconductors, a thorough description of magnetooptical effects (diamagnetic shift) in fact requires the complicated valence band structure. However, in quantum wells the degeneracy of heavy- and light-hole bands at $k_{\|} = 0$ is lifted, and the exciton states formed from the lowest electron and heavy-hole subbands are well described within a two-band model, including only conduction band and the upmost hole band.

Figure 2.9 ("two-particle picture") shows the exciton energy levels, where "0" represents the crystal ground state. The lowest two parabolas show the energies of ground and first excited exciton state as a function of the exciton center-of-mass wavevector $\boldsymbol{K} = \boldsymbol{k}_e + \boldsymbol{k}_h$. Using effective masses m_e, m_h for electron and hole and introducing the effective exciton total mass $M = m_e + m_h$, the total energy of the lowest exciton state is $E_1 = E_G - E_X + \hbar^2/(2M)\boldsymbol{K}^2$, where E_G is the band gap energy and E_X the exciton binding energy. The highest parabola indicates the continuum edge, separating higher excited exciton states from unbound, but electron-hole pair states that exist in the grey shaded area.

According to the Wannier equation [Eq. (2.17)], the binding energy of the exciton

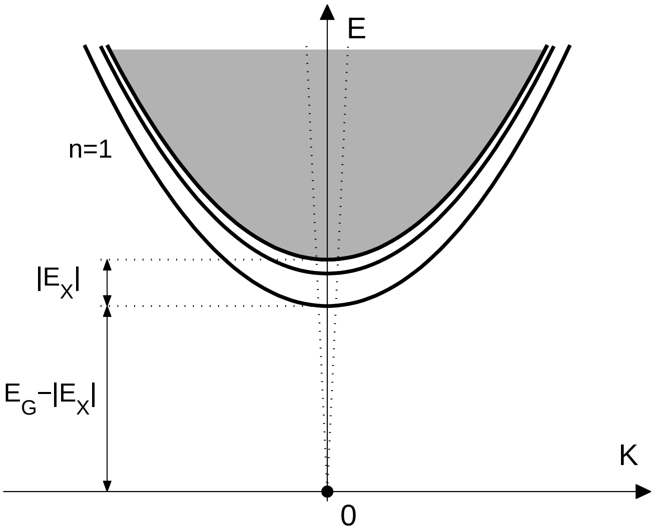

Figure 2.9: *Scheme of exciton energy levels ("two-particle picture"):* $\boldsymbol{K} = \boldsymbol{k}_e + \boldsymbol{k}_h$ *is the center-of-mass momentum of the exciton,* E *the total energy of the two-particle states [Eq. (2.17)]. The lowest (*$n = 1, 2$*) bound states are shown as well as the continuum edge; continuum states are shown shaded grey. Resonant absorption of photons from the crystal ground state ("0") and emission of photons upon exciton recombination occurs at the intersection of exciton dispersion and photon dispersion (*$E = \hbar c K$*).*

ground state can be expressed by the hydrogen Rydberg $\mathrm{Ry} = e^4\mu/(32\pi\hbar^2\epsilon_0^2)$,

$$E_X = -\frac{\mu}{m_0\,\epsilon^2}\,\mathrm{Ry}\,. \tag{2.18}$$

Taking the inverse exciton reduced mass in bulk GaAs, $1/\mu$, as the sum of inverse effective electron mass $m_e = 0.067$ m$_0$ and inverse density-of-states effective hole mass $m_h = 0.5$ m$_0$ [Ada94], and using the zero-frequency dieelectric constant $\epsilon = 12.8$ [Ada90, Ada94],

$$E_X = 4.9 \text{ meV} \tag{2.19}$$

is found for the exciton binding energy in bulk GaAs. Experimentally, a smaller value, $E_X \approx 4.2$ meV, has been reported [Sel72]. More accurate calculations including the complex valence band structure gave similar values [Bal71, Gon90]. The exciton ground state is described by an exponential 1s wave function

$$\varphi_{1\mathrm{s}}(\boldsymbol{r}) = \frac{1}{\sqrt{\pi a_B^3}} \cdot e^{-\frac{|\boldsymbol{r}|}{a_B}}\,, \tag{2.20}$$

where a_B is the exciton Bohr radius. The exciton Bohr radius a_B is related to the hydrogen Bohr radius $a_0 = 0.0529$ nm by

$$a_B = \frac{m_0}{\mu}\,\epsilon\, a_0\,. \tag{2.21}$$

Using the same effective masses m_e, m_h and the same dieelectric constant ϵ as in the calculation of the exciton binding energy above, the value $a_B = 11.5$ nm is found for the exciton Bohr radius in bulk GaAs.

Exciton envelope wave function In a perfectly periodic crystal, the exciton is constituted by Bloch electron and hole states. The exciton wave function can be expressed by single-particle wave functions in a product ansatz [Yu96]

$$\Phi(\boldsymbol{r}_e, \boldsymbol{r}_h) = \sum_{\boldsymbol{k}_e, \boldsymbol{k}_h} C(\boldsymbol{k}_e, \boldsymbol{k}_h)\, \psi_{\boldsymbol{k}_e}(\boldsymbol{r}_e)\, \psi_{\boldsymbol{k}_h}(\boldsymbol{r}_h)\,, \tag{2.22}$$

where $\psi_{\boldsymbol{k}_e}(\boldsymbol{r}_e)$, $\psi_{\boldsymbol{k}_h}(\boldsymbol{r}_h)$ are Bloch functions of electron and hole. To express the spatial correlation of electron and hole, it is convenient to use fourier transforms of the Bloch functions, the so-called *Wannier functions* [Wan37]

$$a_{\boldsymbol{R}}(\boldsymbol{r}) = \sum_{\boldsymbol{k}} \psi_{\boldsymbol{k}}(\boldsymbol{r})\, e^{-i\,\boldsymbol{k}\,\boldsymbol{R}}\,, \tag{2.23}$$

which are labeled by lattice vectors $\boldsymbol{R}$. The total exciton wave function

$$\Phi(\boldsymbol{r}_e, \boldsymbol{r}_h) = N^{-1/2} \sum_{\boldsymbol{R}_e, \boldsymbol{R}_h} \Psi(\boldsymbol{R}_e, \boldsymbol{R}_h)\, a_{\boldsymbol{R}_e}(\boldsymbol{r}_e)\, a_{\boldsymbol{R}_h}(\boldsymbol{r}_h)\,, \tag{2.24}$$

where N is a normalization factor, is then fully characterized by the exciton envelope wave function $\Psi(\boldsymbol{R}_e, \boldsymbol{R}_h)$, which describes relative and center-of-mass (c.m.) motion of electron and hole.

Quantum well excitons

In a quantum well, translational symmetry in growth direction is broken by the QW barriers. Single-particle (electron, hole) states in a QW are described in the envelope function approximation by one-dimensional wave functions [Eq. 2.16)]. In narrow quantum wells, the corresponding single-particle confinement energy is significantly larger than the exciton binding energy (compare Fig. 2.8). Consequently, it can be assumed that the Coulomb interaction between electron and hole barely disturbs the quantized vertical motion of electron and hole. The energy spacings between electron and hole subbands are also large compared to exciton binding energy. Hence, only the lowest electron and hole subbands contribute to the exciton ground state in the quantum well. Therefore, the exciton ground state can be derived from the lowest single-particle electron and hole subbands in narrow quantum wells [Mil85, And90]. Using the envelope function formalism, the motion of electron and hole in z-direction can approximately be factored out from the full exciton wave function of the exciton ground state, separating 3d vectors into in-plane ($\boldsymbol{\rho_e}, \boldsymbol{\rho_h}$) and z components, and taking only the lowest electron and hole subbands into account [Run02]. This separation ansatz leads to the factorization of the full (six-coordinate) envelope wave function of the exciton ground state α in the lowest-subband electron/hole z wave functions $u_e(z_e)$, $u_h(z_h)$ and the in-plane exciton wave function $\phi_\alpha(\boldsymbol{\rho}_e, \boldsymbol{\rho}_h)$,

$$\Psi_\alpha(\boldsymbol{\rho}_e, \boldsymbol{\rho}_h, z_e, z_h) = u_e(z_e)\, u_h(z_h)\, \phi_\alpha(\boldsymbol{\rho}_e, \boldsymbol{\rho}_h)\,. \tag{2.25}$$

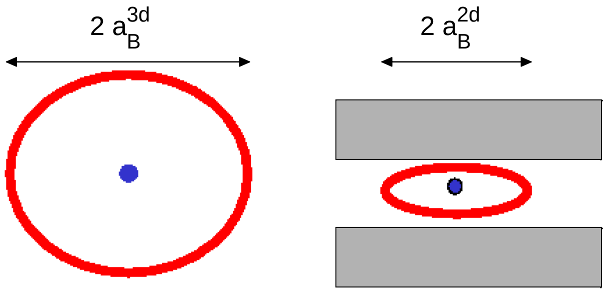

Figure 2.10: *Sketch of bulk and QW excitons. The bulk exciton has spherical symmetry; in a narrow quantum well, the exciton wave function is squeezed in growth direction. The exciton binding energy in a QW is larger than in bulk, and the lateral exciton radius* a_B^{2d} *is smaller than the bulk Bohr radius* a_B^{3d}*.*

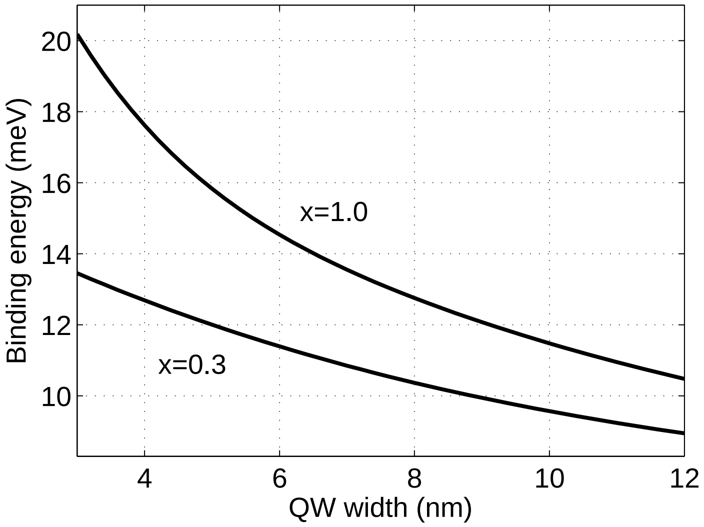

Figure 2.11: *[And90] Well-width dependence of the binding energy of the heavy-hole 1s exciton in GaAs/Al$_x$Ga$_{1-x}$As quantum wells* ($x = 0.3$ *and* $x = 1$)*. Results of numerical calculations by Andreani and Pasquarello.*

The two-particle eigenvalue equation for the (four-coordinate) in-plane exciton wave function $\phi_\alpha(\boldsymbol{\rho}_e, \boldsymbol{\rho}_h)$

$$H\,\phi_\alpha(\boldsymbol{\rho}_e, \boldsymbol{\rho}_h) = E_\alpha\,\phi_\alpha(\boldsymbol{\rho}_e, \boldsymbol{\rho}_h) \tag{2.26}$$

with the Hamiltonian

$$H = \frac{1}{2m_e}\boldsymbol{p}_e^2 + \frac{1}{2m_h}\boldsymbol{p}_h^2 + V_c(\boldsymbol{\rho}_e - \boldsymbol{\rho}_h)\,, \tag{2.27}$$

where m_e, m_h are in-plane effective masses of electron and hole, $\boldsymbol{p}_e$, $\boldsymbol{p}_h$ are the momenta, and $V_c(\boldsymbol{\rho})$ is the modified Coulomb potential

$$V_c(\boldsymbol{\rho}) = -\frac{e^2}{4\pi\epsilon\epsilon_0}\int dz_e \int dz_h\,\frac{u_e^2(z_e)\,u_h^2(z_h)}{\sqrt{\boldsymbol{\rho}^2 + |z_e - z_h|^2}}\,, \tag{2.28}$$

describes the Coulomb-correlated motion of electron and hole in the QW plane.

In a perfect quantum well with ideal, planar interfaces, the in-plane potential of the QW has translational symmetry. In a GaAs/Al$_x$Ga$_{1-x}$As quantum well, translational symmetry is broken by composition fluctuations in the Al$_x$Ga$_{1-x}$As barriers even for a nominally perfect interface between GaAs and Al$_x$Ga$_{1-x}$As. Here, the virtual crystal approximation is applied to the Al$_x$Ga$_{1-x}$As barriers. Translational symmetry in the x-y plane is thereby artificially enforced, and relative and center-of-mass (c.m.) motion of the exciton in the plane of the QW can be separated. The two-particle in-plane wave function $\phi(\boldsymbol{\rho}_e, \boldsymbol{\rho}_h)$ factorizes into a product of c.m. wave function $\psi(\boldsymbol{R})$ and relative wave function $\varphi(\boldsymbol{\rho})$, where the in-plane c.m. and relative coordinates $\boldsymbol{R}$ and $\boldsymbol{\rho}$ have been introduced. The form of the in-plane exciton relative wave function $\varphi(\boldsymbol{\rho})$ is determined by the modified in-plane Coulomb potential $V_c(\boldsymbol{\rho})$ [Eq. (2.28)]. The function $V_c(\boldsymbol{\rho})$ shows a logarithmic divergency at short distances and the expected $1/\rho$ behaviour at large ρ [Run02]. Compared to the $1/r$ singularity of the bare Coulomb potential, the singularity at $\rho = 0$ of $V_c(\boldsymbol{\rho})$ is weak, and the relative wave function has no cusp, but looks like a distorted Gaussian near $\rho = 0$. For increasing ρ, it rapidly changes to an exponential decay. An exponential 1s wave function

$$\varphi_{1s}^{2D}(\boldsymbol{\rho}) = \sqrt{\frac{2}{\pi a_B^2}}\,e^{-|\boldsymbol{\rho}|/a_B}\,, \tag{2.29}$$

where a_B denotes the lateral Bohr radius, is a good overall approximation for the in-plane exciton relative wave function in a narrow quantum well [Run02].

2.5 Quantum well excitons in a magnetic field

This section describes the effect of a perpendicular magnetic field on the 1s exciton ground state in a narrow quantum well. The Hamiltonian for the in-plane exciton motion in a perpendicular magnetic field is obtained from Eq. (2.27) by replacing the kinetic momenta $\boldsymbol{p}_e$, $\boldsymbol{p}_h$ with canonical momenta $\boldsymbol{p}_e' = \boldsymbol{p}_e - e\boldsymbol{A_e}$, $\boldsymbol{p}_h' = \boldsymbol{p}_h - e\boldsymbol{A_h}$. Choosing a Coulomb gauge in relative coordinates [Gro05], the vector potentials $\boldsymbol{A_e}$,

$\boldsymbol{A_h}$ can be defined by

$$\boldsymbol{A}_e = -\frac{1}{2}\boldsymbol{B} \times \boldsymbol{r}\,, \boldsymbol{A}_h = -\boldsymbol{A}_e\,, \tag{2.30}$$

where writing vector components explicitly has been avoided by introducing the three-dimensional vector $\boldsymbol{r} = (\boldsymbol{\rho}, 0)$, and $\boldsymbol{\rho} = \boldsymbol{\rho}_e - \boldsymbol{\rho}_h$ is the in-plane exciton relative coordinate.

The Hamiltonian for the in-plane exciton motion in a perpendicular magnetic field can be written [Gro05]

$$\begin{aligned} H = &-\frac{\hbar^2}{2M}\triangle_R - \frac{\hbar^2}{2\mu}\triangle_r + V_c(\rho) \\ &+ \frac{e^2B^2}{8\mu}\rho^2 + \frac{eB}{2}(\frac{1}{m_e} - \frac{1}{m_h}) \cdot i\hbar(\boldsymbol{r} \times \mathrm{grad}_{\boldsymbol{r}})_z + \frac{eB}{M} i\hbar(\boldsymbol{r} \times \mathrm{grad}_{\boldsymbol{R}})_z\,, \end{aligned} \tag{2.31}$$

where the in-plane c.m. vector $\boldsymbol{R}$ is considered as a three-dimensional vector to avoid writing vector components explicitly in the vector-product-like expressions.

At vanishing magnetic field ($B = 0$), Eq. (2.31) reduces to the Hamiltonian of a quasi-two-dimensional exciton, Eq. (2.27). In this case, c.m. and relative motion are decoupled, and the relative wave function of the ground state is described by an exponential 1s wave function [Eq. (2.29)]. The lateral exciton c.m. motion in the QW plane is described in detail in [Sia00]. Due to the lateral extension of the exciton in real space ($\sim a_B$), the exciton averages over the subband dispersions in k-space on a length scale $\sim 1/a_B$ [Sia00]. The total exciton mass is therefore well described by a k-space average over valence and conduction band dispersion, using the fourier transform of the exciton 1s wave function. This leads to a further increased exciton in-plane total mass M compared to the value obtained by simply taking the sum of the effective electron and hole masses [Sia00].

In presence of a perpendicular magnetic field, three additional terms appear in the exciton Hamiltonian: Due to the three B-dependent terms in Eq. (2.31), the magnetic field couples to the radial part of the exciton relative motion ($\sim \rho^2$), the angular part of the exciton relative motion ($\sim L_z = -i\hbar(\boldsymbol{r} \times \mathrm{grad}_{\boldsymbol{r}})_z$), and to the c.m. motion. The third term also directly couples relative and c.m. motion.

An analytic solution of the full exciton Schrödinger equation at arbitrary magnetic field, described by the the exciton Hamiltonian Eq. (2.31), is largely impossible. Only the limiting cases of low and high magnetic field are accessible to analytic solutions. Two energy scales are involved in the problem of an exciton in a magnetic field: exciton binding energy and cyclotron energy. Equivalenty, the involved length scales can be used: The lateral exciton Bohr radius a_B of the quasi-two-dimensional exciton, and the cyclotron radius or *magnetic length* [Joh49]

$$\lambda = \sqrt{\hbar/eB}\,. \tag{2.32}$$

As long as the cyclotron energy is much smaller than the exciton binding energy, or, equivalenty, the cyclotron radius is larger than the exciton Bohr radius, $\lambda \gg a_B$, the B-field represents a small perturbation of the Coulomb-correlated exciton ground state.

Low-field limit Treating the B-field as a small perturbation of the Coulomb-correlated exciton ground state Eq. (2.29) and denoting the change of the exciton energy of an exciton state α by $\Delta_\alpha(B)$,

$$E_\alpha(B) = E_\alpha(B=0) + \Delta_\alpha(B)\,, \tag{2.33}$$

the effects of the three B-dependent terms in Eq. (2.31) are evaluated separately in lowest-order perturbation theory. The first B-dependent term in Eq. (2.31) causes the diamagnetic shift $\Delta(B)$ of a 1s exciton state [Hop61]

$$\Delta_{dia}(B) = \frac{e^2}{8\mu}\langle\,\rho^2\rangle_{1s}\,B^2\,. \tag{2.34}$$

The resulting shift of the ground state is positive and quadratic in B.

The lowest-order contribution of the second B-dependent term in Eq. (2.31) is linear in B; for states with nonzero angular momentum, it describes the Zeeman effect. For the 1s exciton ground state,

$$\Delta_{\mathrm{zee}}(B) = \frac{eB}{2}\left(\frac{1}{m_h} - \frac{1}{m_e}\right)\cdot\langle\,L_z\,\rangle_{1s} = 0\,, \tag{2.35}$$

since $\langle\,L_z\,\rangle_{1s} = 0$. If the effective in-plane masses of electron and hole were equal, this term would be generally equal to zero, independent of the angular momentum of the exciton state.

Since the first-order contribution of the first term in Eq. (2.31) is proportional to B^2, the second-order perturbation resulting from the second term has to be included, too. It describes the effect of admixing of excited states (i) with higher angular momentum to the ground state (s). For a 1s exciton ground state, the so-called van Vleck paramagnetic term is equal to zero,

$$\Delta_{\mathrm{vv}}(B) = \frac{e^2}{m^2}\,B^2\sum_{i\neq s}\frac{\langle\,i|L_z|s\,\rangle}{E_s - E_i} = 0\,, \tag{2.36}$$

since $L_z|s\,\rangle = 0$.

The third term in Eq. (2.31) is a cross-term which couples relative and c.m. motion in the presence of a B-field. The c.m. motion of two-dimensional excitons in a magnetic field has been recently studied in detail by Lozovik *et al.* [Loz02]. In absence of lateral confinement, the coupling of the B-field to the c.m. motion leads to an increase of the total exciton mass. This effects only becomes important for indirect excitons in coupled quantum wells where charge separation occurs. For direct excitons, this effect is very small [Loz02]. With respect to optical transitions, only excitons (almost) at rest are relevant.

In conclusion, the effect of a perpendicular magnetic field on a quasi-two-dimensional 1s exciton is described in the low-field limit by the diamagnetic shift

$$\Delta_{dia}(B) = \frac{e^2}{8\mu}\langle\,\rho^2\rangle_{1s}\,B^2\,, \tag{2.37}$$

which is positive and quadratic in B. The diamagnetic shift coefficient

$$\gamma_2 = \frac{e^2}{8\mu}\langle \rho^2 \rangle_{1s} \tag{2.38}$$

is proportional to the area of the exciton relative wave function, and depends on the effective in-plane exciton reduced mass.

So far, the spin of electron and hole has been neglected. For excitons composed of an electron ($S_e = 1/2$) and a heavy hole ($J_h = 1/2$), the effective exciton spin $J = S_e + J_h$ is either $J = 1$ or $J = 2$. Since a 1s exciton state carries no angular momentum, the effective exciton spin provides the angular momentum $\hbar$ of an emitted photon. Therefore, only $J = 1$ excitons are optically active ("bright"); $J = 2$ exciton transitions are dipole-forbidden ("dark"). An external magnetic field couples to the effective exciton spin and causes Zeeman splitting of electron and hole levels in doublets with energy separation $\Delta E_e = g_e^* \mu_B B$ and $\Delta E_h = g_h^* \mu_B B$ [Ivc95], where g_e^* and g_h^* are g-factors for electron and hole, and $\mu_B = e\hbar/2m_0 = 57.9\,\mu\text{eV/T}$ is the Bohr magneton. The linear Zeeman splitting of the $J = 1$ exciton doublet is described by an exciton g-factor $g_{ex}^* = g_e^* + g_h^*$ [Sne92].

Returning to the diamagnetic shift, with increasing magnetic field the "cyclotron confinement" of electron and hole causes an increasing deviation from the quadratic shift. The transition from low-field to high-field case in two dimensions has first been described by Akimoto and Hasegawa [Aki67], extending previous work of Elliott and Loudon [Ell60] and Hasegawa and Howard [Has61]. It was realized that in two dimensions, a smooth transition from the Coulomb-correlated exciton motion at low fields to a Landau-like behaviour at high field exists [Aki67]. The reason is that for a two-dimensional exciton, a magnetic field normal to the x-y-plane causes complete confinement, i.e., the magnetoexciton can be considered zero-dimensional. The Coulomb interaction is therefore completely quenched by (i) vertical confinement due to the quantum well and (ii) lateral cyclotron confinement. In comparison, a three-dimensional hydrogen atom laterally confined by a magnetic field still extends into the third dimension. At high fields, the spectrum of the three-dimensional magnetoexciton therefore resembles that of a one-dimensional exciton. Wave functions of exciton s-states thereby acquire

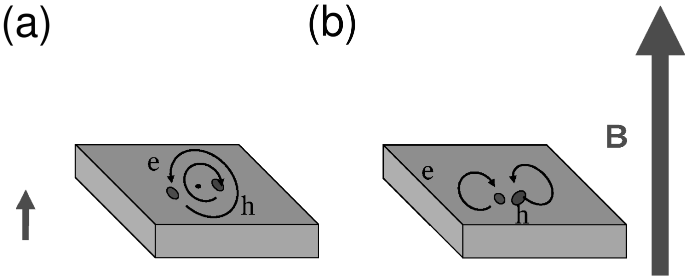

Figure 2.12: *Sketch of the limiting cases of the two-dimensional magnetoexciton motion in a perpendicular magnetic field. (a) Low-field limit: The magnetic field represents a small perturbation of the Coulomb-correlated motion of electron and hole. (b) High-field limit: The Coulomb interaction represents a small perturbation of the cyclotron motion of electron and hole.*

cigar-like shapes [Gar77, RoeW84]. Due to the complete three-dimensional confinement of a quasi-two-dimensional exciton, the magnetoexciton problem in two dimensions in presence of a perpendicular magnetic field is simpler than the three-dimensional magnetoexciton problem.

High-field limit In the high-field limit, the magnetoexciton energy is dominated by the linear B-dependence of the single-particle levels,

$$E(B) = E(0) + (n_e + \frac{1}{2})\,\hbar\omega_e + (n_h + \frac{1}{2})\,\hbar\omega_h \tag{2.39}$$

where $\omega_{e,h} = eB/m_{e,h}$ is the cyclotron frequency of electron and hole. Although n_e, n_h do not exactly correspond to the quantum numbers of Landau levels due to the presence of Coulomb interaction, a magnetic field can be defined for each exciton state above which a Landau-like energy dependence of its energy is observed [Aki67]. In the strict two-dimensional case, a small term $\propto \sqrt{B}$ due to the B-dependence of the magnetoexciton binding energy adds to the linear dependence in Eq. (2.39). Referring to the high-field magnetoexciton levels in Eq. (2.39) as Landau levels for simplicity, the B-dependence of the lowest Landau level is approximately given by

$$\Delta(B) = \Delta_0 + \frac{\hbar e}{2\mu}\,B\,. \tag{2.40}$$

Transition field The magnetic field B_0 where the transition from low field to high field occurs can be defined by comparing exciton Bohr radius a_B and cyclotron radius $\lambda = \sqrt{\hbar/eB}$. More precisely, we define the transition field B_0 by requiring that cyclotron radius λ and lateral exciton Bohr radius a_B be equal. This results in the definition

$$B_0 = \frac{\hbar}{e\,a_B^2}\;. \tag{2.41}$$

Taking as an example the exciton ground state in a 4-nm GaAs/Al$_{0.3}$Ga$_{0.7}$As QW, where $a_B = 8.2$ nm [Gro06], magnetic length λ and exciton Bohr radius a_B coincide at $B_0 \sim 10$ T. This means that a magnetic field achievable with a superconducting laboratory magnet causes a significant perturbation of the wave function of the 1s exciton ground state in a narrow GaAs/Al$_{0.3}$Ga$_{0.7}$As quantum well.

2.5.1 Diamagnetic coefficient

In this subsection, diamagnetic coefficients of 1s exciton states are calculated for the limiting cases of narrow GaAs/AlGaAs quantum wells and of bulk GaAs. Assuming an exponential wave function for the 1s ground state in two dimensions [Eq. (2.29)], straightforward evaluation of the expectation value

$$\begin{aligned}\langle\, \varphi_{1s}^{2D}\,|\,\boldsymbol{\rho}^2\,|\,\varphi_{1s}^{2D}\,\rangle &= \int\limits_{x=-\infty}^{\infty} dx \int\limits_{y=-\infty}^{\infty} dy\; (x^2+y^2)\; |\varphi_{1s}^{2D}(\rho(x,y))|^2 \\ &= \int\limits_{\phi=0}^{2\pi} d\phi \int\limits_{\rho=0}^{\infty} \rho\; d\rho \cdot \rho^2\, \varphi_{1s}^{2D}(\rho) = 2\pi\cdot\frac{2}{\pi a_B^2}\int\limits_{\rho=0}^{\infty}\rho^3\; d\rho\; e^{-2\rho/a_B} = \frac{3}{2}\,a_B^2\end{aligned} \tag{2.42}$$

shows that the effective exciton radius of a 2d exciton is

$$d_{\mathrm{2d}} = \sqrt{\langle\rho_{1s}^2\rangle} = \sqrt{\frac{3}{2}}\,a_B\,, \tag{2.43}$$

where a_B denotes the lateral Bohr radius of the two-dimensional exciton. Since the Bohr radius of a 2d exciton is exactly half the Bohr radius of a three-dimensional exciton, $a_B^{2d} = 1/2\cdot a_B^{3d}$, and using that the bulk exciton radius in GaAs is $a_B^{3d} = 11.5$ nm, we find $d^{2D} = \sqrt{3/2}\,a_B^{2D} = 7.0$ nm for the effective radius of the exciton ground state in an ultranarrow GaAs quantum well with infinite barrier height. The Bohr radius of excitons in real quantum wells is always larger due to the finite barrier height and, consequently, the finite probability to find electron and hole in the barriers.

Using Eq. (2.37) and (2.43), the diamagnetic coefficient of a quasi-two-dimensional exciton is obtained as

$$\gamma_2 = \frac{3}{16}\frac{e^2}{\mu}a_B^2\,, \tag{2.44}$$

where a_B is the lateral Bohr radius. For a 4-nm GaAs/AlGaAs quantum well, $\gamma_2 = 37\,\mu\mathrm{eV/T}^2$ is found using the parameters $m_e = 0.078$ m$_0$, $m_h = 0.23$ m$_0$, and $a_B = 8.2$ nm.

In wide quantum wells with a thickness larger than the exciton diameter, the exciton relative wave function will approach the bulk form

$$\varphi_{1s}^{3D}(\boldsymbol{\rho}) = \frac{1}{\sqrt{\pi\,a_B^3}}\,e^{-|\boldsymbol{\rho}|/a_B}\,, \tag{2.45}$$

where a_B denotes the 3d Bohr radius. In evaluating the integral, the symmetry of the wave function can be exploited: Because the wave function Eq. (2.45) has spherical symmetry, the lateral effective exciton radius, $\langle x^2+y^2\rangle$, is equal to $2/3\;\langle x^2+y^2+z^2\rangle$. The latter expectation value can be calculated by evaluating an integral where the integrand has spherical symmetry,

$$\begin{aligned}\langle\, \varphi_{1s}^{3D}\,|\,\boldsymbol{\rho}^2\,|\,\varphi_{1s}^{3D}\,\rangle &= \int\limits_{x=-\infty}^{\infty} dx \int\limits_{y=-\infty}^{\infty} dy \int\limits_{z=-\infty}^{\infty} dz\; (x^2+y^2)\; |\varphi_{1s}^{3D}(\rho(x,y,z))|^2 \\ &= \frac{2}{3}\,\frac{1}{\pi a_B^3}\int\limits_{\Theta=0}^{\pi} d\Theta\,\sin\Theta \int\limits_{\phi=0}^{2\pi} d\phi \int\limits_{\rho=0}^{\infty} d\rho\;\rho^4\; e^{-2\rho/a_B} = \frac{2}{3}\,\frac{1}{\pi a_B^3}\,4\pi\cdot\frac{3}{4}a_B^5 = 2\,a_B^2\,.\end{aligned} \tag{2.46}$$

The effective exciton radius in three dimensions is therefore

$$d_{2\mathrm{d}} = \sqrt{\langle \rho_{1s}^2 \rangle} = \sqrt{2}\, a_B\,. \tag{2.47}$$

For the bulk GaAs effective exciton radius, $d^{3D} = 16.2$ nm is found. Using the bulk GaAs effective electron mass $\mathrm{m}_e = 0.067\ \mathrm{m}_0$ and the density-of-states hole mass $\mathrm{m}_h = 0.5\ \mathrm{m}_0$, the bulk exciton diamagnetic coefficient in GaAs is obtained as $\gamma^{3D} \approx 95\ \mu\mathrm{eV/T}^2$.

2.5.2 B-field dependence of the exciton radius

The diamagnetic shift of quasi-two-dimensional excitons shows a crossover to linear shift above the transition field B_0 [Eq. (2.41)], related to the balance between the Coulomb-correlated relative motion of electron and hole, and their cyclotron motion in the magnetic field. We consider a simple analytical model which allows to derive the B-field dependent shrinking of the exciton radius as a consequence of the lateral magnetic confinement of electrons and holes. According to the existing theory, the exciton energy dependence on magnetic field is analytically known only in the low-field and high-field case separately. As an approximation, we consider the interpolation formula

$$\Delta(B) = a\,(\sqrt{b^2 + B^2} - b)\,, \tag{2.48}$$

describing the transition from the quadratic diamagnetic shift at low B-field to the linear Landau shift at high B-field (Fig. 2.13). The parameters a and b are related to the exciton radius and the in-plane exciton reduced mass: In the low-field limit

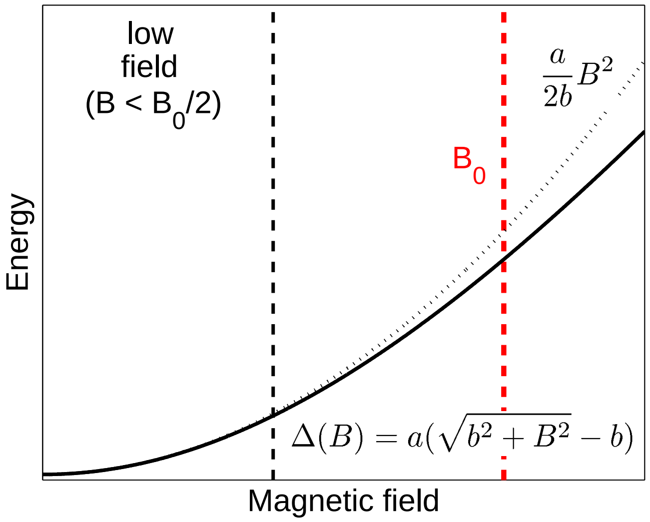

Figure 2.13: *Model for the diamagnetic shift of quasi-two-dimensional magnetoexcitons: The solid curve [Eq. (2.48)] interpolates between quadratic shift in the low-field limit and linear shift in the high-field limit. At the transition field B_0, the curvature of the solid curve has decreased to half of its zero-field value $2\gamma_2 = a/b$. For comparison, the dotted curve shows a parabola with curvature a/b.*

$(B \to 0)$, [1]

$$\Delta_{\text{low}}(B) = \frac{a}{2b}\,B^2 - \frac{a}{8b^3}B^4 + \dots\,, \tag{2.49}$$

i.e., the diamagnetic coefficient is related to the parameters a and b by

$$\gamma_2 = \lim_{B\to 0} \frac{1}{2}\,\frac{d^2\Delta(B)}{dB^2} = \frac{a}{2b}\,. \tag{2.50}$$

In the high-field limit, we have $\Delta_{\text{high}}(B) = a\cdot B$. Using the equations (2.38) and (2.40), we find that the fit parameters a, b are related to effective exciton radius and exciton in-plane reduced mass by

$$a = \frac{e\hbar}{2\mu}\quad, \qquad b = \frac{2\hbar}{e\langle\rho^2\rangle}\,. \tag{2.51}$$

Transition field To verify that the definition of the transition field, Eq. (2.41), is compatible with this interpolation formula, the B-field $B_{1/2}$ is determined where the second derivative of $\Delta(B)$,

$$\frac{\partial^2\Delta(B)}{\partial^2 B^2} = -\frac{aB^2}{(b^2+B^2)^{3/2}} + \frac{a}{\sqrt{b^2+B^2}}\,, \tag{2.52}$$

has decreased to half of its zero-field value a/b. From a plot of Eq. (2.52), the result

$$B_{1/2} = 1.53\frac{\hbar}{e\langle\rho^2\rangle} \approx \frac{3}{2}\frac{\hbar}{e\langle\rho^2\rangle} = \frac{\hbar}{e\,a_B^2} \tag{2.53}$$

is obtained. The relation between exciton Bohr radius and effective lateral exciton exciton radius in the 2d limit, $\langle\rho^2\rangle = 3/2\,a_B^2$, has been used here. The above result for $B_{1/2}$ is in good agreement with the previous definition of the transition field B_0 [Eq. (2.41)]. Using Eq. (2.51), the transition field can be expressed by the parameter b from the interpolation formula Eq. (2.48), yielding $B_0 = 3b/4$.

B-field dependence of the exciton radius Increasing the B-field normal to the quantum well plane does not only result in the diamagnetic shift in exciton transition energy, but also leads to a B-field dependent shrinking of the exciton radius. This is appreciated by comparing the full B-dependence of the XDS, approximately described by the interpolation formula Eq. (2.48), with the quadratic B-dependence in the low-field limit, Eq. (2.37). In this way, the nonparabolicity of the XDS [Eq. (2.48)] is interpreted in terms of a B-dependence of the exciton radius. From the corresponding equation

$$\frac{e^2}{8\mu}\langle\,\rho(B)^2\rangle\,B^2 = \frac{a}{2b}\,B^2 - \frac{a}{8b^3}B^4 + \dots\,, \tag{2.54}$$

the B-dependence of the exciton radius is obtained in lowest order

$$\langle\,\rho(B)^2\rangle = \frac{8\mu}{e^2}\,(\frac{a}{2b} - \frac{a}{8b^3}B^2)\,. \tag{2.55}$$

---

[1] Using the asymptotic expansion $\sqrt{1+x} = 1 + \frac{1}{2}x - \frac{1}{8}x^2 + \dots$ for $x \ll 1$.

Considering that the parameters a, b are determined by Eq. (2.51), we obtain the B-field dependence of the exciton radius

$$\langle \rho(B)^2 \rangle^{1/2} = \langle \rho(0)^2 \rangle^{1/2} \left(1 - \frac{e^2 \langle \rho^2 \rangle^2}{16\hbar^2} B^2 + \dots \right) . \tag{2.56}$$

Expressing the effective exciton radius by the exciton Bohr radius $a_B = \sqrt{2/3}\, \langle \rho^2 \rangle^{1/2}$, we obtain the B-dependence of the Bohr radius

$$a_B(B) = a_B(0) \left(1 - \frac{9}{64} \frac{e^2 a_B^4}{\hbar^2} B^2 + \dots \right) . \tag{2.57}$$

Note that the B-field induced decrease of the exciton radius is a quadratic function in the magnetic field B.

In lack of a complete theory of the quasi-two-dimensional magnetoexciton, the interpolation formula Eq. (2.48) provides a simple example that qualitatively demonstrates that the nonparabolicity of the diamagnetic shift is directly related to a “renormalization” of the exciton wave function by the magnetic field. Without more accurate knowledge about the influence of the magnetic field on the exciton ground state, the choice of Eq. (2.48) is to some extent arbitrary; other choices are possible, and the results for the exciton radius as a function of B-field depend on that choice. The result for the transition field Eq. (2.53) depends on the precise B-dependence of the diamagnetic shift, too.

2.6 Summary

This chapter has introduced the description of single-particle and exciton states in GaAs/Al$_x$Ga$_{1-x}$As quantum wells with in-plane translational symmetry, treating the Al$_x$Ga$_{1-x}$As alloy in the virtual crystal approximation (VCA). Single-particle states in quantum wells with thickness down to a few nm are described using the envelope function approximation (EFA). Confinement energies and wave functions of single-particle (electron, hole) ground states in quantum wells have been calculated in the EFA/VCA. The confinement in growth direction in a GaAs/Al$_x$Ga$_{1-x}$As quantum well releases the degeneracy of the valence band edge in GaAs, resulting in a splitting of several meV between heavy-hole and light-hole subbands in narrow GaAs/Al$_x$Ga$_{1-x}$As QWs. The in-plane band structure can be described using well-width dependent effective in-plane electron and hole masses. Due to the released degeneracy of the valence band edge, the exciton ground state in a narrow QW can be described in a two-band model, including only the lowest conduction and heavy-hole subbands.

The envelope function description of the exciton ground state in narrow QWs has been introduced, separating the full exciton wave function into a product of single-particle z wave functions and the in-plane exciton wave function. Due to the confinement in growth direction, the exciton binding energy is enhanced compared to bulk. In QWs with translational symmetry, the in-plane exciton wave function is a product of relative and center-of-mass (c.m.) wave function. The relative wave function of the ground state can be described by a two-dimensional exponential 1s wave function with lateral

Bohr radius a_B.

The magnetic-field behaviour of a magnetoexciton in a quantum well is determined by two energy scales, or, equivalently and more illustrative, two length scales: In terms of energy, exciton binding energy and cyclotron energy, or, in terms of length scales, lateral exciton Bohr radius and cyclotron radius. Only the limiting cases of low magnetic field and high magnetic field, where the scales are strongly different, are analytically accessible. In the low-field limit, the exciton energy increases quadratically with the magnetic field. In first-order perturbation theory, the diamagnetic shift coefficient of the ground state is proportional to the area of the exciton relative wave function. It is smaller than in bulk and it depends on the QW width, due to the well-width dependent exciton binding energy *and* due to the increased in-plane effective electron mass in narrow QWs. In the high-field limit, the magnetoexciton energy is dominated by the linear B-dependence of the single-particle levels. Therefore, a crossover from quadratic shift to linear shift occurs for two two-dimensional excitons.

A simple model that smoothly interpolates between low-field and high-field limiting cases has been introduced; this model does of course not replace a full theory of the quasi-two-dimensional magnetoexciton. Rather, it provides a simple example showing that the nonparabolicity of the diamagnetic shift of quasi-two-dimensional excitons in narrow QWs is related to a reduction of the exciton radius with increasing magnetic field. Possible consequences of the magnetic-field-dependent shrinking of the exciton radius on disorder-localized exciton states will be considered in chapter 8.

References

[Ada90] S. Adachi, *Excitonic effects in the optical spectrum of GaAs*, *Phys. Rev. B* 41, 1003 (1990).

[Ada94] S. Adachi, *GaAs and related materials*, World Scientific, 1994.

[Aki67] O. Akimoto and H. Hasegawa, *Interband optical transitions in extremely anisotropic semiconductors - 2. Coexistence of exciton and Landau levels*, *J. Phys. Soc. Jpn.* 22, 181 (1967).

[And90] L. C. Andreani and A. Pasquarello, *Accurate theory of excitons in GaAs-*$Ga_{1-x}Al_xAs$ *quantum wells*, *Phys. Rev. B* 42, 8928 (1990).

[Bal70] A. Baldereschi and N. O. Lipari, *Direct exciton spectrum in diamond and zinc-blende semiconductors*, *Phys. Rev. Lett.* 25, 373 (1970).

[Bal71] A. Baldereschi and N. O. Lipari, *Energy levels of direct excitons in semiconductors with degenerate bands*, *Phys. Rev. B* 3, 439 (1971).

[Bar91] G. A. Baraff and D. Gershoni, *Eigenfunction expansion method for solving the quantum wire problem*, *Phys. Rev. B* 43, 4011 (1991).

[Bas88] G. Bastard, *Wave mechanics applied to semiconductor heterostructures*, Les Editions de Physique, 1988.

[Ben66] D. J. BenDaniel and C. B. Duke, *Space-charge effects on electron tunneling*, *Phys. Rev.* 152, 683 (1966).

[Bin91] N. Binggeli and A. Baldereschi, *Determination of the hole effective masses in GaAs from acceptor spectra*, *Phys. Rev. B* 43, 14734 (1991).

[Boy07] T. B. Boykin, N. Kharche, G. Klimeck, and M. Korkusinski, *Approximate bandstructures of semiconductor alloys from tight-binding supercell calculations*, *J. Phys.: Cond. Mat.* 19, (2007).

[Bra85] M. Braun and U. Rössler, *Magnetooptical transitions and non-parabolicity parameters in the conduction band of semiconductors*, *J Phys C Solid State* 18, 3365 (1985).

[Bur92] M. G. Burt, *The justification for applying the effective-mass approximation to microstructures*, *J. Phys.: Cond. Mat.* 4, 6651 (1992).

[Bur94] M. G. Burt, *On the validity and range of applicability of the particle-in-a-box model*, *Appl. Phys. Lett.* 65, 717 (1994).

[Che76] J. R. Chelikowsky and M. L. Cohen, *Nonlocal pseudopotential calculations for electronic structure of 11 diamond and zincblende semiconductors*, *Phys. Rev. B* 14, 556 (1976).

[Cho70] A. Y. Cho, *Morphology of epitaxial growth of GaAs by a molecular-beam method - Observation of surface structures*, *J. Appl. Phys.* 41, 2780 (1970).

[Chu95] S. L. Chuang, *Physics of optoelectronic devices*, Wiley, 1995.

[Dar97] T. G. Dargam, R. B. Capaz, and B. Koiller, *Disorder and size effects in the envelope-function approximation*, *Phys. Rev. B* 56, 9625 (1997).

[DiC03] A. Di Carlo, *Microscopic theory of nanostructured semiconductor devices: Beyond the envelope function approximation*, *Semicond. Sci. Tech.* 18, R1 (2003).

[Din74] R. Dingle, W. Wiegmann, and C. H. Henry, *Quantum states of confined carriers in very thin* $Al_xGa_{1-x}As$*-GaAs-*$Al_xGa_{1-x}As$ *heterostructures*, *Phys. Rev. Lett.* 33, 827 (1974).

[Dre55] G. Dresselhaus, *Spin-orbit coupling effects in zinc blende structures*, *Phys. Rev.* 100, 580 (1955).

[Dug85] G. Duggan, H. I. Ralph, and K. J. Moore, *Reappraisal of the band-edge discontinuities at the* $Al_xGa_{1-x}As$*-GaAs heterojunction*, *Phys. Rev. B* 32, 8395 (1985).

[Eke89] U. Ekenberg, *Nonparabolicity effects in a quantum well - sublevel shift, parallel mass, and Landau levels*, *Phys. Rev. B* 40, 7714 (1989).

[Ell57] R. J. Elliott, *Intensity of optical absorption by excitons*, *Phys. Rev.* 108, 1384 (1957).

[Ell60] R. J. Elliott and R. Loudon, *Theory of the absorption edge in semiconductors in a high magnetic field*, *J. Phys. Chem. Solids* 15, 196 (1960).

[Esa70] L. Esaki and R. Tsu, *Superlattice concept*, *IBM J. Res. Devel.* 14, 61 (1970).

[For94] B. A. Foreman, *Analytic model for the valence band structure of a strained quantum well*, *Phys. Rev. B* 49, 1757 (1994).

[Gar77] R. H. Garstang, *Atoms in high magnetic fields*, *Rep. Prog. Phys.* 40, 105 (1977).

[Gon90] A. R. Goni, A. Cantarero, K. Syassen, and M. Cardona, *Effect of pressure on the low-temperature exciton absorption in GaAs*, *Phys. Rev. B* 41, 10111 (1990).

[Gro06] M. Grochol, private communication (2006).

[Gro05] M. Grochol, F. Grosse, and R. Zimmermann, *Exciton wave function properties probed by diamagnetic shift in disordered quantum wells*, *Phys. Rev. B* 71, 125339 (2005).

[Has61] H. Hasegawa and R. E. Howard, *Optical absorption spectrum of hydrogenic atoms in a strong magnetic Field*, *J. Phys. Chem. Solids* 21, 179 (1961).

[Hau04] H. Haug and S. W. Koch, *Optical and electronic properties of semiconductor heterostructures*, World Scientific, 2004.

[Hei98] A. J. Heinrich, *Ordering in ternary compound semiconductors on the atomic scale*, Ph.D. thesis, Universität Göttingen, 1998.

[Hei99] A. J. Heinrich, M. Wenderoth, K. J. Engel, T. C. G. Reusch, K. Sauthoff, R. G. Ulbrich, and E. R. W. K. Uchida, *Short-range ordering in* $Al_xGa_{1-x}As$ *grown with metal-organic vapor phase epitaxy*, *Phys. Rev. B* 59, 10296 (1999).

[Hop61] J. J. Hopfield and D. G. Thomas, *Fine-structure and magneto-optic effects in exciton spectrum of cadmium sulfide*, *Phys. Rev.* 122, 35 (1961).

[Hou88] M. P. Houng, Y. C. Chang, and W. I. Wang, *Orientation dependence of valence-subband structures in GaAs-*$Al_xGa_{1-x}As$ *quantum well structures*, *J. Appl. Phys.* 64, 4609 (1988).

[Ivc95] E. L. Ivchenko and G. Pikus, *Superlattices and other heterostructures*, Springer, New York, 1995.

[Joh49] M. H. Johnson and B. A. Lippmann, *Motion in a constant magnetic field*, *Phys. Rev.* 76, 828 (1949).

[Kan57] E. O. Kane, *Band structure of indium antimonide*, *J. Phys. Chem. Solids* 1, 249 (1957).

[Kop92] R. F. Kopf, M. H. Herman, M. L. Schnoes, A. P. Perley, G. Livescu, and M. Ohring, *Band offset determination in analog graded parabolic and triangular quantum wells of GaAs/AlGaAs and GaInAs/AlInAs*, *J. Appl. Phys.* 71, 5004 (1992).

[Kos63] G. F. Koster, J. Dimmock, R. G. Wheeler, and H. Statz, *Properties of the thirty-two point groups*, MIT Press, 1963.

[Kro57a] H. Kroemer, *RCA Review* 18, 332 (1957).

[Kro57b] H. Kroemer, *Proc. IRE* 45, 1535 (1957).

[Kua85] S. T. Kuan, T. F. Kuech, W. I. Wang, and E. L. Wilkie, *Long-range order in* $Al_xGa_{1-x}As$, *Phys. Rev. Lett.* 54, 201 (1985).

[Loz02] Y. E. Lozovik, I. V. Ovchinnikov, S. Y. Volkov, L. V. Butov, and D. S. Chemla, *Quasi-two-dimensional excitons in finite magnetic fields*, *Phys. Rev. B* 65, (2002).

[Lut55] J. M. Luttinger, *Quantum theory of cyclotron resonance for degenerate bands*, *Phys. Rev.* 98, 1560 (1955).

[Lut56] J. M. Luttinger, *Quantum theory of cyclotron resonance in semiconductors - General theory*, *Phys. Rev.* 102, 1030 (1956).

[Maa84] J. C. Maan, G. Belle, A. Fasolino, M. Altarelli, and K. Ploog, *Magneto-optical determination of exciton binding energy in* $GaAs/Ga_{1-x}Al_x$ *as quantum wells*, *Phys. Rev. B* 30, 2253 (1984).

[Mal86] F. Malcher, G. Lommer, and U. Rossler, *Electron states in* $GaAs/Ga_{1-x}Al_xAs$ *heterostructures - Nonparabolicity and spin splitting*, *Superlatt. Microst.* 2, 267 (1986).

[Mil85] R. C. Miller and D. A. Kleinman, *Excitons in GaAs quantum wells*, *J. Lumin.* 30, 520 (1985).

[Moo88] K. J. Moore, P. Dawson, and C. T. Foxon, *Effects of electronic coupling on the band alignment of thin GaAs/AlAs quantum well structures*, *Phys. Rev. B* 38, 3368 (1988).

[Nor31] L. Nordheim, *The structure of electronic excitation levels in insulating crystals*, *Ann. Phys.* 9, 607 (1931).

[Ont74] A. Onton, M. R. Lorenz, J. M. Woddall, and R. J. Chicotka, *Optical characterization of compound semiconductor alloys*, *J. Cryst. Growth* 27, 166 (1974).

[RoeW84] W. Rösner, G. Wunner, H. Herold, and H. Ruder, *Hydrogen atoms in arbitrary magnetic fields - Energy levels and wavefunctions*, *J. Phys. B: At. Mol. Opt.* 17, 29 (1984).

[RoeU84] U. Rössler, *Nonparabolicity and warping in the conduction band of GaAs*, *Solid State Commun.* 49, 943 (1984).

[Run02] E. Runge, *Excitons in semiconductor nanostructures*, *Adv Solid State Phys* 57, 149 (2002).

[Sel72] D. D. Sell, *Resolved free-exciton transitions in optical absorption spectrum of GaAs*, *Phys. Rev. B* 6, 3750 (1972).

[Sia00] A. Siarkos, E. Runge, and R. Zimmermann, *Center-of-mass properties of the exciton in quantum wells*, *Phys. Rev. B* 61, 10854 (2000).

[Sne92] M. J. Snelling, E. Blackwood, C. J. Mcdonagh, R. T. Harley, and C. T. B. Foxon, *Exciton, heavy-hole, and electron g-factors in type-I* $GaAs/Al_xGa_{1-x}As$ *quantum wells*, *Phys. Rev. B* 45, 3922 (1992).

[Wan98] L. W. Wang, L. Bellaiche, S. H. Wei, and A. Zunger, *"Majority representation" of alloy electronic states*, *Phys. Rev. Lett.* 80, 4725 (1998).

[Wan37] G. H. Wannier, *The structure of electronic excitation levels in insulating crystals*, *Phys. Rev.* 52, 191 (1937).

[Wol86] D. J. Wolford, T. F. Kuech, J. A. Bradley, M. A. Gell, D. Ninno, and M. Jaros, *Pressure dependence of GaAs/*$Al_xGa_{1-x}As$ *quantum well bound states - the determination of valence band offsets*, *J. Vac. Sci. Technol. B* 4, 1043 (1986).

[Yu96] P. Y. Yu and M. Cardona, *Fundamentals of Semiconductors*, Springer, 1996.

Chapter 3

Fundamentals: Exciton localization in narrow quantum wells

This chapter aims at an understanding of the influence of disorder on different length scales in the interfaces of narrow GaAs/Al$_x$Ga$_{1-x}$As quantum wells on exciton localization. The first section describes the intrinsic atomistic structure of GaAs/Al$_x$Ga$_{1-x}$As heterointerfaces. The theory of exciton disorder-localization in narrow quantum wells is introduced in the second section. The concept of band edge fluctuations is demonstrated at the example of a GaAs/Al$_x$Ga$_{1-x}$As quantum well with nominally perfectly flat interfaces, where only the intrinsic composition fluctuations in the Al$_x$Ga$_{1-x}$As barrier contribute to fluctuations of the local band edges ("interface disorder"). A simplified version of the theory of exciton disorder-localization is described, considering only localization of the exciton center-of-mass and neglecting the influence of disorder on the exciton relative wave function. This theory can be seen as an intermediate step on the way to a complete picture of exciton localization in disordered quantum wells. The third section reviews models of exciton localization that have been introduced in the recent decades to describe exciton localization in real quantum wells. Subsequently, the idea to use magneto-μPL spectroscopy as a tool for the study of disorder in narrow quantum wells is outlined, and the effects of an external magnetic field in growth direction on localized exciton states are described.

3.1 GaAs/Al$_x$Ga$_{1-x}$As heterointerfaces: Intrinsic disorder

Disorder due to composition fluctuations in the Al$_{0.3}$Ga$_{0.7}$As alloy is intrinsic in GaAs/Al$_{0.3}$Ga$_{0.7}$As heterointerfaces. Figure shows a cross section of the cation sublattice of a nominally perfect GaAs/Al$_{0.3}$Ga$_{0.7}$As quantum well with random distribution of Al atoms in the Al$_{0.3}$Ga$_{0.7}$As barriers is shown. Al atoms are indicated in black. The lateral cation distance is 0.4 nm, the monolayer distance is 0.565 nm. [1] In every monolayer, 30 % of the cations are Al atoms. Growth steps, segregation, and short range ordering (SRO) in the alloy distribution, that contribute to interface disorder in a real quantum well, are neglected at this point. In Fig. 3.1(b), the same structure is shown in the virtual crystal approximation (VCA), i.e., the random Al$_{0.3}$Ga$_{0.7}$As alloy

---

[1] Only every second monolayer is shown. The surface structure of the GaAs {110} surfaces is described in detail in chapter 5.

Figure 3.1: *(a) Simulated cross section of a GaAs/Al$_{0.3}$Ga$_{0.7}$As QW (d = 7 ML) with uncorrelated distribution of Al atoms in the Al$_{0.3}$Ga$_{0.7}$As layers. Al atom positions are marked in black. (b) The same structure in the virtual crystal approximation (VCA).*

is treated as a homogeneous crystal consisting of As atoms and Al$_{0.3}$Ga$_{0.7}$ pseudo-atoms. For comparison, the exciton diameter $2a_B$ (a_B = 8.2 nm) of the heavy-hole exciton ground state in a nominally perfect 4-nm GaAs/Al$_{0.3}$Ga$_{0.7}$As quantum well is shown.

That the GaAs/Al$_{0.3}$Ga$_{0.7}$As "interface" seems rough in the atomistic model [Fig. 3.1(a)], but perfectly flat in the heuristic model, where the Al$_{0.3}$Ga$_{0.7}$As barrier is treated as pseudocrystal [Fig. 3.1(b)], demonstrates that the position of the interface between GaAs and the random Al$_{0.3}$Ga$_{0.7}$As alloy can not be unambiguously defined on the atomic scale [Oga87]. Rather, there is a some lattice constants wide region where it is impossible to decide if a Ga atom belongs to the GaAs layer or to the Al$_{0.3}$Ga$_{0.7}$As barrier. Therefore, the concept of "interface roughness" can not be applied to GaAs/Al$_x$Ga$_{1-x}$As heterointerfaces offhand.

The theory of exciton disorder-localization in narrow quantum wells, which has been developed in the envelope function framework [Zim97], puts another concept in the focus: The concept of band edge fluctuations. In the next section, the theory exciton disorder-localization in narrow quantum wells is introduced, and the concept of bandedge fluctuations is demonstrated at the example of a 4-nm GaAs/Al$_{0.3}$Ga$_{0.7}$As quantum well with nominally perfectly flat barriers and random, uncorrelated distribution of Al atoms in the barriers.

3.2 Exciton localization in GaAs/Al$_x$Ga$_{1-x}$As QWs: Intrinsic disorder

The model of a three-dimensional exciton moving between the QW barriers can replaced by that of a quasi-two-dimensional exciton in narrow quantum wells, as described in chapter 2.4 ("Quantum well excitons"). This remains true in disordered quantum wells without in-plane translational symmetry, provided that the disorder strength is not too large [Zim97]. In presence of disorder, the quantum well exciton Hamiltonian [Eq. (2.27)] has to be supplemented by in-plane disorder potentials $V_e(\boldsymbol{\rho}_e)$, $V_h(\boldsymbol{\rho}_h)$ representing the fluctuation of the local band edges. The exciton in-plane motion in disordered narrow QWs is described by the two-particle Schrödinger equation for the (four-coordinate) in-plane exciton wave function $\phi_\alpha(\boldsymbol{\rho}_e, \boldsymbol{\rho}_h)$

$$H\,\phi_\alpha(\boldsymbol{\rho}_e, \boldsymbol{\rho}_h) = E_\alpha\,\phi_\alpha(\boldsymbol{\rho}_e, \boldsymbol{\rho}_h)\,, \tag{3.1}$$

where the exciton Hamiltonian

$$H = -\frac{\hbar^2}{2m_e}\triangle_{\rho_e} - \frac{\hbar^2}{2m_h}\triangle_{\rho_h} + V_e(\boldsymbol{\rho}_e) + V_h(\boldsymbol{\rho}_h) + V_C(\boldsymbol{\rho}_e - \boldsymbol{\rho}_h) \tag{3.2}$$

includes Coulomb interaction and disorder potentials $V_e(\boldsymbol{\rho_e})$, $V_h(\boldsymbol{\rho_h})$ for electrons and holes, representing the spatial variation of the local bandedges, and the modified Coulomb interaction $V_C(\boldsymbol{\rho})$ in the QW plane [Eq. (2.28)].

The determination of the local bandedges is now described at the example of a nominally perfect 4-nm GaAs/Al$_{0.3}$Ga$_{0.7}$As quantum well with random, uncorrelated distribution of Al atoms in the barriers. The steps leading from the alloy composition in the QW interfaces are shown in Fig. 3.2 (a) - (d). Figure 3.2(a) shows the Al distribution in a simulated cross-section of GaAs/Al$_{0.3}$Ga$_{0.7}$As QW (bottom) as well as the average Al concentration $C(z)$ in the single monolayers (top). Single-particle wave functions $u_e(z)$, $u_h(z)$ calculated in square well profiles using the EFA/VCA approximation are shown: The solid black and the dashed gray curve represent probability densities of the electron ($u_e^2(z)$) and the heavy hole ($u_h^2(z)$). The penetration depth of the electron wave function into the Al$_{0.3}$Ga$_{0.7}$As barrier (treated in virtual crystal approximation) is larger than the penetration depth of the heavy hole wave function.

Figures 3.2(b) and (c) show the difference of local and averaged Aluminum concentration $C(x,z) - \overline{C}(z)$ weighted with the probability densities $u_e^2(z)$ and $u_h^2(z)$. Multiplication with $u_e^2(z)$, $u_h^2(z)$ guarantees that the Aluminum distribution in the barriers contributes to lateral disorder only in so far as electrons or holes actually reside there. Integration over the weighted Al concentration difference in z direction gives a measure for the local vertical confinement of electron and hole due to the Al concentration varying along the QW interfaces. Disorder potentials for electron and hole are obtained by scaling to GaAs/Al$_{0.3}$Ga$_{0.7}$As band offsets (a=e,h):

$$V_a(x) = \Delta_a \int dz\, u_a^2(z) \left[C(x,z) - \overline{C}(z)\right], \quad \text{a=e,h}\,. \tag{3.3}$$

The disorder potentials $V_e(x_e)$, $V_h(x_h)$ resulting from alloy disorder in the 4-nm GaAs/ Al$_{0.3}$Ga$_{0.7}$As QW are shown in Fig. 3.2(d): The black line corresponds to the local conduction band edge, the gray line to the local valence band edge. It is clearly observed that a strong correlation exists between electron and hole disorder potential.

The potential value distributions of electron and hole disorder potentials are shown in Fig. 3.3(a) and (b). The number of potential values has been binned over 5 meV windows. That the distributions are not symmetric around zero ($E = 0$) is due to the Al concentration of 0.3: Relative to the average Al concentration, the increase in the local potential is larger when all atoms in a QW cross section are Al atoms than when all atoms are Ga atoms. For comparison, Gaussian distributions $p_\sigma(E) = 1/\sqrt{2\pi}\sigma \cdot \exp\left(-E^2/2\sigma^2\right)$ with $\sigma_e = 33$ meV and $\sigma_h = 8.5$ meV are shown in Figs. 3.3(a) and (b). The autocorrelation functions of electron and hole disorder potentials shows a delta-like peak at zero, since there are no lateral correlations between Al atoms in the barriers. The approximation of the potential value distributions by Gaussians as shown in Fig. 3.3 may seem rather crude, but the exact form of the potential value distribution is not in the focus of our interest, since the example of the 4-nm GaAs/ Al$_{0.3}$Ga$_{0.7}$As QW with nominally perfect interfaces mainly serves for illustrative purposes. However,

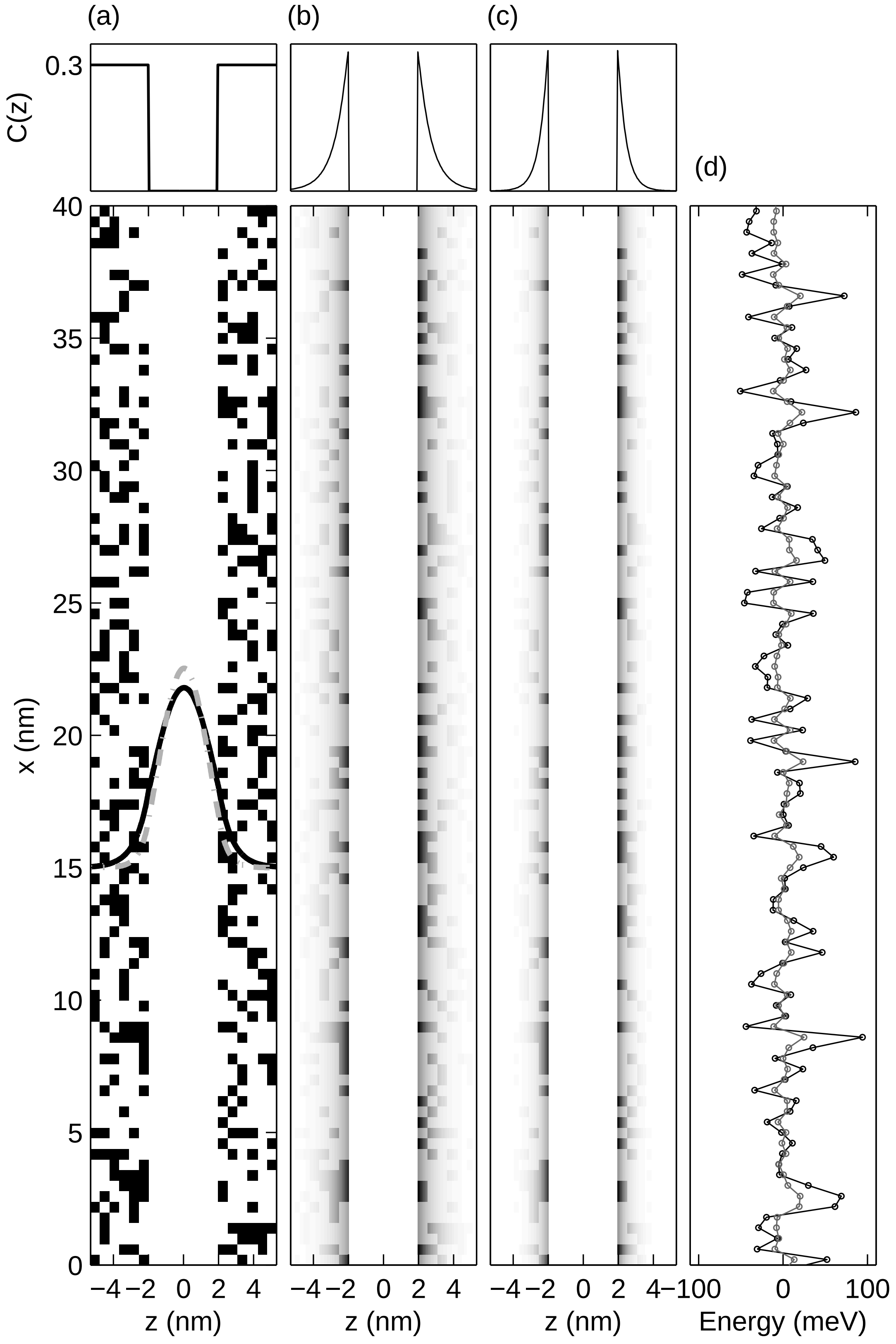

Figure 3.2: *(a) Average Al concentration (top) and spatial positions of Al atoms (bottom) in the barriers of a perfect 4-nm GaAs/$Al_{0.3}Ga_{0.7}As$ QW. (b) Difference between "local bandedge" and bandedge profile averaged along the QW, weighted with electron z-wave function. (c) The same for the heavy hole. (d) Bandedge fluctuations along the QW (black: electron, gray: heavy hole).*

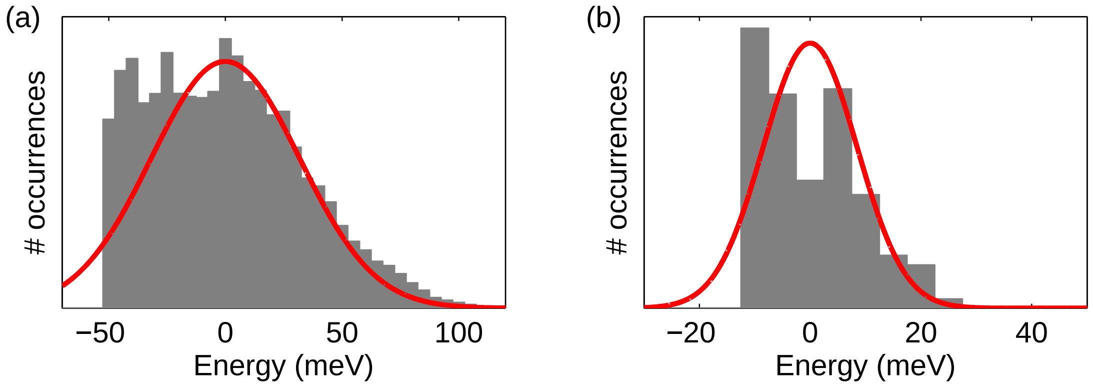

Figure 3.3: *(a) Electron and (b) hole band edge fluctuations resulting from random alloy disorder in the 4-nm* $GaAs/Al_{0.3}Ga_{0.7}As$ *QW [Fig. 3.2]. Zero of energy corresponds to the band edges of a 4-nm* $GaAs/Al_{0.3}Ga_{0.7}As$ *QW where the barriers are treated in virtual crystal approximation. For comparison, Gaussians with* $\sigma_e = 33$ *meV (electron) and* $\sigma_h = 8.5$ *meV (hole) are shown.*

it should be noted that the ratio of potential strengths of the distributions in Fig. 3.3 differs from the band offset ratio $f_e/f_h = 0.65/0.35$. The ratio of the disorder strenghts of electron and hole potential is rather $\sigma_e : \sigma_h \approx 3.5$, i.e., significantly larger than the band offset ratio. This is because electron z-wave function $u_e(z_e)$ and heavy-hole wave function $u_h(z_h)$ have different penetration depth into the QW barriers. The smaller penetration depth of the hole wave function causes the ratio of disorder strengths to be significantly larger than the band offset ratio.

The local band edge fluctuations in the two-dimensional QW plane are described by two-dimensional electron and hole disorder potentials $V_e(\boldsymbol{\rho}_e)$, $V_h(\boldsymbol{\rho}_h)$. The exciton in-plane motion is described by Eq. (3.1) with the exciton Hamiltonian Eq. (3.2). The problem of the three-dimensional exciton motion between corrugated barriers of a narrow QW, involving the six spatial coordinates of electron and hole, has thereby been reduced to a four-dimensional problem. Still, the full description of localized exciton states in two-dimensional disorder is not simple, but involves the four-coordinate exciton wave function.

For the case of weak disorder, [2] Zimmermann *et al.* [Zim97] have proposed an approximate description, assuming that disorder mainly influences the exciton center-of-mass (c.m.) motion, and that in-plane relative and c.m. motion can be separated. To describe in-plane relative and c.m. motion, we define the total exciton mass $M = m_e + m_h$, the in-plane c.m. coordinate $\boldsymbol{R} = (m_e\boldsymbol{\rho}_e + m_h\boldsymbol{\rho}_h)/M$, the reduced mass $\mu = m_e m_h/M$, and the in-plane relative coordinate $\boldsymbol{\rho} = \boldsymbol{\rho}_e - \boldsymbol{\rho}_h$. The two-particle WF ϕ is factorized into a product of c.m. WF $\psi(\boldsymbol{R})$ and relative WF $\varphi(\boldsymbol{\rho})$. To describe the relative motion, a 1s wave function $\varphi_{1s}(\boldsymbol{\rho}) \propto \exp(-\rho/a_B)$ is used which is rigid throughout the structure. In this factorization approach, the exciton averages over underlying disorder with its relative WF. This model results in the eigenvalue equation for the exciton

---

[2] disorder strength on the length scale of the exciton Bohr radius < exciton binding energy

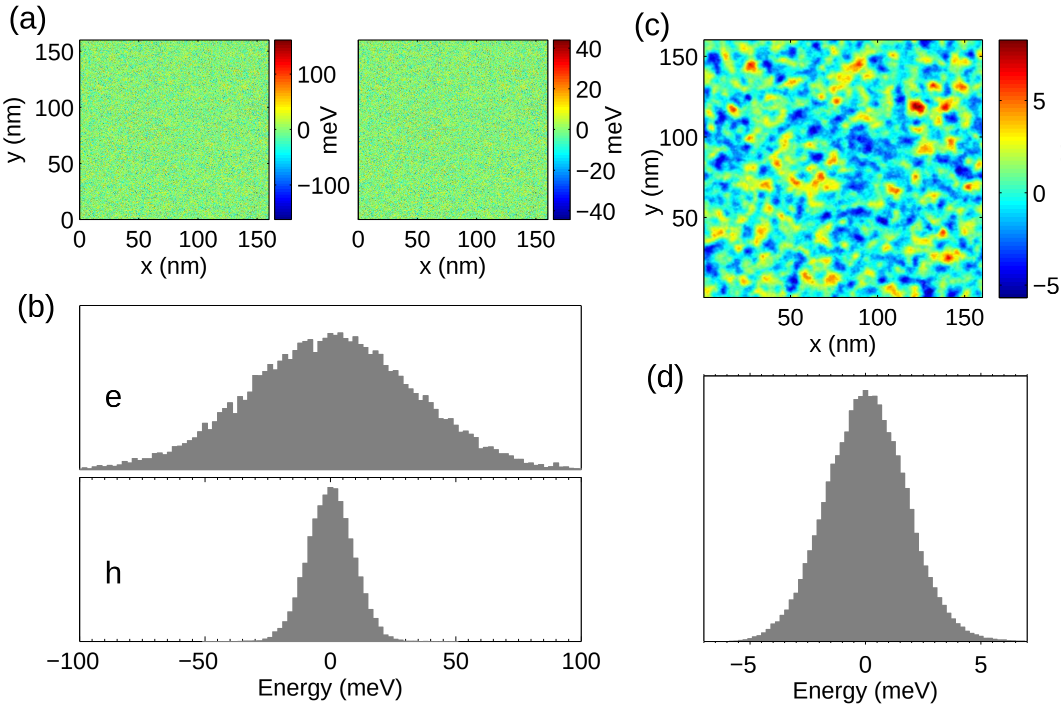

Figure 3.4: *(a) Uncorrelated disorder potentials* $V_e(\boldsymbol{\rho_e})$, $V_h(\boldsymbol{\rho_h})$ *with disorder strengths* $\sigma_e = 33\ meV$ *and* $\sigma_h = 9\ meV$. *(b) Potential value distributions for electron and hole. (c) Effective exciton center-of-mass potential* $V_{eff}(\boldsymbol{R})$, *assuming* a_B *= 8.2 nm for the lateral exciton Bohr radius. (d) Potential value distribution of* $V_{eff}(\boldsymbol{R})$ *with disorder strength* $\sigma_{com} = 1.7\ meV$.

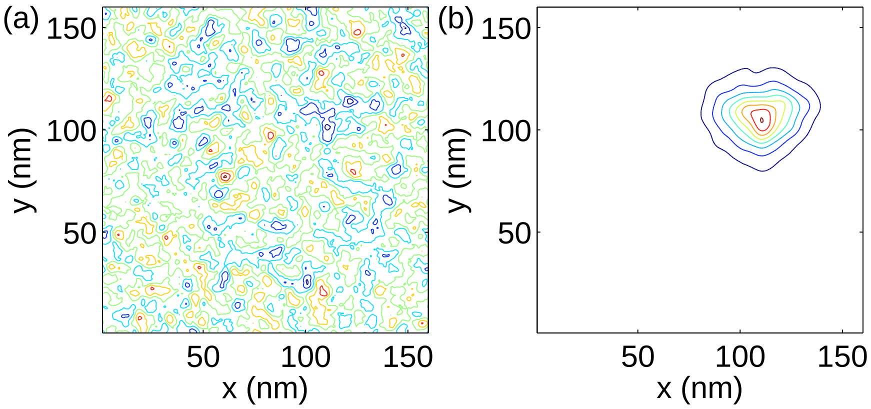

Figure 3.5: *(a) Contour lines of a simulated effective disorder potential* $(160 \times 160\ nm^2)$ *for the exciton c.m. For the lateral Bohr radius,* a_B *= 8.2 nm is assumed. (b) Contour plot of probability density of the c.m. wave function of the energetically lowest eigenstate in (a).*

in-plane c.m. wave function $\psi(\boldsymbol{R})$

$$\left(-\frac{\hbar^2}{2M}\triangle + V_{\text{eff}}(\boldsymbol{R}) - E \right)\psi(\boldsymbol{R}) = 0\,, \tag{3.4}$$

where the effective exciton c.m. potential $V_{\text{eff}}(\boldsymbol{R})$ is determined by a convolution of the underlying (atomic) disorder potential with 1s wave functions scaled differently for electron and hole (taking into account the different localization properties of electrons and holes),

$$V_{\text{eff}}(\boldsymbol{R}) = \sum_{a=e,h} \int d^2\rho_a \, \frac{1}{(\mu/m_a)^2} \, \varphi_{1s}^2 \big(\frac{\boldsymbol{\rho}_a - \boldsymbol{R}}{\mu/m_a} \big) \, V_a(\boldsymbol{\rho}_a)\,. \tag{3.5}$$

Averaging of the exciton over the underlying fluctuations of the local bandedges introduces correlations on the length scale of the exciton Bohr radius, and reduces disorder strength of the effective potential for the exciton center-of-mass. This is demonstrated in Fig. 3.4 at the example of laterally uncorrelated, Gaussian distriuted disorder potential for electron and hole with disorder strengths $\sigma_e = 33$ meV (electron) and $\sigma_h = 8.5$ meV (hole). The reduction factor $\sigma_{\text{com}}/(\sigma_e + \sigma_h) = 1.7/42$ is approximately equal to the ratio $a_{[110]}/a_B = 0.4/8.2$, i.e., to the square root of the inverse ratio of the numbers of independent potential values in the single-particle and the averaged center-of-mass potential. This is interpreted as the $1/\sqrt{N}$ law for the second moments of uncorrelated random events [Run02].

In Figure 3.5(a), a contour-line plot of a simulated effective potential for the exciton c.m. (160×160 nm^2) is shown. This disorder realization has been determined from uncorrelated disorder potential with disorder strengths $\sigma_e = 33$ meV, $\sigma_h = 9$ meV, by convolution with scaled 1s wave functions according to Eq. (3.5). For the lateral Bohr radius, the Bohr radius in a 4-nm GaAs/Al$_{0.3}$Ga$_{0.7}$As QW, $a_B = 8.2$ nm has been assumed. Figure 3.5(b) shows a contour plot of the energetically lowest eigenstate in the potential shown in (a), which has been determined by solving the single-particle Schrödinger equation for the exciton c.m. for the potential (a). The energy of the lowest eigenstate lies 1 meV below the center of the potential value distribution [Fig. 3.4(d)]. The c.m. eigenstate corresponds to an exciton state at a transition energy shifted to lower energy by the amount of the exciton binding energy. The first few eigenstates in the disorder potential shown in Fig. 3.5(a) have spatially well localized center-of-mass wave functions. The wave functions of higher states are more extended and show fractal-like structure [Run02]. Calculation of the optical density (absorption spectrum) according to [Zim97] showed that uncorrelated alloy disorder in a 4-nm GaAs/Al$_{0.3}$Ga$_{0.7}$As QW causes an inhomogeneous broadening of the exciton spectrum on the order of 1 meV.

3.3 Exciton localization in real GaAs/Al$_x$Ga$_{1-x}$As QWs

The model of the GaAs/Al$_{0.3}$Ga$_{0.7}$As quantum well described in the previous section represents a mathematical model that is unlikely to be realized in real MBE-grown quantum well. The atomistic structure of the interfaces of a real quantum well is influenced by several processes that have their origin in the dynamic situation far from

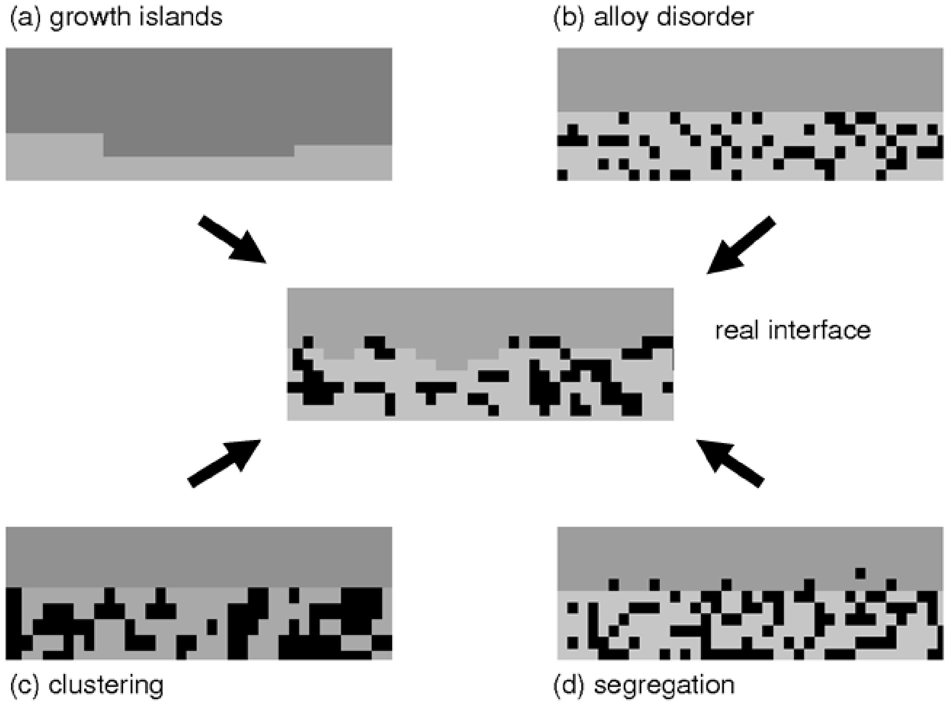

Figure 3.6: *Schematic picture of disorder in a binary/ternary heterointerfaces: Different mechanisms contribute to the total interface disorder. After [Reu98].*

equilibrium during MBE growth: Atoms impinge on an existing growth front; they migrate along the surface (surface diffusion) or dissolve in an already formed layer (segregation). In binary/ternary heterointerfaces, alloy disorder contributes to the total interface disorder. In alloys, atoms of one species may be built in preferentially near atoms of the same species (clustering). All these processes influence the atomic configuration of an MBE-grown heterointerface; they are summarized in Fig. 3.6.

Characterization of the interface structure of buried semiconductor heterostructures has proven a difficult task in the recent decades. While a variety of methods exists that allow to investigate the real structure of surfaces from the atomic scale to macroscopic length scales, e.g., scanning tunneling and atomic force microscopy, scanning electron microscopy, and optical microscopy, interfaces of buried semiconductor heterostructures are not accessible to all of these classical surface investigation methods. Methods that give direct access to the interface structure on the atomic scale of buried semiconductor heterostructures are transmission electron microscopy (TEM) [Pet77], X-ray diffraction [Fle80] and cross-sectional scanning tunneling microscopy (XSTM) [Sal93]. The assessment and microscopic characterization of interface disorder by these methods has proven difficult, e.g, because of the required sample preparation and the limited spatial window. Early on, indirect optical methods such as photoluminescence (PL) and cathodoluminescence (CL) have been used to complement data obtained by direct structural techniques. However, some degree of theoretical modeling is necessary to extract information about structure from data obtained by optical techniques. In the following paragraphs, models of exciton localization in GaAs/Al$_x$Ga$_{1-x}$As quantum wells are described that were developed in the recent decades.

At the beginning stood the recognition that in high-purity $\mathrm{GaAs/Al}_x\mathrm{Ga}_{1-x}\mathrm{As}$ quantum wells free excitons dominate the luminescence spectra, [3] and that spatial fluctuations of the local bandgap in the QW plane lead to the localization of excitons [Wei81]. The inhomogeneous broadening of optical spectra of quantum well heterostructures has first been interpreted as a result of exciton localization in regions of the quantum well where the well thickness is increased by one or several monolayers (Fig. 3.7). The intrinsic short-range disorder in the $\mathrm{GaAs/Al}_x\mathrm{Ga}_{1-x}\mathrm{As}$ interface due to composition fluctuations in the $\mathrm{Al}_x\mathrm{Ga}_{1-x}\mathrm{As}$ barriers was suggested to be not relevant for exciton localization. Consequently, the $\mathrm{Al}_x\mathrm{Ga}_{1-x}\mathrm{As}$ barriers were implicitly treated in the virtual crystal approximation in models of the $\mathrm{GaAs/Al}_x\mathrm{Ga}_{1-x}\mathrm{As}$ interface, as shown in Fig. 3.7. The existence of atomically flat islands in the QW interfaces with lateral extension larger than the exciton Bohr radius ($a_B \sim 10$ nm in GaAs) was postulated [Wei81]. It was assumed that lateral variations of the QW width cause lateral variations of the total confinement energy. In this picture, lateral confinement in a quantum well is caused by a spatial variation of the well width, i.e., of vertical confinement. Weisbuch, Dingle, Gossard and Wiegmann assumed that only ML islands larger than the exciton Bohr radius lead to exciton localization [Wei81]. In Fig. 3.7, it is implicitly assumed that the confinement energy resulting from lateral exciton localization in ML islands is negligible compared to confinement in growth direction.

Subsequently, more detailed interface models were introduced, including, e.g., the effect of island sizes $L < a_B$, and it has been attempted to predict the PL lineshape from the size distribution of ML islands in the QW interfaces using statistical arguments [Sin84]. Also effects of alloy disorder were included in a phenomonological model [Sin85]: This approach appreciated that the local interface position can not be unambiguously defined on the atomic scale. Therefore, to proceed it was assumed that two different, well-

---

[3] In contrast to bulk samples, where the luminescence of impurity-bound excitons dominates.

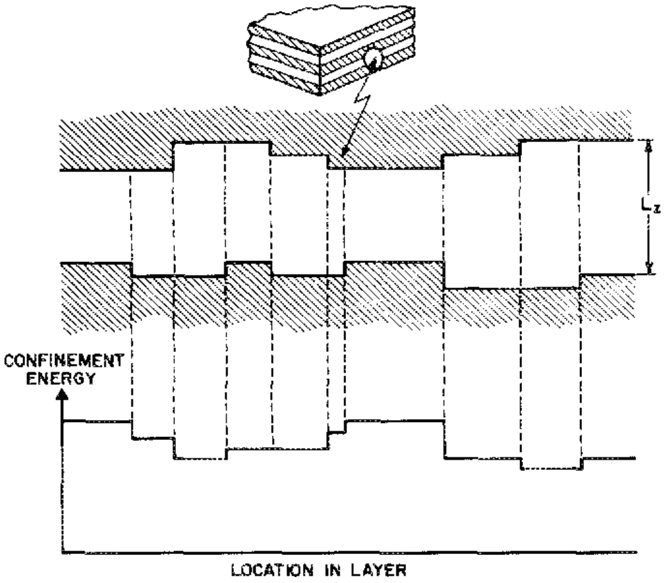

Figure 3.7: *Model of Weisbuch, Dingle, Gossard and Wiegmann [Wei81]: Monolayer fluctuations of the local QW width lead to lateral variations of the confinement energy in growth direction.*

separated length scales of disorder were present. The ternary alloy barriers were in first approximation treated in virtual crystal approximation, and alloy disorder was included as a perturbation.

In the meantime, in-situ growth monitoring techniques like RHEED had lead to an improved understanding of the dynamics of MBE growth. The damping of the RHEED signal after starting growth, the occurrence of RHEED oscillations, and the recovery of the RHEED signal after growth interruption were interpreted as evidence for polynuclear growth, where the growth of a new monolayer started before one monolayer was completed [Nea83]. It was observed that growth interruption could be used to achieve smaller inhomogeneous linewidths of quantum well samples [Nea83, Gro82, Sak85, Lew85]. However, subsequently it was found that growth interruption can also lead to larger linewidths [Bim86]. Since then, basically two classes of quantum well samples exist: Those grown with growth interruption, and those grown without growth interruption.

Photoluminescence spectra of growth-interrupted GaAs/AlAs [Gol83] and GaAs/AlGaAs superlattices [Dev84] showed multiple peaks, that were attributed to exciton recombination in well regions differing in height by integer multiples of a monolayer ("ML splitting"). However, a detailed comparison of the results of direct structural techniques with those of optical experiments showed that the existence of atomically flat QW regions with lateral extension larger than the exciton Bohr radius was not consistent with quantitative microscopic (structural) data [Our89] and also with the results of optical experiments [War90, War92]. Using a combination of different characterization techniques, each sensitive to a limited spatial range of disorder, ample evidence for different length scales of disorder – down to the atomic scale – contributing to the roughness of GaAs/Al$_x$Ga$_{1-x}$As heterointerfaces has been collected [Bim86, Oga87, Bim87, Our89, Jus90, War90, Gam90, Gam91, Kop91, War92, Zre94, Woo95, Jah96, Gam96, Gro97, Fuj97, Leo00]. The "atomically smooth island" model was rejected as oversimplified; consequently, for a realistic description of QW interface roughness, it was postulated that the complete roughness spectrum of the interface had to be included [War92]. Figure 3.8 schematically shows the roughness spectrum of a

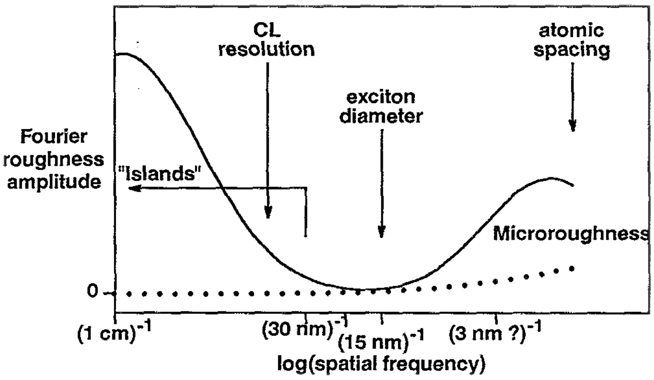

Figure 3.8: *[War92] Schematic representation of the interface roughness spectrum of a quantum well in Fourier space. The bimodal roughness distribution results from the artificial reduction of roughness on the length scale of the exciton diameter by means of growth interruption.*

growth-interrupted quantum well in Fourier space. The roughness amplitude at the exciton diameter has been artificially reduced by growth optimization techniques like growth interruption, and the power spectrum shows a bimodal distribution.

The use of the term "interface roughness" – which implies a definition of the local interface position – in the context of GaAs/Al$_x$Ga$_{1-x}$As heterointerfaces requires a remark. In the work of Singh *et al.* [Sin85], it was appreciated that only in presence of two different, well-separated length scales of disorder, the fluctuations of the local bandedges on the longer-range scale can be associated with fluctuations of the local interface position on that length scale. This limitation has not been mentioned in later work. If this limitation would have been kept in mind, it would probably have been recognized that with respect to binary/ternary alloy interfaces, a rigorous definition of a continuous "interface roughness spectrum" does not exist – at least not based on a definition of the local interface position.

The study of Ogale *et al.* [Oga87] pointed out for the first time the primary importance of composition fluctuations in the Al$_x$Ga$_{1-x}$As barriers for optical properties of GaAs/Al$_x$Ga$_{1-x}$As quantum wells. However, it remained singular in this conclusion for many years. In most studies, short-range disorder on the atomic scale in GaAs/Al$_x$Ga$_{1-x}$As quantum wells, resulting from composition fluctuations in the Al$_x$Ga$_{1-x}$As barriers, has been considered to be irrelevant for exciton localization [Wei81], or at least of secondary importance [War92].

A possible reason for the predominance of a single model, i.e, that of "large islands with nanoroughness superimposed", is its simplicity. Actually, two fundamentally different pictures explain localization of a quantum-mechanical particle by either short-range disorder or long-range disorder: Localization by long-range disorder is explained in the "particle-in-a-box" picture; for an extended particle like the exciton it has often been assumed that the lateral extension of the box needs to be larger than the exciton diameter to cause localization. In contrast, quantum-mechanical localization also occurs if the correlation length of the underlying disorder potential is much smaller than the characteristic length scale of the particle, since quantum mechanics allows the particle wave function to penetrate into classically forbidden areas. This is demonstrated in

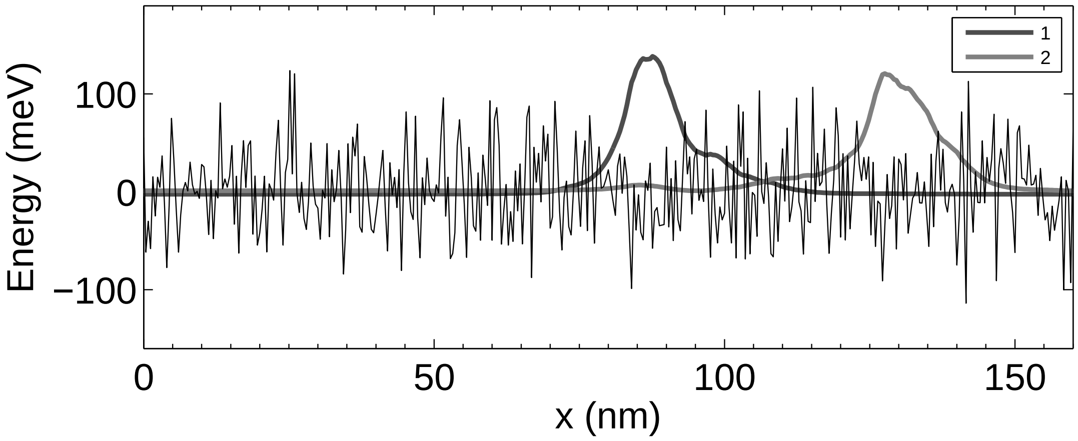

Figure 3.9: *Single-particle (electron) disorder eigenstates in a Gaussian random potential.*

Fig. 3.9, where the lowest disorder eigenstates in a random (uncorrelated) Gaussian-distributed potential are shown. The figure demonstrates – on the single-particle level – the fundamental difference between "quantum mechanical" and "classical" localization: Due to the penetration of wave functions into classical forbidden areas, the lateral wave function extension can be significantly larger than the correlation length of the disorder potential, and only the lowest tail states are well localized. The two limiting cases of quantum-mechanical disorder localization can be characterized by a different ratio of disorder strength and kinetic energy (confinement energy) [Sav99]. The so-called *classical limiting case* is characterized by a long correlation length of the underlying disorder potential and small confinement energies. In this case, the particle hardly penetrates into the classically forbidden areas. On the other hand, the so-called *extreme quantum limit* is characterized by a short correlation length and a strong penetration of the wave function in classically prohibited areas [Run02].

Localization by short-range disorder was demonstrated in Fig. 3.9 on a single-particle level. The somewhat more complicated case of exciton localization by short-range disorder has already been described in the previous section at the example of random, uncorrelated alloy disorder in the plane of a GaAs/$Al_xGa_{1-x}As$ quantum well. In the theory of exciton disorder-localization [Zim97], a reinterpretation of the "interface roughness" models described above is possible. In contrast to the concept of well width fluctuations, the concept of band edge fluctuations is well-defined in GaAs/$Al_xGa_{1-x}As$ quantum wells. [4] The "roughness spectrum" shown in Fig. 3.8 can therefore be reinterpreted as the spectrum of the band edge fluctuations (note that conduction and valence band edge are strongly correlated).

Figure 3.10 summarizes the description of localization of the exciton center-of-mass in the approximate theory of exciton disorder-localization [Zim97], which has been described in the previous section. The case of a quantum well where the position of the

---

[4] Neglecting for the moment the question of the range of applicability of the virtual crystal approximation to bulk $Al_xGa_{1-x}As$.

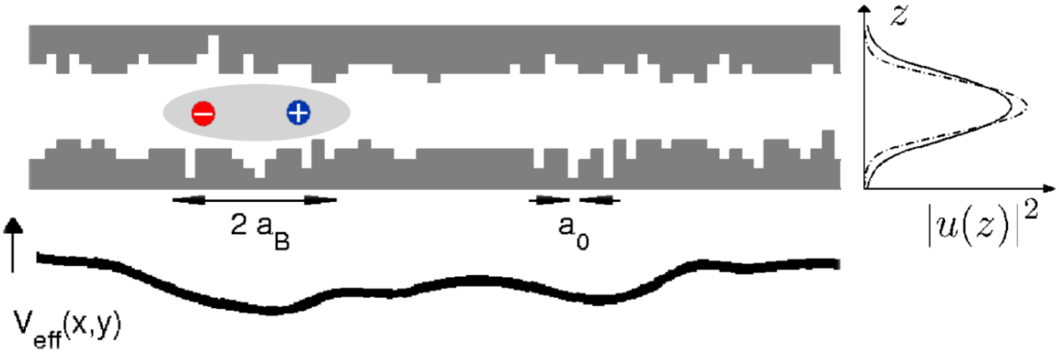

Figure 3.10: *Schematic view of an exciton between the corrugated interfaces of a narrow quantum well. The single-particle envelope wave functions* $|u_e(z)|^2$, $|u_h(z)|^2$ *describing the localization in growth direction are shown on the right. In lateral direction, the exciton averages over underlying disorder with its relative wave function. Minima in the resulting effective potential* $V_{eff}(x,y)$ *for the exciton center-of-mass act as natural quantum dots.*

interfaces can be defined on the atomic scale is shown; the barrier region is drawn in gray. The exciton averages over fluctuations of the local band edges (not shown) on a length scale below the exciton Bohr radius with its relative wave function (Figure 3.10). Local minima in the resulting effective disorder potential for the exciton center-of-mass, $V_{\mathrm{eff}}(x, y)$, act as natural quantum dots (QDs), also called quantum well dots (QWDs). The influence of disorder on the exciton relative wave function is neglected in this model.

3.4 Exciton diamagnetic shift as a probe of disorder

Spatially averaging luminescence techniques do not give direct access to the parameters of the interface disorder in quantum wells, since the exciton averages over the underlying band edge fluctuations. Due to the effects of motional narrowing and the relaxation of excitons before recombination, the inhomogeneous broadening of spatially averaged low-temperature PL spectra does not even give a measure of the disorder strength of this averaged potential [Zim94, Zim97]. Therefore, there is the need for an optical technique that allows to characterize interface disorder in quantum wells more directly.

The idea to use magneto-μPL spectroscopy to study interface disorder in narrow quantum wells is motivated by two experimental observations:

- Experimental techniques like near-field scanning optical spectroscopy or μPL have demonstrated that at least for low temperatures the line shape of narrow quantum well PL spectra is the envelope of many narrow lines due to disorder-localized exciton states [Zre94, Bru94]. In μPL spectra of narrow GaAs/Al$_x$Ga$_{1-x}$As QWs, the spectrally narrow emission lines of localized exciton states have been observed down to several standard deviations (σ) below the center of the QW emission peak. The c.m. wave functions of the lowest tail states in a short-range correlated disorder potential are well localized and can be described in analogy to quantum dots, hence their designation as *natural quantum dots* or *quantum well dots* (QWD). The diamagnetic shift has been found to vary between different natural quantum dots, but no systematic behaviour has been observed yet [Hes94, Ste02].
- For cylinder-shaped In$_{0.1}$Ga$_{0.9}$As/GaAs quantum dots with varying dot diameters, it has been observed that the diamagnetic coefficient of exciton ground states in the QDs increases monotonously with increasing dot diameter [Bay98]. Consequently, the exciton diamagnetic coefficient is a measure of the lateral extension of the confinement potential, here of the QD diameter.

We describe the experimental results for diamagnetic coefficients of quantum dot exciton ground states in cylinder-shaped In$_{0.1}$Ga$_{0.9}$As/GaAs quantum dots with varying dot diameters [Bay98]. The quantum dots were fabricated by electron-beam lithography and wet chemical etching on a 5 nm In$_{0.1}$Ga$_{0.9}$As/GaAs quantum well. Experimental results for diamagnetic coefficients are shown in Fig. 3.11 for dot diameters in the range 25-200 nm. The quasi-two-dimensional limit is $\sim 70\,\mu\text{eV/T}^2$. The lateral exciton Bohr radius is on the order of 10 nm. For dot diameters of $\sim$ 100 nm, i.e., about ten times the exciton Bohr radius, a reduction of the diamagnetic coefficients is observed. For the smallest dots with $\sim$ 20 nm diameter, a reduction of the diamagnetic coefficient

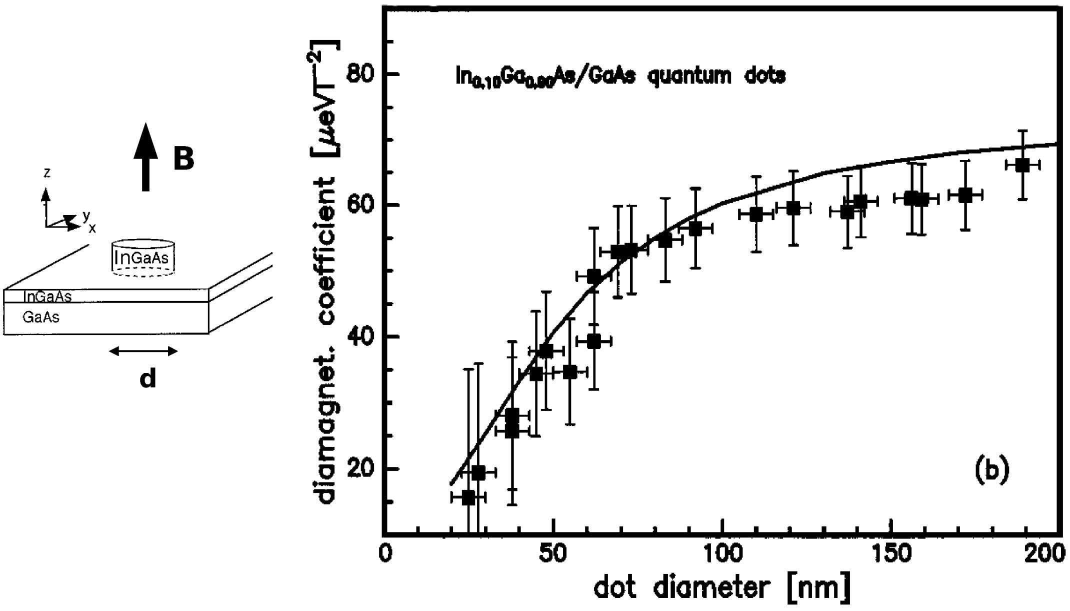

Figure 3.11: *[Bay98] Exciton diamagnetic coefficients of* $In_{0.1}Ga_{0.9}As/GaAs$ *quantum dots with circular symmetry and varying dot diameter. The solid line shows the result of numerical calculations.*

to $\sim 20\,\mu\text{eV/T}^2$ is found. The fact that the diamagnetic coefficient is reduced below the two-dimensional value even for quantum dot diameter on the order of ten exciton Bohr radii shows that already relatively weak lateral confinement leads to a coupling of relative and center-of-mass motion, resulting in a reduction of the exciton radius compared to a laterally unconfined exciton.

One possibility to transfer this approach to the study of disorder in quantum wells is as follows:

- In the case of these cylinder-shaped quantum dots, the experiment has established an empirical link between quantum dot size and diamagnetic coefficients. Numerical simulations have been used to calculate the diamagnetic coefficient as a function of the quantum dot size.

- In attempt to transfer such an approach to the study of disorder in quantum wells, statistical quantities have to be considered. The direct way would be to try to establish, e.g., a relation between the correlation length of the band edge fluctuations and the distribution of diamagnetic coefficients in magneto-μPL spectra. The theory of exciton disorder-localization does in principle provide the machinery that is necessary to establish such a relation theoretically. Experimentally, disordered quantum wells with different correlation lengths have to be investigated.

The aim of this thesis is slightly different: The aim is to first observe at all a systematic pattern in the diamagnetic shift distribution in magneto-μPL spectra of narrow quantum wells, and to develop a qualitative understanding of the relation between the underlying interface disorder and the diamagnetic shift distribution.

For a qualitative understanding of the effects of a magnetic field on localized exciton states, it is useful to introduce an intermediate level in the discussion of diamagnetic coefficients of natural quantum dots, and to express the diamagnetic coefficient in terms of the exciton wave function. Experimentally, the exciton wave function is not directly accessible with μPL spectroscopy, but only the exciton diamagnetic shift. We do not discuss here optical techniques like near-field optical spectroscopy, which could be used to resolve the wave function of exciton states directly [Run05, Run06].

The full description of localized exciton states in two-dimensional disorder is qnot simple, but involves the four-coordinate exciton wave function ϕ_α [Eq. 3.1]. For a qualitative discussion, a simplified language is therefore chosen throughout this work: Although the presence of disorder prohibits the exact separation of the exciton motion in relative and center-of-mass (c.m.) coordinates, it is assumed that an approximate separation is possible locally. More precisely, the projections of the full two-particle wave function ϕ_α of an exciton state α are considered [Gro05],

$$\begin{aligned} \varphi_\alpha(\boldsymbol{\rho}) &= \int d\boldsymbol{R}\, \phi_\alpha(\boldsymbol{\rho}, \boldsymbol{R})\,, \\ \psi_\alpha(\boldsymbol{R}) &= \int d\boldsymbol{\rho}\, \phi_\alpha(\boldsymbol{\rho}, \boldsymbol{R})\,. \end{aligned} \tag{3.6}$$

Here, $\boldsymbol{\rho}$ denotes the two-dimensional vector of the exciton relative coordinate and $\boldsymbol{R}$ the vector of the exciton c.m. coordinate. It is implied that c.m. and relative WF are well-defined for each individual QD, i.e., non-overlapping natural QD states are assumed. Relative and c.m. coordinates are therefore further used to describe localized exciton states. The influence of a lateral confinement potential on the exciton wave function can be included in a heuristic way: Considering that the exciton diamagnetic coefficient is reduced due to lateral confinement also in quantum dots with a diameter ten times the exciton Bohr radius (Fig. 3.11), it can be assumed that exciton c.m. and relative wave function are coupled, and that, due to this coupling, a localization of the exciton c.m. results in a shrinking of the exciton relative wave function. Clearly, this is a heuristic picture, since in principle the full four-coordinate exciton wave function has to be considered.

The subsequent paragraphs describe the effects of lateral confinement on the diamagnetic shift of the exciton ground state in the simpler case of quantum dots with circular symmetry, where some analytical results exists.

3.5 Diamagnetic shift in artificial QDs

The effect of a perpendicular magnetic field on quasi-two-dimensional excitons has been described in chapter 2. Two energy scales, or, equivalently and more illustrative, two length scales determine the magnetic-field behaviour of a magnetoexciton in a quantum well with in-plane translational symmetry: In terms of energy, exciton binding energy and cyclotron energy, or, in terms of length scales, lateral exciton Bohr radius and cyclotron radius. In presence of lateral confinement, a third energy (length) scale comes into play. Taking as an example the simple case of lateral confinement with circular symmetry, this length scale is defined by the lateral radius of the confinement

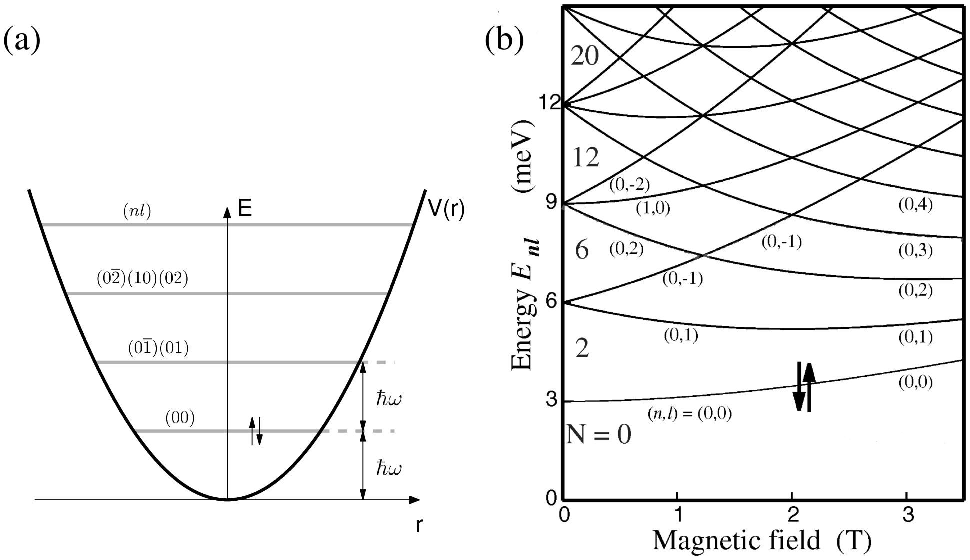

Figure 3.12: *(a) The lowest quantum-mechanical eigenstates in a two-dimensional parabolic confinement potential $V_e(r)$, labeled by their quantum numbers n, l. Each orbital state is twofold spin-degenerate. (b) [Kou01] Magnetic field-dependence of single-particle (electron) states in a two-dimensional parabolic potential ("Fock-Darwin spectrum"). The case $\hbar\omega_e = 3$ meV is shown.*

potential ("dot radius").

The next paragraph first treats the simpler, analytically accessible case of a single particle (electron) in a two-dimensional parabolic confinement potential in presence of a perpendicular magnetic field. In this case, only the two length scales of lateral dot radius and cyclotron radius are involved.

Diamagnetic shift – Electron The discrete energy spectrum of a single electron in a two-dimensional parabolic confinement potential $V_e(r_e) = 1/2\, m_e\, \omega_e^2 r_e^2$ is determined by the eigenstates of the two-dimensional quantum-mechanical harmonic oscillator $E_{nl} = (2n + |l| + 1)\hbar\omega_e$, where $n = 0, 1, 2, \ldots$ is the radial quantum number, and $l = 0, \pm 1, \pm 2, \ldots$ is the angular momentum quantum number. Each orbital state is two-fold spin-degenerate ($S_z = \pm 1/2$). The magnetic-field dependence of the eigenenergies E_{nl} can be calculated analytically [Foc28, Dar30]. The resulting Fock-Darwin spectrum

$$E_{nl}(B) = (2n + |l| + 1)\hbar(\omega_e^2 + \frac{1}{4}\omega_c^2)^{1/2} - \frac{1}{2}\, l\, \hbar\omega_e\,, \tag{3.7}$$

where $\hbar\omega_c = \hbar eB/m_e$ is the cyclotron energy, is shown in Figure 3.12 for a parabolic potential with $\hbar\omega_e = 3$ meV. The magnetic field lifts the orbital degeneracies; this is the normal Zeeman effect.

The magnetic field-dependent increase in the electron ground state energy is quadratic in the low-field limit and changes to a linear, Landau-level-like behaviour at higher fields. The diamagnetic coefficient of the electron ground state decreases monotonously with increasing geometric confinement. This is understood by considering that the total confinement energy is the geometric mean value of geometric confinement ($\sim \omega_e$) and magnetic confinement ($\sim 1/2\,\omega_c$).

Diamagnetic shift – Exciton With a focus on the effect of lateral confinement of the exciton ground state, Halonen *et al.* [Hal92] have numerically studied two-dimensional excitons in parabolic minima. Assuming lateral confinement potentials for electron and hole $V_e(r_e) = 1/2\, m_e\, \omega_e^2 r_e^2$, $V_h(r_h) = 1/2\, m_e\, \omega_e^2 r_h^2$, wave functions and magnetic shifts of heavy-hole exciton ground states were numerically studied, and GaAs parameters for electron and hole masses were used. To describe the two-dimensional (x, y) exciton motion in an external magnetic field $\boldsymbol{B}$ normal to the $x-y$ plane, the total Hamiltonian is written as a sum of c.m. part $H_{\text{c.m.}}$, relative part H_{rel}, and a coupling term H_{x},

$$H = H_{\text{c.m.}} + H_{\text{rel}} + H_{\text{x}}\,. \tag{3.8}$$

The following abbreviations are introduced: Total exciton mass $M = m_e + m_h$, exciton reduced mass $\mu = m_e m_h/M$, and $\gamma = (m_h - m_e)/M$. In-plane c.m. coordinate $\boldsymbol{R} = (m_e\boldsymbol{r}_e + m_h\boldsymbol{r}_h)/M$ and in-plane relative coordinate $\boldsymbol{r} = \boldsymbol{r}_e - \boldsymbol{r}_h$ are used. The c.m. part of the exciton Hamiltonian, $H_{\text{c.m.}}$, is that of a harmonic oscillator,

$$H_{\text{c.m.}} = -\frac{\hbar^2}{2M}\triangle_R + \frac{1}{2}M\left(\frac{1}{M}(m_e\omega_e^2 + m_h\omega_h^2)\right)R^2\,. \tag{3.9}$$

The relative part H_{rel} contains five terms: (i) kinetic energy of the relative motion, (ii) the interaction between B-field and angular momentum of the relative motion, (iii) the diamagnetic shift, (iv) a term related to confinement, and (v) Coulomb energy,

$$H_{\text{rel}} = -\frac{\hbar^2}{2\mu}\triangle_r + \frac{i\hbar e}{2\mu}\gamma\boldsymbol{B}\cdot\boldsymbol{r}\times\boldsymbol{\nabla}_r + \frac{1}{2}\mu\left(\frac{e^2B^2}{4\mu^2} + \frac{1}{M}(m_e\omega_e^2 + m_h\omega_h^2)\right)r^2 - \frac{e^2}{\epsilon}\frac{1}{r}\,. \tag{3.10}$$

The third part of the exciton Hamiltonian contains a B-field dependent term related to the coupling of relative and c.m. motion, and a confinement-related term,

$$H_{\text{x}} = \frac{i\hbar e}{2M}\gamma\boldsymbol{B}\cdot\boldsymbol{r}\times\boldsymbol{\nabla}_R + \mu(\omega_e^2 - \omega_h^2)\boldsymbol{R}\cdot\boldsymbol{r}\,. \tag{3.11}$$

Figure 3.13(a) shows the energies of excitons confined to parabolic minima with curvatures corresponding to (i) $\hbar\omega_e = 5$ meV, (ii) $\hbar\omega_e = 15$ meV, (iii) $\hbar\omega_e = 25$ meV as a function of magnetic field B. The B-dependence of exciton energies is quadratic at low B-fields; a transition to linear shifts occurs at $B_0 \approx 10$ T. The diamagnetic coefficients decrease with increasing lateral confinement, similar to the result for a single particle. As discussed in chapter 2 for laterally unconfined excitons, the nonparabolicity of the diamagnetic shift is related to a reduction of the exciton radius with increasing magnetic field.

Figure 3.13(b) shows the B-dependence of the exciton Bohr radius ($\sqrt{2/3}\,\langle\,\rho^2\,\rangle$) for the three confined exciton states. The decrease in exciton radius is quadratic for low fields and amounts to some percent at $B = 10$ T. To give the numbers, the exciton Bohr radii at $B = 0$ T are (i) $a_B = 5.99$ nm, (ii) $a_B = 5.28$ nm, and (iii) $a_B = 4.77$ nm. At $B = 10$ T, a reduction of the exciton radii by (i) 11 %, (ii) 6 %, and (iii) 3.6 % is observed. From the interpolation formula Eq. (2.48) and the low-field and high-field

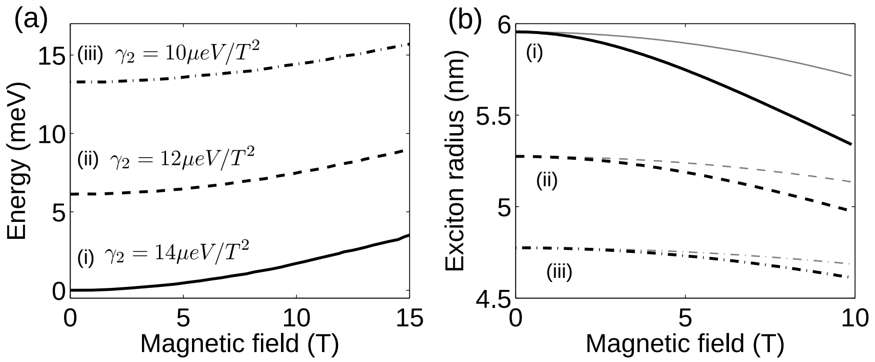

Figure 3.13: *[Hal92] (a) Magnetic field-dependence of the exciton ground state in two-dimensional QDs with parabolic confinement (i) $\hbar\omega_e = 5$ meV, (ii) $\hbar\omega_e = 15$ meV, (iii) $\hbar\omega_e = 25$ meV. (b) Exciton radius as a function of magnetic field for (i)-(iii). GaAs parameters were used.*

limiting cases, an expression for the decrease in exciton radius was determined that depends only on the exciton radius [Eq. 2.57]. The gray lines in Fig. 3.13(b) show the B-dependence of the exciton radius according to Eq. 2.57 for the three exciton radii (i) - (iii). Figure 3.13(b) shows that this expression predicts a too small decrease in exciton radius for the laterally confined exciton states in the parabolic minima (gray curves) as compared to the numerical results (black curves).

Theory of the exciton diamagnetic coefficient A rather general theory of the diamagnetic coefficient of exciton ground states applicable in situations where the lateral confinement potentials of electron and hole exhibit some sort of symmetry has been developed by Walck and Reinecke [Wal98]. It is found that the diamagnetic coefficient results from the combination of electron- and hole-confinement and the electron-hole Coulomb interaction. For an exciton in a lateral confinement potential with circular symmetry, the relative influence of the lateral confinement of electron and hole and electron-hole Coulomb interaction on the diamagnetic coefficient can be characterized by the parameter

$$\lambda = \frac{\langle\rho_e^2\rangle + \langle\rho_h^2\rangle - \langle\rho^2\rangle}{2\frac{\mu}{m_h}\langle\rho_e^2\rangle + 2\frac{\mu}{m_e}\langle\rho_h^2\rangle} \quad (0 \leq \lambda \leq 1)\,, \tag{3.12}$$

where ρ_e, ρ_h are in-plane coordinates of electron and holes, ρ is the exciton relative coordinate, m_e, m_h are in-plane effective masses of electron and hole, and μ is the in-plane exciton reduced mass. In the special case of a lateral confinement potential with circular symmetry, the expression for the diamagnetic coefficient becomes

$$\gamma_2 = \frac{e^2}{8}\frac{\lambda}{\mu}\langle\rho^2\rangle + \frac{e^2}{8}\Big[\frac{1}{m_e} + \frac{\lambda^2}{m_h} - \frac{\lambda}{\mu}\Big]\langle\rho_e^2\rangle + \frac{e^2}{8}\Big[\frac{1}{m_h} + \frac{\lambda^2}{m_e} - \frac{\lambda}{\mu}\Big]\langle\rho_h^2\rangle\,. \tag{3.13}$$

In this particularly simple case, the significance of the scaling parameter λ is evident: Taking $\lambda = 0$, $\gamma_2 \sim \langle\rho_e^2\rangle + \langle\rho_h^2\rangle$ is a measure of lateral confinement of the electron and the hole; this is the limiting case of strong confinement. For $\lambda = 1$, $\gamma_2 \sim \langle\rho^2\rangle$ is a measure of in-plane electron-hole separation. This situation corresponds to the weak-confinement limit [Wal98]. Of course, the result in the weak-confinement limit is identical with the result obtained for a two-dimensional exciton obtained in the previous chapter. For completeness, we state that in the weak-confinement limit the diamagnetic coefficient of the exciton ground state

$$\gamma_2 = \frac{e^2}{8\mu}\langle \rho^2 \rangle \tag{3.14}$$

is proportional to the area of the exciton relative wave function, and depends inversely on the effective in-plane exciton reduced mass.

3.6 Summary

A certain amount of disorder is always present in the interfaces of narrow GaAs/Al$_x$Ga$_{1-x}$As quantum wells. A conceptually clear description of the effects of interface disorder in GaAs/Al$_x$Ga$_{1-x}$As quantum wells on exciton localization requires the concept of band edge fluctuations. This concept has been introduced in this chapter along with the theory of exciton disorder-localization. The strength of band edge fluctuations due to the intrinsic composition fluctuations in GaAs/Al$_x$Ga$_{1-x}$As quantum wells has been determined in a simple model. It demonstrates that an a-priori-classification of alloy disorder as a “perturbation” with respect to exciton localization is not meaningful. In the language of band edge fluctuations, the idea that the complete range of spatial frequencies in the spectrum of interface disorder in narrow quantum wells contributes to exciton localization can be precisely formulated. The two limiting cases of exciton localization by either short-range disorder (“quantum-mechanical limiting case”) or long-range disorder (“exciton-in-a-box”) have been discussed.

The effects of a perpendicular magnetic field on laterally confined exciton states depend on three energy scales, or, equivalently, length scales: The lateral exciton Bohr radius, the cyclotron radius, and the length scale of the lateral confinement potential. The simpler case of an electron in a (circular symmetric) lateral confinement potential, where only two length scales are involved and that is analytically accessible, has been introduced. In the framework of the theory of the exciton diamagnetic coefficient [Wal98], the dependence of the diamagnetic coefficient on single-particle coordinates and exciton relative coordinate in the limiting cases of strong and weak lateral confinement has been described, demonstrating the competing influence of single-particle confinement and Coulomb interaction on the diamagnetic coefficient.

The idea has been outlined that optical techniques with high spatial resolution like μPL spectroscopy open up a new possibility to study exciton localization in narrow quantum wells: Magneto-μPL spectroscopy should give access to the diamagnetic shift distribution of individual local exciton ground states in the low-energy tail of μPL spectra. For a qualitative interpretation of the effect of lateral confinement on the exciton wave function in natural quantum dots, the following qualitative picture has been introduced: The lateral confinement in a natural quantum dot leads to a coupling of c.m. and relative motion of the exciton, and the lateral confinement of the c.m. wave function is accompanied by a simultaneous decrease in exciton radius.

References

[Bay98] M. Bayer, S. N. Walck, T. L. Reinecke, and A. Forchel, *Exciton binding energies and diamagnetic shifts in semiconductor quantum wires and quantum dots*, *Phys. Rev. B* 57, 6584 (1998).

[Bim87] D. Bimberg, J. Christen, T. Fukunaga, H. Nakashima, D. E. Mars, and J. N. Miller, *Cathodoluminescence atomic scale images of monolayer islands at GaAs/GaAlAs interfaces*, *J. Vac. Sci. Technol. B* 5, 1191 (1987).

[Bim86] D. Bimberg, D. Mars, J. N. Miller, R. Bauer, and D. Oertel, *Structural changes of the interface, enhanced interface incorporation of acceptors, and luminescence efficiency degradation in GaAs quantum wells grown by MBE upon growth interruption*, *J. Vac. Sci. Technol. B* 4, 1014 (1986).

[Bru94] K. Brunner, G. Abstreiter, G. Böhm, G. Tränkle, and G. Weimann, *Sharp-line photoluminescence and 2-photon absorption of zero-dimensional biexcitons in a GaAs/AlGaAss structure*, *Phys. Rev. Lett.* 73, 1138 (1994).

[Dar30] C. G. Darwin, *Proc. Camb. phil. Soc. Math. Phys. Sci.* 27, 86 (1930).

[Dev84] B. Deveaud, J. Y. Emery, A. Chomette, B. Lambert, and M. Baudet, *Observation of one-monolayer size-fluctuations in a GaAs/GaAlAs superlattice*, *Appl. Phys. Lett.* 45, 1078 (1984).

[Fle80] R. M. Fleming, D. B. Mcwhan, A. C. Gossard, W. Wiegmann, and R. A. Logan, *X-ray diffraction study of inter-diffusion and growth in* $(GaAs)_n(AlAs)_m$ *multilayers*, *J. Appl. Phys.* 51, 357 (1980).

[Foc28] V. Fock, *Bemerkung zur Quantelung des harmonischen Oszillators im Magnetfeld*, *Z. Phys.* 47, 446 (1928).

[Fuj97] K. Fujiwara, H. T. Grahn, and K. H. Ploog, *Dynamical Stokes shift due to interface nanoroughness in growth islands of GaAs single quantum wells*, *Phys. Rev. B* 56, 1081 (1997).

[Gam90] D. Gammon, B. V. Shanabrook, and D. S. Katzer, *Interfaces in GaAs/AlAs quantum well structures*, *Appl. Phys. Lett.* 57, 2710 (1990).

[Gam91] D. Gammon, B. V. Shanabrook, and D. S. Katzer, *Excitons, phonons, and interfaces in GaAs/AlAs quantum well structures*, *Phys. Rev. Lett.* 67, 1547 (1991).

[Gam96] D. Gammon, E. S. Snow, and D. S. Katzer, *Naturally formed GaAs quantum dots*, *Surf. Sci.* 362, 814 (1996).

[Gol83] L. Goldstein, Y. Horikoshi, S. Tarucha, and H. Okamoto, *Effect of well size fluctuations on photoluminescence spectrum of AlAs/GaAs superlattices*, *Jpn. J. Appl. Phys.* 22, 1489 (1983).

[Gro05] M. Grochol, F. Grosse, and R. Zimmermann, *Exciton wave function properties probed by diamagnetic shift in disordered quantum wells*, *Phys. Rev. B* 71, 125339 (2005).

[Gro82] K. D. Gronwald and M. Henzler, *Epitaxy of Si(111) as studied with a new high resolving LEED system*, *Surf. Sci.* 117, 180 (1982).

[Gro97] R. Grousson, V. Voliotis, N. Grandjean, J. Massies, M. Leroux, and C. Deparis, *Microroughness and exciton localization in (Al,Ga)As/GaAs quantum wells*, *Phys. Rev. B* 55, 5253 (1997).

[Hal92] V. Halonen, T. Chakraborty, and P. Pietilainen, *Excitons in a parabolic quantum dot in magnetic fields*, *Phys. Rev. B* 45, 5980 (1992).

[Hes94] H. F. Hess, E. Betzig, T. D. Harris, L. N. Pfeiffer, and K. W. West, *Near-field spectroscopy of the quantum constituents of a luminescent system*, *Science* 264, 1740 (1994).

[Jah96] U. Jahn, S. H. Kwok, M. Ramsteiner, R. Hey, H. T. Grahn, and E. Runge, *Exciton localization, photoluminescence spectra, and interface roughness in thin quantum wells*, *Phys. Rev. B* 54, 2733 (1996).

[Jus90] B. Jusserand, F. Mollot, J. M. Moison, and G. Leroux, *Atomic-scale roughness of GaAs/AlAs interfaces - a Raman-scattering study of asymmetrical short-period superlattices*, *Appl. Phys. Lett.* 57, 560 (1990).

[Kop91] R. F. Kopf, E. F. Schubert, T. D. Harris, and R. S. Becker, *Photoluminescence of GaAs quantum wells grown by molecular-beam epitaxy with growth interruptions*, *Appl. Phys. Lett.* 58, 631 (1991).

[Kou01] L. P. Kouwenhoven, D. G. Austing, and S. Tarucha, *Few-electron quantum dots*, *Rep. Prog. Phys.* 64, 701 (2001).

[Leo00] K. Leosson, J. R. Jensen, W. Langbein, and J. M. Hvam, *Exciton localization and interface roughness in growth-interrupted GaAs/AlAs quantum wells*, *Phys. Rev. B* 61, 10322 (2000).

[Lew85] B. F. Lewis, F. J. Grunthaner, A. Madhukar, T. C. Lee, and R. Fernandez, *RHEED intensity behavior during homoepitaxial MBE growth of GaAs and implications for growth kinetics and mechanisms*, *J. Vac. Sci. Technol. B* 3, 1317 (1985).

[Nea83] J. H. Neave, B. A. Joyce, P. J. Dobson, and N. Norton, *Dynamics of film growth of GaAs by MBE from RHEED observations*, *Appl. Phys. A* 31, 1 (1983).

[Oga87] S. B. Ogale, A. Madhukar, F. Voillot, M. Thomsen, W. C. Tang, T. C. Lee, J. Y. Kim, and P. Chen, *Atomistic nature of heterointerfaces in III-V semiconductor-based quantum well structures and its consequences for photoluminescence behavior*, *Phys. Rev. B* 36, 1662 (1987).

[Our89] A. Ourmazd, D. W. Taylor, and J. Cunningham, *Chemical mapping of semiconductor interfaces at near-atomic resolution*, *Phys. Rev. Lett.* 62, 933 (1989).

[Pet77] P. M. Petroff, *Transmission electron-microscopy of interfaces in III-V compound semiconductors*, *J. Vac. Sci. Technol.* 14, 973 (1977).

[Reu98] T. C. G. Reusch, *Strukturelle Untersuchungen an GaAs/AlGaAs-Grenzflächen auf der atomaren Skala*, 1998.

[Run02] E. Runge, *Excitons in semiconductor nanostructures*, *Adv Solid State Phys* 57, 149 (2002).

[Run05] E. Runge and C. Lienau, *Near-field wave-function spectroscopy of excitons and biexcitons*, *Phys. Rev. B* 71, 35347 (2005).

[Run06] E. Runge and C. Lienau, *Interpretation of near-field images of semiconductor nanostructures*, *Appl Phys B-Lasers O* 84, 103 (2006).

[Sak85] T. Sakamoto, H. Funabashi, K. Ohta, T. Nakagawa, N. J. Kawai, T. Kojima, and Y. Bando, *Well-defined superlattice structures made by phase-locked epitaxy using RHEED intensity oscillations*, *Superlatt. Microst.* 1, 347 (1985).

[Sal93] H. W. M. Salemink and O. Albrektsen, *Atomic-scale composition fluctuations in III-V semiconductor alloys*, *Phys. Rev. B* 47, 16044 (1993).

[Sav99] V. Savona and R. Zimmermann, *Time-resolved Rayleigh scattering of excitons: Evidence for level repulsion in a disordered system*, *Phys. Rev. B* 60, 4928 (1999).

[Sin85] J. Singh and K. K. Bajaj, *Role of interface roughness and alloy disorder in photoluminescence in quantum well structures*, *J. Appl. Phys.* 57, 5433 (1985).

[Sin84] J. Singh, K. K. Bajaj, and S. Chaudhuri, *Theory of photoluminescence line-shape due to interfacial quality in quantum well structures*, *Appl. Phys. Lett.* 44, 805 (1984).

[Ste02] A. G. Steffan and R. T. Phillips, *Exciton g-factors, diamagnetic shifts, and exchange splittings in quantum dots in GaAs quantum wells*, *phys. stat. sol. a* 190, 541 (2002).

[Wal98] S. N. Walck and T. L. Reinecke, *Exciton diamagnetic shift in semiconductor nanostructures*, *Phys. Rev. B* 57, 9088 (1998).

[War90] C. A. Warwick, W. Y. Jan, A. Ourmazd, and T. D. Harris, *Does luminescence show semiconductor interfaces to be atomically smooth?*, *Appl. Phys. Lett.* 56, 2666 (1990).

[War92] C. A. Warwick and R. F. Kopf, *Microscopic thickness variation of macroscopically uniform quantum wells*, *Appl. Phys. Lett.* 60, 386 (1992).

[Wei81] C. Weisbuch, R. Dingle, A. C. Gossard, and W. Wiegmann, *Optical characterization of interface disorder in GaAs/$Ga_{1-x}Al_xAs$ multi-quantum well structures*, *Solid State Commun.* 38, 709 (1981).

[Woo95] J. C. Woo, S. J. Rhee, Y. M. Kim, H. S. Ko, W. S. Kim, and D. W. Kim, *Bimodal roughness of heterointerface in quantum wells analyzed by photoluminescence excitation spectroscopy*, *Appl. Phys. Lett.* 66, 338 (1995).

[Zim97] R. Zimmermann, F. Grosse, and E. Runge, *Excitons in semiconductor nanostructures with disorder*, *Pure Appl. Chem.* 69, 1179 (1997).

[Zim94] R. Zimmermann and E. Runge, *Exciton lineshape in semiconductor quantum structures with interface roughness*, *J. Lumin.* 60-1, 320 (1994).

[Zre94] A. Zrenner, L. V. Butov, M. Hagn, G. Abstreiter, G. Bohm, and G. Weimann, *Quantum dots formed by interface fluctuations in AlAs/GaAs coupled quantum well structures*, *Phys. Rev. Lett.* 72, 3382 (1994).

Chapter 4

Samples

The samples studied in this thesis were grown by molecular beam epitaxy (MBE) by Dr. Stefan Malzer (Max-Planck Research Group, Institute for Optics, Information, and Photonics, Universität Erlangen-Nürnberg).

The combined study of structural and optical properties of semiconductor heterostructures requires a sample design which is adapted to the requirements of the different measurement techniques used. For scanning tunneling experiments, a sufficiently high concentration of charge carriers in the QWs is necessary to provide the tunneling current. On the other hand, photoluminescence efficiency is highest for intrinsic samples. These at first sight contradicting requirements can be met, however, with a special sample design, since structural and optical measurements are conducted at different temperatures. The chosen sample design is shown in Figures 4.1(a), 4.2(a), and 4.3(a). The arrangement of n-doped barriers in adequate distance from the intrinsic quantum wells ensures (a) negligible charge concentration in the quantum wells at the low temperatures of the μPL measurements (T = 3 K), and (b) sufficient carrier concentration in the QWs in the tunneling experiments performed at room temperature. The QW heterostructures were grown by molecular beam epitaxy (MBE) on exactly (001)-oriented (misorientation $< 0.5°$), n-doped (10^{18} cm^{-3}) GaAs substrates. In all three samples, an n-doped 400 nm buffer layer was grown directly on the substrate, followed by a 50 nm intrinsic GaAs layer. On top, three different quantum well sequences were grown in samples QW$_1$, QW$_2$ and QW$_3$.

In case of sample QW$_1$, the quantum well barriers consist of 15 nm thick intrinsic Al$_{0.3}$Ga$_{0.7}$As layers. Intrinsic GaAs QWs with 4, 6, 8, 10, and 20 nm nominal thickness were grown by turning off the Al flux for well-defined, increasing time intervals [Fig. 4.1(b)]. On top of the quantum well sequence, another 50 nm intrinsic GaAs layer was grown, followed by a 100-nm n-doped GaAs layer and a 200-nm intrinsic Al$_{0.3}$Ga$_{0.7}$As layer. A 50 nm n-GaAs capping covers the QW sample [Fig. 4.1(b)].

Figures 4.2 and 4.3 show the structure of samples QW$_2$ and QW$_3$. The surrounding of the QW sequence is identical in both samples: Like in sample QW$_1$, an n-doped 400 nm buffer layer was grown directly on the substrate, followed by a 50 nm intrinsic GaAs layer. On top of the QW sequence, another 50 nm intrinsic GaAs layer is grown, followed by a 100 nm n-doped GaAs capping layer.

In sample QW$_2$, the quantum well barriers are formed by 20 nm thick layers of intrinsic

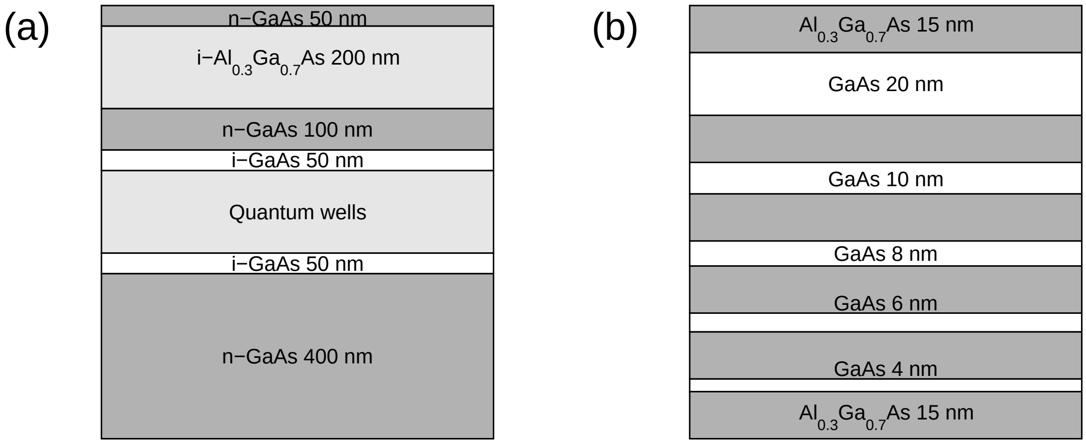

Figure 4.1: *(a) Structure of the GaAs/$Al_{0.3}Ga_{0.7}As$ quantum well sample QW_1, and (b) zoom into the QW sequence.*

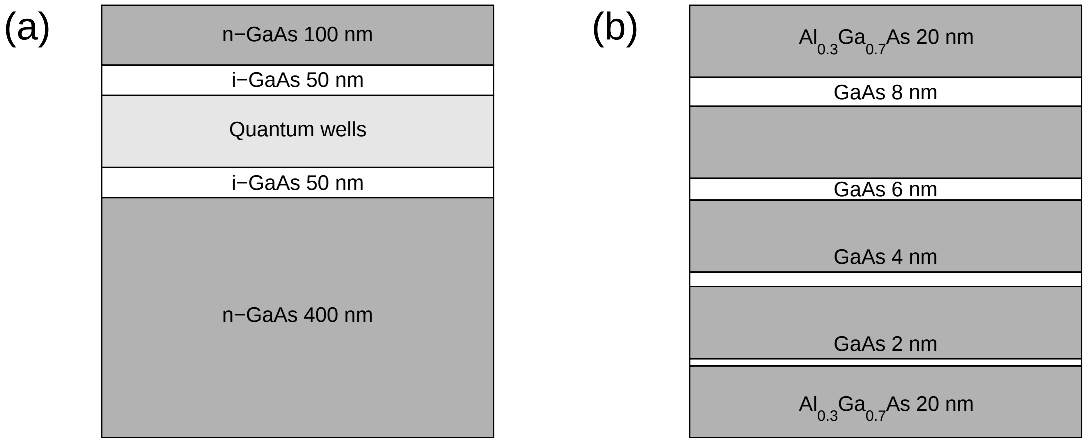

Figure 4.2: *(a) Structure of the GaAs/$Al_{0.3}Ga_{0.7}As$ quantum well sample QW_2, and (b) zoom into the QW sequence.*

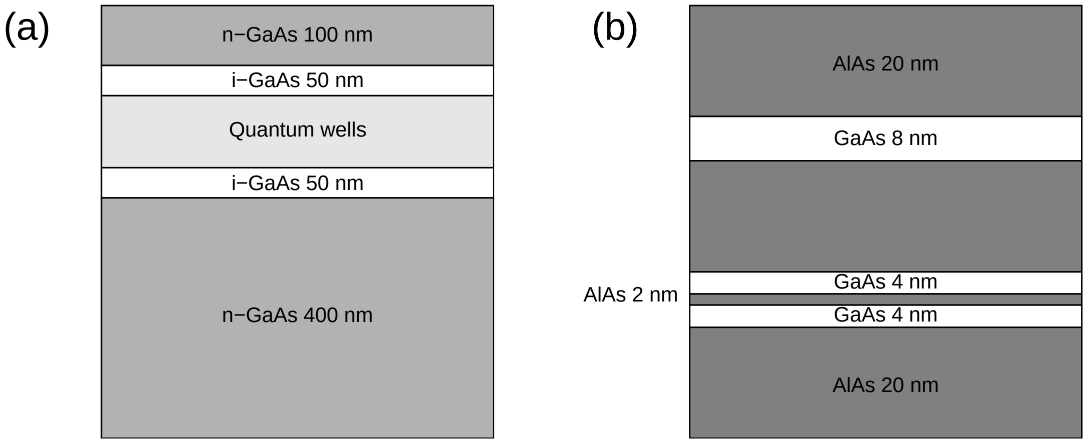

Figure 4.3: *(a) Structure of the GaAs/AlAs quantum well sample QW_3, and (b) zoom into the QW sequence.*

$Al_{0.3}Ga_{0.7}As$, and a sequence of intrinsic GaAs QWs with nominal widths of 2, 4, 6, and 8 nm has been grown [Fig. 4.2(b)].

The QW sequence in sample QW_3 consists of alternating intrinsic GaAs and AlAs layers that were grown by alternately opening the Al shutter and simultaneously closing the Ga shutter, and vice versa. The QW sequence consists of a 20-nm AlAs barrier, two 4-nm GaAs wells separated by a 2-nm AlAs tunneling barrier, a second 20-nm AlAs barrier, an 8-nm GaAs well, and a third 20-nm AlAs barrier.

The carrier concentration in the intrinsic QWs resulting from the thermally activated diffusion of carriers from the n-doped (10^{18} cm^{-3}) barriers has been simulated using the heterostructure modeling program HETMOD [1]. The one-dimensional coupled Schrödinger-Poisson equations in the nominal heterostructure profiles were solved numerically for room temperature ($T = 295$ K) and for $T = 3$ K, using nominal dimensions, composition, and doping level of the QW samples samples QW_1 and QW_3.

Figure 4.4 shows the $T = 3$ K band edges at Γ of the GaAs/$Al_{0.3}Ga_{0.7}As$ sample QW_1 and the simulated charge densities at $T = 3$ K and $T = 295$ K. At low temperatures ($T = 3$ K), the carrier concentration decreases from the doping level of the n-doped barriers ($< 10^{18}$ cm^{-3}) to $\sim 3 \cdot 10^{15}$ cm^{-3} outside the QW sequence. The carrier concentration in the wells is negligible ($< 10^{8}$ cm^{-3}). At room temperature, the carrier concentration outside the wells increases to $\sim 3 \cdot 10^{16}$ cm^{-3}, and the concentration in the wells ranges from $\sim 1 \cdot 10^{16}$ cm^{-3} in the 4-nm well to $\sim 1 \cdot 10^{16}$ cm^{-3} in the 20-nm well. Similar results are obtained for the GaAs/AlAs sample QW_3, shown in Fig. 4.5.

---

[1] Software package written by Alan C. Warren of the Thomas J. Watson Research Center, Yorktown Heights, NY

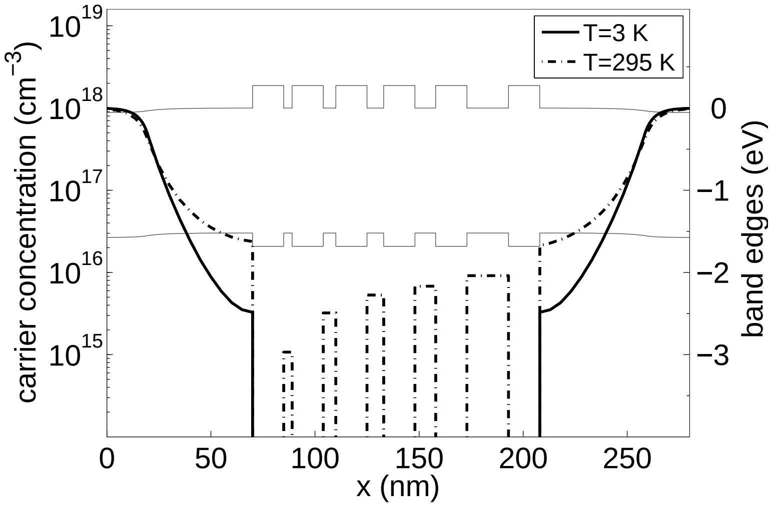

Figure 4.4: *Simulated electron concentration profile in the GaAs/*$Al_{0.3}Ga_{0.7}As$ *quantum well sample* QW_1 *at room temperature (dashed line) and* $T = 3$ *K (solid black line). The HETMOD program has been used to solve the one-dimensional Schrödinger-Poisson equation. Valence and conduction band edges of the heterostructure (*$T = 3$ *K) are indicated as gray lines (right axis).*

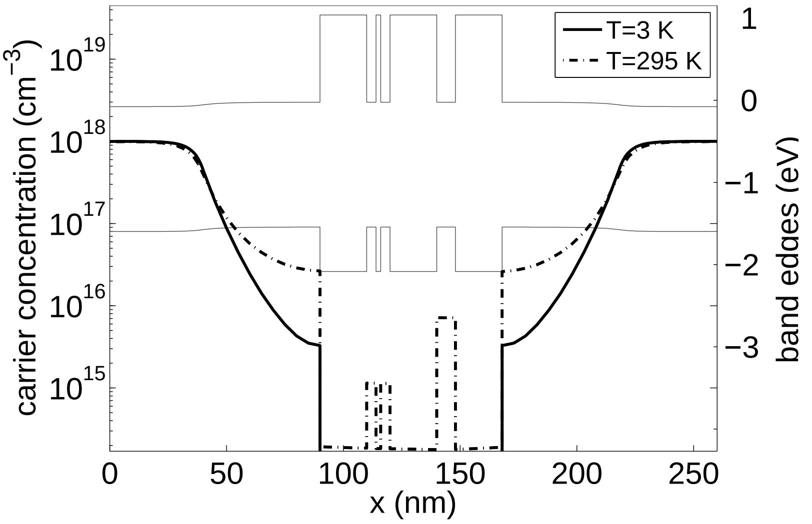

Figure 4.5: *Simulated electron concentration profile in the GaAs/AlAs quantum well sample* QW_3 *at room temperature (dashed line) and* $T = 3$ *K (solid black line). The HETMOD program has been used to solve the one-dimensional Schrödinger-Poisson equation. Valence and conduction band edges of the heterostructure (*$T = 3$ *K) are indicated as gray lines (right axis).*

Chapter 5

Scanning tunneling microscopy

The sample design of the QW heterostructures allows the investigation of the real space structure of the quantum well interfaces with scanning tunneling microscopy (STM). The first section of this chapter introduces basics of STM. The experimental steps required for cross-sectional STM (XSTM) on the quantum well samples are described in the second section. The third section describes the structure of the GaAs (110) surface. In the last section, STM topographies of the 4-nm GaAs/$Al_{0.3}Ga_{0.7}As$ quantum well in cross-sectional geometry are shown. Using an envelope function approach, the interface disorder along the QW cross section in the (110) cleavage plane is analyzed.

5.1 Basic principles

Scanning tunneling microscopy enables the study of the surface electronic structure of a wide variety of materials, including semiconductors, with atomic resolution. The main experimental limitation on the sample type is the requirement of conducting surfaces and electrical contact to this surface. The scanning tunneling microscope shares its basic principles with several other local probe techniques: A sharp probe ("tip") is positioned close to a surface until probe and surface begin to interact locally. The local interaction (I), that depends on the tip-sample distance, is measured, and used to control the tip-sample distance using a feedback loop.

The STM measures the quantum-mechanical electron tunneling current between a sample surface and a metal tip. Tip and sample are placed in close proximity ($\sim 0.5-1$ nm) and a bias voltage U is applied between them. Due to the overlap between electronic orbitals of tip and sample atoms, a tunneling current flows through the potential barrier of the vacuum gap. To obtain the experimental data shown in this chapter, a tungsten tip with $\sim$ 10 nm radius was used. A bias voltage $|U| = 2$ V was applied, and the tunneling current was $\sim$ 100 pA. To image the surface electronic structure, the tip is scanned over the sample, while the tunneling current is held constant (constant-current mode). The map of the tip height (constant current topography) shows an isosurface of the electronic density of the surface. The resulting image reflects the morphology of the sample surface with features of pure electronic origin superimposed. Since the electronic density of states at the sample surface depends on the atom species, mapping of surfaces with chemical element sensitivity is possible with STM.

One basic feature of the STM, the strong sensitivity of the tunneling current on the tip-sample distance, is already evident from the simple model of a one-dimensional tunneling barrier. Considering electrons tunneling through the vacuum barrier from the tip into the sample, the barrier height is defined by the work function of the metal tip Φ_t and the electron affinity of the sample Φ_s. Defining the effective barrier height $\Phi = (\Phi_s + \Phi_t)/2$ for a trapezoidal tunneling barrier, the dependence of the tunneling current on barrier width can be expressed by [Hof03]

$$I(z) \propto e^{-k\sqrt{2\Phi}\,z}\,, \tag{5.1}$$

where k is a constant and z is the barrier width, i.e., the tip-sample distance. The exponential dependence of the tunneling current on the vacuum barrier width explains the extreme height sensitivity of the STM.

In contrast to the rather simple principle of STM, a complete theoretical description requires a significant amount of theoretical machinery, depending on the degree of accuracy that is to be achieved. A relatively simple model describing elastic tunneling processes, which is widely used for the interpretation of STM experiments, has been developed by Tersoff and Hamann [Ter83, Ter85]. This model neglects many of the factors that actually influence the tunneling current. It makes use of a modification of the perturbation approach of Bardeen [Bar61], which was originally conceived to describe the tunneling current in one dimension observed in experiments on macroscopic tunneling junctions. The Bardeen approach assumed that the tunneling current can be expressed in terms of the undisturbed eigenfunctions of two isolated subsystems.

The Tersoff-Hamann model assumes that the tunneling process in an STM experiment can be described by the wave function overlap between a single s-orbital at the apex of the tip and the sample wave functions. The bias voltage U is assumed to be small ($|U| \sim 10$ mV) [Ter85]. Then, the Fermi levels of sample and tip are approximately

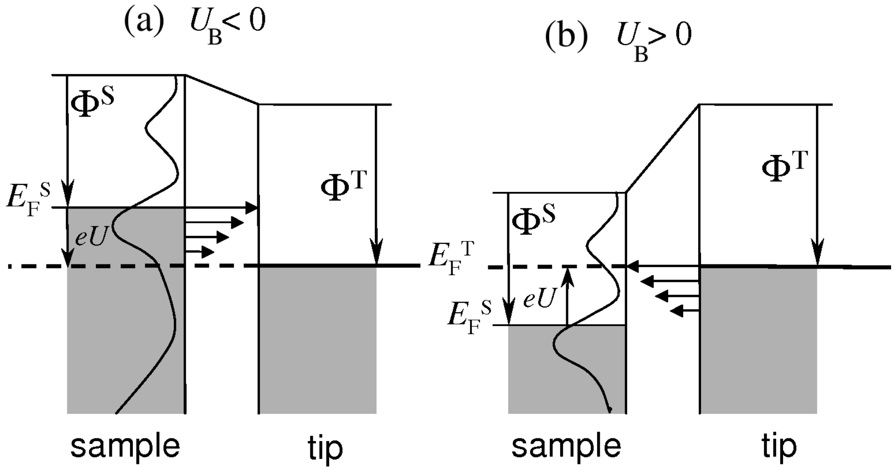

Figure 5.1: *[Qua03] A one-dimensional model of the tunneling junction at finite bias voltages* U_B *applied at the sample. The barrier is defined by the electron affinity of the semiconductor surface* (Φ_s) *and the work function of the metal tip* (Φ_t).

equal ($E_{F,t} = E_{F,s} \equiv E_F$). As a further simplification, it is assumed that experiments are conducted at low temperature, where Fermi functions can be approximated by step functions. In the Tersoff-Hamann model, the tunneling current is proportional to the bias voltage U and to the local density of states (LDOS) $\rho_s(\boldsymbol{r}, E_F)$ of the sample surface at the position of the tip $\boldsymbol{r}$ and at the Fermi energy E_F,

$$I \propto U\,\rho_s(\boldsymbol{r}, E_F)\,, \quad \rho_s(\boldsymbol{r}, E_F) = \sum_\nu \left|\psi_\nu(\boldsymbol{r})\right|^2 \delta(E_\nu - E_F)\,, \tag{5.2}$$

where the local density of states of the sample is defined as the sum over the sample wave functions at a given energy. The assumption of small bias voltage allows to neglect the energy dependence of tip and sample wave functions. In tunneling experiments on semiconductors, bias voltages on the order of 1 V are applied, i.e., the low-voltage assumption is violated. Hamers *et al.* [Ham01] have therefore extended the Tersoff-Hamann model to the case of finite bias voltage. Following Hamers *et al.*, the tunneling current can be written

$$I \propto \int\limits_0^{eU} \rho_s(\boldsymbol{r}, E)\,\rho_t(\boldsymbol{r}, E - eU)\big|T(E)\big|\,dE\,, \tag{5.3}$$

where $\rho_s(r, E)$ and $\rho_t(r, E)$ denote the LDOS of states of sample and tip with $\rho_s(r, E)$ and $\rho_t(r, E)$, and the energy-dependent transmission probability $T(E)$ has been introduced. The transmission probability $T(E)$ can be approximated using the Wentzel-Kramers-Brillouin (WKB) method by

$$T(E, eU) = \exp\left(-\frac{2z\sqrt{2m}}{\hbar}\sqrt{\frac{\Phi_s + \Phi_t}{2} + \frac{eU}{2} - E}\right), \tag{5.4}$$

where z is the distance from sample to tip, and Φ_s and Φ_t are the work functions of sample and tip. The tunneling current now arises from a range of states within eU of the Fermi level. This situation is visualized in Fig. 5.1, showing a one-dimensional sketch of the tunneling junction of sample, vacuum barrier, and tip. The electronic density of states of sample and tip are indicated (ρ_s, ρ_t) and the occupied electron states (at $T = 0$ K) are shown shaded grey. Φ_s is the electron affinity of the semiconductor surface, and Φ_t is the work function of the metal tip. A negative bias voltage U is applied at the sample. Due to the difference between Fermi levels $E_{F,s}$ in the sample and $E_{F,t}$ in the tip, an electron tunneling current I flows from the occupied sample states in the energy range between the Fermi levels of tip $E_{F,t}$ and sample $E_{F_s} = E_{F_t} + eU$ into the unoccupied tip states in the tip. The different lengths of the arrows indicate the energy-dependence of the transmission probability $T(E)$.

5.2 Cross-sectional scanning tunneling microscopy

Having described basics of STM, this section describes experimental requirements and methods that enable the application of STM to the study of the atomic structure of semiconductor surfaces. Semiconductor surfaces in general have high adsorption coefficients due to their free dangling bonds at the surface. Therefore, all STM work on

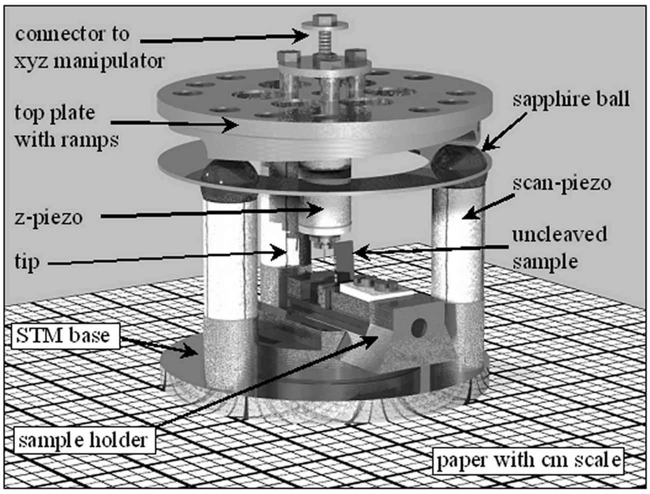

Figure 5.2: *[Hei98] The "beetle"-STM based on the design by Besocke [Bes87]. The top plate can be lifted off with a manipulator for tip and sample exchange. Lateral coarse positioning is done via slip-stick movements of the scan piezos. Tip transporters and sample holders are inserted into the dovetail sample support in the center.*

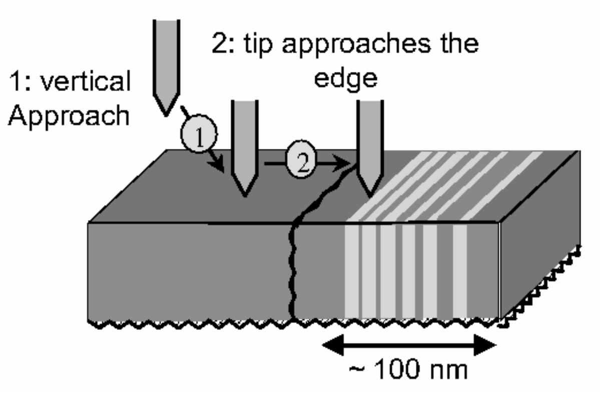

Figure 5.3: *Sketch of the approach and positioning procedure for XSTM. (1) The tip is approached vertically to the sample surface. (2) The tip is positioned laterally at the heterostructures. Adapted from [Hei98].*

semiconductor surfaces requires ultra high vacuum (UHV) systems with base pressure around $1 \cdot 10^{-10}$ mbar. The design of the UHV vacuum chamber and of the STM used for the measurements shown here has been described in detail in [Hei98]. Figure 5.2 shows the design of the STM head used for the XSTM measurements; it is based on the "beetle"-type design developed by Besocke [Bes87]. The most important advantage of this type of microscope is the fact that it does not need any mechanical feedthroughs for the coarse vertical approach and the lateral positioning of the tip. The "beetle"-type STM is made up of two parts that can be moved with respect to each other: The base, which includes the sample and the scan piezos (outer piezo tubes), and the top plate, which contains the z piezo and the tip. By rotating the top plate with respect to the base, the distance between tip and sample can be changed macroscopically. Moving the top plate laterally results in a coarse lateral positioning of the tip with respect to the sample, which is necessary to locate the tip at the heterostructures.

The uncleaved sample is shown in the sample holder inserted in the STM base in Figure 5.2. The most important requirement for successful XSTM work in terms of sample preparation is the need to obtain perfectly flat surfaces in the cleavage process in the vacuum chamber. A sample of typical dimensions of 2 mm × 10 mm is cut from the wafer and is then chemo-mechanically thinned and polished to a typical thickness of about 100 μm. Then a notch is prescribed on the front surface [the (001) growth surface] at a height of 3 mm. The last ex-situ step in sample preparation is the mounting of the sample in a small UHV compatible vice.

The cleavage process is conducted under UHV conditions. After introducing the samples into the UHV system, the actual cleavage surface is prepared by applying a force to the upper part of the sample. This process breaks the sample at the height of the notch and results in a cleavage surface. As mentioned above, the heterostructures are located at one edge of this cleavage surface toward the [001] growth direction. Figure 5.3 shows the two approach mechanisms needed for XSTM of the QW heterostructures. First, the tip has to be approached to the sample vertically. Second, it has to positioned laterally over the heterostructures. Moving the tip laterally to the heterostructures as indicated in Figure 5.3 is done with a slip-stick motion. In the setup used, optical access to the UHV chamber with a high-quality optical microscope helps in the coarse lateral approach of the tip to the position of the heterostructures.

5.3 Atomic structure of the GaAs (110) surface

In the XSTM experiment on the GaAs/$Al_{0.3}Ga_{0.7}As$ heterostructure, a cleaved (110) surface with low step-density was obtained. This section describes the atomic structure of the GaAs (110) surface. The GaAs {110} surfaces form the set of natural cleavage surface of the GaAs crystal. Every GaAs {110} surface contains the same number of Ga and As atoms in the top layer. The surface atoms form so-called zigzag chains, consisting of rows of Ga bonded to two surface As atoms, and As atoms bonded to two Ga surface atoms. The surface unit cell is rectangular with the surface lattice constants 5.65 Å along [001] and 4.0 Å along [110] and $[1\bar{1}0]$ [Ada94]. A ball-and-stick model of the GaAs (110) surface is shown in Fig. 5.4; atoms in the surface layer are drawn larger as atoms in the first subsurface layer.

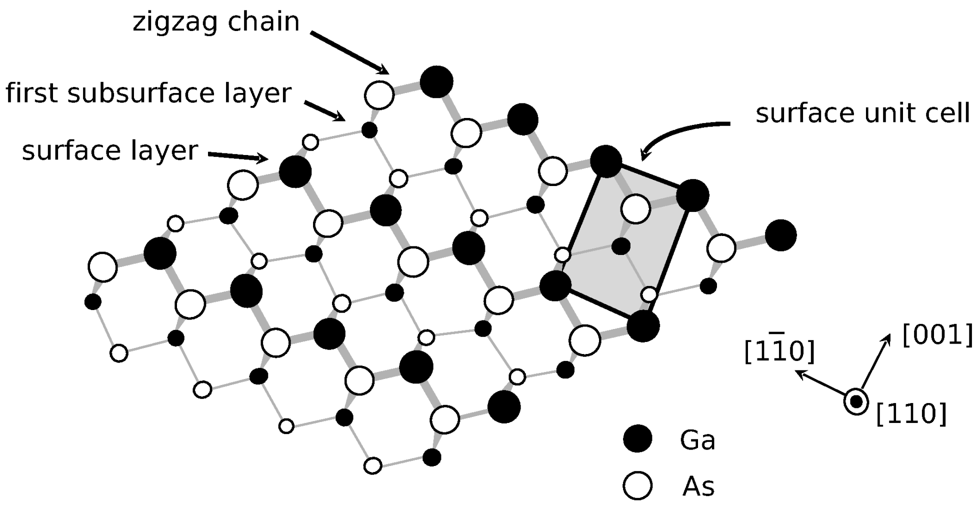

Figure 5.4: *[Hei98] Top view on a ball and stick model of the GaAs (110) surface with Ga (filled circles), As (open circles), bonds (gray lines). Large atoms: surface layer, small atoms: first subsurface layer.*

Every surface atom of the GaAs (110) surface has one broken bond, called the dangling bond, which points out of the surface into the vacuum. The top layer As atoms are moved out of the surface, and the Ga atoms are moved into the bulk [Smi85, Fee87]. This structural relaxation goes along with the electronic relaxation, transferring charge from the dangling bonds at the Ga atoms into the dangling bonds at the As atoms. The dangling bonds at the As atoms are therefore filled states, whereas those at the Ga atoms are empty states [Lub76, Ter85]. The empty dangling bond surface states of the Ga atoms are located above the energy of the bulk conduction band onset, whereas the the filled dangling bond states of the As atoms are below the valence band onset. The dangling bond states dominate the STM image because they have a larger local density of states close to the surface than the evanescent bulk states [Hei98]. Comparison with Fig. 5.1 shows that at positive sample voltage, the empty dangling bonds corresponding to the Ga atoms are imaged. At negative sample voltage, the As atoms are imaged [Ter85, Fee85, Fee87, Ebe96].

On a cleavage surface of the $\mathrm{Al}_x\mathrm{Ga}_{1-x}\mathrm{As}$ alloy, every group-III site is occupied either by a Ga or an Al atom. In empty-state XSTM images on highly p-doped $\mathrm{Al}_x\mathrm{Ga}_{1-x}\mathrm{As}$ with Al concentration $x = 0.35$, the composition fluctuations in the $\mathrm{Al}_x\mathrm{Ga}_{1-x}\mathrm{As}$ surface were observed directly [Sal93]. While in empty-state images the dangling bonds of the group-III atoms are directly imaged, it has been observed that individual Al atoms induce a local contrast on their surface As neighbours that allows their identification also in filled-state XSTM images of n-doped $\mathrm{Al}_x\mathrm{Ga}_{1-x}\mathrm{As}$. In filled-state XSTM images on $\mathrm{Al}_{0.15}\mathrm{Ga}_{0.85}\mathrm{As}$, this Al-induced contrast has been used to identify individual and pairs of surface-layer Al atoms on the atomic scale [Hei98, Hei99]. At the Al concentration of $x = 0.15$, it was possible to use the concept of an $\mathrm{Al}_{0.15}\mathrm{Ga}_{0.85}\mathrm{As}$ layer as a GaAs matrix with point defects introduced by individual Al atoms or pairs of Al atoms. At higher Al concentration, it becomes difficult to identify individual Al atoms. Second layer Al atoms were not seen due to the relatively high Al concentration of $x = 0.15$.

5.4 XSTM topographies of the GaAs/$Al_{0.3}Ga_{0.7}As$ heterostructure

On the GaAs/$Al_{0.3}Ga_{0.7}As$ quantum wells in sample QW_1, room-temperature STM has been performed in cross-sectional geometry. The XSTM measurements were performed on an atomically smooth (110) surface, which had been prepared by in-situ cleavage of the sample in a UHV chamber with a base pressure of less than $5 \cdot 10^{-11}$ mbar. The XSTM tips were etched from polycrystalline tungsten. After transfer into UHV, the tips were annealed at 1200 K, sputtered with 4 kV Ar ions and characterized by field emission. Cross-sectional constant-current topographs of all five QWs in sample QW_1 were taken with atomic resolution over lateral lengths of typically 200 nm. The XSTM experiments have been performed by Lars Winking and Thilo Reusch (4. Physikalisches Institut, Universität Göttingen).

Figure 5.5 shows a constant-current topography of the 4-nm GaAs/$Al_{0.3}Ga_{0.7}As$ quantum well. The STM topography on the cleaved (110) surface of the sample was taken at a bias voltage $U_B = -2$ V and a tunneling current $I_T = 100$ pA. The crystallographic axes are indicated. The coordinate in $[1\bar{1}0]$ direction is denoted as x-coordinate, the coordinate in growth direction ([001]) as z-coordinate; the topographic height in the cleavage plane is denoted as $h(x, z)$. Several constant-current topographies from overlapping areas of 20×20 nm^2 each were obtained along the 4-nm QW under practically identical conditions and coalesced into a single, 160 nm long topography. [1] The linear grayscale image clearly shows a clear contrast between well and barrier regions. The contrast in Fig. 5.5 is due to a difference in the average topographic height $\langle h(x, z)\rangle_x$ between well and barrier regions: The average topographic height in the barrier region is lower than in the well region. The topograpic height is related to the electronic structure at the surface; since the constant-current tunneling measurements were made at negative bias voltages, only the cation (group-V) sublattice is visible [Sal93]. Also note that, as a consequence of the arrangement of the atoms at the GaAs surface (Fig. 5.4), only every second monolayer is imaged. Nonetheless, the topographic variation on an atomic scale demonstrates the sensitivity to the Aluminum distribution.

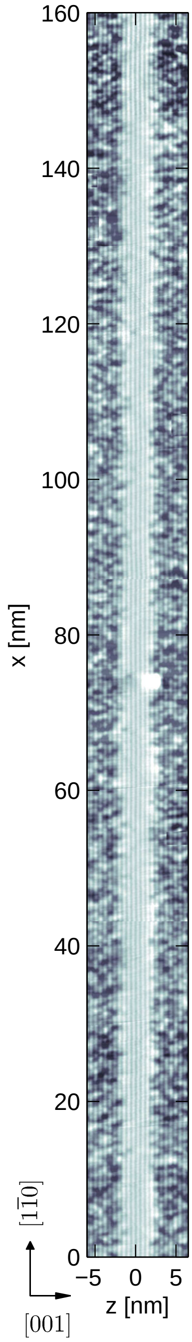

Figure 5.5: *XSTM topography of the 4-nm QW.*

Figure 5.6(a) zooms into a section of the XSTM topography of the 4-nm GaAs/$Al_{0.3}Ga_{0.7}As$ quantum well. The bright stripes along the $[1\bar{1}0]$ direction that are clearly visible in the well region reflect the surface corrugation of the GaAs (110) surface. Figure 5.6(b) shows the topographic height profile of the 4-nm QW averaged over a length of 160 nm in $[1\bar{1}0]$ direction. The averaged height profile demonstrates (i) that the contrast between well and barrier observed in Figure 5.6(a) is due to a difference in the average height $\langle h(x, z)\rangle_x$

---

[1] At $x = 74$ nm, an adsorbat atom masks the right interface region of the QW.

between the well and the barrier regions of about 25 pm, and (ii) that a modulation with an amplitude of $\sim$ 10 pm and a period of 0.565 nm is superimposed in z-direction, resulting from the morphology of the GaAs surface.

To proceed, the atomic corrugation in z-direction is fourier-filtered from the averaged height profile $\langle h(x,z)\rangle_x$. The resulting corrugation-filtered height profile $h(z)$ is shown as red line in Fig. 5.6(a). The same procedure is also applied to the complete topography $h(x,z)$; the result is shown in Fig. 5.6(c).

Finally, it is presumed that the average height difference of 25 pm between well and barrier not only reflects the global difference in the average Aluminum concentration, but that it can also serve as a local gauge for the Aluminum distribution in the barriers and at the interfaces. This assumption provides the basis to convert the corrugation-filtered topography into a map of the local band gap.

First, however, the corrugation-filtered, x-averaged height profile $h(z)$ [red line in Figure 5.6(b)] is fitted with an exponentially smoothed ("Woods-Saxon") profile

$$h^*(z) = h_0 + \Delta h \cdot \left(\frac{1}{1+e^{(z-z_l)/w_l}} + \frac{1}{1+e^{(z-z_r)/w_r}}\right), \tag{5.5}$$

where h_0 is the averaged topographic height in the barriers and $\Delta h = 25$ pm is the average height difference between well and barrier. Here, z_l and z_r denote the inflection points of the left and right interface transition regions, and w_l, w_r denote the widths of the transition regions. Both transition regions are about 1 nm wide.

Then, a linear scaling to the local band gap is applied to the smoothed height profile $h^*(z)$

$$E_G(z) = E_{\mathrm{G,GaAs}} + b \cdot (h^*(z) - h_0) \tag{5.6}$$

with $b = -19.8$ mV/pm. The negative scaling factor b reflects the lower topographic height in the barrier; it is determined by the 436 meV bandgap difference between the GaAs well and the $\mathrm{Al_{0.3}Ga_{0.7}As}$ barrier. For the GaAs band gap, the $T = 4$ K value $E_G = 1.519$ eV is taken. Distributing the total band gap difference $E_G(z) - E_{\mathrm{G,GaAs}}$ between barrier and well according to the band offset ratio $f_e/f_h = 0.65/0.35$ results in band offset profiles for conduction and valence band.

The same linear scaling is applied to the complete corrugation-filtered topography in Fig. 5.6(c), thereby converting it into a map of the local bandgap. Averaging along the x-direction results in the bandgap profile shown as black line in Fig. 5.6(d). The exponentially smoothed bandgap profile is also shown as red line in Fig. 5.6(d).

The determination of the local band edges now proceeds largely as described in chapter 3 (Fig. 3.2). To obtain envelope wave functions of the lowest electron and hole subbands in the 4-nm QW, the exponentially smoothed x-averaged valence and conduction band offset profiles are used here. The finite-difference method that has been used for numerically solving the single-particle Schrödinger equation in these band offset profiles is described in Appendix A. Figure 5.6(c) shows the calculated probability densities $u_e(z)^2$, $u_h(z)^2$ of the envelope wave functions of electron (black) and heavy hole (white).

The same scaling parameters b and h_0 as in Eq. (5.6) can be used to scale the topography

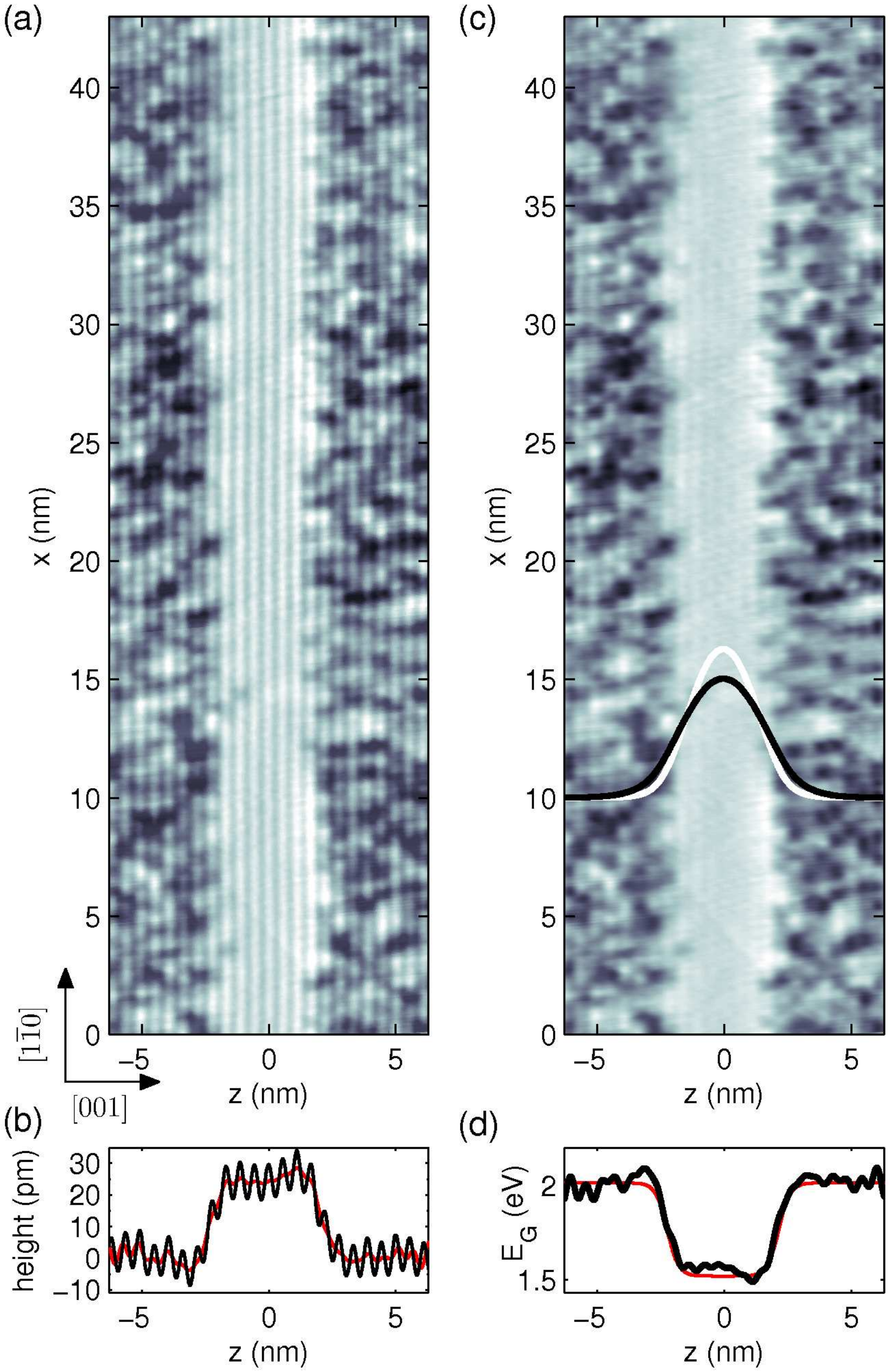

Figure 5.6: *(a) Constant-current topography of the 4-nm GaAs/*$Al_{0.3}Ga_{0.7}As$ *quantum well; (b) topography averaged along the* $[1\bar{1}0]$ *direction; (c) corrugation-filtered topography; (d) average profile of the local band gap. Envelope wave functions of electron (black) and heavy hole (white) have been calculated in symmetric, exponentially smoothed band offset profiles (red) distributed among conduction and valence band according to the band offset ratio* $f_e/f_h = 0.65/0.35$.

$h(x, z)$ to band offsets of valence and conduction bands,

$$E_G(x, z) = E_{\mathrm{G,GaAs}} + b \cdot (h(x, z) - h_0)\,. \tag{5.7}$$

Analogous to the proceeding in chapter 3, disorder potentials $V_e(x)$, $V_h(x)$ for electron and hole along the $[1\bar{1}0]$ direction are determined by weighting the difference between local bandgap $E_G(x, z)$ and the bandgap profile averaged in z-direction, $E_G(z) = \langle E_G(x, z)\rangle_x$, with the envelope wave functions $u_e(z)^2$, $u_h(z)^2$ and integration in z-direction. The resulting one-dimensional disorder potentials for electron and hole along the quantum well cross-section,

$$V_a(x) = \int dz\, u_a^2(z) \left[E_G(x, z) - \overline{E}(z)\right], \quad a = e, h\,, \tag{5.8}$$

are shown in Fig. 5.8(a). The potential values are approximately Gaussian distributed [Fig. 5.8(b)]. Therefore, $V_e(x)$ and $V_h(x)$ can be characterized by their standard deviations σ (potential strength) and by their spatial autocorrelations

$$C_a(\Delta) = \int V_a(\Delta)(x)\, V_a(x - \Delta)\, dx\,, \quad a = e, h\,. \tag{5.9}$$

In turn, if a normalized correlation function $W(r)$ ($\int dr\, W(r) = 1$) is given, a correlated

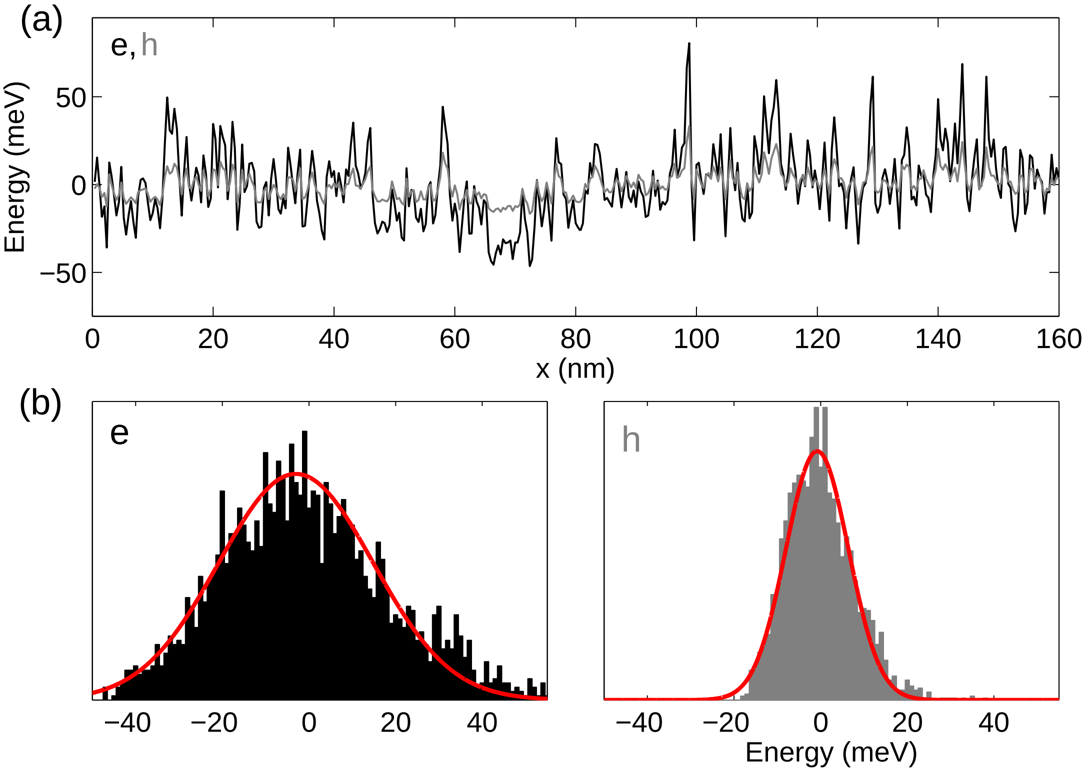

Figure 5.7: *(a) Disorder potential for electron (black) and heavy-hole (gray) along the cross section of the 4-nm GaAs/Al*$_{0.3}$*Ga*$_{0.7}$*As QW. (b) Potential value distribution of the in-plane electron and hole disorder potentials.*

potential is obtained by convolution with an uncorrelated ("white noise") disorder potential $U(r)$,

$$V(r) = \int dr'\, W(r - r')\, U(r)\,. \tag{5.10}$$

The disorder strengths determined from the potential value distributions shown in Fig. 5.8(b) are $\sigma_e = 20.5$ meV and $\sigma_h = 7.7$ meV.

The information on the correlations in the growth direction (z) is qualitatively contained in the values σ_e, σ_h. This can be seen as follows: The value of σ is completely insensitive to lateral (x) correlations as it only represents the standard deviation of the potential. If there are, however, correlations of the local bandgap in the growth direction, this will result in increased fluctuations of the weighted z-average in Eq. (5.8), compared with a completely uncorrelated Aluminum distribution. This can be easily demonstrated by, e.g., starting from the model of a random, uncorrelated Al distribution in the AlGaAs barriers as shown in Fig. 3.2(a). Correlations in z-direction can be introduced, e.g., by inserting double layers by hand, where the same lateral lattice positions are occupied by Al atoms in neighbouring layers. Determination of the band edge fluctuations according to the procedure demonstrated in Fig. 3.2 readily shows that the presence of z-correlations leads to increased disorder strength.

The effect of z-correlations in the Al distribution represented by the XSTM topography in Fig. 5.5 can be quantified by comparing the determined σ-value with that obtained after an intentional removal of all z-correlations from the XSTM image. This can be done in the following way: First, the XSTM data have to be binned on an atomic grid in x-direction (row distance 0.4 nm). Then, z-correlations are removed by randomly shifting the individual atomic rows in the barriers along the x-direction with respect to each other [Rop07]. For this situation, one obtains a standard deviation about 30 % smaller than the original one. Therefore, it is asserted that z-correlations contribute significantly to the inhomogeneous broadening of the optical spectra. In fact, certain z-correlations are already discernible by close inspection of the topography in Fig. 5.6, where weak stripe-like contrasts in the z-direction are visible, especially in the right barrier regions.

The correlations in x-direction are contained in the autocorrelation functions of electron and hole disorder potentials. The autocorrelations of $V_e(x)$ and $V_h(x)$ do not differ significantly; therefore, only the correlation function of $V_e(x)$ is shown in Fig. 5.8. Figure 5.8(a) shows the normalized autocorrelation function (black line) on an 80 nm length scale; the grid step in x-direction of the XSTM data is 0.06 nm. For comparison, an uncorrelated disorder potential has been simulated on a 0.4 nm grid, corresponding to the lattice constant in x-direction; its autocorrelation is shown as blue line in Fig. 5.8(a). The central autocorrelation peak of this uncorrelated potential on an atomic grid is narrower than that of the autocorrelation of the band edge fluctuations determined from the XSTM data.

Figure 5.8(b) zooms into the central autocorrelation peak. The width of the central peaks is 0.8 nm for the experimental band edge fluctuations and 0.4 nm for the uncorrelated potential on the atomic grid. The increased width of the central autocorrelation peak of the band edge fluctuations demonstrates that correlations between Al atoms in x-direction are present in the 4-nm QW.

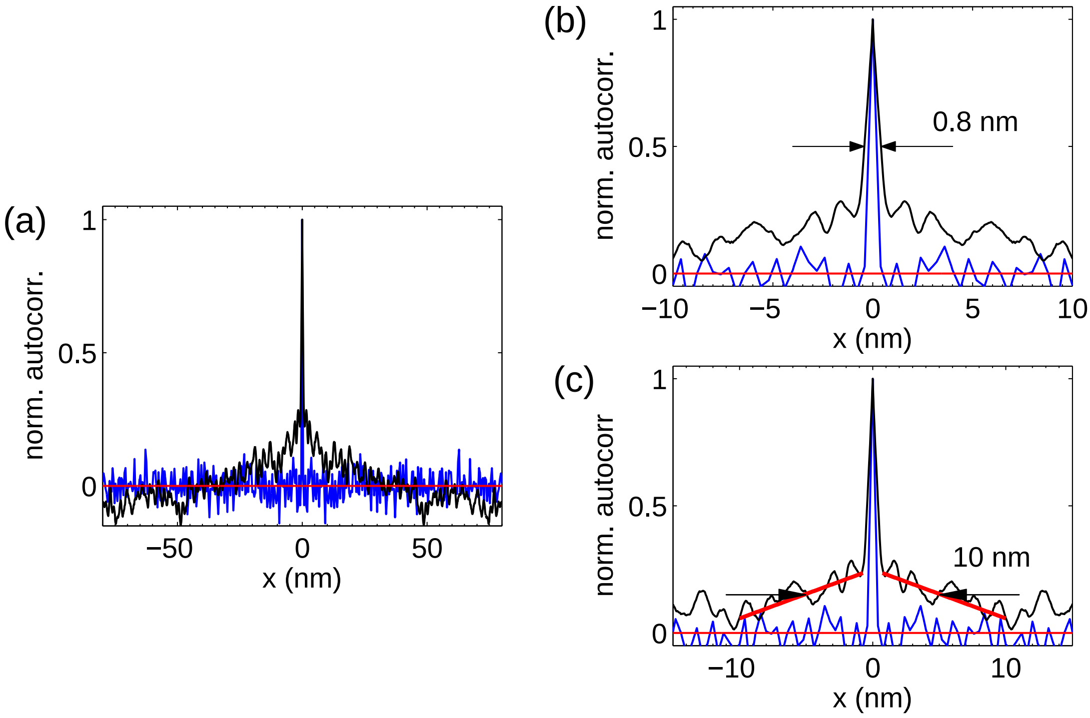

Figure 5.8: *(a) The autocorrelation of the band edge fluctuations in the cross section of the 4-nm GaAs/Al$_{0.3}$Ga$_{0.7}$As QW is shown (black). For comparison, the autocorrelation of an uncorrelated disorder potential on an atomic grid is shown in blue. (b) Zoom into the central autocorrelation peak. The full width of the central peak is 0.8 nm; the width of the blue peak is 0.4 nm. (c) Beyond the central peak, the autocorrelation decays to zero on a 10 nm length scale.*

The attempt to precisely determine the correlation length from the width of the central correlation peak holds some ambiguity, since the very definition of the correlation length will in turn depend of the type of correlations that are considered. Assuming a “square box” model for the correlations, the FHWM of the central correlation peak would translate to a correlation length of 0.8 nm. On the other hand, if exponential correlations, described by a correlation function

$$W(r) = c \cdot e^{-r/\xi}\,, \tag{5.11}$$

are assumed, a correlation length $\xi \approx 0.4$ nm is found to correspond to the width of the central correlation peak. The shortest relevant length scale in the decay of the autocorrelation function, and consequently of lateral correlations between Al atoms in the cross section of the 4-nm QW, is therefore given by $1-2$ lattice constants.

The shoulders of the central correlation peak indicate that also a small amount of correlations on larger length scales is present in the 4-nm QW. A second relevant length scale beyond the 0.8 nm wide central peak is indicated in Fig. 5.8(c): The subsequent decay of the autocorrelation function up to about 10 nm is illustrated by a straight-line fit to the autocorrelation $C(x)$ in the range $x = 1..10$ nm (red lines). The decay on a 10 nm length scale represented by the straight red lines in Fig. 5.8(c) corresponds to a second correlation length of $5 - 10$ nm, the exact value depending on the choice of square-box or exponential correlations. For comparison, the lateral exciton Bohr radius in a nominally perfect 4-nm GaAs/Al$_{0.3}$Ga$_{0.7}$As quantum well is $a_B = 8.2$ nm.

5.5 Conclusions

STM on a (110) cleavage surface of sample QW$_1$ has given access to the atomic scale structure of a cross section of the 4-nm GaAs/Al$_{0.3}$Ga$_{0.7}$As QW over a length of 160 nm. The constant-current topography of the QW cross section displays a clear topographic height contrast between well and barrier. Using a linear scaling to the bandgaps of well and barrier material, a map of the local bandgap in the imaged QW cross section has been obtained. Using an envelope function approach, it was possible to determine the fluctuations of the local band edges along the cross section of the 4-nm QW. The potential values of the corresponding disorder potentials are to a good approximation Gaussian distributed. The autocorrelation functions of the in-plane disorder potentials were determined, and two length scales were identified: A short length scale of 1-2 lattice constants, and a longer length scale of $5-10$ nm. This result is interpreted as evidence that the Al atoms in the Al$_{0.3}$Ga$_{0.7}$As barriers show the tendency of short-range ordering on neighbouring lattice sites along the $[1\bar{1}0]$ direction, and that modulations of the Al concentration occur on a length scale of $5 - 10$ nm. That also correlations between Al atoms in z-direction are present can already be seen by direct inspection of the STM images, where strings of Al atoms along the growth direction are visible especially in the right barrier region. These results agree well with previous work on MOVPE-grown Al$_{0.15}$Ga$_{0.85}$As, where short-range correlations between Al atoms of 2-3 lattice constants and modulations of the local Al concentration on a length scale of 5 nm were observed[Hei99]. In contrast, a study of MBE-grown dilute Al$_x$Ga$_{1-x}$As with $x = 0.05$ had concluded that Al atoms are incorporated completely randomly [Smi96].

References

[Ada94] S. Adachi, *GaAs and related materials*, World Scientific, 1994.

[Bar61] J. Bardeen, *Tunnelling from a many-particle point of view*, *Phys. Rev. Lett.* 6, 57 (1961).

[Bes87] K. Besocke, *An easily operable scanning tunneling microscope*, *Surf. Sci.* 181, 145 (1987).

[Ebe96] P. Ebert, B. Engels, P. Richard, K. Schroeder, S. Blugel, C. Domke, M. Heinrich, and K. Urban, *Contribution of surface resonances to scanning tunneling microscopy images: (110) surfaces of III-V semiconductors*, *Phys. Rev. Lett.* 77, 2997 (1996).

[Fee85] R. M. Feenstra and A. P. Fein, *Surface morphology of GaAs (110) by Scanning Tunneling Microscopy*, *Phys. Rev. B* 32, 1394 (1985).

[Fee87] R. M. Feenstra, J. A. Stroscio, J. Tersoff, and A. P. Fein, *Atom-selective imaging of the GaAs (110) Surface*, *Phys. Rev. Lett.* 58, 1192 (1987).

[Ham01] R. J. Hamers and D. F. Padowitz, *Methods of tunneling spectroscopy with the STM*, in *Scanning Probe Microscopy and Spectroscopy*, Wiley VCH, New York, 2001, p. 59ff.

[Hei98] A. J. Heinrich, *Ordering in ternary compound semiconductors on the atomic scale*, Ph.D. thesis, Universität Göttingen, 1998.

[Hei99] A. J. Heinrich, M. Wenderoth, K. J. Engel, T. C. G. Reusch, K. Sauthoff, R. G. Ulbrich, and E. R. W. K. Uchida, *Short-range ordering in* $Al_xGa_{1-x}As$ *grown with metal-organic vapor phase epitaxy*, *Phys. Rev. B* 59, 10296 (1999).

[Hof03] W. A. Hofer, A. S. Foster, and A. L. Shluger, *Theories of scanning probe microscopes at the atomic scale*, *Rev. Mod. Phys.* 75, 1287 (2003).

[Lub76] A. R. Lubinsky, C. B. Duke, B. W. Lee, and P. Mark, *Phys. Rev. Lett.* (1976).

[Qua03] N. Quaas, *Scanning tunneling microscopy of Co-impurified noble metal surfaces*, Ph.D. thesis, Universität Göttingen, 2003.

[Rop07] C. Ropers, M. Wenderoth, L. Winking, T. C. G. Reusch, M. Erdmann, R. G. Ulbrich, M. Grochol, F. Grosse, R. Zimmermann, S. Malzer, and G. H. Döhler, *Atomic scale structure and optical emission of AlGaAs/GaAs quantum wells*, Phys. Rev. B (2007).

[Sal93] H. W. M. Salemink and O. Albrektsen, *Atomic-scale composition fluctuations in III-V semiconductor alloys*, *Phys. Rev. B* 47, 16044 (1993).

[Smi85] L. Smit, T. E. Derry, and J. F. van der Veen, *Surf. Sci.* 150, 245 (1985).

[Smi96] A. R. Smith, K. J. Chao, C. K. Shih, K. A. Anselm, A. Srinivasan, and B. G. Streetman, *Identification of first and second layer Al atoms in dilute AlGaAs using cross-sectional scanning tunneling microscopy*, *Appl. Phys. Lett.* 69, 1214 (1996).

[Ter83] J. Tersoff and D. R. Hamann, *Theory and application for the Scanning Tunneling Microscope*, *Phys. Rev. Lett.* 50, 1998 (1983).

[Ter85] J. Tersoff and D. R. Hamann, *Theory of the scanning tunneling microscope*, *Phys. Rev. B* 31, 805 (1985).

Chapter 6

Micro-photoluminescence spectroscopy

This work uses scanning microphotoluminescence (μPL) spectroscopy as a technique that enables "single-dot" spectroscopy of natural quantum dots formed by local bandgap fluctuations in single quantum wells [Mar94, Zre94, Bru94, Hes94, Zre01]. Basics of micro-photoluminescence (μPL) spectroscopy and the experimental setup used for this study are described in the first and second section of this chapter. In the third section, macro-PL and micro-PL spectra of the studied QW samples are shown, and the results of various μPL experiments that have been performed to study localization properties of single natural quantum dots are described. The fourth section describes the simulation of optical spectra of the 4-nm GaAs/$\mathrm{Al_{0.3}Ga_{0.7}As}$ QW on the basis of the structural XSTM data. In the fifth section, relaxation effects and the Stokes shift are studied via temperature-dependent μPL spectroscopy on the 4-nm QW in sample $\mathrm{QW_1}$. Finally, experimental and simulated μPL spectra of the 4-nm QW are directly compared in the sixth section.

6.1 Basic principles

Photoluminescence spectroscopy is based on nonresonant optical excitation of a sample with a well-defined photon energy $E > E_0$, where E_0 is the upper limit of the range of transition energies of the electronic states that one intends to study. In a simple picture (Figure 6.1), nonresonant optical excitation creates a nonequilibrium distribution of charge carriers in a semiconductor with direct bandgap. If the sample is excited by a short laser pulse, the injected energy is rapidly redistributed via different channels: Electron-electron scattering redistributes energy in the electron and hole ensembles on a ps time scale, and carrier and excitonic cooling by emission of acoustic phonons leads to relaxation of the initially nonthermal carrier distribution [Ulb73]. At low temperature and low excitation density, an exciton population builds up, and low-momentum excitons recombine after their lifetime on the order of $\sim$ 1 ns. Under continuous-wave (cw) excitation, steady-state spectra evolve. The spectral intensity of the emission signal depends both on the absorption in the sample and on the relaxation of the excited charge-carrier distribution before recombination.

Photoluminescence spectra of bulk semiconductors are usually complex and show recombination radiation from free electron-hole pairs as well as from impurity-bound

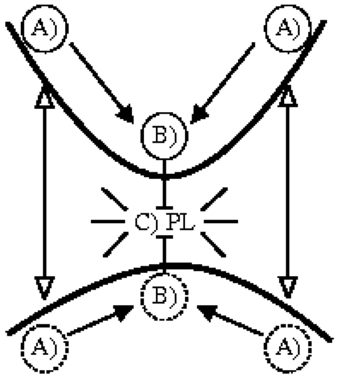

Figure 6.1: *[Kir98] Schematic picture of the PL process: (a) Excitation of electron-hole plasma energetically high in the bands; (b) carrier relaxation towards low momentum states and buildup of Coulomb-correlated electron-hole pair population; (c) PL resulting from the recombination of low momentum excitons.*

electron-hole pairs. At low excitation densities and low temperatures, recombination radiation from free and impurity-bound exciton states is observed. The strength of excitonic features in PL spectra is determined by the size of the exciton binding energy; larger exciton binding energy generally increases the oscillator strength of exciton transitions. Therefore, the increased exciton binding energy in low-dimensional semiconductor heterostructures leads to a predominance of the excitonic features in their PL spectra [Wei81, Din82].

Disordered systems like, e.g., narrow quantum wells with interface disorder are characterized by a position-dependent local bandgap. Fluctuations of the local bandgap lead to exciton localization; for weak disorder, an approximate description using an effective potential for the exciton center-of-mass is possible with minima of this effective potential acting as natural quantum dots [Zim97]. Spatially averaged optical spectra show inhomogeneous broadening, since the excitation focus is in most cases much larger than the extension of individual exciton states in this disorder potential. The effect of carrier relaxation before recombination, due to the different timescales of relaxation ($\sim$ ps) and recombination ($\sim$ ns), is manifest in disorder PL spectra in terms of a temperature-dependent redshift relative to the absorption [Bas84, Heg84], the so-called Stokes shift.

Optical techniques with high spectral and spatial resolution ($< 1\ \mu$m) such as microphotoluminescence (μPL) or near-field optical microscopy have enabled the study of single-dot properties of individual localized exciton states in single quantum wells [Zre94, Bru94, Hes94]. In μPL experiments, an optical microscopy setup is used in combination with photoluminescence spectroscopy. The sample area that contributes to the luminescence signal is typically reduced by about two orders of magnitude compared to conventional PL with $\sim 10\,\mu$m focus diameter. In optical near-field experiments, even higher spatial resolution (down to several 10 nm) is obtained at the price of small intensities and the unclear influence of the near-field tip on the optical spectra [Mat03].

In our μPL experiment, a Schwarzschild-Cassegrain mirror objective is used in a confocal microscopy setup. The technique of confocal illumination and detection has been originally invented to increase contrast in microscope images [Min88]. Figure 6.2(a) shows a sketch of a confocal setup. A beam splitter is used to couple a laser beam into the optical path. The beam is focused on a small sample volume by a microscope objective, and the light emitted from the sample is imaged by the same objective. The pinhole in the image plane blocks light from different sample volumes; this explains

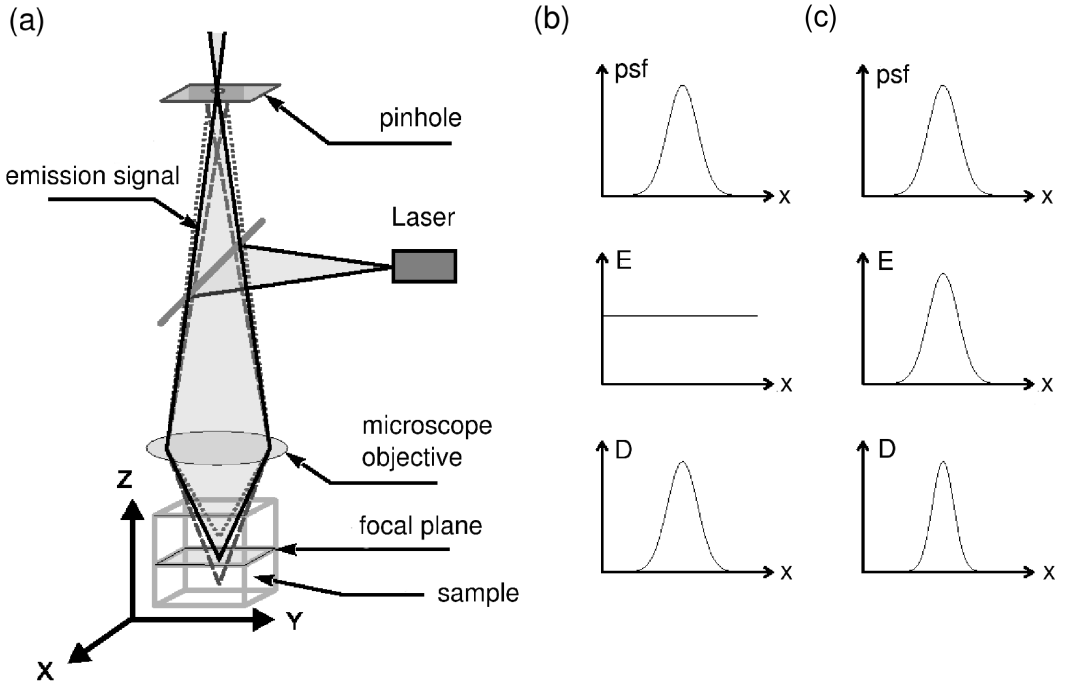

Figure 6.2: *(a) Schematic of a confocal setup. The same objective is used for focussing light on a small sample volume and for detection of the light emitted from this volume. The enhanced lateral resolution for confocal illumination and detection is demonstrated in (b) and (c) for a point emitter in the focal plane: The point spread function of the objective (psf), the excitation profile in the focal plane (E), and the detection profile in the image plane (D) are shown in (b) for the case of broad excitation, in (c) for the case of confocal illumination and detection.*

the enhanced contrast in confocal microscope images. Since only a small volume of the sample is illuminated at a time, an image of the sample has to be reconstructed by scanning the laser spot over the sample.

Figure 6.2(b) and (c) illustrate the enhanced spatial resolution compared to a far-field setup using the concept of the point spread function. Due to diffraction at the lens or objective aperture, a point source is not imaged to a point in the image plane, but – for a circular aperture – a circular diffraction pattern is observed. The normalized intensity of this diffraction pattern is called the point spread function. We assume that an objective with refraction index n and *numerical aperture* $\mathrm{NA} = n \sin(\theta)$ is used, where θ is the half angle of the cone of light converging to an illuminated spot or diverging from one. It is convenient to define the scaled variables (also called *optical units*) [Web96]

$$\rho = 2\pi/\lambda \cdot \mathrm{NA}\, r\,, \quad \zeta = 2\pi/(n\lambda)\, \mathrm{NA}^2\, z\,, \tag{6.1}$$

where r is the radial coordinate in the image plane, and z is the coordinate along the optical axis. Using the scaled radius ρ, the radial intensity of the diffraction pattern in the image plane, $I(\rho)$, is expressed by the projection of the three-dimensional point spread function in the image plane, which we denote as psf here,

$$I(\rho)/I_0 = \mathrm{psf}(\rho)\,. \tag{6.2}$$

The expression for the complete psf for a circular aperture was derived in [Ric59], but it is very complicated. In the most common approximation for paraxial optics, i.e., small numerical aperture NA, an Airy function is obtained,

$$\mathrm{psf}(\rho) = \frac{2J_1^2(\rho)}{\rho^2}\,. \tag{6.3}$$

The μPL measurements of this work were made in a confocal setup using a Schwarzschild-Cassegrain mirror objective with numerical aperture NA $= 0.75$. The approximation of small numerical aperture is therefore, as generally in the context of microscopy, not very lucky. However, the qualitative form of the full psf is not very different from Eq. (6.3). The main difference is that dark fringes never quite go to zero and that the width of the central peak is slightly larger than the approximation predicts [Web96]. On the other hand, for the mirror objective used here, this value has to be slightly corrected since the aperture is effectively ring-shaped due to the obstruction by the central mirror. Comparison of the diffraction patterns of a ring-shaped and a circular aperture shows that the central maximum is slightly narrower for a ring-shaped aperture.

Often, the Rayleigh criterion is used as a measure of the spatial resolution of a conventional microscopy setup. Since the first radial node of the Airy function $J_1^2(\rho)/\rho^2$ is at $\rho_0 = 3.83$, the distance of two neighbouring, incoherent point emitters that can be resolved in the image plane according to the Rayleigh criterion is $\Delta r = 0.61\,\lambda/\mathrm{NA}$. The full width (FWHM) $\Delta\rho$ of the central peak of the Airy function is slightly smaller than the radial distance from the center of the Airy peak to the first radial node. From $\Delta\rho = 3.23$, the resolution limit $\Delta r_{\mathrm{psf}} = 0.51\,\lambda/\mathrm{NA}$ is obtained.

The difference in resolution of a far-field microscopy setup with broad illumination and of a confocal setup with focused illumination and detection is demonstrated in Fig. 6.2(b) and (c) in terms of the width of the detected intensity profile of a point emitter in the sample. In (b), the case is shown that the point emitter in the sample is illuminated by a broad excitation focus. The intensity profile detected in the image plane is the product of the excitation profile with the point spread function of

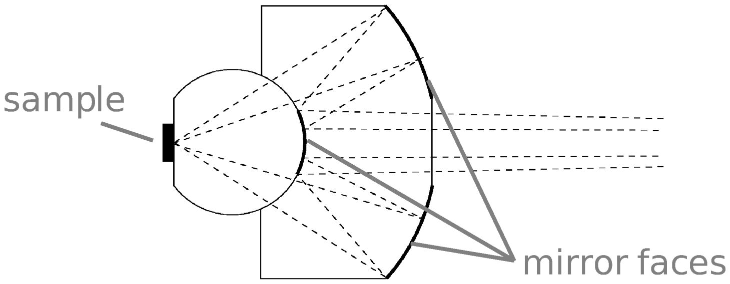

Figure 6.3: *Sectional drawing of the Schwarzschild-Cassegrain mirror objective. Two optically contacted Quartz bodies define the mirror faces. The sample is mounted directly on the back face plate of the objective.*

the objective, i.e., the shape is identical with the objective psf in the case of broad illumination. In (c), the case of confocal illumination and detection is shown. In the confocal case, the detected emission profile D is the square of the point spread function of the objective, $D = \text{psf}^2$. The FWHM of the central maximum of D is approximately reduced by a factor $\sim \sqrt{2}$ compared to the width of the objective point spread function.

6.2 Experimental setup

The geometry of the Schwarzschild-Cassegrain mirror objective used in our experimental setup is shown in Fig. 6.3. The objective consists of two optically contacted Quartz bodies that define the radii of the mirror faces. The mirror objective has the advantage of minimizing chromatic aberrations. The sample is mounted directly on the back face plate of the objective. The position of the optical focus on the sample can be controlled to an accuracy of $\sim 100\,\mu$m by manual translation stages.

A schematic of the experimental setup is shown in Fig. 6.4. Optical cw excitation is provided either by a SpectraPhysics 2080 Ar$^+$-laser (514.5 nm), by an Ar+-pumped Coherent 599 dye laser (emission wavelength dependent on dye used, tuneable by Lyot filter), or by a HeNe laser (λ = 632.8 nm). The slightly divergent beam emerging from the pinhole P is coupled into the optical path using a beam splitter. Two broadband anti-reflection coated Quartz plates (x,y) with 50 mm diameter that can each be rotated about orthogonal axes by stepper motors allow to translate the beam laterally. The excitation focus on the sample is thereby translated on a μm scale. The mirror objective images light emitted from the sample onto the crossed 80 μm entrance slits of the spectrometer at a distance of 80 cm and with a magnification of 150.

In the configuration shown in Fig. 6.4, the scanning mechanism is placed between the mirror objective and the beam splitter. In this configuration, rotation of the Quartz

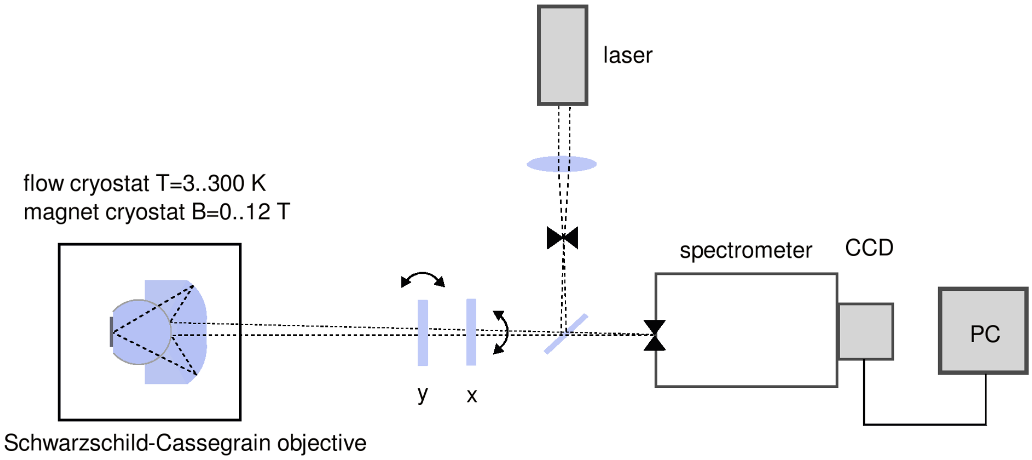

Figure 6.4: *Confocal setup for micro-magneto-photoluminescence spectroscopy. The scanning mechanism allows to scan the laser spot over a sample region of* $\sim 40 \times 40\,\mu m^2$.

plates causes a simultaneous translation of excitation and detection focus. The accessible sample area is $\sim 40 \times 40\,\mu\mathrm{m}^2$ large. The spectrometer is a double-grating Czerny-Turner monochromator with focal length $f = 60$ cm. Using a single grating, a spectral resolution of 140 μeV has been obtained; using two gratings in series, lines separated by 80 μeV could be resolved. The spectrally resolved emission signal is detected by a liquid-nitrogen-cooled charge-coupled device (CCD) camera with a back-coated Si chip.

For the spectroscopic measurements, the objective is placed in the flow cryostat inset of a superconducting magnet. The Helium flow cryostat allows to reach temperatures in the range $T = 2.9 - 300$ K with controlled heating. The horizontal superconducting magnet allows to apply magnetic fields of $B = 0 - 12$ T parallel to the optical axis.

As a prerequisite for the experiments performed during this thesis, a versatile data acquisition program was developed using the object-oriented programming language C++ [Str00] and the QT graphical user interface library [QT]. The program runs on a personal computer (PC) with double-processor mainboard and Linux operating system (Kernel 2.4.20). The CCD controller is read out via a separate DOS computer. A program running in server mode on the second computer uses the DOS driver of the CCD controller to obtain single spectra from the liquid nitrogen-cooled CCD and passes them to the data acquisition program running on the Linux computer. The PC-to-PC communication is realized via an internal ISA I/O card connection. A second 72-bit I/O card in the Linux computer is used to control (i) the optical focus position on the sample, i.e., the stepper motors rotating the Quartz glass plates in the optical setup; (ii) the excitation intensity, i.e., rotating a circular variable-density gray filter (Coherent) with neutral density varying linearly as a function of rotation angle; (iii) the central wavelength of the spectral window; and (iv) the rotation angle of a half-wave plate in combination with a linear polarizer. The serial interface (RS232) of the Linux computer is used to control (i) the superconducting magnet controller (Oxford PS120-10), and (ii) the flow cryostat temperature controller/heater (Oxford ITC-4). The data acquisition program has two basic data acquisition modi for (i) manual control of the setup and the acquisition of single spectra ("single spectrum mode"), and (ii) for the acquisition of maps of spectra ("scan mode"). In scan mode operation, two parameters of the setup can be varied independently, e.g.,

- the spatial coordinates of the excitation and detection focus (x,y) for acquisition of spatially resolved μPL maps,
- the excitation intensity,
- the magnetic field along the optical axis,
- the polarization state of the laser and of the detected emission, etc.

Combination of the listed and other parameters allows the efficient realization of various experiments.

6.3 PL and μPL spectra of the QW samples

Macro-photoluminescence spectra Low-temperature overview spectra of the QW samples QW_1, QW_2 and QW_3 with “broad” excitation focus ($d \sim 10\,\mu$m) are shown in Figs. 6.5, 6.6 and 6.7. For the measurements, the samples were placed in a He_4 bath cryostat ($T = 2$ K), and a conventional PL setup was used. Optical continuous-wave (cw) excitation was provided by a HeNe laser at 1.95 eV with a total power of ~ 0.1 mW. The emission was detected using a 60 cm Czerny-Turner spectrometer and a liquid-nitrogen cooled CCD camera.

The macro-PL spectra show the inhomogeneously broadened emission bands of the QW heterostructures. Due to the quantum confinement, the peak energies of the quantum wells are all well above the GaAs bandgap ($E_g = 1.519$ eV at $T = 2$ K). The peak at 1.515 eV corresponds to the recombination of free excitons in the 50-nm GaAs layers surrounding the QW growth sequence in all three samples. The exciton binding energy of the effectively unconfined excitons in these layers is approximately the bulk binding energy of ~ 4 meV. In Figures 6.6 and 6.7, emission bands below 1.5 eV indicate the recombination of donor- and acceptor-bound excitons.

Figure 6.5 shows an overview macro-PL spectrum of sample QW_1. The sample contains five GaAs/$Al_{0.3}Ga_{0.7}As$ QWs with 4, 6, 8, 10 and 20 nm nominal thickness. Comparison of the peak energies with confinement energies for the nominal square-well structures (see Fig. 2.8) shows that the emission peaks correspond to exciton recombination in the lowest electron-heavy hole QW subbands (E_0-HH_0). The emission from light-hole excitons is generally negligible in quantum wells due to several reasons, including the smaller transition matrix elements of electron-light hole transitions [Run02]. Monolayer splitting of the QW spectra is not observed for the narrow quantum wells. The inhomogeneous broadening of the emission peaks is roughly Gaussian for all wells. Table 6.1 gives the nominal widths, experimental peak energies and inhomogeneous broadening (FWHM) of the quantum wells in sample QW_1. The semilogarithmic representation shows that almost all quantum well PL spectra have an exponential high-energy tail over at least one order of magnitude in PL intensity.

d (nm)	4	6	8	10	20
E (eV)	1.643	1.591	1.564	1.549	1.524
ΔE (meV)	4.5	2.2	1.5	1.1	0.8

Table 6.1: *Nominal widths, experimental peak energies and inhomogeneous broadening (FWHM) of the quantum wells in sample* QW_1.

Figure 6.6 shows an overview macro-PL spectrum of the GaAs/$Al_{0.3}Ga_{0.7}As$ QW sample QW_2. Table 6.2 lists the nominal widths, experimental peak energies and inhomogeneous broadening (FWHM) of the quantum wells in sample QW_2.

Figure 6.7 shows an overview macro-PL spectrum of the GaAs/AlAs DQW sample. The emission peak of the 8-nm GaAs/AlAs quantum well is observed at 1.576 eV, the emission peak of the 4-nm GaAs/AlAs double quantum well at 1.69 eV. Calculations of single-particle energies in a one-dimensional double square well model yield a splitting of symmetric and antisymmetric single-particle states in the DQW structure of ~ 1 meV,

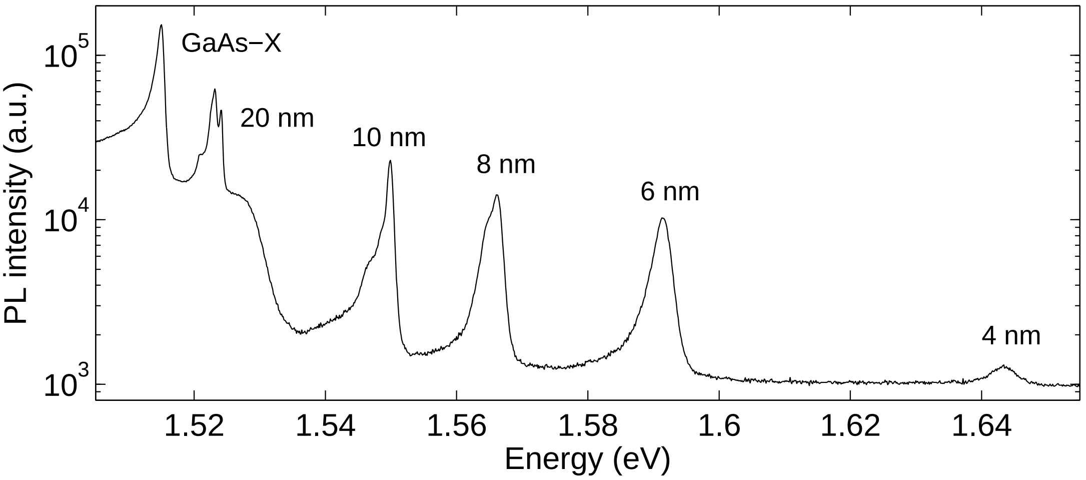

Figure 6.5: *Overview macro-PL spectrum of the GaAs/*$Al_{0.3}Ga_{0.7}As$ *sample* QW_1.

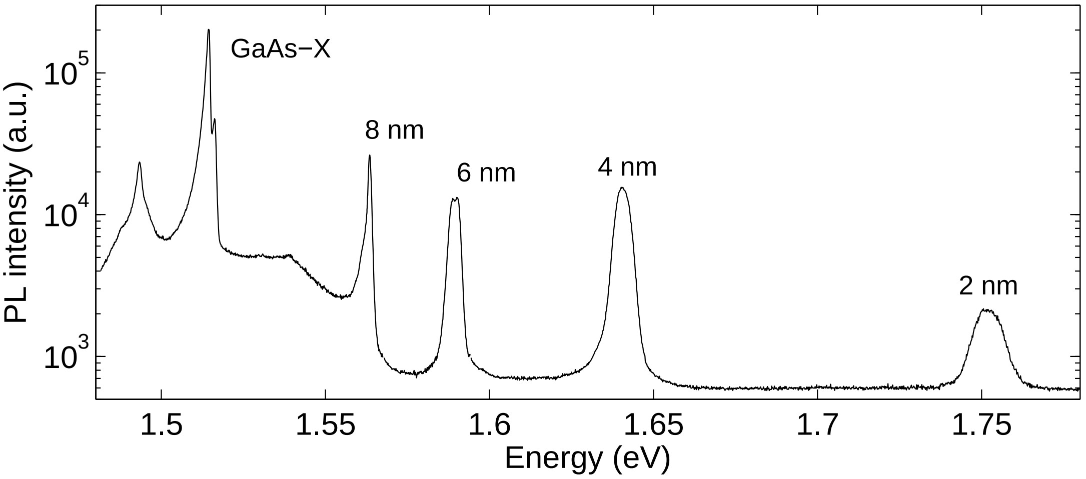

Figure 6.6: *Overview macro-PL spectrum of the GaAs/*$Al_{0.3}Ga_{0.7}As$ *sample* QW_2.

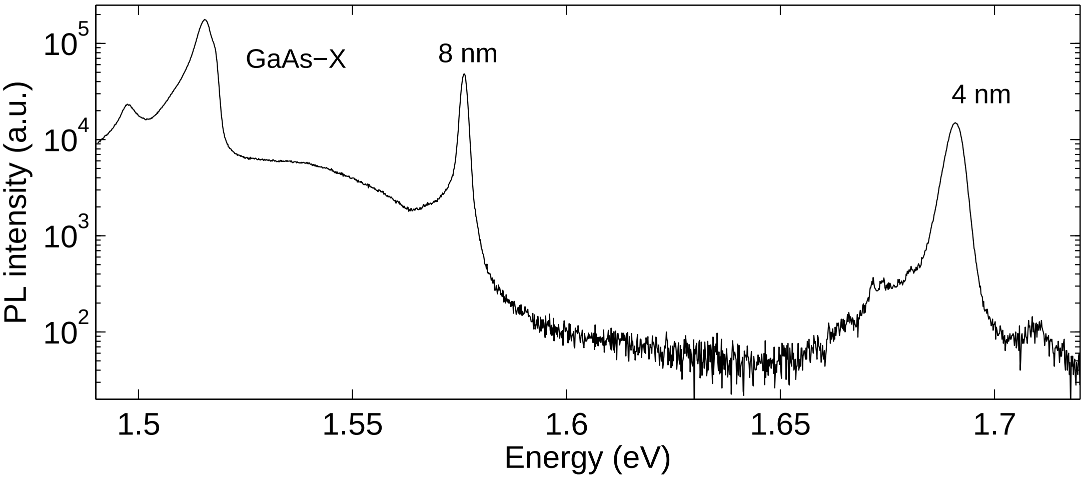

Figure 6.7: *Overview macro-PL spectrum of the GaAs/AlAs sample* QW_3.

which is significantly smaller than the inhomogeneous broadening of 5.5 meV.

d (nm)	2	4	6	8
E (eV)	1.752	1.643	1.591	1.564
ΔE (meV)	7.4	4.6	2.2	1.15

Table 6.2: *Nominal widths, experimental peak energies and inhomogeneous broadening (FWHM) of the quantum wells in sample* QW_2.

Micro-photoluminescence spectra A $12 \times 12\,\mu\mathrm{m}^2$ μPL map of sample QW_3 is shown in Fig. 6.8(a). The spatially resolved luminescence map was obtained by simultaneous displacement of excitation and detection focus. The sample temperature was $T = 3$ K, and optical excitation was at 1.95 eV with excitation intensity $I \sim 1\,\mu\mathrm{W}$. The emission has been spectrally integrated over a 5 meV wide spectral window below the DQW peak at 1.69 eV. Several localized emission centers are observed. Figure 6.8(b) and (c) show sections through the μPL map along the lines A and B that are shown in red in Figure 6.8(a). The halfwidth of the emission center located in the crossing point of lines A and B is $\sim$ 500 nm.

Assuming a diameter of the optical focus $d \approx 600$ nm (FWHM of the objective point spread function), a lateral resolution in the confocal configuration of $\sim$ 450 nm is predicted. The experimental value of $\sim$ 500 nm obtained at a detection wavelength

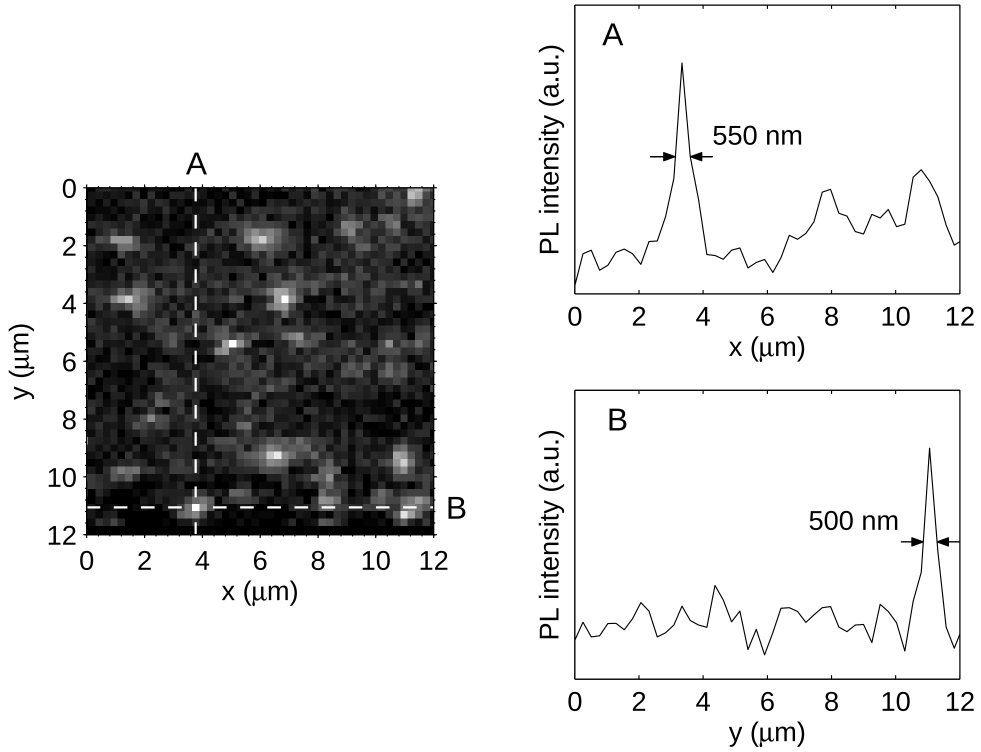

Figure 6.8: *μPL map of the 4-nm GaAs/AlAs double quantum well, and sections along lines A and B.*

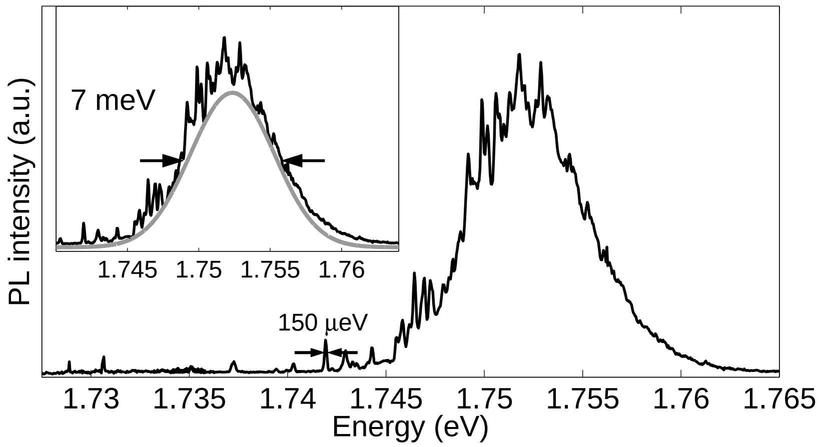

Figure 6.9: *µPL spectrum of the 2-nm GaAs/Al$_{0.3}$Ga$_{0.7}$As QW in sample QW$_2$.*

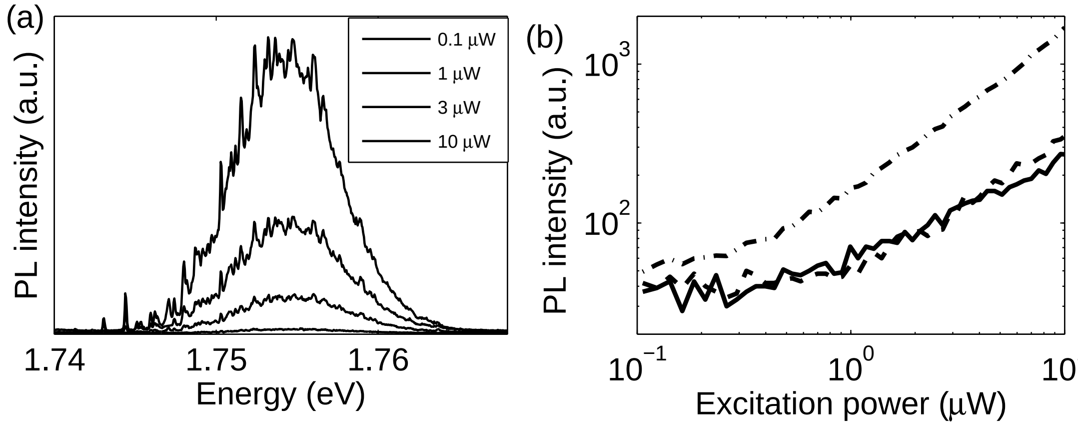

Figure 6.10: *(a) Excitation power-dependence of µPL spectra of the 2-nm QW in the GaAs/Al$_{0.3}$Ga$_{0.7}$As QW sample QW$_2$. (b) Power dependence (double-logarithmic plot) of two single exciton transitions in the µPL low-energy tail.*

$\lambda \approx 750$ nm obtained here is slightly larger. The obtained resolution depends on the perfection of the optical focus that is reached and therefore slightly varies between different measurement series. U. Kops and P. Blome determined the spatial resolution obtained with the Schwarzschild-Cassegrain mirror objective in a confocal setup using a laterally structured GaInP QW sample with 160 nm quantum dots on a 1 μm lattice [Bur97, Blo99]. In a 10 nm wide partially ordered GaInP quantum well, an array of circular QD regions of disordered GaInP with smaller bandgap than the surrounding partially ordered GaInP had been produced. At a detection wavelength $\lambda \approx 640$ nm, they obtained a FWHM of the QD luminescence of $\sim$ 450 nm. Considering the different wavelengths, this value compares quite well with the resolution determined here.

Figure 6.9 shows a μPL spectrum of the 2-nm QW in sample QW$_2$, taken at a sample temperature of $T = 3$ K. The sample was optically excited by a HeNe laser at 1.95 eV with a total power of $I \sim 1\,\mu$W. The spectrum consists of spectrally narrow lines on top of a broad background with with approximately Gaussian shape. The inset shows a Gaussian with 7.4 meV FWHM adjusted to the μPL spectrum. The μPL lineshape deviates from a Gaussian both on low- and high-energy side. Below the emission peak at 1.752 eV, the rare occurrence of localized exciton transitions with rather large oscillator strength leads to the characteristic low-energy tail with well-separated, spectrally narrow lines. The spectral linewidth of these transitions is limited due the instrumental resolution of $\sim 150\,\mu$eV in our experiment. In the literature, linewidths of natural QD transitions down to several μeV have been observed in μPL experiments [Zre05]. Above the emission peak, the spectrum displays a rather smooth high-energy tail due to a rather large density of states with relatively small oscillator strength.

In Figure 6.10(a), μPL spectra of the 2-nm QW are shown at varying excitation intensity. The excitation power was varied in the range $I = 0.1 \ldots 10$ μW using a circular variable neutral density filter. The lineshape does not vary significantly in this power range. The emission center and the inhomogeneous broadening are largely constant, except at very low power levels of $0.1\,\mu$W when the collected emission intensity reaches the noise level of the CCD. Significant sample heating due to optical excitation can be excluded by checking against the effect of the raising sample temperature by controlled heating. It was observed that the luminescence intensity of the transitions deep in the low-energy tail was very sensitive to a rise in temperature; most lines showed significant intensity loss already at a temperature rise of a few Kelvin. Figure 6.10(b) shows the excitation power-dependence of two transitions in the low-energy tail of the 2-nm QW spectrum. Approximately the same power dependence is found for different tail states. The dash-dotted line shows the power dependence at the center of the QW emission peak. Saturation of the emission was observed at excitation power significantly above 10 μW. In what follows, almost all spectra were taken at an excitation power of ~ 1 μW.

Low-temperature μPL spectra of the GaAs/Al$_{0.3}$Ga$_{0.7}$As QWs with 4, 6, 8 and 10 nm nominal width in sample QW$_1$ are shown in Fig. 6.11. Optical excitation of the sample

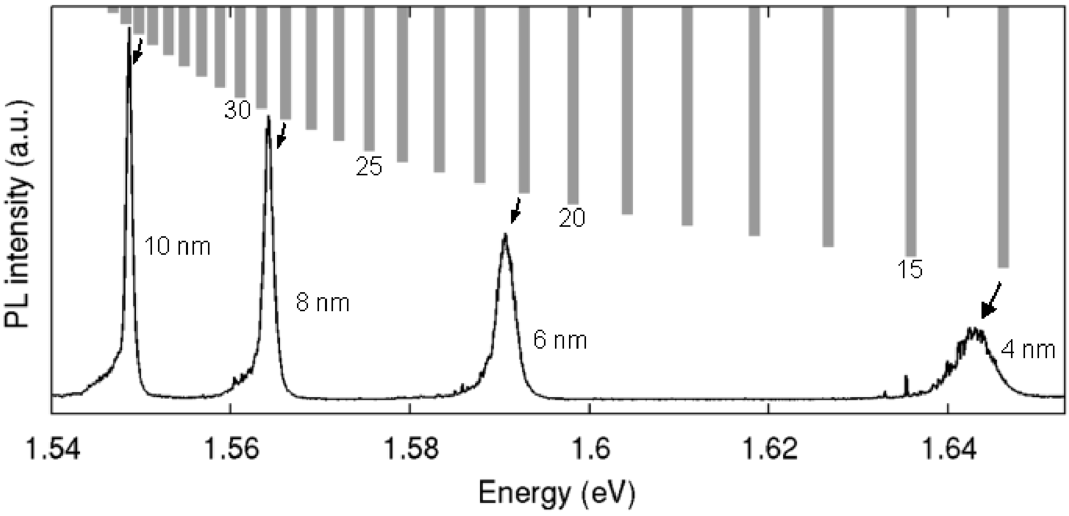

Figure 6.11: *μPL spectrum of 4 QWs in the GaAs/Al$_{0.3}$Ga$_{0.7}$As QW sample QW$_1$. The gray bars indicate the transition energies in ideal GaAs/Al$_{0.3}$Ga$_{0.7}$As QWs that are integral multiples of a monolayer (1 ML = 0.28 nm) wide.*

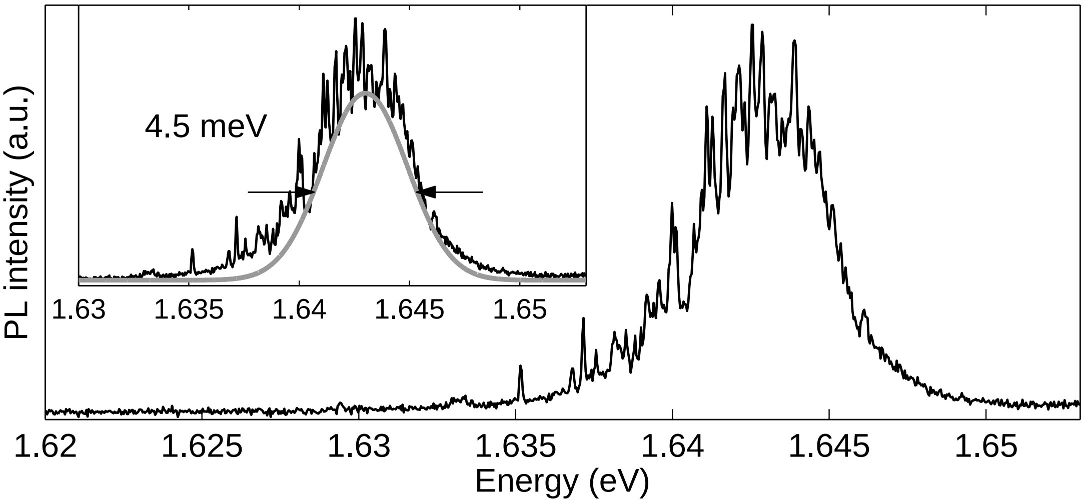

Figure 6.12: *µPL spectrum of the 4-nm GaAs/*$Al_{0.3}Ga_{0.7}As$ *QW in sample* QW_1.

was provided by a dye laser at $E = 1.9$ eV, the total excitation power was $I \sim 1\,\mu$W. The overall shape of the inhomogeneously broadened electron-heavy hole QW emission bands is approximately Gaussian. On the low-energy side of the spectra, some spectrally narrow features can be detected, while the high-energy side is rather smooth. The gray bars in Fig. 6.11 indicate the transition energies in ideal GaAs/$Al_{0.3}Ga_{0.7}$As QWs that are integral multiples of a monolayer (1 ML = 0.28 nm) wide; the numbers at the gray bars give the number of monolayers. The positions of the bars have been obtained as the sum of (i) GaAs bandgap at $T = 3$ K, (ii) single-particle confinement energies as shown in Fig. 2.8, and (iii) exciton binding energies from Fig. 2.11. The nominal widths of the samples are not exactly integral multiples of a monolayer; the most adjacent integral number of MLs has been chosen for the comparison (indicated by the arrows). The increasing difference with shrinking QW width, 3 meV for the 4-nm QW, can at this point be readily attributed to the Stokes shift between inhomogeneously broadened QW absorption and emission.

Figure 6.12 zooms into a μPL spectrum of the 4-nm QW in sample QW_1. The inset shows a Gaussian with 4.5 meV FWHM adjusted to the μPL spectrum. Below the center of the emission peak at 1.643 eV, several bright lines of localized exciton transitions are observed. The high-energy tail is rather smooth. In the inset, a Gaussian with 4.5 meV FWHM is adjusted to the μPL spectrum.

Micro-PL spectra of the 4-nm QW obtained on a 10 μm long line scan are shown in Fig. 6.13(a). The spatial variation of the tail states below the emission peak is clearly observed. The position of the QW peak as well as the inhomogeneous broadening is largely constant. Figure 6.13(b) shows a plot of five spectra from Fig. 6.13(a).

Unambiguous evidence that the tail states lines below the QW emission peak originate from localized exciton states comes from the observation of their fine structure. The fine structure splitting of localized exciton states into linearly polarized components has first been observed by Gammon *et al.* [Gam96] in a 2.8-nm GaAs/$Al_{0.3}Ga_{0.7}$As QW grown with growth interruption at the interfaces. Using polarization-sensitive μPL excitation spectroscopy, they observed a splitting of ground and excited state transitions in two

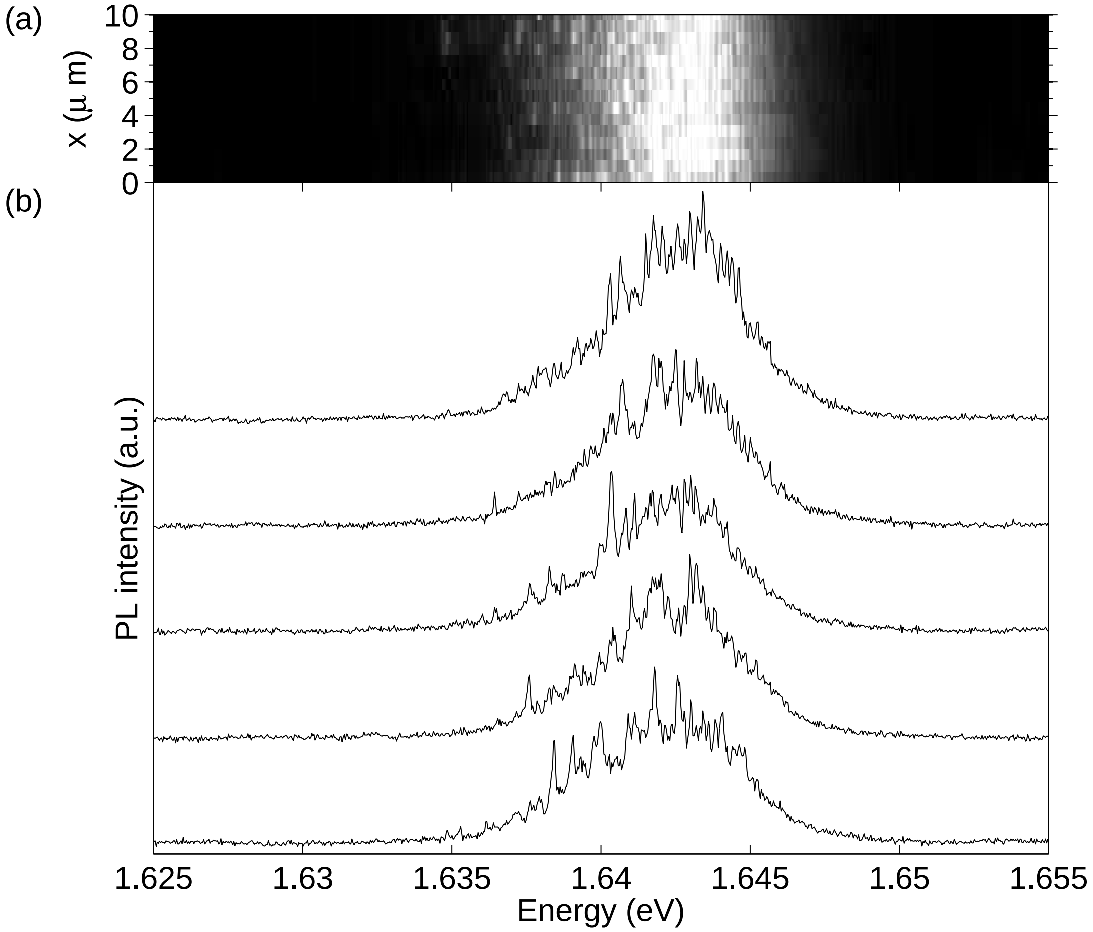

Figure 6.13: *(a) μPL spectra of the 4-nm GaAs/$Al_{0.3}Ga_{0.7}$As QW; 10 μm line scan. (b) Four of the μPL spectra shown in (a).*

orthogonal linearly polarized fine structure components; the fine structure splitting was found to be on the order of $20 - 50\,\mu$eV. Today, it is understood that this splitting arises from the long-range part of the electron-hole exchange interaction [Ivc95] in asymmetric quantum dots [Bay02]. In quantum dots with circular symmetry, no fine structure splitting of the optically active exciton transitions ($J_z = \pm 1$) is expected. In turn, a fine structure splitting in the optically active exciton transitions is evidence for exciton localization in an asymmetric confinement potential, caused by fluctuations of the QW interfaces.

Differential polarisation spectroscopy has been here used to study the fine structure splitting. Figure 6.14 shows a μPL spectrum of the 4-nm QW in sample QW_1. Two transitions (“A”, “B”) with relatively large, but spectrally still unresolved fine-structure splitting are marked. By placing a $\lambda/2$ wave plate and a linear polarizer between mirror objective and beam splitter and varying the rotation angle of the half wave plate, the polarization state of the laser and of the detected emission is varied simultaneously. In the following experiments, the two gratings of the double monochromator were used in additive mode for enhanced spectral resolution. Figure 6.15(a) shows the intensity variation of the copolarized emission in the low-energy tail of the 4-nm

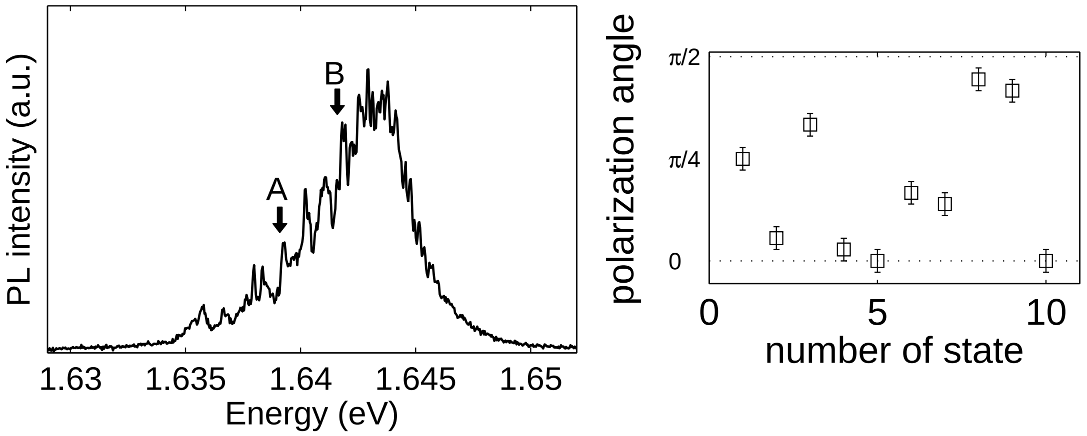

Figure 6.14: *μPL spectrum of the 4-nm GaAs/Al$_{0.3}$Ga$_{0.7}$As QW. The arrows mark two exciton transitions with relatively large fine-structure splitting ("A", "B").*

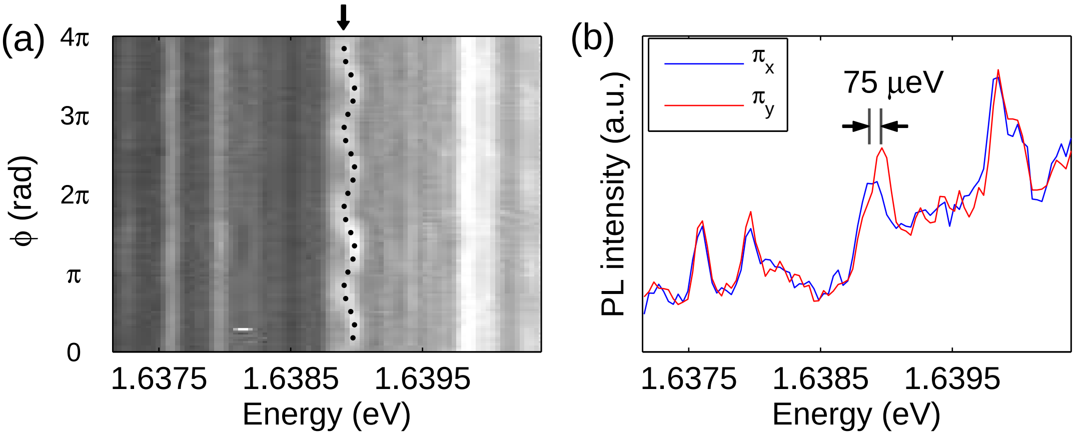

Figure 6.15: *(a) Polarization angle scan of transition "A" in the low-energy tail of the μPL spectrum in Fig. 6.14. The arrow marks an exciton transition with 75 μeV fine structure splitting at 1.6385 eV. The fine structure components are linearly polarized under 45° relative to the (110) directions. (b) μPL spectra at orthogonal linear polarization.*

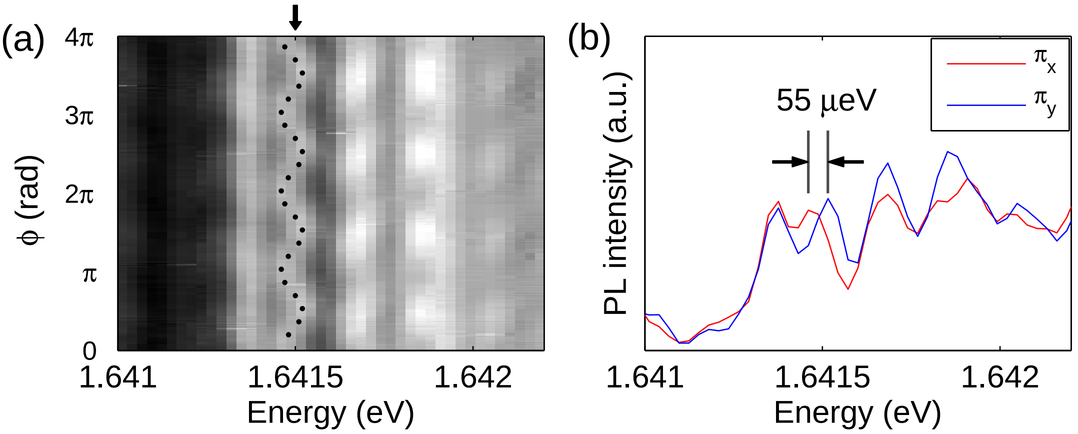

Figure 6.16: *(a) Polarization angle scan of transition "B" in the low-energy tail of the μPL spectrum in Fig. 6.14. The arrow marks an exciton transition with 55 μeV fine structure splitting at 1.641 eV. The fine structure components are linearly polarized along* $[1\bar{1}0]$ *and* $[110]$*. (b) μPL spectra at orthogonal linear polarization along* $[1\bar{1}0]$ *and* $[110]$.

GaAs/$Al_{0.3}Ga_{0.7}$As QW in sample QW_1 under variation of the angle of the linearly polarized excitation and detection, measured relative to the $[1\bar{1}0]$ crystal axis. Zero angle $\phi = 0$ corresponds to polarization along $[1\bar{1}0]$, and $\phi = \pi/2$ corresponds to polarization along [110]. The $\lambda/2$ wave plate was rotated by 2π, therefore the polarization angle spans the range from 0 to 4π. The maximum of the two spectrally unresolved fine-structure components at $E \approx 1.639$ eV in Fig. 6.15(a) oscillates between two energy values separated by $\Delta E \approx 75\,\mu$eV with the period π in the polarization angle. The fine-structure components, shown in Fig. 6.15(b), are polarized under 45° relative to the ⟨110⟩ directions. Figure 6.16(a) shows another fine-structure split transition with fine structure components linearly polarized along the ⟨110⟩ directions. The fine structure splitting $\Delta E \approx 55\,\mu$eV, shown in Fig 6.16(b). Further fine-structure split doublets polarized along varying directions have been observed. Evaluation of 10 fine structure-split exciton states with rather large splitting $\Delta E > 40\,\mu$eV showed no clear preferential direction of the linear polarization (Fig. 6.14).

In QW samples grown with growth interruption at the interfaces, as in the sample of Gammon *et al.*, a preferential orientation of the linearly polarized fine structure components along the ⟨110⟩ directions has been observed [Gam96]. This effect has been explained to result from an alignment of growth islands, i.e., regions where the film thickness is increased by one monolayer compared to the nominal film thickness, along the $[1\bar{1}0]$ direction. The elongated shape of the center-of-mass wave function of exciton states localized in islands elongated along $[1\bar{1}0]$ is responsible for the fine structure splitting into the two linearly polarized components along ⟨110⟩ directions [Mai93, Nic98, Mai00]. While in zincblende crystals the [110] and $[1\bar{1}0]$ directions are crystallographically equivalent, the growth takes place on reconstructed surfaces leading to a possible growth anisotropy in the quantum well plane. If the growth is interrupted at the QW interfaces, large anisotropic islands can form with diameters larger than the exciton Bohr diameter ($\approx$ 20 nm).

Since the samples studied in this thesis have been grown without growth interruption at the QW interfaces, the formation of large anisotropic islands aligned along the $[1\bar{1}0]$ direction is not expected. Also, the formation of islands in the interfaces is not evident in the XSTM-images, where we primarily find very short-range correlations. In addition, the formation of monolayer islands does not appear in the form of a monolayer splitting in the PL spectra. Therefore, we conclude that our observations indicate the lack of large, anisotropic growth islands in the QW interfaces of our sample.

6.4 Simulated optical spectra

In a concomitant study, μPL spectra of the 4-nm GaAs/$Al_{0.3}Ga_{0.7}$As quantum well in sample QW_1 have been simulated on the basis of the structural data from the cross-sectional STM experiment (described in chapter 5). This study was commenced by Claus Ropers [Rop03] and has been pursued together with the semiconductor theory group at the Humboldt-Universität Berlin (Michal Grochol, Dr. Frank Grosse, Prof. Dr. Roland Zimmermann).

From the topographic data of the 4-nm GaAs/$Al_{0.3}Ga_{0.7}$As QW, one-dimensional disorder potentials in the cleavage plane have been determined, which contain the information on the strength and the correlations of the lateral disorder along the quantum well cross-section. The potential extracted from a 160 nm long cross-section of the 4-nm QW has been analyzed. In the single-sublevel approximation, the effective in-plane bandgap fluctuations along the x-direction have been expressed as

$$W(x) = \sum_{a=e,h} f_a \int dz\, |u_a(z)|^2 \left(E_G(x,z) - \langle E_G(x,z)\rangle_x\right), \tag{6.4}$$

where $f_e/f_h = 0.65/0.35$ is the band offset ratio, and the $u_a(z)$ are the single-particle wave functions in the one-dimensional potential derived from the x-averaged confinement potential $\overline{E}_G(z) = \langle E_G(x,z)\rangle_x\big)$. The lateral bandgap fluctuations $W(x)$ cause lateral electron and hole localization in this QW, resulting in the inhomogeneous broadening of the optical spectra.

As a surface-sensitive method, the STM experiment gives no information about the disorder properties of the quantum well in the direction perpendicular to the plane of the STM image, which are also relevant for the inhomogeneous broadening of excitonic transitions. We presume at this stage that the correlations in the y-direction do not differ from those in the x-direction. In particular, the two-dimensional autocorrelation of the in-plane disorder potential is assumed to be isotropic in the x-y plane. This allows to generate two-dimensional in-plane potentials, which contain the disorder properties found in the XSTM measurement. The following paragraphs describe the proceeding in [Rop07].

First, the potential $W(x)$ is binned on the atomic grid in the x-direction (atomic row distance 0.4 nm), leading to a row vector $W(x_j)$ with $j \in \{1, 2, ..., 400\}$. Figure 6.17(a) shows the bandgap fluctuations binned on the atomic grid along the 160 nm cross-section of the 4-nm QW. A histogram of the potential values is shown in Fig. 6.17(b); the potential values are approximately Gaussian distributed. The statistical information of the potential is fully contained in the autocorrelation

$$C(x_j) = \frac{1}{N}\sum_{l=1}^{N} W(x_j + x_l) W(x_l). \tag{6.5}$$

In a next step, two-dimensional in-plane disorder potentials can be obtained by a convolution between a suitable averaging function $A(\boldsymbol{r})$ and random fluctuations $U(\boldsymbol{r})$ [Zim97],

$$W(\boldsymbol{r}_j) = \sum_l A(\boldsymbol{r}_j - \boldsymbol{r}_l)\, U(\boldsymbol{r}_l), \tag{6.6}$$

where $\boldsymbol{r}_j$ is a two-dimensional vector on a square grid in the x-y-plane. The averaging function $A(\boldsymbol{r}_j)$ is directly related to the one-dimensional correlation function $C(x_j)$, which in terms of their Fourier components can be expressed as [1]

$$\tilde{C}_j = \frac{1}{N^2}\sum_i |\tilde{A}_{ji}|^2. \tag{6.7}$$

In the past, different models for the averaging function A and the resulting types of

---

[1] Using the standard definitions for the Fourier coefficients, $\tilde{C}_j^{(i)} = \sum_k C(x_k) exp(-i\,2\pi\frac{jk}{N})$ and $\tilde{A}_{jk} = \sum_{m,n} A(x_m, y_n) exp(-i\,2\pi\frac{jm+kn}{N})$ and $\tilde{A}_{jk}$.

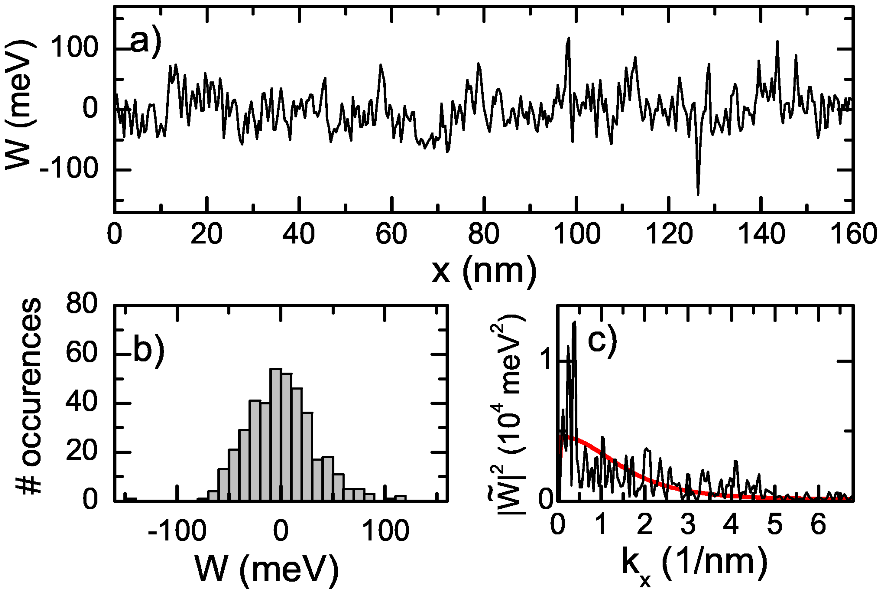

Figure 6.17: *[Rop07] (a) One-dimensional effective disorder potential $W(x)$ (bandgap fluctuations) along the XSTM topography of the 4 nm GaAs/Al$_{0.3}$Ga$_{0.7}$As QW. (b) The potential value distribution on the atomic grid is roughly Gaussian with 33 meV standard deviation. (c) The power spectrum of the spatial fluctuations of W (black line) with a fit for exponential correlations (red line).*

correlations have been proposed [Run02]. The best results have been obtained for an exponential ansatz of the form

$$A(\boldsymbol{r}_j) = \frac{\sigma}{\eta} e^{-|\boldsymbol{r}_j|/l_c}, \quad \eta^2 = \sum_j e^{-2|\boldsymbol{r}_j|/l_c}, \tag{6.8}$$

where σ^2 is the potential variance and l_c the correlation length. These fitting parameters were determined by a least-squares fit of the one-dimensional correlation functions generated using Eq. (6.7) to the experimentally determined correlation Eq. (6.5). A fit in k-space [see Fig. 6.17(c)] yielded $\sigma = 33.4$ meV and $l_c = 0.39$ nm. [2] The value of l_c on the order of the lattice constant indicates that in the investigated structure, mostly short-ranged correlations over a few lattice constants are present in the Aluminum distribution along the x-direction. The potential generated via Eq. (6.6) is then distributed between the electron and the hole as $W_a(x, y) = f_a W(x, y)$.

Subsequently, the four-dimensional Schrödinger equation with these potentials has been solved for the in-plane exciton motion. This is detailed in the following two sections. The in-plane Hamiltonian for excitons in a disordered quantum well in effective-mass approximation, neglecting the small spin-orbit coupling, reads [Gro05]:

$$H = -\frac{\hbar^2}{2m_e}\triangle_{\boldsymbol{r}_e} - \frac{\hbar^2}{2m_e}\triangle_{\boldsymbol{r}_h} + W_e(\boldsymbol{r}_e) + W_h(\boldsymbol{r}_h) - V_C(r)\,, \tag{6.9}$$

---

[2] Due to the binning procedure, the z-correlations in the Al distribution on the simulated atomic grid are slightly increased compared to the original image, hence the larger disorder strength. On the other hand, correlations in x-direction beyond ∼ 1 nm are reduced: The central peak of the autocorrelation (Fig. 5.8) remains unchanged, but the width of the shoulders is reduced.

where $\boldsymbol{r}_a = (x_a, y_a)$ are in-plane coordinates, and all effective masses are in-plane masses. The material parameters used in the calculations are listed in Table 6.3. $W_e(\boldsymbol{r}_e)$ and $W_h(\boldsymbol{r}_h)$ denote the disorder potentials for electron and hole, and $V_C(r)$ is the effective in-plane Coulomb potential [Eq. (2.28)].

	GaAs	$\mathrm{Al_{0.3}Ga_{0.7}As}$
$m_{e,z}$	0.070 [Eke89]	0.084 [Ada94]
$m_{h,z}$	0.36 [Ada94]	0.39 [Ada94]
E_G (eV)	1.519 [Ada94]	2.0128 [Sch06]
$m_{e,\parallel}$	0.078 [Eke89]	
$m_{h,\parallel}$	0.233 [Sia00]	
ϵ_S	12.5 [Ada94]	

Table 6.3: *Electron and hole effective masses, bulk bandgaps at $T = 4$ K and static dielectric constant used in the calculation.*

The two-particle (exciton) Schrödinger equation with the Hamiltonian Eq. (6.9)

$$H(\boldsymbol{r}_e, \boldsymbol{r}_h)\Psi_\alpha(\boldsymbol{r}_e, \boldsymbol{r}_h) = E_\alpha \Psi_\alpha(\boldsymbol{r}_e, \boldsymbol{r}_h) \tag{6.10}$$

has been solved numerically and eigenstates and eigenvalues E_α of localized exciton states are obtained. The calculated energies and wave functions are ingredients for the subsequent calculation of oscillator strengths M_α, absorption spectrum $D(\omega)$ (optical density), and photoluminescence spectrum $P(\omega)$.

For dipole-allowed transitions, the exciton oscillator strength is related to the probability of finding electron and hole at the same position [Zim97],

$$M_\alpha \propto \int dr\, \Psi_\alpha(r, r) = \int dz\, u_e(z)\, u_h(z) \cdot \varphi_{1s}(0) \cdot \int dR\, \psi_\alpha(R)\,. \tag{6.11}$$

Optical density and PL spectrum are calculated by summing over the eigenstates α [Run02]

$$\begin{aligned} D(\omega) &= \sum_\alpha |M_\alpha|^2\, \pi\, \delta(\hbar\omega - \epsilon_\alpha)\,, \\ P(\omega) &= \sum_\alpha |M_\alpha|^2\, N_\alpha\, \pi\, \delta(\hbar\omega - \epsilon_\alpha)\,, \end{aligned} \tag{6.12}$$

where N_α is the occupation of the state α. The calculations were performed for 100 realizations of two-dimensional disorder potentials with an area 100×100 μm^2 each, yielding a total simulation area of 1 μm^2. Spectra were obtained by convolution of the optical density with a Lorentz curve with 200 μeV width. Subsequently, the spectra were added with a spatial weight corresponding to the experimental focus, which was approximated by an Airy function with a FWHM of 600 nm.

6.5 Relaxation and Stokes shift

In order to obtain calculated PL spectra for a useful comparison between experiment and computation, the occupation number N_α of the individual states should be known.

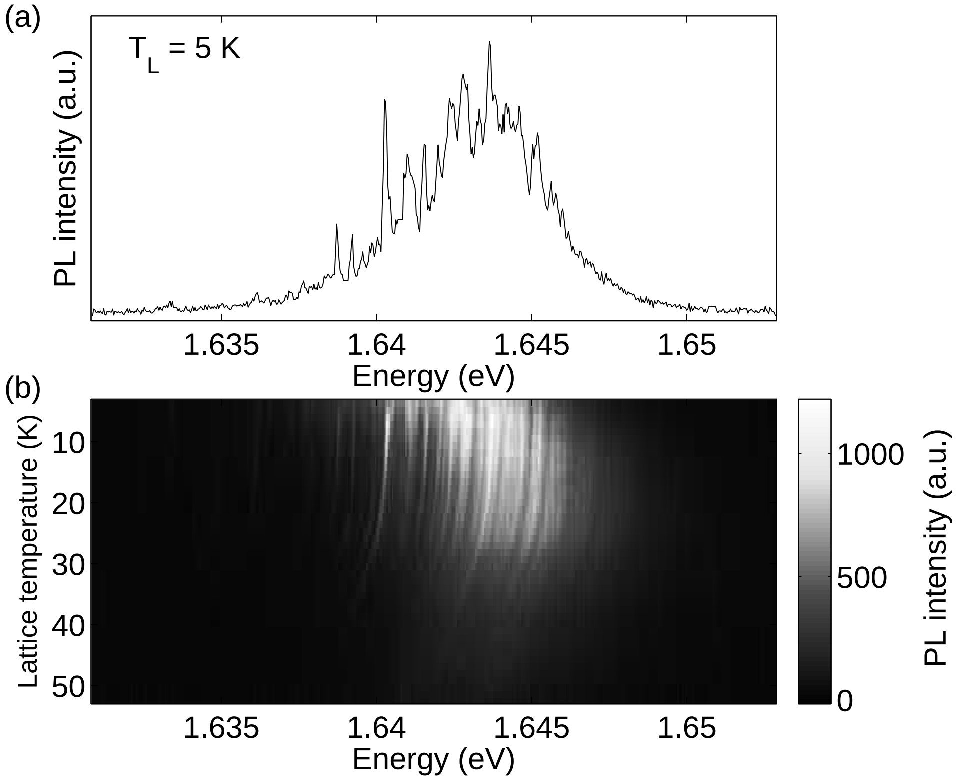

Figure 6.18: *(a) μPL spectrum of the 4-nm GaAs/Al$_{0.3}$Ga$_{0.7}$As QW at $T_L = 5$ K. (b) Temperature-dependent μPL spectra in the temperature range $T_L = 3 - 50$ K.*

A proper calculation of all N_α by solving the kinetic equations is technically very demanding in this case; this approach is not pursued here.

The effects of the temperature-dependent relaxation on μPL spectra have therefore been studied experimentally. By controlled heating of the sample in the flow cryostat, μPL spectra of the 4 nm GaAs/Al$_{0.3}$Ga$_{0.7}$As QW have been measured at varying lattice temperatures. Temperature-dependent μPL spectra of the 4-nm QW in the temperature range $T = 3 - 50$ K are shown in Fig. 6.18. The sample was optically excited by an Ar$^+$-pumped dye laser at 1.9 eV. The total excitation power ($\sim 1\,\mu$W) was held constant during the measurements. The bandgap renormalization with increasing temperature is directly observed in the monotonous red-shift of single exciton transitions in the temperature-dependent μPL spectra. A phenomenological description of the decrease of the bandgap with increasing lattice temperature is provided by the Varshni formula [Var67]

$$E_G(T) = E_G(0) - \gamma \frac{T^2}{T + \Theta}, \tag{6.13}$$

where T is the lattice temperature and $E_G(T)$ is the temperature-dependent bandgap. Using bulk GaAs parameters $\gamma = 0.58$ meV/K, $\Theta = 300$ K, $E_G(0) = 1.522$ eV [Pan69], the increase in lattice temperature has been determined directly from the temperature-dependent μPL spectra.

The direct observation of the bandgap shift for single exciton states allows to remove the shift from the temperature-dependent spectra. In Figure 6.19(a), bandgap shift-

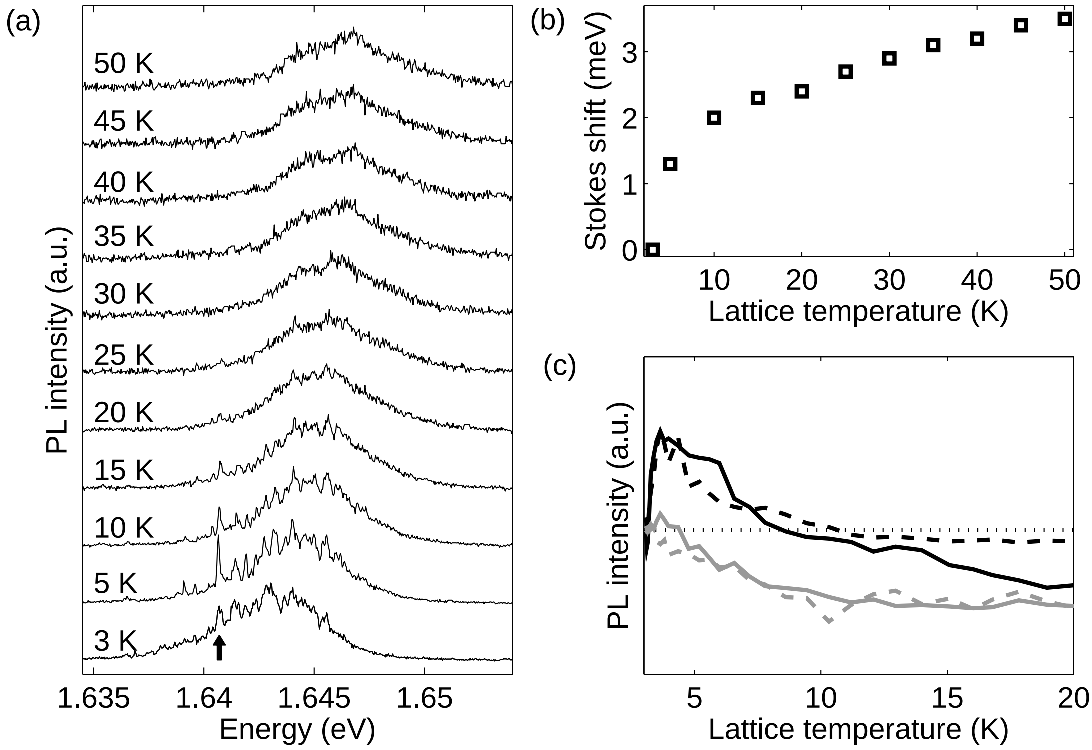

Figure 6.19: *(a) Temperature-dependent μPL spectra of the 4-nm GaAs/Al$_{0.3}$Ga$_{0.7}$As QW; for better comparison of the lineshape, the total area under the spectra has been normalized. The lattice temperature T_L is indicated. (b) Stokes shift of the center of QW emission relative to the position at $T_L = 3$ K. (c) Temperature dependence of the emission of a few exciton states in the low-energy tail. Some states show increasing absolute emission intensity in the temperature range $3 - 50$ K.*

corrected spectra of the 4-nm QW are shown as a function of lattice temperature. Figure 6.18 showed that the total luminescence intensity decreases strongly above $T_L \approx$ 20 K; for easier comparison of the QW emission lineshape, the total area under the spectra in Fig. 6.19(a) has been normalized.

Three effects are prominent in the μPL spectra in Fig. 6.19(a): The temperature-dependent change in the intensity of single exciton lines in the low-energy tail, the shift of the maximum of the QW emission, and the decreasing slope of the high-energy tail. While the shift of the maximum and the decreasing slope of the high-energy tail indicate a thermalized exciton distribution, the temperature-dependence of several single exciton lines below $\sim$ 1.642 eV is quite obviously not compatible with the simple picture of a thermal population of potential minima. Figure 6.19(b) shows the relative change in luminescence intensity of some localized exciton states as a function of temperature. While the intensity of most lines decreases with increasing temperature, some lines [the position of the most prominent line at 1.6407 eV is marked by an arrow in Fig. 6.19(a)] exhibit increasing emission intensity in the temperature range $3 - 5$ K. At still higher temperature, intensity decreases again. The prominent line at 1.6407 eV gains intensity from 3 K to 5 K, then its intensity decreases and reaches its 3 K-value at $\sim$ 10 K. This effect is indicative of thermal activation of carriers from nearby minima into a larger

Figure 6.20: *[Col89] Well width-dependence of the effective carrier temperature T_{eff} in GaAs/Al$_{0.3}$Ga$_{0.7}$As QWs. Experimental values determined from the logarithmic high-energy slope of μPL spectra (T_L = 4 K) are shown in black. The gray line indicates experimental results of Colvard et al. obtained at T_L = 2 K; the difference in lattice temperature between both experiments (2 K) has been added for easier comparison.*

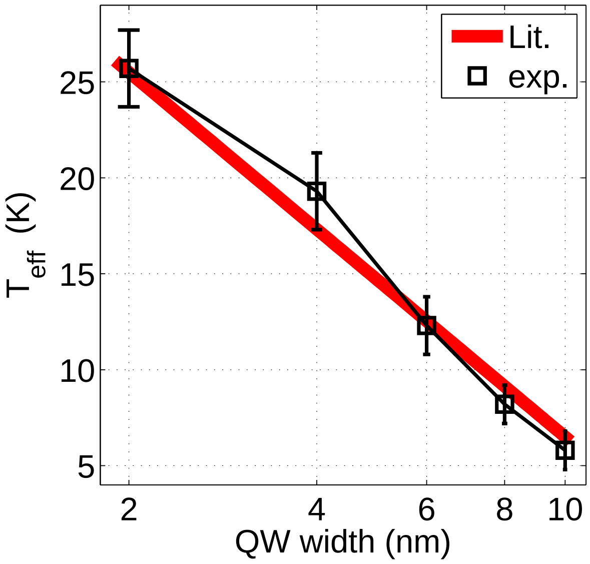

minimum, and of incomplete thermalization of the exciton population in the low-energy tail of the exciton spectra.

The overall shape of the spectrum, however, clearly shows the effects of carrier thermalization: (i) The blue-shift of the center-of-mass of the emission spectrum, (ii) the increase of the inhomogeneous linewidth, and (iii) the slower decrease in the high-energy tail with increasing lattice temperature. The high-energy tail is well described by an exponential decay over more than an order of magnitude in the experimental μPL spectra. From the logarithmic slope of the high-energy tail, an effective carrier temperature T_{eff} can be determined that is higher than the lattice temperature T_L [Col89]. The difference $T_{\text{eff}} - T_L$ decreases with increasing lattice temperature; above $T_L = 50$ K, T_{eff} and T_L are practically equal. From the high-energy tail of the experimental μPL spectrum of the 4-nm QW at $T = 4$ K, we obtain an effective carrier temperature $T_{\text{eff}} = 20 \pm 1$ K. This value is in good agreement with previous findings. Figure 6.20 shows the effective carrier temperatures determined under similar excitation conditions and at a sample temperature $T = 4$ K for the 2-nm QW in sample QW$_2$ and the 4, 6, 8 and 10 nm thick QWs in sample QW$_1$. The gray line indicates experimental results of Colvard *et al.* for GaAs/Al$_{0.3}$Ga$_{0.7}$As QWs of varying thickness [Col89] obtained at $T_L = 2$ K; the difference in lattice temperature between both experiments (2 K) has been added for easier comparison. Rather good agreement of the values is observed.

6.6 Comparison of simulated and experimental μPL spectra

The position in the STM measurements on the 4-nm QW described in chapter 5 was determined using an optical microscope while the experiment was performed. The distance to the sample edge was determined, and in the subsequent optical experiments, the same sample position was placed in the optical focus by manual translation stages. The accuracy with which the optical focus and the position of the XSTM measurements coincided was better than 200 μm. In a scanning macro-PL setup, it was checked that neither the emission energy nor the inhomogeneous linewidth varied over such a distance. A μPL spectrum of the 4-nm QW taken in the vicinity of the position of the STM measurements, recorded at a temperature of 4 K, is shown in Fig. 6.21(a). The spectrum shows inhomogeneous broadening with individual bright peaks on the low-energy side due to strongly localized excitons. On the high-energy side, the more continuous spectrum consists of many closely spaced peaks.

A numerically computed absorption spectrum ($D(\omega)$) for an area corresponding to the experimental focus is shown as black line in Figure 6.21(b). Multiplying the calculated absorption spectrum with a Maxwell-Boltzmann factor results in a simulated PL spectrum

$$P(\omega) = C\, e^{-\hbar\omega/k_B T_{\text{eff}}}\, D(\omega)\,, \tag{6.14}$$

where $T_{\text{eff}} = 20$ K is assumed. The simulated PL spectrum is shown as gray curve in Fig. 6.21(b). A Stokes shift with respect to the absorption of ~ 3.5 meV is observed. In Figure 6.21(c), the experimental and the predicted μPL curves are shown together. The qualitative and quantitative agreement of both curves of both curves is excellent. Due to the randomization procedure that is involved in the generation of the in-plane disorder potentials, the individual peak positions and peak heights are not significant. Instead, the overall spectral structure and the size of the inhomogeneous broadening should be characteristic for the disorder potential studied. These features are clearly reproduced by the calculations. Certain qualitative deviations are discernible at the low energy tail of the luminescence, where the predicted luminescence strength of individual states in the calculations tends to exceed those found in the experiments. This is clearly a result of the deviation from an exactly thermal occupation of those tail states in the experiment. Finally, in Fig. 6.21(d), an experimental μPL spectrum at an elevated temperature of 50 K (black) is compared with the calculated PL spectrum for $T_{\text{eff}} = 50$ K. Again, good agreement of both curves is found, which indicates that the carriers are well equilibrated among themselves and with the lattice at this temperature. The temperature dependent change in transition energy due to bandgap reduction was taken into account in the calculations of the spectra at the higher temperature. A bandgap difference of 2.5 meV between the lattice temperatures $T_L = 4$ K and $T_L = 50$ K was precisely determined in the experiment from the shift of individual localized states when the temperature was continuously raised. It should be noted that the absolute energy of all theoretical curves was blue-shifted by 4 meV in order to achieve the agreement shown above. As the absolute transition energy is a very sensitive function of the material parameters as well as the average QW thickness, possible strain contributions, image charge effects on the binding energy etc., a more accurate prediction of the absolute energy cannot be expected, given the precision of all known input quantities to the calculation.

In light of the limited number of simple assumptions made in the calculations, the rather accurate prediction of the inhomogeneous broadening and the temperature-dependent lineshapes of the ensemble of excitonic states is striking.

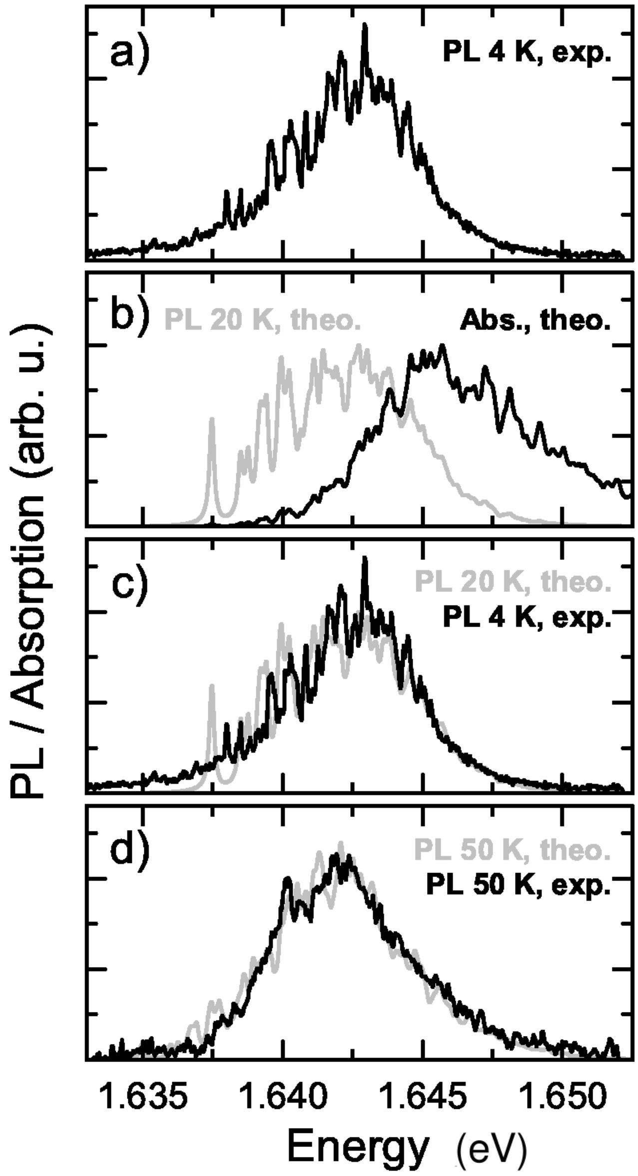

Figure 6.21: *[Rop07] Comparison between measured μPL spectra and spectra calculated from the XSTM data. (a) Experimental μPL spectrum measured at* $T = 4$ *K. (b) Calculated absorption spectrum (black) and predicted luminescence (gray), assuming an effective carrier temperature of 20 K, which is a realistic value for a 4-nm QW at 4 K lattice temperature. (c) For easier comparison, experimental μPL (4 K, black) and calculated PL (20 K, gray) plotted in the same graph. (d) Experimental μPL spectrum measured at* $T = 50$ *K (black) and calculated PL (gray) for a thermal carrier population at 50 K.*

6.7 Conclusions

The spectrally narrow emission lines of disorder-localized exciton states have been resolved in the low-energy tail of μPL spectra of the narrow GaAs/Al$_{0.3}$Ga$_{0.7}$As quantum wells. The fine-structure splitting of low-energy tail states has been investigated via polarization-dependent spectroscopy, and no clear preferential direction of the linearly polarized fine-structure components has been found. This is in contrast to growth-interrupted samples, where a preferential orientation along the $[1\bar{1}0]$ direction has been reported [Gam96], caused by exciton localization in large anisotropic islands aligned along the $[1\bar{1}0]$ direction. Our observation therefore indicates that such large anisotropic islands aligned along the $[1\bar{1}0]$ direction are not responsible for exciton localization in the investigated non-growth interrupted quantum well. Rather, it indicates exciton localization by short-range correlated disorder.

The simulation of optical spectra on the basis of the structural data from the XSTM experiment on the 4-nm QW has been described. Two-dimensional disorder potentials were simulated, representing the band edge fluctuations in the QW plane. Isotropic exponential correlations in the QW plane were assumed with a correlation length of 0.4 nm, corresponding to the shortest correlation length observed in the XSTM experiments. Justification for the assumption of isotropic correlations comes from the observation that fine-structure components of localized exciton states show no clear preferential direction.

Temperature-dependent μPL experiments have been performed on the 4-nm QW to study relaxation effects and the Stokes shift. Based on the insight that μPL spectra can be characterized by an effective carrier temperature that is higher than the lattice temperature, experimental and simulated μPL spectra of the 4-nm GaAs/Al$_{0.3}$Ga$_{0.7}$As quantum well could be directly compared. Very good agreement is observed between inhomogeneous broadening and temperature-dependent lineshapes of experimental and simulated μPL spectra. This results is further evidence that mainly short-range correlated disorder on a length scale of a few lattice constants is responsible for exciton localization in the 4-nm GaAs/Al$_{0.3}$Ga$_{0.7}$As quantum well.

References

[QT] Trolltech Inc., http://www.trolltech.com/products/qt/.

[Ada94] S. Adachi, *GaAs and related materials*, World Scientific, 1994.

[Bas84] G. Bastard, C. Delalande, M. H. Meynadier, P. M. Frijlink, and M. Voos, *Low-temperature exciton trapping on interface defects in semiconductor quantum wells*, *Phys. Rev. B* 29, 7042 (1984).

[Bay02] M. Bayer, G. Ortner, O. Stern, A. Kuther, A. A. Gorbunov, A. Forchel, P. Hawrylak, S. F. K. Hinzer, T. L. Reinecke, S. N. Walck, J. P. Reithmaier, F. Klopf, and F. Schafer, *Fine structure of neutral and charged excitons in self-assembled In(Ga)As/(Al)GaAs quantum dots*, *Phys. Rev. B* 65, 195315 (2002).

[Blo99] P. G. Blome, *Mikro-Photolumineszenz an InP/GaInP-Quantenpunkten*, Ph.D. thesis, Universität Göttingen, 1999.

[Bru94] K. Brunner, G. Abstreiter, G. Böhm, G. Tränkle, and G. Weimann, *Sharp-line photoluminescence and 2-photon absorption of zero-dimensional biexcitons in a GaAs/AlGaAss structure*, *Phys. Rev. Lett.* 73, 1138 (1994).

[Bur97] M. Burkard, C. Geng, A. Muhe, F. Scholz, H. Schweizer, and F. Phillipp, *Transmission electron microscopy observation of lateral order/disorder structures in (Al)GaInP*, *Appl. Phys. Lett.* 70, 1290 (1997).

[Col89] C. Colvard, D. Bimberg, K. Alavi, C. Maierhofer, and N. Nouri, *Localization-dependent thermalization of excitons in GaAs/*$Al_xGa_{1-x}As$ *quantum wells*, *Phys. Rev. B* 39, 3419 (1989).

[Din82] R. Dingle, C. Weisbuch, H. L. Störmer, H. Morkoc, and A. Y. Cho, *Characterization of high-purity GaAs grown by MBE*, *Appl. Phys. Lett.* 40, 507 (1982).

[Eke89] U. Ekenberg, *Nonparabolicity effects in a quantum well - sublevel shift, parallel mass, and Landau levels*, *Phys. Rev. B* 40, 7714 (1989).

[Gam96] D. Gammon, E. S. Snow, and D. S. Katzer, *Naturally formed GaAs quantum dots*, *Surf. Sci.* 362, 814 (1996).

[Gro05] M. Grochol, F. Grosse, and R. Zimmermann, *Exciton wave function properties probed by diamagnetic shift in disordered quantum wells*, *Phys. Rev. B* 71, 125339 (2005).

[Heg84] J. Hegarty, L. Goldner, and M. D. Sturge, *Localized and delocalized two-dimensional excitons in GaAs/AlGaAs multiple-quantum well structures*, *Phys. Rev. B* 30, 7346 (1984).

[Hes94] H. F. Hess, E. Betzig, T. D. Harris, L. N. Pfeiffer, and K. W. West, *Near-field spectroscopy of the quantum constituents of a luminescent system*, *Science* 264, 1740 (1994).

[Ivc95] E. L. Ivchenko and G. Pikus, *Superlattices and other heterostructures*, Springer, New York, 1995.

[Kir98] M. Kira, F. Jahnke, and S. W. Koch, *Microscopic theory of excitonic signatures in semiconductor photoluminescence*, *Phys. Rev. Lett.* 81, 3263 (1998).

[Mai00] M. Z. Maialle, *Spin dynamics of localized excitons in semiconductor quantum wells in an applied magnetic field*, *Phys. Rev. B* 61, 10877 (2000).

[Mai93] M. Z. Maialle, E. A. D. E. Silva, and L. J. Sham, *Exciton spin dynamics in quantum wells*, *Phys. Rev. B* 47, 15776 (1993).

[Mar94] J. Y. Marzin, J. M. Gerard, A. Izrael, D. Barrier, and G. Bastard, *Photoluminescence of single InAs quantum dots obtained by self-organized growth on GaAs*, *Phys. Rev. Lett.* 73, 716 (1994).

[Mat03] K. Matsuda, T. Saiki, S. Nomura, M. Mihara, Y. Aoyagi, S. Nair, and T. Takagahara, *Near-field optical mapping of exciton wave functions in a GaAs quantum dot*, *Phys. Rev. Lett.* 91, 177401 (2003).

[Min88] M. Minsky, *Memoir on inventing the confocal scanning microscope*, *Scanning* 10, 128 (1988).

[Nic98] H. Nickolaus, H. J. Wunsche, and F. Henneberger, *Exciton spin relaxation in semiconductor quantum wells: The role of disorder*, *Phys. Rev. Lett.* 81, 2586 (1998).

[Pan69] M. B. Panish and H. C. Casey, *Temperature dependence of the energy gap in GaAs and GaP*, *J. Appl. Phys.* 40, 163 (1969).

[Ric59] B. Richards and E. Wolf, *Electromagnetic diffraction in optical systems - 2. Structure of the image field in an aplanatic system*, *Proc. Royal Soc. London, Ser. A* 253, 358 (1959).

[Rop03] C. Ropers, *Exzitonlokalisierung in AlGaAs/GaAs-Quantenfilmen*, Diploma thesis, Universität Göttingen, 2003.

[Rop07] C. Ropers, M. Wenderoth, L. Winking, T. C. G. Reusch, M. Erdmann, R. G. Ulbrich, M. Grochol, F. Grosse, R. Zimmermann, S. Malzer, and G. H. Döhler, *Atomic scale structure and optical emission of AlGaAs/GaAs quantum wells*, Phys. Rev. B (2007).

[Run02] E. Runge, *Excitons in semiconductor nanostructures*, *Adv Solid State Phys* 57, 149 (2002).

[Sch06] R. Scholz and P. Vogl, private communication (M. Grochol), recent tight binding calculations (2006).

[Sia00] A. Siarkos, E. Runge, and R. Zimmermann, *Center-of-mass properties of the exciton in quantum wells*, *Phys. Rev. B* 61, 10854 (2000).

[Str00] B. Stroustrup, *The C++ Programming Language*, Addison Wesley, 2000.

[Ulb73] R. Ulbrich, *Energy relaxation of photoexcited hot electrons in GaAs*, *Phys. Rev. B* 8, 5719 (1973).

[Var67] Y. P. Varshni, *Temperature dependence of the energy gap in semiconductors*, *Physica* 34, 149 (1967).

[Web96] R. H. Webb, *Confocal optical microscopy*, *Rep. Prog. Phys.* 59, 427 (1996).

[Wei81] C. Weisbuch, R. Dingle, A. C. Gossard, and W. Wiegmann, *Optical characterization of interface disorder in GaAs/*$Ga_{1-x}Al_xAs$ *multi-quantum well structures*, *Solid State Commun.* 38, 709 (1981).

[Zim97] R. Zimmermann, F. Grosse, and E. Runge, *Excitons in semiconductor nanostructures with disorder*, *Pure Appl. Chem.* 69, 1179 (1997).

[Zre94] A. Zrenner, L. V. Butov, M. Hagn, G. Abstreiter, G. Bohm, and G. Weimann, *Quantum dots formed by interface fluctuations in AlAs/GaAs coupled quantum well structures*, *Phys. Rev. Lett.* 72, 3382 (1994).

[Zre01] A. Zrenner, F. Findeis, M. Baier, M. Bichler, and G. Abstreiter, *Magneto-optics on single quantum dots*, *Physica B* 298, 239 (2001).

Chapter 7

Diamagnetic shift distribution in single GaAs/$\mathrm{Al}_{0.3}\mathrm{Ga}_{0.7}$As QWs

In this chapter, the application of magneto-μPL spectroscopy to the study of disorder in narrow GaAs/$\mathrm{Al}_{0.3}\mathrm{Ga}_{0.7}$As single QWs is described. First, the concept of disorder characterization via the diamagnetic shift is outlined. Magneto-μPL spectra of 2-nm and 4-nm QWs are shown and diamagnetic shift coefficients and effective exciton g-factors of single exciton states in the low-energy tail of the spectra are determined. Then, the observed correlation between diamagnetic coefficients and transition energy is discussed in detail. Finally, the experimental results for the 4-nm QW are compared with theoretical calculations of diamagnetic shift coefficients based on the XSTM data of the 4-nm QW, thereby extending the comparison of optical and structural properties of this QW.

7.1 Concept

Exciton diamagnetic shift has been experimentally studied for low-dimensional quantum structures (QW, QWR, QD) [Tar84, Rog86, Som95, Bay98], and for disorder-localized excitons in narrow QWs [Hes94, Ste02, Ste03, Phi03]. For disorder-localized excitons in narrow QWs, a variation of the XDS between different exciton eigenstates has been observed [Hes94]. This variation is explained by the fact that disorder influences both exciton c.m. and relative WF, and relative and c.m. motion are coupled. Although the wave functions of disorder-localized exciton states will generally exhibit no perfect circular symmetry, we assume 1s relative wave functions for simplicity. Any attempt to go beyond this assumption would make the following considerations less transparent. Therefore, we assume that the effects of lateral exciton confinement can be described by a localization of the exciton center-of-mass and a reduction of the exciton radius. A magnetic field B normal to the QW plane increases the transition energy of a given exciton state α,

$$E_\alpha(B) = E_\alpha(B=0) + \Delta_\alpha(B)\,. \tag{7.1}$$

In the regime of relatively weak lateral confinement, which is assumed to be realized in natural quantum dots, the diamagnetic shift Δ_α of a 1s exciton state α is a measure of the electron-hole separation [Wal98]

$$\Delta_\alpha(B) = \frac{e^2}{8\mu} \langle \rho_\alpha^2 \rangle \, B^2 \,, \tag{7.2}$$

where $\langle \rho_\alpha^2 \rangle^{1/2}$ is the effective lateral exciton radius. The expression for the XDS is more complicated in presence of disorder [Gro05]. Within the scope of the discussion of our experimental results, it is however reasonable to use Eq. (7.2), and to express the diamagnetic shift Δ_α by the diamagnetic coefficent

$$\gamma_2^{(\alpha)} = \frac{e^2}{8\mu} \langle \rho_\alpha^2 \rangle \,. \tag{7.3}$$

Confinement influences both the effective exciton radius ρ_α and the exciton reduced mass μ [Sch05]: Stronger confinement decreases the exciton radius and increases the exciton reduced mass μ. Both factors decrease the diamagnetic coefficient. Therefore, a reduction of the XDS is consistently interpreted as a confinement effect. Quantitative interpretation of XDS values requires consideration of the dependence of the in-plane electron mass and, consequently, the in-plane exciton reduced mass, on QW width.

The dependence of the exciton diamagnetic shift in quantum dots on the lateral confinement potential suggests the following concept for disorder characterization via magneto-μPL spectroscopy: "Single-dot" magneto-μPL spectroscopy gives access to diamagnetic shift and Zeeman splitting of individual QD states in an external magnetic field. Since the exciton diamagnetic shift (XDS) of natural QD states in a magnetic field normal to the QW plane is sensitive to the lateral extension of the exciton relative wave function, and thereby to lateral confinement, study of the XDS gives access to the shapes of potential minima: While the exciton transition energy is sensitive to the total confinement volume, the XDS is a measure of the lateral extension of the confinement potential; combination of both should provide information about the shape of a potential minimum. The statistics of potential minimum shapes should provide information about the correlation length of the lateral interface disorder potential.

7.2 Experimental results

Low-temperature ($T = 3$ K) μPL spectra of the 4-nm QW in sample QW_1 and of the 2-nm QW in sample QW_2 were obtained during linearly polarized optical excitation with ~ 10 W/cm^2 at 514 nm. A magnetic field up to 10 T was applied in growth direction (Faraday configuration). Figure 7.1(a) shows μPL spectra of the 2-nm GaAs/$Al_{0.3}Ga_{0.7}$As QW at $B = 0$ T and $B = 10$ T. Single exciton states as low as 20 meV below the center of the QW emission peak are observed.

Figure 7.1(b) shows color-coded μPL spectra of the 2 nm QW for magnetic fields between $B = 0$ T and $B = 10$ T. Zeeman splitting of the localized exciton states is resolved above $B = 1$ T. The Zeeman components of the lowest-energy exciton states are clearly identified in Fig. 7.1 and Fig. 7.2. Higher-lying lines are less well separated, and for several closely spaced states at the QW emission peak it is impossible to trace the Zeeman components over the complete B-field range. However, for several emission

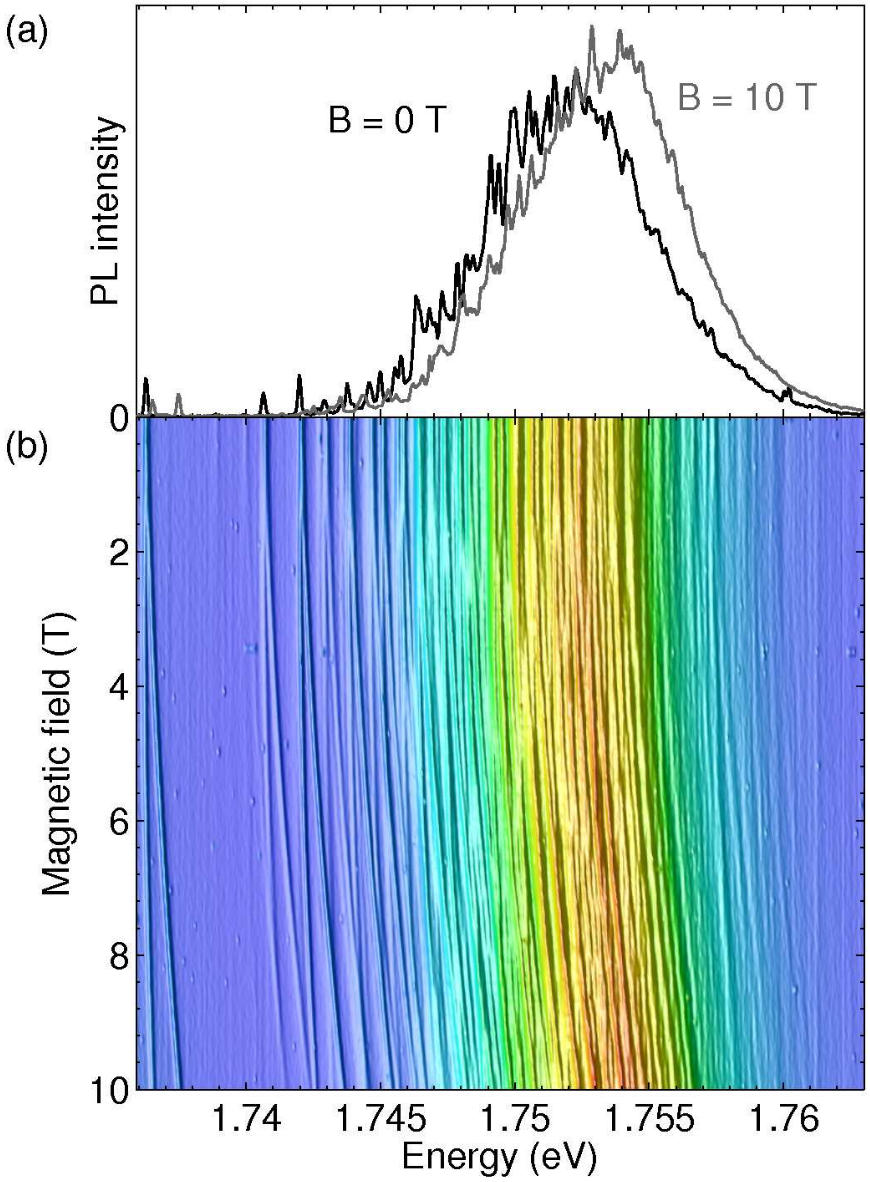

Figure 7.1: *(a) µPL spectra of the 2 nm GaAs/Al*$_{0.3}$*Ga*$_{0.7}$*As QW at B=0 T (black) and B=10 T (gray). (b) Color-coded magneto-µPL spectrum (B=0..10 T) of the 2-nm GaAs/Al*$_{0.3}$*Ga*$_{0.7}$*As QW. The magnetic field was increased in steps of 50 mT.*

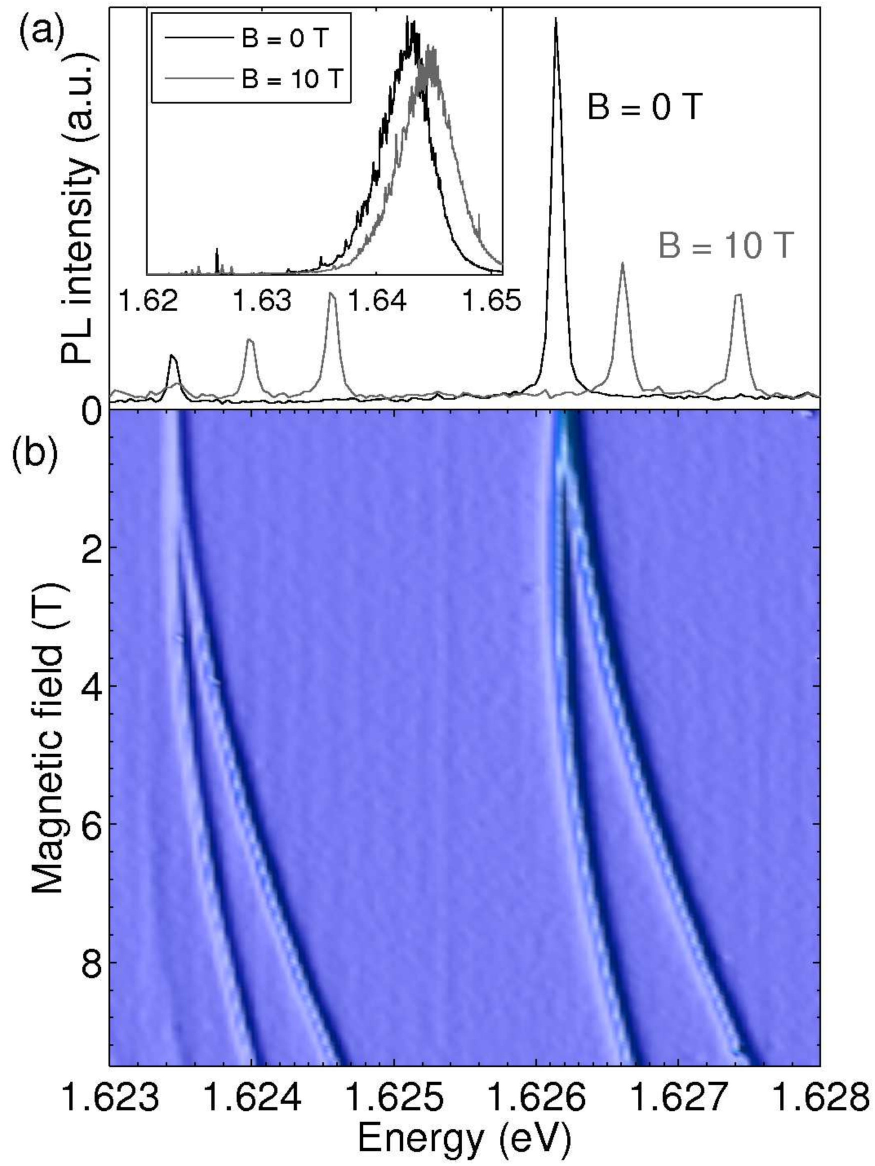

Figure 7.2: *(a) Inset: μPL spectra of the 4-nm GaAs/$Al_{0.3}Ga_{0.7}$As QW at B=0 T and B=9.5 T; emission lines of two localized exciton states at B=0 T (black) and B=9.5 T (gray). (b) Color-coded magneto-μPL spectrum (B=0..9.5 T) showing Zeeman splitting and diamagnetic shift of two of the lowest-energy localized exciton states in the 4-nm QW.*

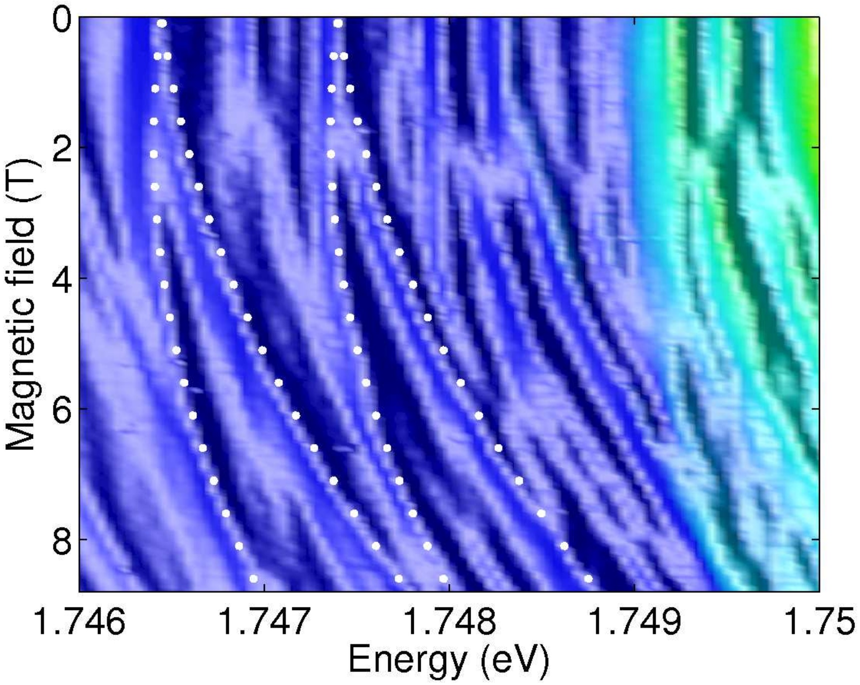

Figure 7.3: *Section of Figure 7.1(b): The dotted lines mark Zeeman components of two higher-energy emission lines below the 2 nm QW emission peak.*

lines unambiguous identification is possible. As an example, Fig. 7.3 shows two higher-lying emission lines below the QW emission peak of the 2-nm QW.

Experimentally, the diamagnetic shift of localized exciton levels is determined from the B-field dependent optical spectra by taking the mean value of the Zeeman components. The magnetic length scale given by $\lambda = \sqrt{\hbar/eB}$ determines the crossover from low-field to high-field regime. As long as $\lambda \ll a_B$ or, equivalently, if the cyclotron energy $\hbar eB/\mu$ is much smaller than the exciton binding energy E_B, the B-dependence of the exciton energy is dominated by the diamagnetic shift. The Bohr radius of the lowest exciton state in a nominally perfect 4 nm GaAs/Al$_{0.3}$Ga$_{0.7}$As QW is $a_B \approx 8.2$ nm, and therefore

$$\lambda(B = 8T) \approx a_B\,. \tag{7.4}$$

Consequently, the diamagnetic coefficient is determined by a quadratic fit of the mean value of the Zeeman components up to $B = 4$ T. At higher fields, the cyclotron-confinement of electron and hole causes a deviation from the quadratic shift. In the high-field limit, the cyclotron energy $\hbar\omega_c$ dominates over the exciton Coulomb energy E_B, and a Landau-like linear increase of energy with magnetic field is predicted [Aki67]. The B-dependence of the exciton diamagnetic shift for any magnetic field is therefore well described by an interpolation formula

$$\Delta(B) = a \cdot (\sqrt{b^2 + B^2} - b). \tag{7.5}$$

The diamagnetic coefficient

$$\gamma_2 = \lim_{B\to 0} \frac{1}{2} \frac{d^2\Delta(B)}{dB^2} \tag{7.6}$$

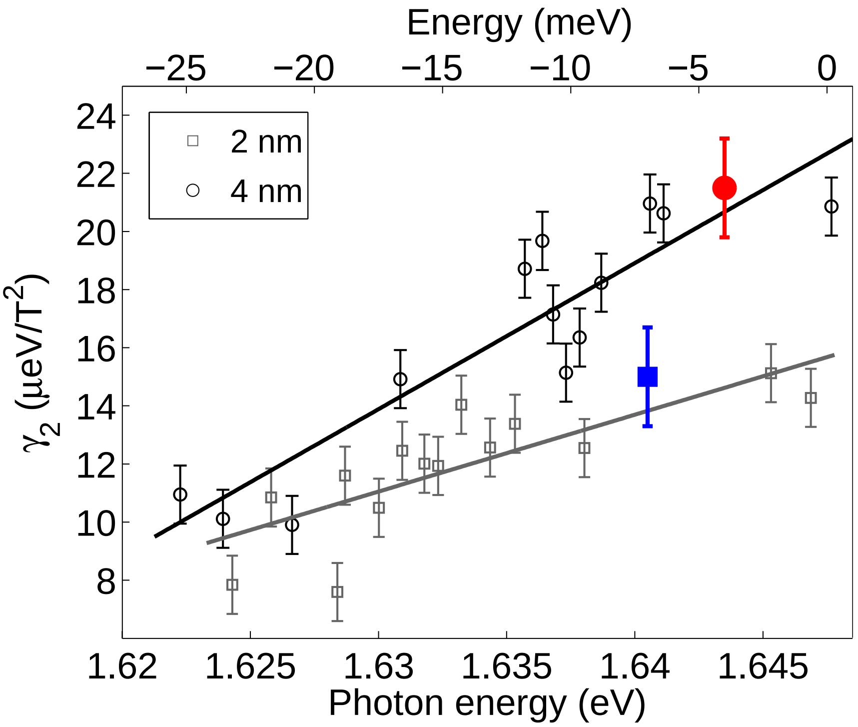

Figure 7.4: *Diamagnetic coefficients of exciton states in 2-nm (gray squares) and 4-nm (black circles) GaAs/Al$_{0.3}$Ga$_{0.7}$As QWs as a function of transition energy. The bottom energy axis applies to the 4-nm QW; values for the 2-nm QW have been shifted by -110 meV. Zero of the top energy axis is the center of a simulated QW absorption spectrum, i.e., QW emission peak energy plus Stokes shift (2-nm QW: 7 meV, 4-nm QW: 4 meV). Diamagnetic coefficients at the QW emission peaks are shown as solid symbols.*

is obtained from the fit as $\gamma_2 = a/2b$. Parameters a and b are determined by fitting the mean value of the Zeeman components up to $B = 10$ T. This fit procedure leads to nearly identical results for the diamagnetic coefficient γ_2 as the quadratic fit up to 4 T.

Figure 7.4 shows diamagnetic coefficients of localized exciton states in the 2-nm and 4-nm GaAs/Al$_{0.3}$Ga$_{0.7}$As QWs as a function of transition energy. The top energy axis is the common energy axis for both QWs; zero energy is chosen as the center of a simulated QW absorption spectrum. Carrier relaxation in the inhomogeneously broadened QW exciton band is responsible for a temperature-dependent Stokes shift that varies with disorder strength [Gur94]. Therefore, the peak energy of the QW luminescence is not a well suited reference energy. To overcome this problem, the top energy axis of Fig. 7.4 has been renormalized by the Stokes shift. Stokes shifts of 7 meV (2-nm QW) and 4 meV (4-nm QW) have been assumed.

The determination of diamagnetic coefficients from μ-magnetoluminescence spectra has been described above. The diamagnetic coefficients at the emission peaks of both QWs are shown as solid symbols. The emission peak of the 4-nm QW shifts with $\gamma_2 = 22\,\mu\text{eV}/\text{T}^2$, while for the emission peak of the 2-nm QW, a diamagnetic coefficient $\gamma_2 = 15\,\mu\text{eV}/\text{T}^2$ is observed. The lowest-energy exciton states are observed $\sim$ 20 meV below the QW emission peaks. The lowest exciton states in the 4-nm QW have diamagnetic

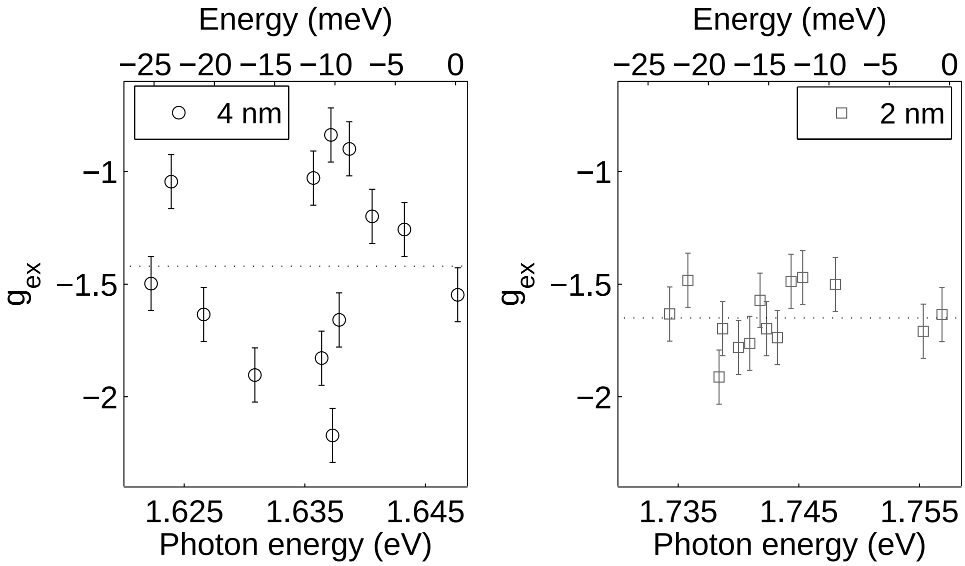

Figure 7.5: *Exciton g-factor of localized exciton states in 2-nm and 4-nm GaAs/Al$_{0.3}$Ga$_{0.7}$As QWs as a function of emission energy. The same top energy axis as in Fig. 7.4 is used, and the same exciton states are shown. Mean values of the exciton g-factors are indicated by the dotted lines.*

coefficients of $\sim 10\,\mu\text{eV/T}^2$, less than 1/2 the magnitude of the XDS at the QW emission peak. For the 2-nm QW, the diamagnetic coefficients of the lowest exciton states are reduced to $\sim 8\,\mu\text{eV/T}^2$. The diamagnetic coefficients show a systematic increase with transition energy. The slope of the trend line the for 2-nm QW is smaller than that for the 4-nm QW.

The Zeeman splitting is also influenced by confinement. Experimentally determined exciton g-factors for the same exciton states as in Fig. 7.4 are shown in Fig. 7.5, separately for 4-nm QW and 2-nm QW. The mean values in the 4-nm QW ($\bar{g}_{ex} = -1.4$) and in the 2-nm QW ($\bar{g}_{ex} = -1.65$) are indicated by the dotted lines. While the g-factors of single exciton states in the 4-nm QW show relatively large scatter, the exciton g-factor distribution observed in the 2-nm QW is rather narrow.

7.3 Discussion

This section discusses the experimental results the for diamagnetic shift of localized excitons in the narrow GaAs/Al$_{0.3}$Ga$_{0.7}$As QWs, and the interpretation of the observed correlation between XDS and localization energy in terms of the QW interface structure.

Confinement-dependent reduction of diamagnetic coefficients has been observed for excitons in quantum structures, i.e., QW, QWR and QD [Tar84, Som95, Bay98]. The confinement increases the overlap between electron and hole WFs, leading to a larger exciton binding energy, and in turn to a smaller exciton Bohr radius. Consequently, the diamagnetic coefficient is a measure of confinement in these simple cases of nearly ideal 1d, 2d or 3d confinement. The effect of QW confinement is apparent in Fig. 7.4: The average diamagnetic coefficient is larger for the 4-nm QW than for the 2-nm QW.

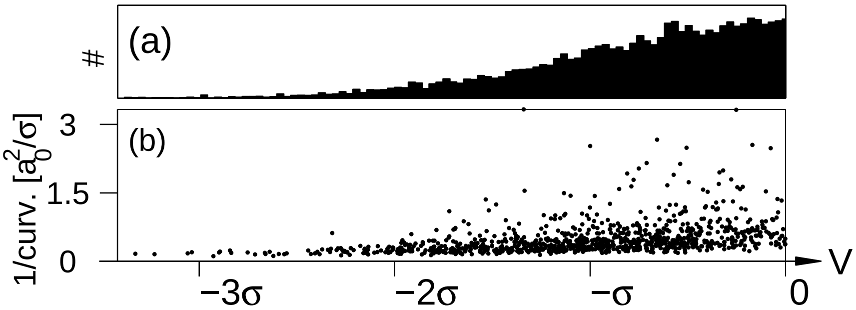

Figure 7.6: *(a) Histogram of a Gaussian disorder potential* $V(r)$ *with variance* σ^2*, (b) inverse curvature of potential minima of the uncorrelated potential* $V(r)$ *as a function of potential values.* a_0 *denotes the lattice constant, and # the number of potential values.*

Exciton localization by random fluctuations of the local bandedges in narrow QWs has been studied in recent theoretical work, taking the full Coulomb-correlated two-particle motion into account [Gro05]. Energies and wave functions of exciton tail states were calculated with and without B-field normal to the QW plane, and diamagnetic shifts were determined from simulated optical spectra. A correlation between XDS and lateral wave function extension was observed, showing that the most strongly localized exciton states have the smallest diamagnetic coefficients. This means that the XDS is a measure of lateral confinement also in the case of disorder-localized excitons. Note that we will use the interpretation of the diamagnetic coefficient valid in the weak confinement limit throughout our qualitative discussion. It is assumed that lateral confinement in natural quantum dots generally can be described in this limiting case.

In our experiments on 2-nm and 4-nm GaAs/Al$_{0.3}$Ga$_{0.7}$As QWs, diamagnetic coefficients on the order of $10-20$ μeV/T^2 have been observed for all localized exciton states (Fig. 7.4), showing that all observed exciton states are 1s states. An XDS more than one order of magnitude larger than for 1s excitons would be expected for 2s excitons because of their much larger lateral radius. Equation (7.3) and 2s wave functions for two-dimensional excitons [Hau04] were used for this rough estimate. At the low excitation densities used in our experiments, biexcitons are not observed. We also have not found exceptionally small XDS on the order of 1 μeV/T^2, as reported by Phillips *et al.* for particular exciton states in a narrow GaAs/Al$_{0.3}$Ga$_{0.7}$As QW [Ste03, Phi03].

The positive slope in the XDS distribution as a function of transition energy (Fig. 7.4) shows that the lowest exciton tail states have the smallest diamagnetic coefficients, corresponding to small relative wave functions [Gro05]. Consequently, the lowest exciton states are laterally strongly confined states. This result requires detailed dicussion.

To explain the positive slope in Fig. 7.4, we consider the simple model of a one-dimensional uncorrelated, Gaussian distributed disorder potential $V(r)$ with variance σ^2 ("white noise"). Figure 7.6(a) shows a histogram of the potential values of $V(r)$, and Fig. 7.6(b) the inverse curvature of potential minima as a function of potential values. The inverse curvature is determined numerically from the discrete second derivate of $V(r)$ at the potential minima. The inverse curvature is a rough measure of lateral extension of potential minima. The result (Fig. 7.6(b)) shows a general property of random Gaussian disorder: The inverse curvature of potential minima increases with increasing potential values, which means deep potential minima are spatially narrow. This is plausible because the probability of finding several nearly equal potential values E on L neighbouring sites decreases with larger potential fluctuation E. The stated result can also be obtained in the framework of optimum fluctuation theory or with methods of statistical topography [Lif88, Run02].

We consider the simple model of a one-dimensional uncorrelated, Gaussian distributed disorder potential $V(r)$ with variance σ^2 ("white noise"). Figure 7.6(a) shows a histogram of the potential values of $V(r)$, and Fig. 7.6(b) the inverse curvature of potential minima as a function of potential values. The inverse curvature is determined numerically from the discrete second derivate of $V(r)$ at the potential minima. The inverse curvature is a rough measure of lateral extension of potential minima. The result (Fig. 7.6(b)) shows a general property of random Gaussian disorder: The inverse curvature of potential minima increases with increasing potential values, which means deep potential minima are spatially narrow. This is plausible because the probability of finding several nearly equal potential values E on L neighbouring sites decreases with larger potential fluctuation E. The stated result can also be obtained in the framework of optimum fluctuation theory or with methods of statistical topography [Lif88, Run02].

To relate this feature of a random Gaussian-distributed disorder potential to exciton localization by this potential, it is necessary to take the averaging of the exciton over underlying disorder into account. We assume that the two-dimensional uncorrelated Gaussian potential $V(r)$ describes the spatial variation of the local bandedges in the QW plane. The averaging with the exciton relative wave function leads to a reduction of disorder strength, and introduces correlations on the length scale of the exciton Bohr radius. Potential minima of the underlying disorder potential are smeared out. Taking the inverse curvature of potential minima as a measure for their lateral extension, we state that minima in the resulting effective potential $V_{\text{eff}}(R)$ for the exciton center-of-mass extend over several minima of $V(r)$, denoting with R the c.m. coordinate of the exciton. Excitons are localized at positions where the underlying potential $V(r)$ is strongly reduced at several neighbouring sites, i.e., where several deep minima of the uncorrelated disorder potential occur in close vicinity. Width and depth of minima in $V_{\text{eff}}(R)$ are therefore determined by the probability of finding several deep minima in $V(r)$ at nearby sites. If $V(r)$ is uncorrelated or exhibits only short-range correlations below the length scale of the exciton Bohr radius, this probability decreases with increasing depth and number of potential minima involved. It is therefore plausible that deep minima of $V_{\text{eff}}(R)$ tend to be spatially narrow.

It is important to note that the exciton radius is itself confinement-dependent: Stronger lateral confinement leads to a reduced Bohr radius. Therefore, minima of the underlying disorder potential are not just averaged out with the same relative wave function, rather the deep, narrow minima are averaged with the smallest WFs. Because averaging with a smaller relative wave function is less effective, the inverse curvature of deep minima increases less than that of higher minima.

Figure 7.7 schematically shows several minima in the effective potential $V_{\text{eff}}(R)$ for the exciton center-of-mass resulting from underlying short-range disorder, as well as transition energies and c.m. wave functions of local exciton ground states. Exciton states are schematically assigned to transitions in the low-energy tail of the μPL spectrum of a disordered QW. The total localization energy of an exciton state is inversely related to its localization volume. Short-scale well width fluctuations present near the *white noise* limit eventually lead to a strong local reduction of vertical confinement energy, resulting in deep, rare minima in $V_{\text{eff}}(R)$. Our result that the lowest exciton states have the smallest diamagnetic coefficients (Fig. 7.4) means that exciton states in deep minima have small wave functions. This is schematically depicted in Fig. 7.7. The reduction in vertical confinement energy prevails over the increase in lateral confinement energy.

The dependence of the minimum curvature on potential minimum values in effective potentials resulting from underlying short-range correlated disorder is shown in Fig. 7.8. For the simple model of a one-dimensional, uncorrelated, Gaussian-distributed disorder potential on a 1 μm long grid with 0.4 nm grid step, smoothed effective potentials have been determined by convolution of the disorder potential with squared 1s wave functions with Bohr radii $a_B = 1 \dots 5$ nm. For each value of the Bohr radius, the curvature of potential minima in the resulting effective potential has been determined as a function of potential minimum values. The obtained distribution for all 5 values of the Bohr radius has been plotted in Fig. 7.8 (small black dots), and a straight line has been fitted to the distribution that shows relatively large scatter. The inhomogeneous distribution of potential minima shows that deep minima are likely to be narrow, i.e., to have high curvature; a clear increase in average potential minimum curvature is observed with increasing potential minimum depth. The same procedure has also been performed for four correlated potentials. The dashed curve ("exp. corr.") shows a straight-line fit to the minimum curvature distribution resulting from a potential that has been simulated

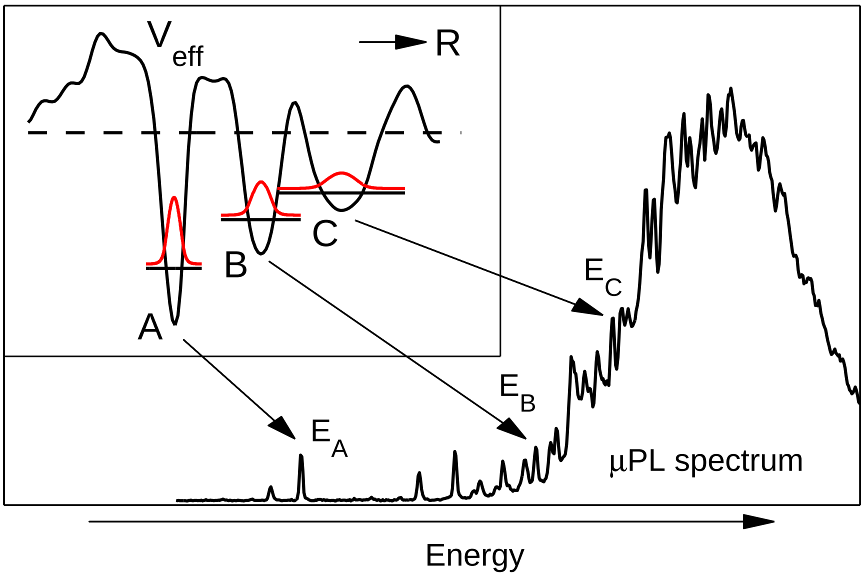

Figure 7.7: *Schematic representation of the physical situation of exciton localization by short-range correlated disorder (inset). Effective potential* $V_{\text{eff}}(R)$ *and wave functions for the exciton center-of-mass in three potential minima (A, B, C) are depicted. Exciton states are schematically assigned to transitions in the low-energy tail of the* μ*PL spectrum of a disordered QW. The experimentally observed correlation between XDS and transition energy (Fig. 7.4) shows that deep-lying exciton states have small wave functions, as demonstrated in the inset.*

from an uncorrelated potential by convolution with the experimentally determined correlation function [Fig. 5.8(c), Eq. (5.10)]. The remaining three lines in Fig. 7.8 show minimum curvature distributions of exponentially correlated potentials with correlation lengths $\xi = 1$ nm (dark gray), $\xi = 3$ nm (gray), and $\xi = 5$ nm (light gray). The correlated potentials have been obtained from an uncorrelated potential by convolution with an exponential function according to Eq. (5.11). The width of the inhomogeneous distributions is significantly reduced by the convolution, and the slope in the minimum curvature distributions is further reduced.

This simple model is of course far from an accurate quantitative description of exciton localization in correlated disorder potentials. First of all, a one-dimensional model is considered where averaging is considerably less effective than in two dimensions. In one dimension, the reduction in strength of a potential by averaging with a 1s wave function with Bohr radius a_B is proportional to $\sqrt{a_B}$, whereas in two dimensions the reduction is proportional to a_B, because averaging is done over a two-dimensional area instead of a straight line ("$\sqrt{N}$ law"). Second, if a variation of the Bohr radius is allowed, the radius would in principle have to be determined for each potential minimum separately. To keep the model manageable, we have just prescribed different values of the Bohr radius and determined effective potentials by a global convolution procedure. The

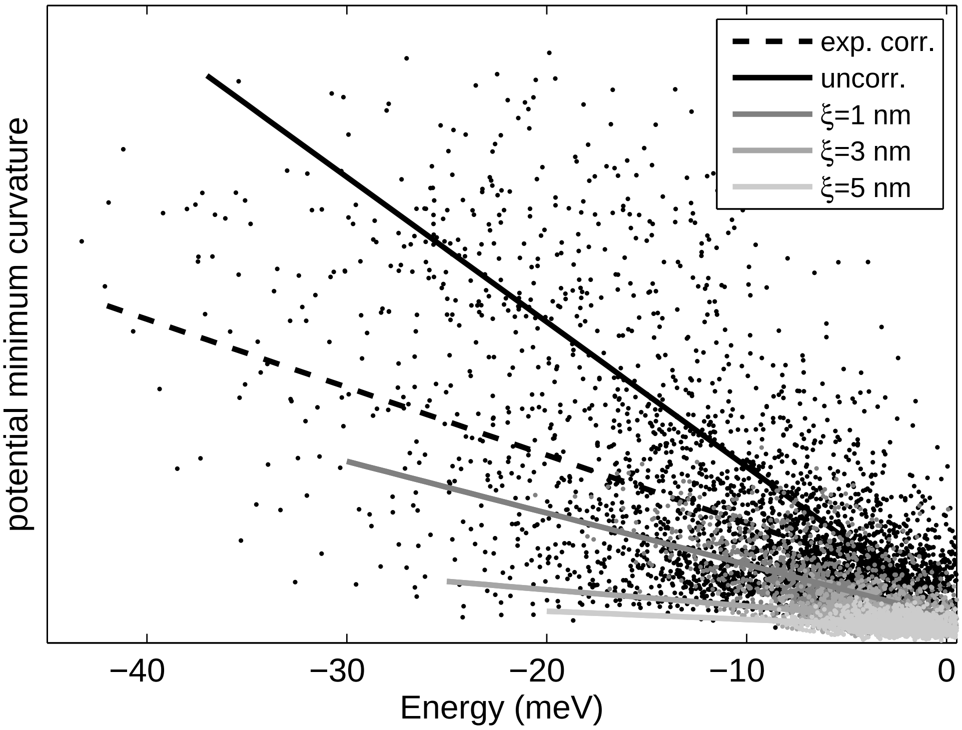

Figure 7.8: *A simple model demonstrates the dependence of the potential minimum distribution on the correlation length of the underlying potential: Minimum curvature distributions of simulated Gaussian-distributed 1d potentials with exponential correlations (correlation length ξ) show that the deepest minima have the largest curvature. The slope in the distribution of potential minima increases with decreasing correlation length of the underlying potential. Details are described in the text.*

different potential minimum values and minimum curvatures resulting from the same minimum in the underlying disorder potential upon averaging with different radii have been plotted together in Fig. 7.8. Very small values of the Bohr radius down to 1 nm had to be allowed to obtain a clearly visible trend. Finally, straight lines have been fitted to the obtained minimum curvature distributions. Considering the numerous simplifications in this model, it would certainly be exaggerated to try to determine the dependence of minimum curvature values on potential depth more accurately. No claim is made that the average curvature values should actually linearly increase with increasing effective potential minimum depth.

In view of the simplicity of this model, it is interesting to note the slope of the dashed curve, representing an underlying potential with correlations determined from the XSTM experiment. While the solid black curve corresponds to an uncorrelated potential with 0.4 nm "square-box correlations" due to the choice of the grid step, the dark-gray curve represents a potential with exponential correlations of 1 nm correlation length. In Fig. 7.8, a value for the correlation length of the experimentally determined potential can be determined from comparison with the slope of the lines representing the simulated correlated potentials. The slope of the line representing experimental correlations is larger than that for the uncorrelated potential, but smaller than that for the exponentially correlated potential with correlation length 1 nm. This compares well with the fact that the experimentally determined correlation length lies between 0.4 nm and 0.8 nm (see Chapter 5). In summary, this "minimal" model demonstrates that the correlation length of the underlying disorder is encoded in the distribution of potential minimum curvature as a function of potential minimum values ("minimum curvature distribution").

As yet another argument that exciton wave function statistics provides information about the correlation length of the interface disorder, we consider a different scenario of exciton localization, where negative slope is expected for the relation between XDS and localization energy. We focus on localization of excitons by ML islands in the interfaces of a QW. This type of disorder has been found for GaAs/$Al_{0.3}Ga_{0.7}$As QWs grown with growth interruption [Gro97]. For islands with diameters on the order of the exciton Bohr radius, the diamagnetic shift of a localized exciton state will be proportional to the area of the island, while the lateral confinement energy is inversely proportional to that area. The vertical confinement energy is independent of the lateral extension of an island. Therefore, there is a different relation between lateral extension of fluctuations and transition energy of localized exciton states than in the previously studied case of short-range disorder: The lowest exciton states will show the largest diamagnetic shift. As a result, negative slope in the XDS distribution of localized exciton states as a function of transition energy (Fig. 7.4) would be expected, if only ML fluctuations were present in the QW interfaces [Bar03]. The positive slope observed in our experiment therefore excludes this situation. Also note that we observe no ML splitting in the QW luminescence spectra. The energy difference corresponding to a ML fluctuation in the 2-nm QW is ~ 20 meV. [1]

Recent theoretical work supports our explanation of the positive slope in Fig. 7.4

---

[1] A one-dimensional square well model has been used to calculate single-particle ground state energies for a perfect QW. For the GaAs/$Al_{0.3}Ga_{0.7}$As band offset, the values $\Delta_e + \Delta_h = 436$ meV and $\Delta_e : \Delta_h = 65 : 35$ were used (Adachi 1994).

as a result of exciton localization by short-range correlated disorder [Gro05]. In the theoretical study, a positive correlation between XDS and transition energy of exciton states localized by a random Gaussian potential was observed. The lowest exciton states had diamagnetic coefficients of $\sim 10\,\mu\text{eV/T}^2$. The XDS showed an increase by a factor of 3 over the range of the localized exciton tail of $\sim$ 20 meV, in reasonable agreement with our experimental result. The positive correlation between XDS and transition energy enables the experimental study of exciton wave function statistics. For random disorder it was shown that the XDS is determined by the local potential only. Consequently, study of exciton wave function statistics allows the discrimination between several underlying disorder configurations.

We therefore relate the experimentally observed increase of the XDS as a function of emission energy to the interface structure of our samples. The qualitative agreement between our experimental result (Fig. 7.4) and theoretical XDS calculations for exciton localization by random Gaussian disorder [Gro05], that both show increase of the XDS as a function of transition energy, reveals that lateral confinement of the exciton states in our samples is caused by short-range interface disorder. Indeed, large-scale (160 nm) cross-sectional STM topography of the 4-nm GaAs/$\text{Al}_{0.3}\text{Ga}_{0.7}$As QW obtained in a recent study shows mainly short-range correlations on the atomic scale [Rop07].

Finally, we compare our experimental diamagnetic coefficients with theoretical results. For laterally free excitons in a 4-nm GaAs/$\text{Al}_{0.3}\text{Ga}_{0.7}$As QW (corresponding to $E = 0$ in Fig. 7.4), theoretical calculations obtained a diamagnetic coefficient $\gamma_2 = 44\,\mu\text{eV/T}^2$, assuming bulk values for the electron in-plane mass [Gro05, Wal98]. However, our experimental diamagnetic coefficient of $\sim 22\,\mu\text{eV/T}^2$ observed for the emission peak of the 4-nm QW is consistent with previous experimental studies: In all magnetoluminescence experiments of $\sim$ 5 nm wide GaAs/$\text{Al}_{0.3}\text{Ga}_{0.7}$As QWs, values of $\sim 25\,\mu\text{eV/T}^2$ have been found [Tar84, Rog86, Som95]. Previous studies attributed discrepancies between experimental and theoretical values for QW diamagnetic coefficients to exciton localization [Oss87], or to confinement-related enhancement of the exciton in-plane reduced mass [Nas89]. Since we observe the strongest reduction of the XDS for the lowest-energy exciton states several meV below the QW emission peak, exciton localization is unlikely to explain the entire difference between our experimental XDS value at the QW emission peak and theoretical values for laterally free excitons. Rather, we attribute the discrepancy to the fact that the theoretical studies did not take the enhancement of the in-plane electron mass in narrow QWs into account.

Newest calculations show that including the mass enhancement improves the agreement between our experiment and theory. In Fig. 7.9, the measured diamagnetic shift coefficient $\gamma_{2,\alpha}$ is plotted for several individual localized states as a function of state energy E_α (squares), together with the shift coefficient of the inhomogeneously broadened PL line ($\gamma_{2,tot} = 22\mu\text{eV/T}^2$, full circle). Very accurate shift coefficients could only be obtained for states well separated from the broadened PL line and by averaging over the Zeeman doublet, which poses a limit on the statistics. The large number of small dots corresponds to the calculated shift coefficients for the states in the disorder potentials simulated from the disorder parameters determined from the XSTM data. Both the absolute magnitude of the shift coefficients as well as the small increase of the coefficients with increasing state energy is reproduced by the calculations [Rop07].

As well diamagnetic shift coefficients γ_2 as effective exciton g-factors g_{ex} have been

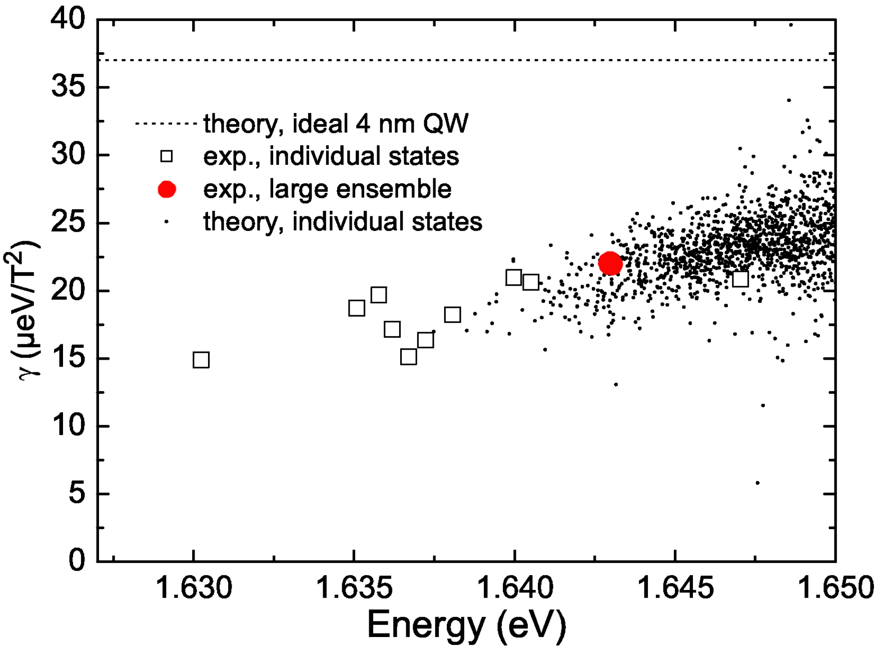

Figure 7.9: *[Rop07] Diamagnetic coefficients of single exciton states in the 4-nm GaAs/Al$_{0.3}$Ga$_{0.7}$As QW (open squares show experimental values) and shift coefficient of the broadened PL line (full circle). Results of numerical two-particle simulations including disorder and the full Coulomb-correlated electron-hole motion, based on disorder parameters determined from the XSTM experiment on the 4-nm QW, are shown as dots. The dotted line at 37 $\mu eV/T^2$ shows the no-disorder case in a 4-nm QW with perfect interfaces.*

determined for all localized exciton states in the measurements described above. The exciton g-factors of the same states as shown in Fig. 7.4 are displayed in Fig. 7.5, separately for 4-nm and 2-nm QW. The size of the exciton g-factors is comparable to values for natural quantum dot states reported by other authors [Boc97, Ste02]. The dependence of the exciton g-factor on quantum well width is mainly due to a drastic increase of the hole g-factor with decreasing QW width caused by valence-band mixing [Sne92]. With decreasing QW width, the modulus of the exciton g-factor increases (Fig. 7.5), consistent with previous results for the exciton g-factor in quantum wells [Sne92]. The confinement dependence of the effective exciton g-factor is dominated by the confinement dependence of the effective hole g-factor, g_h, which is caused by valence band-mixing. The effective electron g-factor becomes positive in narrow QW, but it is overpowered by the much stronger decrease of the negative hole g-factor [Sne92]. The influence of lateral confinement on the exciton g-factor has been studied by Kotlyar *et al.*, who considered a contribution to the g-factor that depends on the in-plane momentum of the exciton state [Kot01]. The results showed that the modulus of the g-factor of strongly localized QD excitons increases with decreasing lateral QD extension, in agreement with experimental results for QDs. The stronger lateral confinement of the low-energy exciton states deduced from the diamagnetic coefficients in our experiment would be consistent with a decrease of the exciton g-factor modulus with uncreasing emission energy (Fig. 7.5). However, no such tendency is observed in the data shown here.

7.4 Further findings

In magneto-μPL experiments on wider GaAs/Al$_{0.3}$Ga$_{0.7}$As quantum wells, features have been observed that were not found in the 2-nm and 4-nm QWs. Figure 7.10 shows μPL spectra of the 6-nm GaAs/Al$_{0.3}$Ga$_{0.7}$As QW in sample QW$_2$ in the range from $B = 0$ T to $B = 10$ T in steps of 2 T. At zero field, the spectrum shows a single peak and inhomogeneous broadening is $\sim$ 1.5 meV. With increasing field, the PL maximum shifts with $\sim 25\,\mu$eV/T^2. About 2.5 meV below the PL maximum, a second, broader peak appears. As a guide to the eye, the diamagnetic shift at the PL maximum ($25\,\mu$eV/T^2) and 2.5 meV below the maximum ($15\,\mu$eV/T^2) are shown. The gray bars mark transition energies at integer multiples of a monolayer.

Figure 7.11(a) shows the magneto-μPL spectrum of the 8-nm GaAs/Al$_{0.3}$Ga$_{0.7}$As QW in sample QW$_2$. The magnetic field was increased from $B = 0$ T to $B = 10$ T in steps of 50 mT, the emission in the energy range $1.555 - 1.568$ eV is shown. Far below the QW peak (a), transitions with linear Zeeman splitting and very large diamagnetic shift are observed that show linear shift at low B-field of $B \approx 4$ T. Since the observed shift coefficient $\gamma_2 \approx 120$ μeV/T^2 is larger than of a 1s exciton in bulk GaAs, these transitions are attributed to 2s excitons. The corresponding 1s exciton transitions are not observed. – At position (b), a transition is observed that shows eightfold splitting and the same parabolic diamagnetic shift for all eight lines.

These findings are not discussed in detail in the framework of our study of the diamagnetic shift properties of disorder-localized exciton ground states. Yet they may

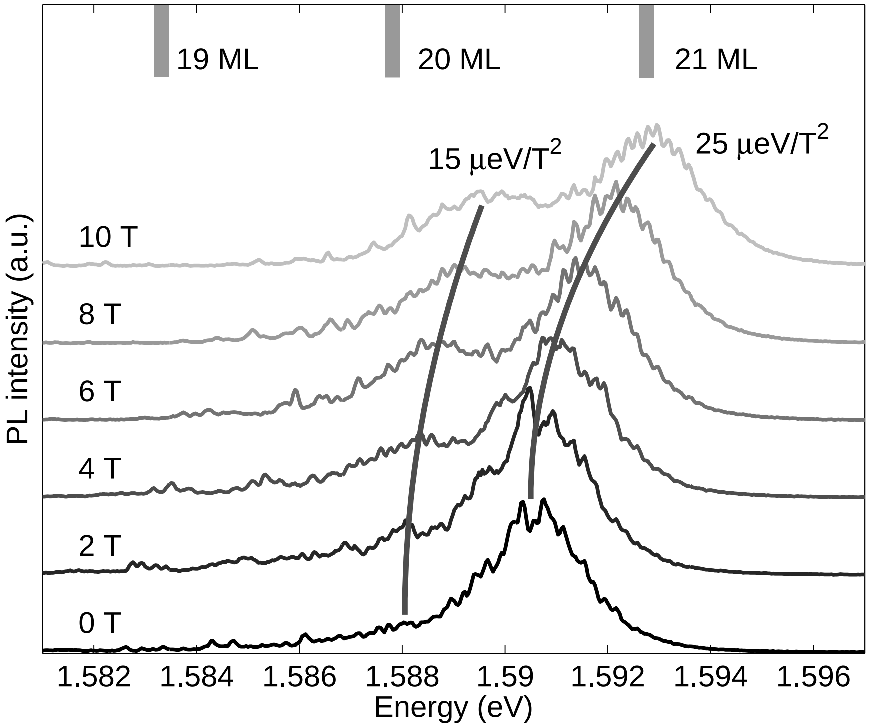

Figure 7.10: *μPL spectra of the 6-nm GaAs/Al$_{0.3}$Ga$_{0.7}$As QW in sample QW$_2$. The magnetic field has been increased from $B = 0$ T to $B = 10$ T.*

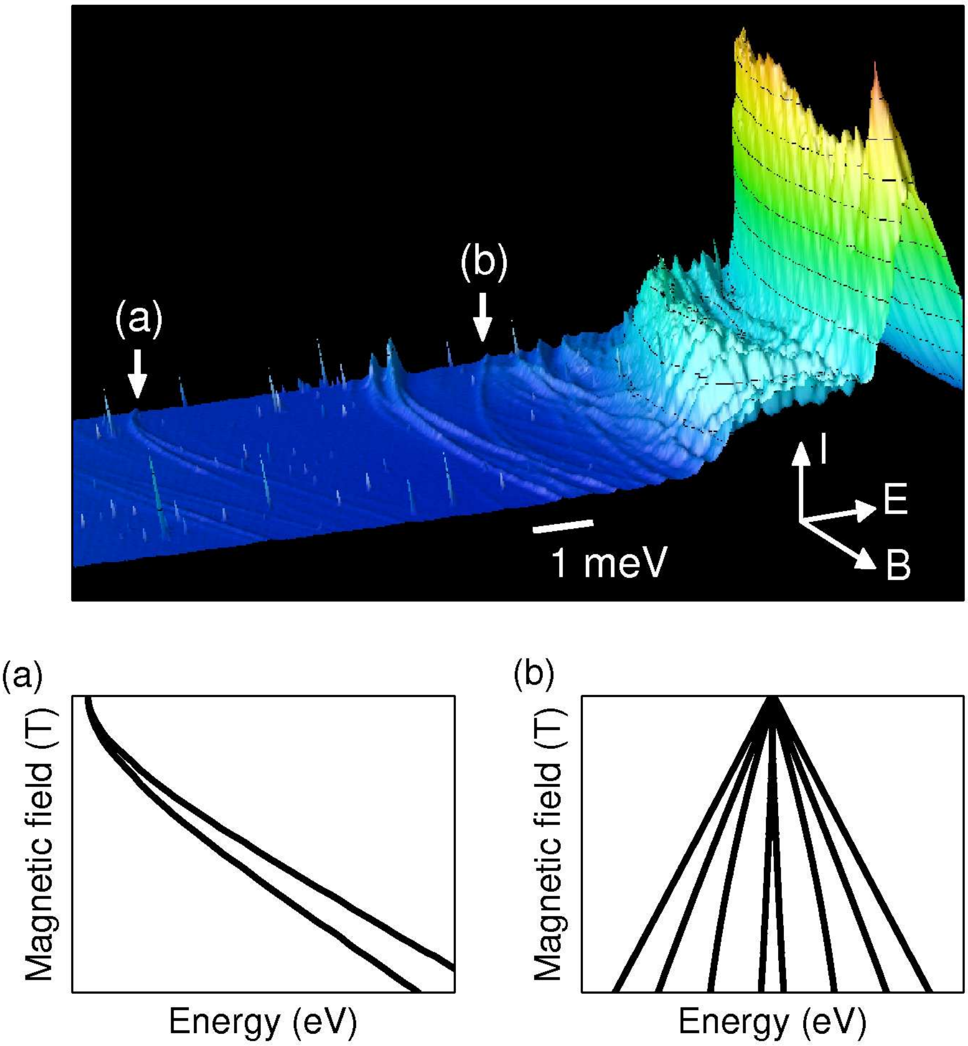

Figure 7.11: *(a) Magneto-μPL spectrum of the 8-nm GaAs/$Al_{0.3}Ga_{0.7}$As QW in sample QW_2. (b) Localized 2s exciton transition with linear Zeeman splitting. The diamagnetic coefficient $\gamma_2 = 120\,\mu eV/T^2$ is larger than the XDS of a bulk GaAs 1s exciton. The transition from quadratic to linear shift ("exciton-magnetoexciton transition") occurs at $B \approx 4$ T. (c) Eight-fold splitting of a transition; the diamagnetic shift has been removed.*

serve to demonstrate the potential of magneto-μPL spectroscopy with respect to the investigation of disorder in single quantum wells.

7.5 Conclusions

In the low-energy tail of magneto-μPL spectra of the narrow GaAs/$Al_{0.3}Ga_{0.7}$As QWs, positive slope has been observed in the diamagnetic shift distribution as a function of transition energy. A detailed qualitative discussion of this result has been given, based on the qualitative picture of the influence of lateral confinement on the exciton wave function in natural quantum dots that had been introduced in chapter 3, and assuming a simple relation between exciton radius and diamagnetic shift.

It was demonstrated in a one-dimensional model that the correlation length of the underlying disorder potential determines the potential minimum distribution, i.e., the distribution of the lateral extension of potential minima as a function of potential values. It has been made plausible that the potential minimum statistics determines the exciton wave function statistics, i.e., the distribution of exciton radii as a function of transition energy. This suggests that the correlation length of the underlying disorder potential determines the slope in the diamagnetic shift distribution. Thus, the concepts and models that have been introduced allow a qualitative understanding of the slope in the diamagnetic shift distribution in the low-energy tail of magneto-μPL spectra.

Due to the complexity of the problem of exciton disorder-localization, the introduced models do, however, not allow a quantitative prediction of the slope in the diamagnetic shift distribution. For example, one-dimensional models are not suitable for quantitative predictions of diamagnetic coefficients because of the different effect of averaging of the exciton over underlying disorder in one and two dimensions. Furthermore, the assumption of the simple relation between diamagnetic shift coefficient and exciton radius [Eq. 7.3] is not exactly valid in presence of disorder [Gro05]. This fact will be discussed in the next chapter. – As a consequence, numerical two-particle calculations in the framework of the theory of exciton disorder-localization provide the only way of an accurate prediction of the diamagnetic shift distribution.

A quantitative comparison of experimental diamagnetic coefficients with theoretical values showed that the effect of in-plane electron mass enhancement in narrow QWs significantly affects the diamagnetic coefficients of exciton states. The in-plane electron mass enhancement in narrow QWs had not been taken into account in previous theoretical studies. Including the enhanced in-plane electron mass, and extending the comparison of simulated and experimental μPL spectra of the 4-nm GaAs/Al$_{0.3}$Ga$_{0.7}$As QW, two-particle calculations on the basis of XSTM data have shown good agreement between theoretical and experimental shift coefficients. The size of diamagnetic coefficients and the slope in the shift distribution are well reproduced by theoretical calculations based on in-plane disorder with isotropic exponential correlations with 0.4 nm correlation length and the disorder strength determined from the XSTM data. This result is further evidence that mainly short-range correlated disorder on a length scale of a few lattice constants is responsible for exciton localization in the 4-nm GaAs/Al$_{0.3}$Ga$_{0.7}$As quantum well.

References

[Aki67] O. Akimoto and H. Hasegawa, *Interband optical transitions in extremely anisotropic semiconductors - 2. Coexistence of exciton and Landau levels*, *J. Phys. Soc. Jpn.* 22, 181 (1967).

[Bar03] Z. Barticevic, M. Pacheco, C. A. Duque, and L. E. Oliveira, *Magnetic-field effects on excitons trapped in quantum dots/interface defects in narrow quantum wells*, *Phys. Rev. B* 68, (2003).

[Bay98] M. Bayer, S. N. Walck, T. L. Reinecke, and A. Forchel, *Exciton binding energies and diamagnetic shifts in semiconductor quantum wires and quantum dots*, *Phys. Rev. B* 57, 6584 (1998).

[Boc97] U. Bockelmann, W. Heller, and G. Abstreiter, *Microphotoluminescence studies of single quantum dots - 2. Magnetic-field experiments*, *Phys. Rev. B* 55, 4469 (1997).

[Gro05] M. Grochol, F. Grosse, and R. Zimmermann, *Exciton wave function properties probed by diamagnetic shift in disordered quantum wells*, *Phys. Rev. B* 71, 125339 (2005).

[Gro97] R. Grousson, V. Voliotis, N. Grandjean, J. Massies, M. Leroux, and C. Deparis, *Microroughness and exciton localization in (Al,Ga)As/GaAs quantum wells*, *Phys. Rev. B* 55, 5253 (1997).

[Gur94] M. Gurioli, A. Vinattieri, J. Martinez-Pastor, and M. Colocci, *Exciton thermalization in quantum-well structures*, *Phys. Rev. B* 50, 11817 (1994).

[Hau04] H. Haug and S. W. Koch, *Optical and electronic properties of semiconductor heterostructures*, World Scientific, 2004.

[Hes94] H. F. Hess, E. Betzig, T. D. Harris, L. N. Pfeiffer, and K. W. West, *Near-field spectroscopy of the quantum constituents of a luminescent system*, *Science* 264, 1740 (1994).

[Kot01] R. Kotlyar, T. L. Reinecke, M. Bayer, and A. Forchel, *Zeeman spin splittings in semiconductor nanostructures*, *Phys. Rev. B* 6308, 85310 (2001).

[Lif88] I. M. Lifshitz, S. A. Gredeskul, and L. A. Pastur, *Introduction to the theory of disordered systems*, Wiley, New York, 1988.

[Nas89] K. J. Nash, M. S. Skolnick, P. A. Claxton, and J. S. Roberts, *Diamagnetism as a probe of exciton localization in quantum wells*, *Phys. Rev. B* 39, 10943 (1989).

[Oss87] W. Ossau, B. Jäkel, and E. Bangert, in *High Magnetic Fields in Semiconductor Physics*, Springer Verlag, Berlin, 1987, vol. 71 of *Springer Series in Solid State Sciences*, p. 213ff.

[Phi03] R. T. Phillips, A. G. Steffan, S. R. Newton, T. L. Reinecke, and R. Kotlyar, *Exciton fine structure in interfacial quantum dots*, *phys. stat. sol. b* 238, 601 (2003).

[Rog86] D. C. Rogers, J. Singleton, R. J. Nicholas, C. T. Foxon, and K. Woodbridge, *Magnetooptics in GaAs-Ga$_{1-x}$Al$_x$As quantum wells*, *Phys. Rev. B* 34, 4002 (1986).

[Rop07] C. Ropers, M. Wenderoth, L. Winking, T. C. G. Reusch, M. Erdmann, R. G. Ulbrich, M. Grochol, F. Grosse, R. Zimmermann, S. Malzer, and G. H. Döhler, *Atomic scale structure and optical emission of AlGaAs/GaAs quantum wells*, Phys. Rev. B (2007).

[Run02] E. Runge, *Excitons in semiconductor nanostructures*, *Adv Solid State Phys* 57, 149 (2002).

[Sch05] N. Schildermans, M. Hayne, V. V. Moshchalkov, A. Rastelli, and O. G. Schmidt, *Nonparabolic band effects in GaAs/*$Al_xGa_{1-x}As$ *quantum dots and ultrathin quantum wells*, *Phys. Rev. B* 72, 115312 (2005).

[Sne92] M. J. Snelling, E. Blackwood, C. J. Mcdonagh, R. T. Harley, and C. T. B. Foxon, *Exciton, heavy-hole, and electron g-factors in type-I GaAs/*$Al_xGa_{1-x}As$ *quantum wells*, *Phys. Rev. B* 45, 3922 (1992).

[Som95] T. Someya, H. Akiyama, and H. Sakaki, *Laterally squeezed excitonic wavefunction in quantum wires*, *Phys. Rev. Lett.* 74, 3664 (1995).

[Ste02] A. G. Steffan and R. T. Phillips, *Exciton g-factors, diamagnetic shifts, and exchange splittings in quantum dots in GaAs quantum wells*, *phys. stat. sol. a* 190, 541 (2002).

[Ste03] A. G. Steffan and R. T. Phillips, *Two different types of 'natural' quantum dots in narrow GaAs/AlGaAs QWs*, *Physica E* 17, 15 (2003).

[Tar84] S. Tarucha, H. Okamoto, Y. Iwasa, and N. Miura, *Exciton binding energy in GaAs quantum wells deduced from magnetooptical absorption measurement*, *Solid State Commun.* 52, 815 (1984).

[Wal98] S. N. Walck and T. L. Reinecke, *Exciton diamagnetic shift in semiconductor nanostructures*, *Phys. Rev. B* 57, 9088 (1998).

Chapter 8

Negative diamagnetic shift in a GaAs/AlAs DQW

In the previous chapter, a simple model of the exciton diamagnetic shift neglecting disorder was used for the interpretation of XDS coefficients of natural quantum dots in GaAs/$Al_{0.3}Ga_{0.7}As$ single quantum wells. In this model, the XDS is always positive and proportional to the area of the exciton relative wave function. The situation is more difficult in the presence of disorder. In the framework of the theory of exciton disorder-localization, a negative contribution to the XDS of disorder-localized excitons has been observed recently, and the question was posed if also negative diamagnetic coefficients could occur for exciton ground states [Gro05].

This chapter presents magneto-μPL measurements on a GaAs/AlAs double quantum well consisting of two 4-nm GaAs wells separated by a 2-nm AlAs barrier (sample QW_3). In a region of the 4-nm GaAs/AlAs DQW sample showing signatures of strong disorder, some low-energy transitions with negative diamagnetic coefficients have been observed. The data represent the first clear-cut evidence of negative diamagnetic coefficients of localized excitonic transitions in a semiconductor heterostructure. Simultaneously to the negative shift, complicated B-field patterns are observed at the low-energy end of the spectral emission region below the DQW peak. To the best of our knowledge, similar line patterns in magneto-μPL spectra have not been reported.

In the first section, the experimental results are described. The second section discusses the origin of the observed negative diamagnetic coefficients and the complex magnetic-field patterns. Recent theoretical investigations, stimulated by our experimental observation of negative diamagnetic coefficients, arrived at the result that negative shift does not occur for exciton ground states under rather general circumstances [Mul06]. Nevertheless, we discuss a simple model that suggested that the combination of disorder and the influence of the magnetic field on the exciton wave function could account for the negative shift. Subsequently, the question is discussed if the observed negative diamagnetic coefficients and the complex magnetic-field patterns are related to charged exciton transitions.

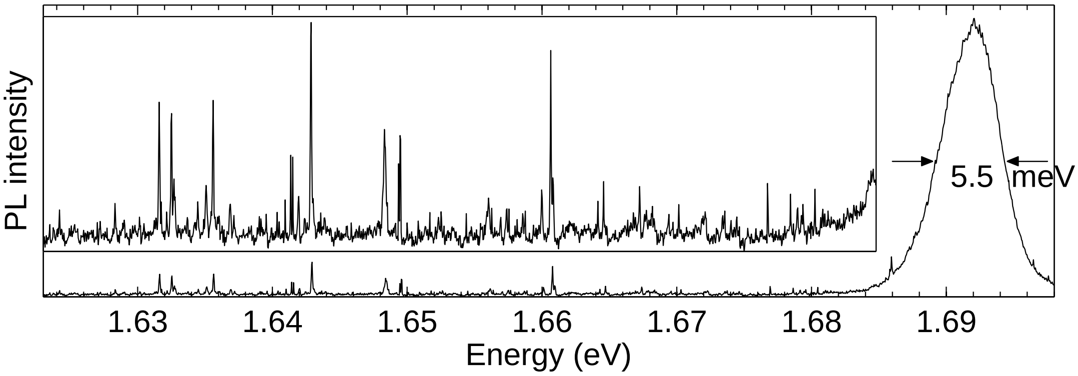

Figure 8.1: *Spatially integrated luminescence of the studied region of the GaAs/AlAs DQW from an area of* 4×15 *μm^2 ($T = 3$ K, $I \sim 1\,\mu W$). The inset zooms into the low-energy tail of the luminescence spectrum. The lowest transitions are found* ~ 70 *meV below the DQW emission peak.*

8.1 Experimental results

The spatially integrated emission of the DQW heterostructure from a 4×15 μm^2 large region is shown in Fig. 8.1. The sample temperature was $T = 3$ K. The sample was optically excited by a cw argon laser (514 nm, linearly polarized) with a total power of $\sim 1\,\mu$W. The luminescence is attributed to $E_0^\Gamma - HH_0$ transitions [Moo88]. Below the DQW emission peak, many spectrally narrow emission lines are observed, that are tentatively attributed to localized exciton transitions. The occurrence of many low-energy emission lines down to 70 meV below the center of the DQW emission peak at 1.69 eV is interpreted as a signature of strong interface disorder in the studied DQW region.

To estimate the strength of the involved interface fluctuations, single-particle confinement energies have been calculated for symmetric double square well structures with varying widths of the wells and the central barrier. For GaAs/AlAs band offset and offset ratio, the values $\Delta = 1.58$ eV and $f_e/f_h = 0.65/0.35$ have been used [Ada94]. Figure 8.2 gives a quick overview of the influence of variation of well and central barrier width on the transition energy. For simplicity, well and barrier widths have been varied independently, and a variation of the exciton binding energy has been neglected. The isoenergy lines in the plane of well width and central barrier width are shown. Since the energy of localized transitions is still increased by lateral confinement energy, transitions as low as 1.63 eV require a combination of local increase in well width by several monolayers and a strong reduction, or even local perforation, of the central barrier.

Before the results of the magneto-μPL experiments are shown and discussed, some words to the electronic structure of the double well heterostructure are necessary. Figure 8.3 shows the band edges in a symmetric 4-nm GaAs/AlAs DQW with 2-nm central AlAs barrier. The conduction band edge at the center of the Brillouin zone (Γ) is shown as solid line. Since AlAs has an indirect band gap, also the conduction band edge at the X-point of the Brillouin zone is shown as a dashed line. In addition, the energy of the lowest electron state in the GaAs wells is indicated by the dash-dotted lines.

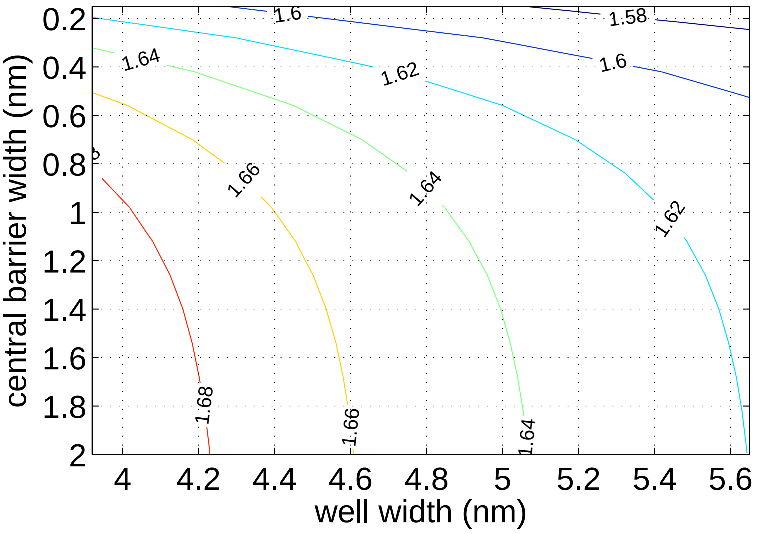

Figure 8.2: *Ground state exciton transition energy in a symmetric GaAs/AlAs double square well with central AlAs barrier. Lines of constant energy are shown under variation of well width and central barrier width.*

While the conduction band offsets at Γ cause exciton localization in the GaAs wells, the conduction band offsets at X lead to localized electron states in the central AlAs barrier. Figure 8.3 shows that the width of the GaAs wells is large enough to prevent the formation of a type-II ground state: The lowest electron state in the GaAs wells lies below the conduction band minimum at X in the AlAs barrier ($E^X_{\mathrm{c,AlAs}}$). Type-II ground states occur for GaAs wells narrower than 3.5 nm; then the E^Γ_0 ground state in the wells is pushed above the E^X_0 ground state in the AlAs barrier [Moo88].

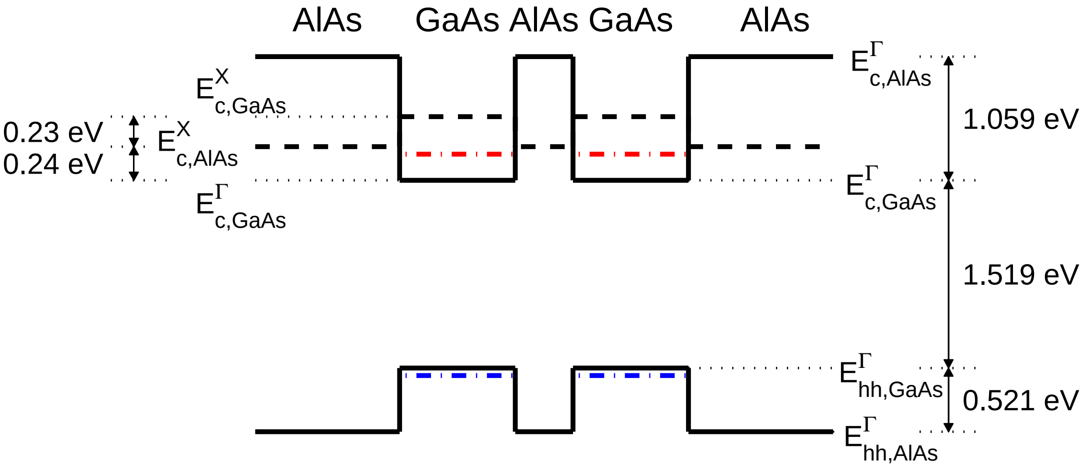

Figure 8.3: *Band edges in a GaAs/AlAs double quantum well heterostructure. Solid lines represent conduction and valence band edges of the bulk material at Γ; dashed lines represent the conduction band edge at the X-point. A band offset ratio $f_e/f_h =$ 0.65/0.35 is assumed. Confinement energies of the lowest Γ electron state and the lowest hole state are shown dash-dotted.*

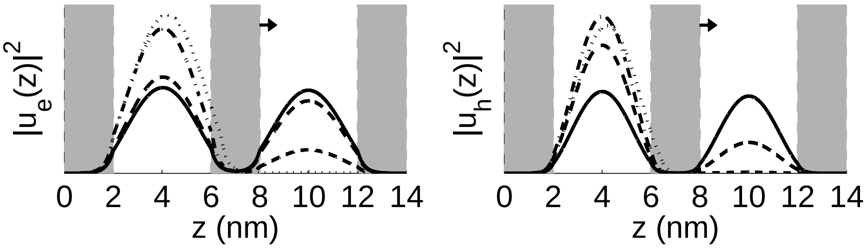

Figure 8.4: *Well asymmetry dependence of the ground state z wave functions in a GaAs/AlAs double quantum well. The solid lines show electron (e) and heavy-hole (h) ground state wave functions in a symmetric DQW. The effect of a displacement of the central barrier by 0.1, 1, and 10 % of the well width is shown: The wave function amplitude in the narrower well is strongly suppressed.*

In a symmetric type-I DQW, where two quantum wells are separated by a narrow tunneling barrier, the single-particle ground state has the same symmetry as the heterostructure. In the symmetric ground state, the probability for the electron to be in either one of the wells is identical, and the ground state wave function has a local minimum in the central barrier. In a perfectly symmetric DQW, the single-particle ground state z wave functions are either symmetric or antisymmetric. In the symmetric ground state, the probability for the electron to be in either one of the wells is identical, and the ground state wave function has a local minimum in the central barrier (Fig. 8.4). The first excited state is antisymmetric and its wave function has a node in the center of the tunneling barrier. Asymmetry of the wells leads to a mixing of symmetric and antisymmetric states; even a slight asymmetry has drastic effects on the ground state wave functions [Gal89]. As shown in Fig. 8.4, already a displacement of the central barrier by 1 % of the well width strongly suppresses the wave function amplitude in the narrower well.

In a real heterostructure, deviations from the ideal structure always introduce slight asymmetry. Therefore, interface fluctuations in the DQW cause a prevalence of localized excciton states in the locally wider well. We therefore suggest that local well width fluctuations, in combination with the relatively weak coupling between the wells, preferrably lead to the formation of quantum well dot (QWD) exciton states in one of the wells. Therefore, within the scope of the discussion of our experimental results the simple picture of an exciton localized in a two-dimensional disorder potential will be tentatively used in the following paragraphs. Specifically, it is – again tentatively – assumed that a B-field normal to the QW planes does not change the z-symmetry of a local exciton ground state. We will therefore relate the diamagnetic shift of localized exciton states in the DQW to the structure of the local lateral disorder potential for the moment.

Magneto-μPL experiments

Two magneto-μPL spectra from the strong-disorder region, taken at positions separated by a few μm, are shown in Fig 8.6. The spectra were taken at $T = 3$ K and under low excitation conditions ($I \sim 1\,\mu$W). The B-field was increased in steps of 50 mT from $B = 0$ T to $B = 10$ T. In the region of the DQW emission peak at $E = 1.69$ eV, the positive quadratic diamagnetic shift of all transitions is cleary observed. At the DQW peak, exciton states have diamagnetic coefficients of $\sim 17\,\mu$eV/T^2. In the energy region down to 70 meV below the DQW emission peak, spectrally narrow emission lines of localized exciton states are observed. Below $\sim$ 1.64 eV, deviations from the positive quadratic B-field shift are found. Figure 8.5(b) shows that also negative value occur in the distribution of diamagnetic coefficients.

The diamagnetic shift coefficients of $\sim 17\,\mu$eV/T^2 at the DQW emission peak are significantly smaller than, e.g., in a 4-nm GaAs/Al$_{0.3}$Ga$_{0.7}$As quantum well, where shift coefficients $\gamma_2 \sim 25\,\mu$eV/T^2 have been found [Tar84, Rog86, Som95, Erd06]. This is consistent with the fact that the exciton binding energy in a GaAs/AlAs QW is larger than in a GaAs/Al$_{0.3}$Ga$_{0.7}$As QW of the same width, which is caused by the combination of conduction band nonparabolicity and the dieelectric mismatch between GaAs and AlAs [And90]. For a perfect 4-nm GaAs/AlAs QW, Andreani *et al.* obtained an exciton binding energy $E_b = 17$ meV. From the conduction band nonparabolicity in GaAs, an effective in-plane electron mass $m_e = 0.9$ m$_0$ was determined. Here, this value for the effective in-plane electron mass and the in-plane heavy-hole mass $m = 0.23$ m$_0$ are to used to calculate the exciton Bohr radius corresponding to the shift coefficient $\gamma_2 = 17\,\mu$eV/T^2 from the relation $\gamma_2 = \frac{3}{16}\frac{e^2}{\mu}a_B^2$. As a result, the lateral Bohr radius $a_B \approx 6$ nm is found.

For most emission lines below the DQW peak, the Zeeman split components can be followed over the complete B-field range $B = 0 - 10$ T. Small linear Zeeman splitting is observed, corresponding to an exciton g-factor $|g_{ex}| \approx 1$ [Sne92]. The average of the observed exciton g-factors is smaller than in the 4-nm GaAs/Al$_{0.3}$Ga$_{0.7}$As QW, where the average value $|\bar{g}_{ex}| = 1.4$ has been found.

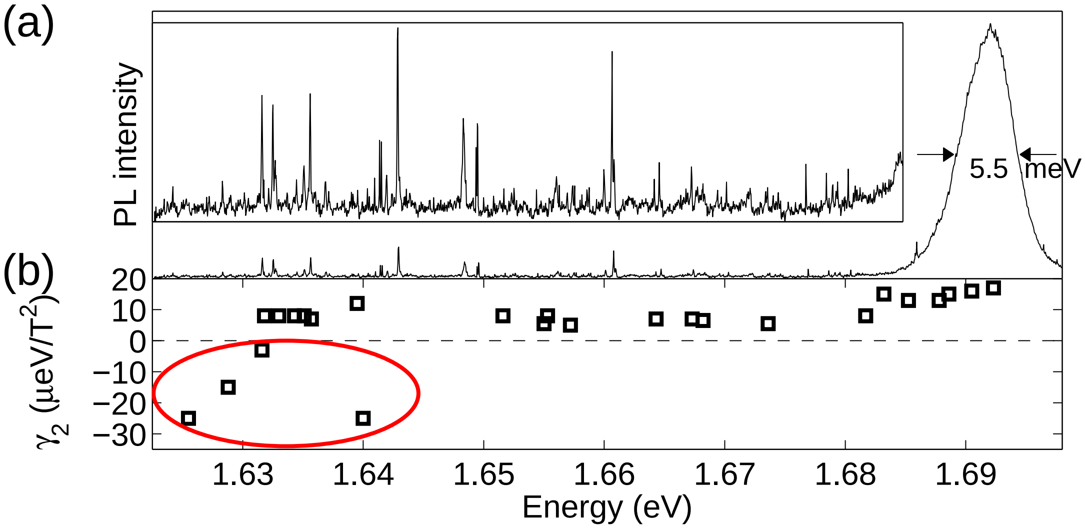

Figure 8.5: *(a) Spatially integrated luminescence of the studied region of the GaAs/AlAs DQW from an area of* 4×15 μm^2*. The inset zooms into the low-energy tail of the luminescence spectrum. The lowest exciton states are found* $\sim$ *70 meV below DQW emission peak. (b) Diamagnetic coefficients of localized exciton states as a function of transition energy. Between 50 and 65 meV below the DQW peak, negative diamagnetic coefficients are observed.*

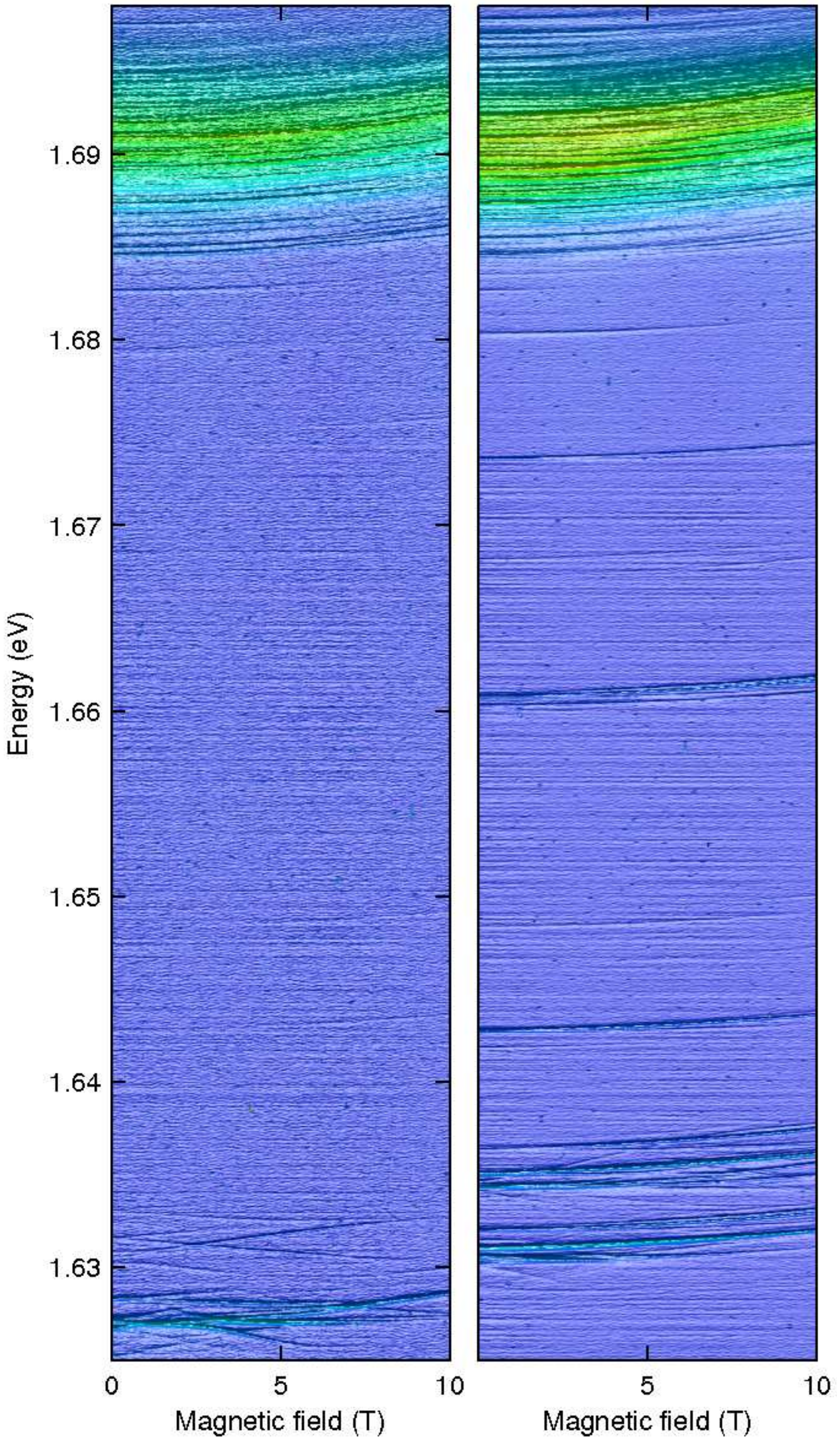

Figure 8.6: *Magneto-µPL spectra of the 4-nm GaAs/AlAs DQW at two different spatial positions some µm apart. Energy is specified relative to the DQW emission peak at 1.69 eV. The magnetic field was increased in steps of 50 mT.*

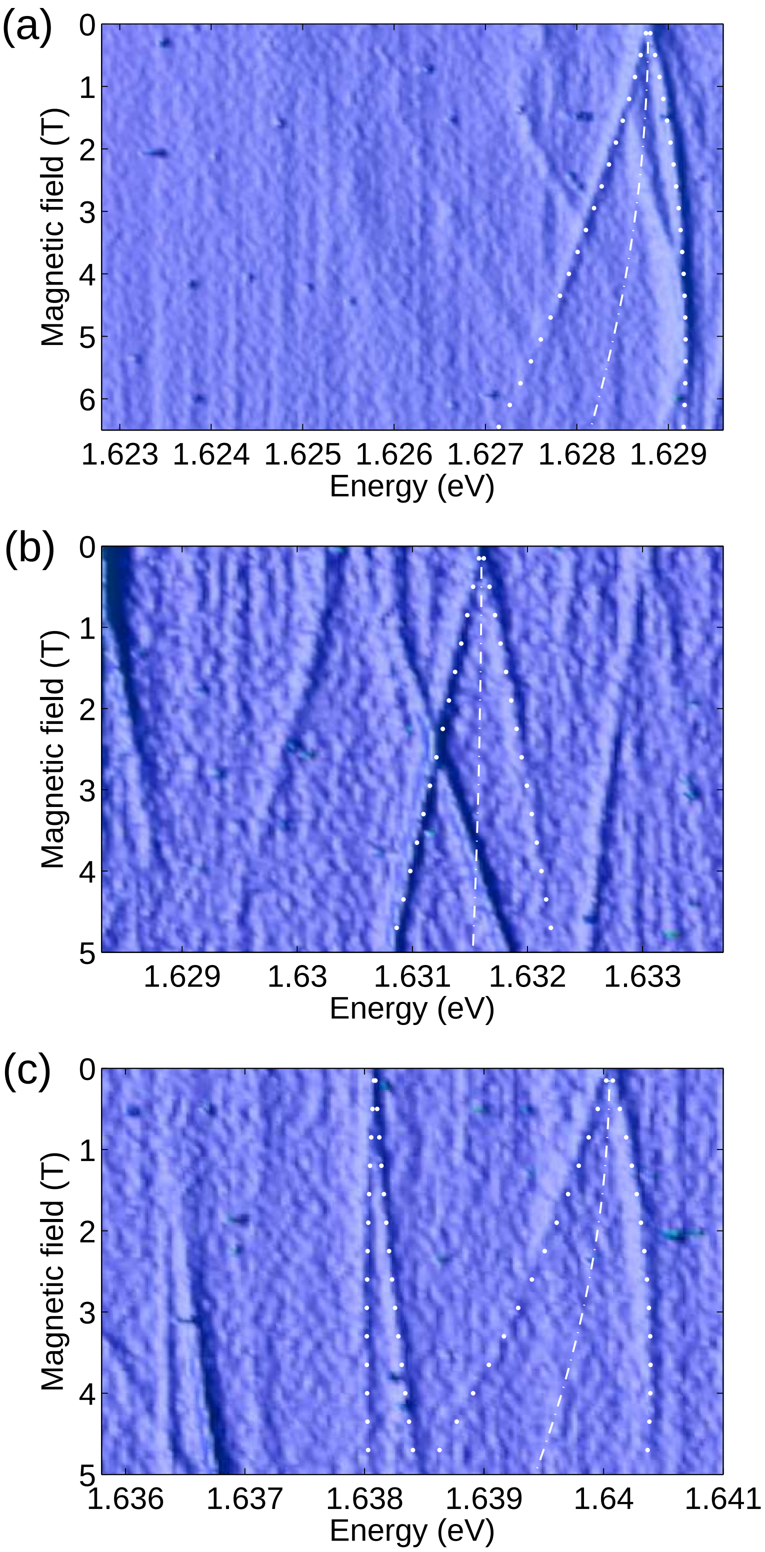

Figure 8.7: *Magneto-μPL spectra in the low-energy tail of the emission spectrum showing exciton states with negative diamagnetic coefficients. The emission lines with negative shift are fitted by* $\Delta(B)_\pm = \gamma_2 \cdot B^2 \pm g_{ex}B$ *using the fit parameters: (a)* $\gamma_2 = -15\,\mu eV/T^2$, $|g_{ex}| = 5.5$, *(b)* $\gamma_2 = -3\,\mu eV/T^2$, $|g_{ex}| = 5$, *(c)* $\gamma_2 = -25\,\mu eV/T^2$, $|g_{ex}| = 6.5$.

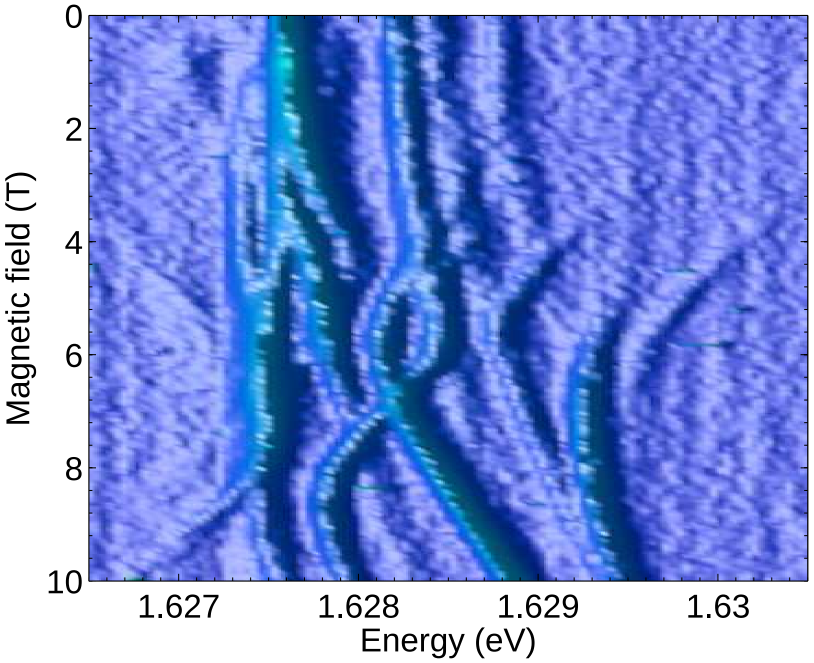

Figure 8.8: *Magneto-μPL spectrum of the low-energy end of the spectral emission region below the DQW peak. Complicated shifts, line crossings and anticrossings, and emerging lines as a function of increasing magnetic field.*

At energies above ~ 1.64 eV, all transitions show simple, linear Zeeman splitting and positive, quadratic diamagnetic shift. Below ~ 1.64 eV, also different behaviour is observed. Figure 8.7 shows emission lines with negative XDS coefficients and clearly resolved linear Zeeman splitting in the energy range between 1.62 eV and 1.64 eV at three different spatial positions. The magnetic field-dependence of the Zeeman components can be followed in the B-field range up to ~ 5 T. In Fig. 8.7, the Zeeman components of the three transitions with negative shift coefficients are marked by white dots. The exciton doublets are well fitted by $\Delta(B)_{\pm} = \gamma_2 \cdot B^2 \pm g_{ex}B$, using the fit parameters (a) $\gamma_2 = -15\,\mu\text{eV/T}^2$, $|g_{ex}| = 5.5$, (b) $\gamma_2 = -3\,\mu\text{eV/T}^2$, $|g_{ex}| = 5$, (c) $\gamma_2 = -25\,\mu\text{eV/T}^2$, $|g_{ex}| = 6.5$. The precision of the diamagnetic coefficients is 1 μeV/T^2, the g-factors have been determined with an accuracy of $\pm\,0.2$. Figure also shows an emission line with positive shift coefficient $\gamma_2 = 5\,\mu\text{eV/T}^2$ and exciton g-factor $|g_{ex}| = 1.4$ about 2 meV below the transition with negative diamagnetic coefficient.

Figure 8.8 shows the B-field dependence of some emission lines at the very low-energy end of the spectral emission region below the DQW emission peak. We observe complicated shifts, crossings and anticrossings, and both emerging and vanishing lines. At $B \approx 5.5$ T, an anticrossing between two lines at $E \approx 1.6287$ eV is visible in Fig. 8.8; at $E \approx 1.628$ eV and $B \approx 7$ T, a crossing is observed. A line visible at $E \approx 1.629$ eV at low magnetic field is no longer observed at $B > 4$ T; at $E \approx 1.6295$ eV and $B \approx 6$ T, another line becomes visible that is not observed at lower field strength.

In total four transitions with negative diamagnetic coefficients have been observed at spatial positions separated by some μm. All lines with negative coefficients are very weak, especially the energetically lowest transition at 1.6254 eV, which is not shown in

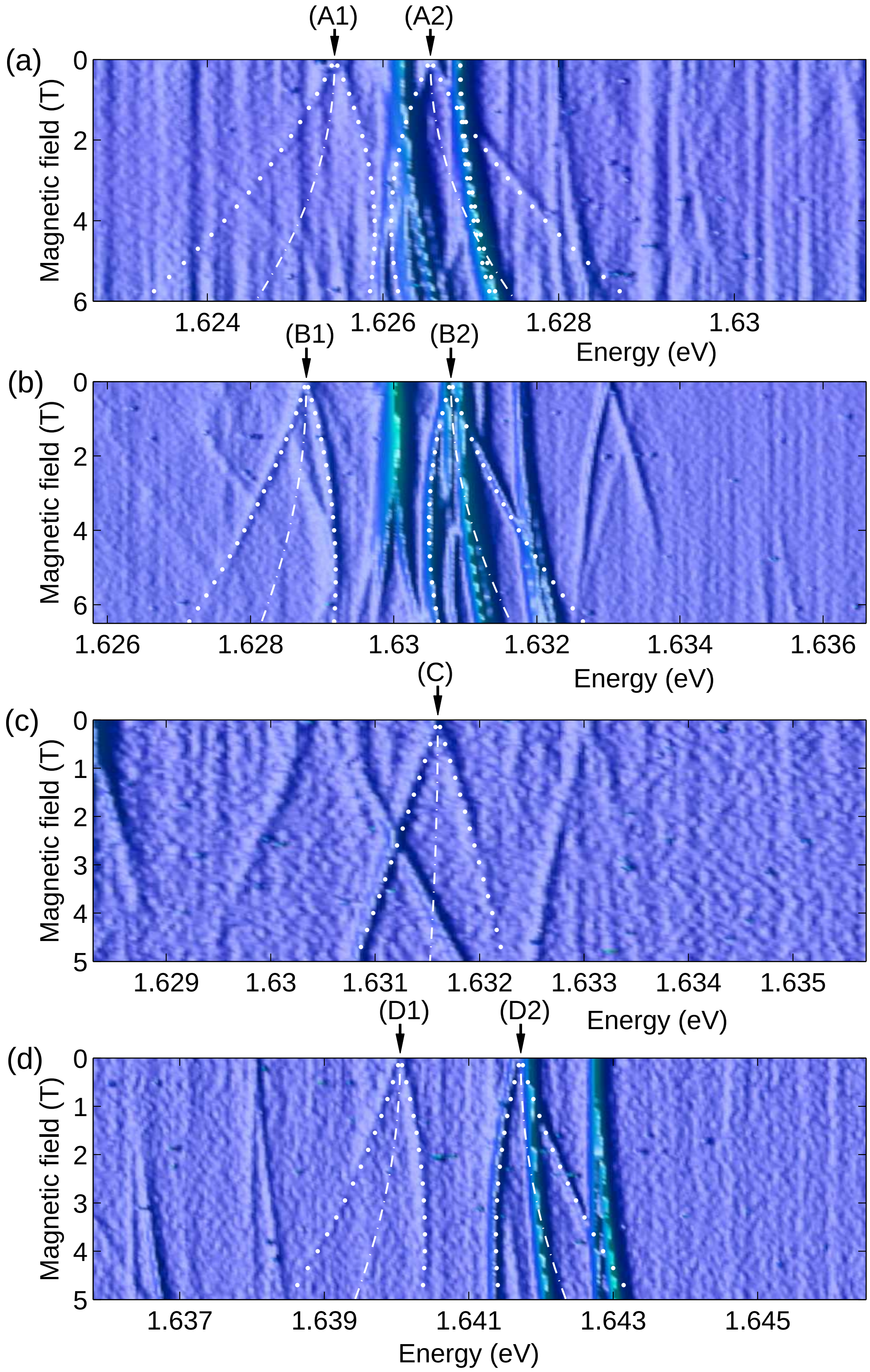

Figure 8.9: *Magneto-μPL spectra at four different spatial positions. Zeeman components of the transitions with negative diamagnetic coefficients are marked by white dots; the mean value of the Zeeman components is marked by a dash-dotted line. In (a), (b) and (d), pairs of transitions with approximately equal negative and positive diamagnetic coefficients and large Zeeman splitting are observed. Zeeman components of the corresponding transitions with positive curvature are marked by white dots, too.*

Fig. 8.7. The intensity of these transitions is close to the noise level of the CCD.

All four negative-curvature lines are shown in Fig. 8.9 together with additional lines that appear in close vicinity to the negative-shift transitions at slightly higher energy. In what follows, the transitions with negative curvature in Fig. 8.9(a)-(d) will be referred to by “A” to “D”.

The lowest-energy negative-curvature transition in Fig. 8.9(a) (line “A1”) is especially weak. Close inspection of the magnetoluminescence data allows to follow the Zeeman components in Fig. 8.9(a) up to about $B = 4.5$ T. The Zeeman splitting is extremely large with an effective exciton g-factor modulus $|g_{ex}| = 7.5 \pm 0.2$. The diamagnetic shift of the mean value of the Zeeman doublet is to a good approximation parabolic with a shift coefficient $\gamma_2 = -25 \pm 1$ μeV/T^2. At close inspection of the magneto-μPL spectrum, an additional weak transition (“A2”) is observed at 1.6265 eV ($B = 0$ T) with almost the same extremely large g-factor ($|g_{ex}| = 7.7 \pm 0.2$) as transition “A1” and diamagnetic coefficient $\gamma_2 = +27 \pm 1$ μeV/T^2. Some meV above “A1”, a pair of stronger lines is observed: The line at $\sim$ 1.626 eV shifts with $\gamma_2 \approx 7$ μeV/T^2 and displays small Zeeman splitting ($|g_{ex}| = 0.7 \pm 0.1$). A possible Zeeman splitting of the emission line at $\sim$ 1.627 eV can not be resolved; the corresponding exciton g-factor is on the order of or smaller than $|g_{ex}| = 0.1$.

Figure 8.9(b) shows the second-lowest transition with negative curvature at $\sim$ 1.629 eV (“B1”). With increasing B-field, it shifts to lower energy with diamagnetic coefficient $\gamma_2 = -15 \pm 1$ μeV/T^2. The linear Zeeman splitting is described by $|g_{ex}| = 5.5 \pm 0.2$. In a $\sim$ 4 meV wide spectral region above “B1”, several lines with strongly differing shift- and splitting-patterns are observed. The transition at $\sim$ 1.63 eV displays zero magnetic shift and small, nonlinear splitting with increasing magnetic field. This line has slightly larger full halfwidth (200 μeV) than the other strong lines in Fig. 8.9(b). Line “B2” shifts to higher energy with $\gamma_2 = +20 \pm 1$ μeV/T^2. Like in transition “B1”, the Zeeman splitting is described by an exciton g-factor $|g_{ex}| = 5.5 \pm 0.2$. At zero magnetic field, the line “B2” is surrounded by two lines with small positive shift and unresolved Zeeman splitting. The lower line shifts with $\gamma_2 = 3 \pm 1$ μeV/T^2, the higher line with $\gamma_2 = 8 \pm 1$ μeV/T^2. At about 1 meV higher energy, another line with shift coefficient $\gamma_2 = 8 \pm 1$ μeV/T^2 and unresolved Zeeman splitting ($|g_{ex}| < 0.2$) is observed.

In contrast to the patterns in Fig. 8.9(a) and (b), no strong lines are observed in the direct vicinity of the negative-curvature line “C” in Fig. 8.9(c). The shift coefficient of this line is $\gamma_2 = -3 \pm 1$ μeV/T^2, the Zeeman splitting is described by $|g_{ex}| = 5 \pm 0.2$. About one meV below this line, two weak lines are observed. The splitting pattern resembles that of a “dark exciton” transition with large fine-structure splitting; however, the splitting observed here is extremely large ($\Delta E = 0.6$ meV). The mean value of these two weak lines displays the same diamagnetic shift as line “C”, $\gamma_2 = -3 \pm 1$ μeV/T^2. The magnetic-field behavior of the transition at 1.633 eV, about 1.5 meV above “C”, can not be determined, because only one of two Zeeman components can be followed with sufficient precision.

Finally, Figure 8.9(d) shows line “D1” with negative diamagnetic coefficient $\gamma_2 = -25 \pm 1$ μeV/T^2 and exciton g-factor modulus $|g_{ex}| = 6.5 \pm 0.2$. About 2 meV below line “D1”, a transition with small positive shift coefficient $\gamma_2 = 5 \pm 1$ μeV/T^2 and small Zeeman splitting ($|g_{ex}| = 1.4 \pm 0.1$) is observed. Above “D1”, a pattern consisting of one line

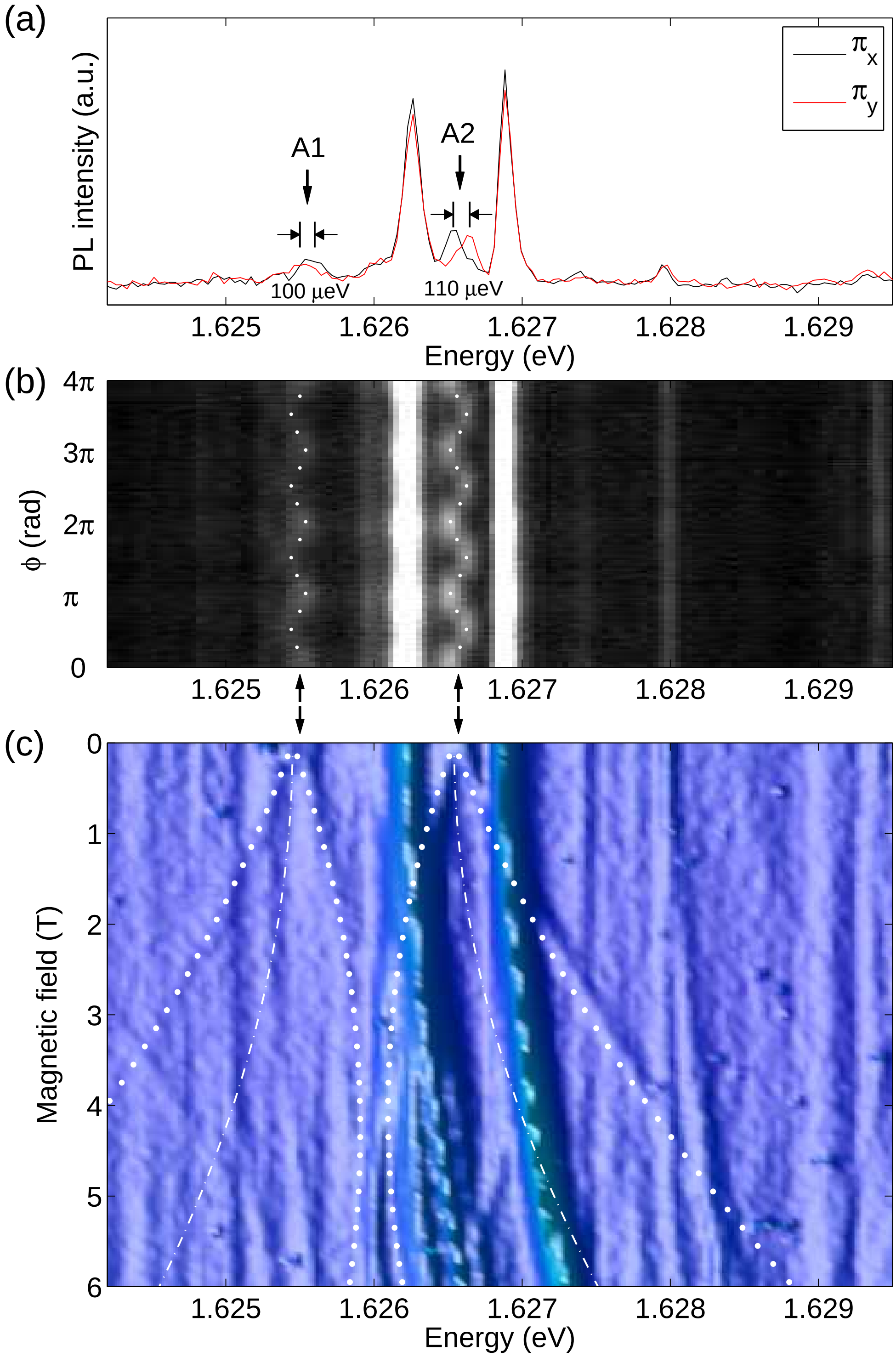

Figure 8.10: *(a) Linearly polarized emission of the transitions shown in Fig. 8.9(a), and (b) polarization angle scan, (c) magnetic-field dependence of the same transitions.*

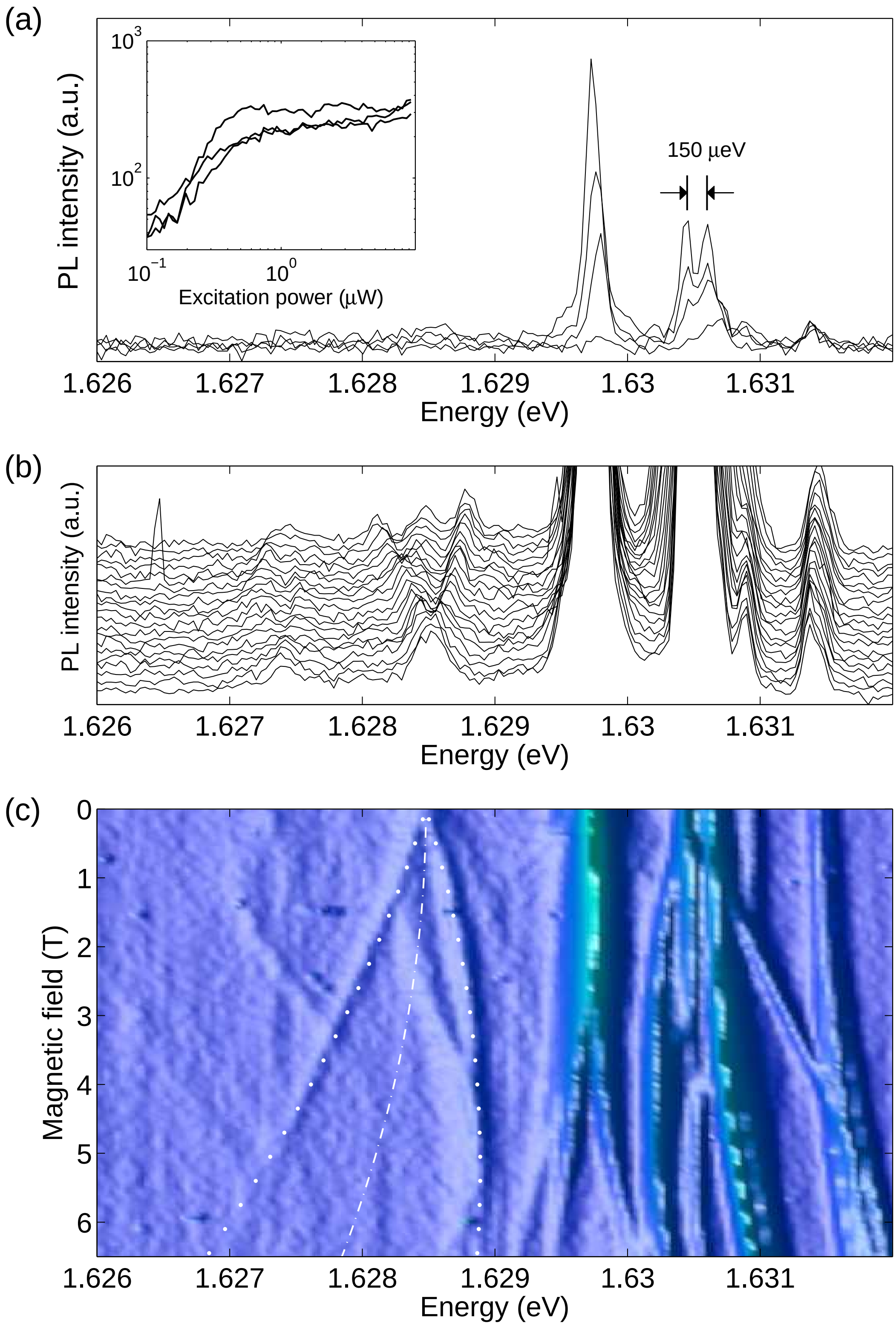

Figure 8.11: *(a) Excitation power dependence and (b), (c) magnetic field dependence of the transitions shown in Fig. 8.9(b).*

with large shift and large Zeeman splitting ($\gamma_2 = 25 \pm 1\ \mu\text{eV/T}^2$, $|g_{ex}| = 6.5 \pm 0.2$) and two lines with unresolved Zeeman splitting and smaller shift is observed, somewhat similar to the patterns that are found in Fig. 8.9(a) and (b).

Additional information about transitions “A1” and “A2” has been obtained from differential polarization spectroscopy by varying the linear polarization state of excitation and detection simultaneously. Figure 8.10(a) shows a polarization-angle scan of the zero-field spectrum in Fig. 8.9(a). The fine-structure splitting of transitions “A1” ($\Delta E = 100 \pm 10\,\mu\text{eV}$) and “A2” ($\Delta E = 110 \pm 10\,\mu\text{eV}$) is clearly observed in the oscillation of the sum of the non-resolved fine-structure components with period π in the polarization angle. The fine-structure components are polarized along [110] and [1$\bar{1}$0] directions of the crystal and, strikingly, the polarization of lower and higher fine-structure components is reversed in both transitions. This is rather clear evidence that the transitions “A1” and “A2”, which display almost equal modulus of their diamagnetic coefficients (“A1”: $\gamma_2 = -25 \pm 1\ \mu\text{eV/T}^2$, “A2”: $\gamma_2 = +27 \pm 1\ \mu\text{eV/T}^2$), are closely related.

Fig. 8.11 shows the zero-field spectrum from Fig. 8.9(b), and the excitation-power dependence of the strong lines. The intensity of the three strong lines in Fig. 8.11(a) increases approximately at the same rate as the QW emission peak and saturates at rather low excitation power ($\sim 1\ \mu$W). The intensity of the lines “B1” and “B2” is very low and not shown in Fig. 8.9(b). Line “B3” shifts to lower energy with increasing excitation power; this indicates that it involves (at least) two spectrally non-resolved components. For comparison with the μPL spectrum in Fig. 8.11(a), the corresponding magneto-μPL spectra are shown in Fig. 8.11(b) and (c).

8.2 Discussion

In the following paragraphs, possible explanations for the observation of negative diamagnetic coefficients and complex line patterns are discussed. First, a simplified model of disorder-localized exciton ground states in deep, narrow minima in presence of a magnetic field is described that suggested that negative diamagnetic coefficients could occur for exciton ground states in presence of strong disorder.

Exciton center-of-mass shift

The question if negative diamagnetic shift occurs for exciton ground states in presence of strong disorder was raised recently [Gro05]. The idea that this might happen is based on the following reasoning: The magnetic field influences the exciton relative wave function. With increasing magnetic field, the exciton radius decreases; this effect has been discussed in chapter 2 in this work. Since, in presence of disorder, exciton relative and center-of-mass motion are coupled, the magnetic field also acts on the c.m. wave function. The following section introduces a simplified model to discuss the question if this could lead to negative diamagnetic shift for exciton states in deep, narrow minima.

The idea is that, loosely speaking, in certain disorder configurations the total volume

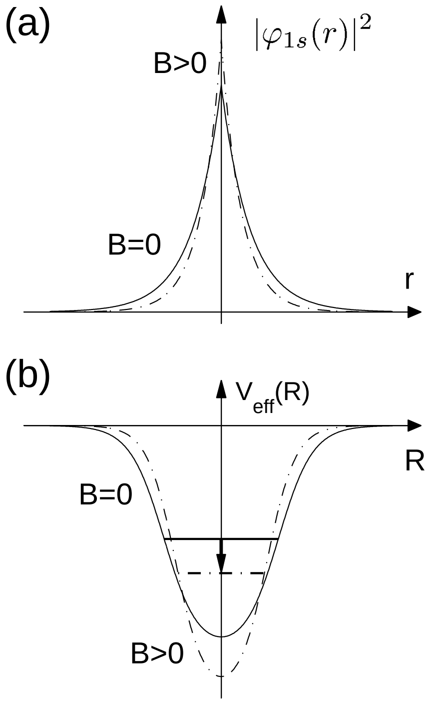

Figure 8.12: *(a) Exciton relative wave function at* $B = 0$ *and* $B > 0$. *(b) Shape of a potential minimum in* $V_{\mathrm{eff}}(\boldsymbol{R})$ *at* $B = 0$ *and* $B > 0$. *The shift of the exciton c.m. ground state to lower energy with increasing B-field is indicated.*

of the confined exciton might *increase* while the magnetic field leads to a shrinking of the lateral exciton radius, due to the possibility to extend further in vertical direction in deep, narrow effective minima that become even deeper due to the less effective averaging with a smaller lateral wave function.

The negative contribution to the diamagnetic shift of exciton ground states described above has been discovered in a recent theoretical study [Gro05]. The basic idea is schematically shown in Fig. 8.13(a) and (b) in the envelope function picture. Short-range correlated disorder in the QW interfaces [the underlying single-particle disorder potential is not shown in Fig. 8.13(b)] is assumed to lead to the localization of an exciton state in the effective potential $V_{\mathrm{eff}}(\boldsymbol{R})$, resulting from averaging of the exciton over underlying disorder with its Bohr radius a_B. The solid line in Fig. 8.13(a) shows the radial part of the exciton relative wave function for zero magnetic field. The dash-dotted line indicates the relative wave function at $B > 0$; the Bohr radius is reduced due to the magnetic field. Figure 8.13(b) shows the shape of a potential minimum in the effective potential for the exciton center-of-mass, resulting from the averaging of the exciton over underlying disorder with its zero-field Bohr radius a_B. The eigenenergy of the local exciton ground state in $V_{\mathrm{eff}}(\boldsymbol{R})$ is shown as a solid horizontal line. At $B > 0$, the averaging of the exciton with the reduced Bohr radius is less effective. For disorder configurations with correlation lengths below the exciton Bohr radius, the shape of the effective potential minimum will therefore change with increasing magnetic field: In Fig. 8.13(b) the case is shown that the minimum becomes steeper and deeper. Correspondingly, the eigenenergy of the exciton c.m. ground state will change; in Fig. 8.13(b) it decreases with increasing magnetic field. The (negative) difference between the eigenenergies of the exciton c.m. states at $B > 0$ and $B = 0$ is the center-of-mass shift.

For an accurate determination of exciton energies and magnetic shifts in a given disorder potential, two-particle calculations are necessary [Gro05]. Since such two-particle calculations are far beyond the possibilities of our study, we determine an estimate of the center-of-mass shift in a simple model. Values for the reduction of the Bohr radius of laterally confined excitons in two-dimensional parabolic minima from Halonen *et al.* [Hal92] are used as a clue; the results of these numerical calculations have been described in chapter 3.

According to Eq. 2.48, the low-field B-dependence of the exciton Bohr radius can be expressed as

$$\langle \rho(B)^2 \rangle^{1/2} = \langle \rho(0)^2 \rangle^{1/2} \left(1 - \frac{B^2}{16B_0^2} + \dots\right), \tag{8.1}$$

where $B_0 = \hbar/(e\langle \rho^2 \rangle)$ is the characteristic field describing the transition from low-field to high-field (exciton/magnetoexciton) regime defined in Eq. (2.41). Next, the effect of B-dependent averaging on the depth of potential minima in $V_{\text{eff}}(\boldsymbol{R})$ is evaluated. The averaging of the exciton with its relative wave function reduces the strength of the local band edge fluctuations, and consequently the depth of potential minima in $V_{\text{eff}}(\boldsymbol{R})$. Assuming isotropic correlations with correlation length ξ for the underlying disorder potentials $V_e(\boldsymbol{\rho_e})$, $V_h(\boldsymbol{\rho_h})$, the ratio of the numbers of independent potential values in the single-particle and the averaged c.m. potential is $\sim (a_B/\xi)^2$ in two dimensions. Therefore, on average the depth of potential minima is reduced by the factor a_B/ξ ("$1/\sqrt{N}$ law"). Denoting with E the values of potential minima in the underlying disorder potential, we obtain for the B-dependence of potential minimum values E' in $V_{\text{eff}}(\boldsymbol{R})$ (see also Fig. 8.13)

$$E'(B) = -\frac{c|E|}{a_B(1 - 1/(16B_0^2) \cdot B^2)} \approx -\frac{c|E|}{a_B} + \gamma_{\text{c.m.}} B^2. \tag{8.2}$$

Here, $c > 0$ is a factor that depends on the effective shape of the potential minimum, and we have defined the (negative) c.m. diamagnetic coefficient $\gamma_{\text{c.m.}}$. Since the transition energy of the local exciton ground state is obtained by adding confinement energy E_c and exciton binding energy E_X, the B-dependence of these energy terms contributes to the B-dependence of the exciton transition energy. However, the influence of the magnetic field on the exciton binding energy, that occurs concomitantly to the shrinking of the exciton radius, is a higher-order effect, just like in the no-disorder case. The confinement energy E_c significantly contributes to the exciton transition energy in deep, narrow minima. However, our subsequent simulations of disorder-localized c.m. exciton states showed that including the confinement energy does not qualitatively affect the B-dependence expressed in Eq. (8.2). Therefore, it is suggested that the total diamagnetic coefficient γ_2 of a disorder-localized exciton state is approximately the sum of the positive coefficient γ_{rel} ("relative shift") and the negative c.m. coefficient $\gamma_{\text{c.m.}}$ ("c.m. shift"),

$$\gamma_2 = \gamma_{\text{rel}} + \gamma_{\text{c.m.}} \,. \tag{8.3}$$

For a numerical estimate of the c.m. shift, a simple model is introduced, since a numerical treatment of the full Coulomb-correlated exciton motion in lateral disorder is beyond the scope of this study. For the underlying disorder, several realizations of two-dimensional, uncorrelated, Gaussian-distributed disorder potentials are taken (grid size 160 × 160 nm^2, grid step = lattice constant $a_{[110]} = 0.4$ nm). Effective

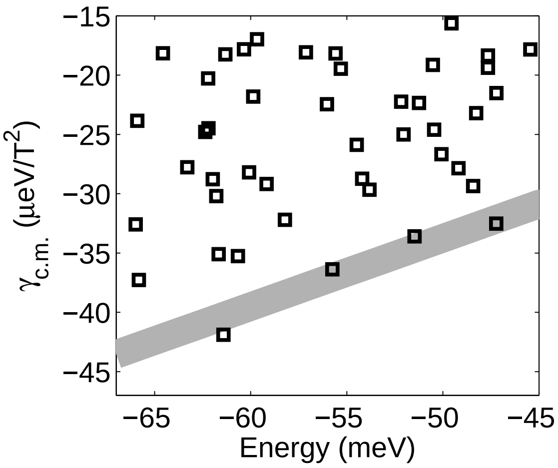

Figure 8.13: *C.m. coefficients of disorder-localized exciton states as a function of exciton transition energy (relative to the mean value of the underlying disorder potential) in simulated, uncorrelated, Gaussian-distributed c.m. potentials (*160 × 160 *nm*^{2}*, grid step 0.4 nm) averaged with 1s wave functions with Bohr radius* $a_B = 4.5$ *nm. The gray bar indicates the lower bound of the c.m. coefficients in the deepest minima.*

c.m. potentials are obtained by convolution with scaled 1s wave functions, according to [Zim97]. For the Bohr radius of the exciton states in deep minima, $a_B = 4.5$ nm is taken. This value corresponds to a relative shift of $\gamma_2 \approx 10\,\mu\text{eV/T}^2$, using $m_e = 0.09$ m$_0$ and $m_h = 0.23$ m$_0$ for the in-plane electron and heavy-hole mass. The shift coefficient $\gamma_2 \approx 10\,\mu\text{eV/T}^2$ conforms with the largest shifts observed in the low-energy tail of the QW spectrum [Fig. 8.5(b)]. We choose the strength of the underlying disorder large enough so that the lowest exciton ground states in $V_{\text{eff}}(\boldsymbol{R})$ occur between 70 and 50 meV below the mean value of the disorder potential. We study the effect of a reduction of a_B by a few percent. Figure 8.13(c) shows calculated c.m. coefficients, assuming a reduction of the exciton radius by 5% at $B = 10$ T. The size of the c.m. shift depends on the potential minimum shape; the steepest minima have the largest negative c.m. shifts. At energies around −50 meV, the largest negative c.m. coefficients are $\gamma_{\text{c.m.}} \approx -35\,\mu\text{eV/T}^2$.

Contrary to this estimate suggesting that the observed negative diamagnetic coefficients might be explained by the center-of-mass shift of exciton ground states in deep, narrow potential minima, a theoretical results has been obtained very recently that excludes negative shift for exciton ground states under rather general conditions. Stimulated by our observation of negative diamagnetic shift coefficients, Muljarov and Zimmermann have established the following

Theorem [Mul06]: The diamagnetic shift $\Delta_\alpha(B) = E_\alpha(B) - E_\alpha(0)$ of a (local) exciton ground state α in arbitrary three-dimensional confinement potential is always positive, $\Delta_\alpha(B) \geq 0$.

The discrepancy between the above estimate and the stated theoretical result is explained by the fact that the influence of the magnetic field on the exciton wave function is not limited to the reduction of the exciton radius. In an external magnetic field, the exciton wave function acquires a phase, which is related to the beginning cyclotron motion of electron and hole. Actually, this effect has to be included in a calculation of the exciton energy shift already at arbitrary low magnetic field. What is more, the factorization in center-of-mass and relative wave function leads to wrong results in presence of strong disorder in this situation. Only the full two-particle exciton Hamiltonian including disorder and magnetic field [Gro05] gives reliable results. A corresponding positive (second-order) contribution to the exciton energy results that prevents the diamagnetic shift of exciton ground states from becoming negative in rather general disorder. For details of the result of Muljarov and Zimmermann, the reader is referred to their intended publication [Mul06].

The conclusion remains that the center-of-mass shift leads to a negative contribution to the diamagnetic shift of exciton ground states in presence of disorder, but that negative diamagnetic shift does not occur. However, it can lead to exciton transitions with very small diamagnetic shift. Such a transition has been observed in a recent experiment [Phi03]; the extremely small diamagnetic shift coefficient $\gamma_2 = 0.6\,\mu\text{eV/T}^2$ observed in this experiment can probably be attributed to the influence of the negative center-of-mass shift.

The diamagnetic shift of *excited* exciton states is not necessarily positive [Mul06]. However, if excited state transitions were involved, then also corresponding ground state transitions with significantly larger oscillator strength should be observed at lower energy. At least for transition “A1”, this can be excluded: Figure 8.7(a) shows that no transitions are observed at least in a several meV wide region below “A1”.

Another hypothetic explanation for the appearance of pairs of transitions with negative and positive shift (Fig. 8.9) is immediately excluded by the result of Muljarov and Zimmermann: The possibility that the magnetic-field dependent splitting between these pairs is caused by a magnetic-field dependent tunnel coupling between neutral exciton states in the two GaAs wells separated by a narrow AlAs barrier can be excluded, because the above result is valid for exciton ground states in an arbitrary three-dimensional confinement potential.

On the other hand, the complicated shifts, level anticrossings and crossings shown in Fig. 8.8 are in fact likely explained by the complicated interactions between (possibly charged) exciton states in coupled natural quantum dots, most probably separated by a thin AlAs barrier. Optical spectra of coupled quantum dots have been measured in recent years [Sch97, Bay01, Kre05, Ort05]. Recently, optical spectra of an asymmetric pair of coupled InAs quantum dots have been measured. The states of both QDs could be tuned into resonance by application of an external electric field [Sti06]. The observed rich patterns of level anticrossings and crossings in electric-field-dependent spectra were interpreted as evidence for a superposition of charge and spin configurations of the two dots. A distinct X-pattern, where anticrossings and crossings are observed at slightly differing detuning, was explained by the Coulomb energy shift between two charged exciton states in the coupled dots. This result will be discussed in a bit more detail in the next section in the context of charged exciton transitions.

Exciton complexes and charged exciton transitions

In presence of residual impurities (donors, acceptors) in an intrinsic crystal or in presence of a background charge density, excitons form different types of bound complexes.

Before exciton transitions in three-particle complexes of an electron or hole bound to an exciton are treated, the possibility that the observed line patterns described above are related to transitions of excitons bound to residual impurities is briefly considered.

There are many arguments against the observation of impurity-bound exciton transitions in our experiments. First, even more and more closely spaced spectral components are expected for the principal transition region of impurity-bound excitons [Tho62, Kar94], making impurity analysis difficult. Therefore, in practically all studies concerned with impurity analysis, the spectral region corresponding to transitions which leave the donors in one of the excited hydrogenic states ($n > 1$) has been used, where the PL intensity is much weaker than in the principal region, but the separations between PL peaks of different donors are much larger. The relatively well separated lines in Fig. 8.9 do therefore not exactly comply with spectral patterns expected for the principal region of impurity-related transitions. Another, possibly much stronger argument is related to the fact that it could be expected that single impurities would be observed in a narrow quantum well; the differing impurity positions in the well would make the occurrence of different transition energies for the same type of impurity-related exciton transitions plausible. In this context, it is interesting that almost all impurity-related luminescence measurements to date have probed a large collection of emitters. The fine structure luminescence of excitons bound to single impurities in GaAs has been reported only recently [Fra04]. Polarization-angle-dependent PL measurements showed that the polarization anisotropy of the impurity-related transitions reached unity, as expected for a single emitter [Fra04]. Previously, the averaging over a large number of emitters had concealed this effect.

Such a polarization anisotropy is not observed here, as demonstrated in Fig. 8.10. Rather, the polarization-angle-dependent spectra in Fig. 8.10 show fine structure splitting of the transitions “A1” and “A2”, and the characteristic oscillation of the intensity maximum of the two spectrally unresolved fine structure components reveals polarization of the fine-structure components along [110] and [$1\bar{1}0$] directions. This exchange-induced fine structure has been interpreted as unambiguous evidence for exciton localization in anisotropic confinement potentials [Gam96]. It is concluded that impurity-related transitions constitute no plausible explanation at least for transitions “A1” and “A2”.

Next, three-particle complexes of an electron or hole bound to an exciton are considered. The existence of three-particle complexes of an electron or hole bound to an exciton in a semiconductor in presence of a small background electron density has been predicted by Lampert [Lam58]. The negatively charged trion, X^-, consisting of two conduction band electrons bound to a valence-band hole, is the analogon of H^-, while X^+, consisting of two holes bound to an electron, is the analogon of H_2^+. Experimentally, trion transitions have been first observed in quantum wells [Khe93, Fin95, Shi95, Fin96b], where the trion binding energy is enhanced by approximately an order of magnitude relative to bulk [Tho90]. The trion binding energy is defined as the difference between exciton energy and trion energy, $B_{X^-} = E_X - E_{X^-}$.

It has been pointed out that mixed type-I/type-II GaAs/AlAs double quantum wells are an especially interesting system for the study of trions [Bar05]: In an asymmetric GaAs/AlAs structure, where two GaAs wells with different widths are separated by a narrow AlAs barrier. The staggered arrangement of the confined electronic states E_Γ in

Figure 8.14: *Schematic diagram of the conduction and valence band edges of an asymmetric GaAs/AlAs DQW showing the lowest confined X and Γ electron states and hole states. The dominant excitation mechanism and the limiting electron and hole relaxation mechanisms are indicated by arrows. After [Daw03].*

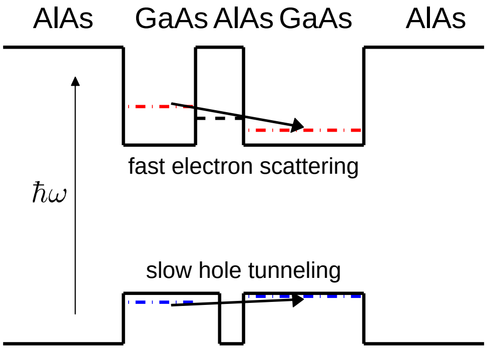

the narrower well, E_X in the barrier, and E_Γ in the wider well gives rise to an efficient transfer of photoexcited electrons from the narrow to the wide well. As a result, the electrons which are photoexcited in the narrow QW accumulate in the wide well, while the photoexcited holes remain trapped in the narrow well [Bar05]. Even in a well wider than 3.5 nm as in our case, where the minimum of the lowest electron subband is *below* the energy of the X-electron in the AlAs barrier, a situation may be realized locally that enables efficient electron transfer from one to the other well: Lateral confinement of an electron may locally increase the electron energy above E^X_{AlAs}, enabling efficient transfer of electrons from one well into the other locally. The situation resembles that of two coupled quantum dots with different confinement energies, where an intermediate level in the barrier allows effective tunneling from one to the other dot. This effect will lead to a locally increased electron density in one of the wells *near* this “charge-transfer channel”. Due to this process, the formation of negative trion states is favored in the locally wider well.

Figures 8.15(a) and (b) schematically show negatively charged trion states in the non-interacting particle approximation. The lowest electron and hole sublevels are indicated. In a negative trion, a heavy hole with total angular momentum $J = 3/2$ and angular momentum projection $J_z = \pm 3/2$ binds to two electrons with spin $S = 1/2$, $S_z = 1/2$. In the lowest trion states, both electrons populate the lowest electron sublevel. Figure 8.15(a) represents the trion singlet state; of course, the wave function in the singlet state is actually the difference of two spin configurations with reversed spins. Due to the antiparallel electron spins, the total spin of the negative trion singlet is given by the effective hole spin $S = 3/2$, $S_z = \pm 3/2$. The two configurations in Fig. 8.15(b) represent the trion singlet state, where the spins of the two electron are aligned in parallel; the third spin configuration is not shown. The total spin of the trion triplet state is $S = 5/2$, and S_z takes the half-integer values $\pm 1/2$, $\pm 3/2$ and $\pm 5/2$. Figure 8.15(c) shows the term scheme of electron (e), singlet trion (T_s) and triplet trion (T_t) states and the allowed dipole transitions. Dark states exist in the triplet channel ($S_z = \pm 5/2$). The transition energy of the triplet states is higher than of the singlet due to the exchange interaction.

The magnetooptical spectra of trions are not yet well-known and more complex than neutral exciton spectra because of the more elaborate Coulomb interactions. A negative diamagnetic shift of the recombination line of the quantum well trion singlet in a weak magnetic field and the existence of cyclotron replica due to the transfer of a quantum of cyclotron energy in the process of electron-hole recombination has been observed

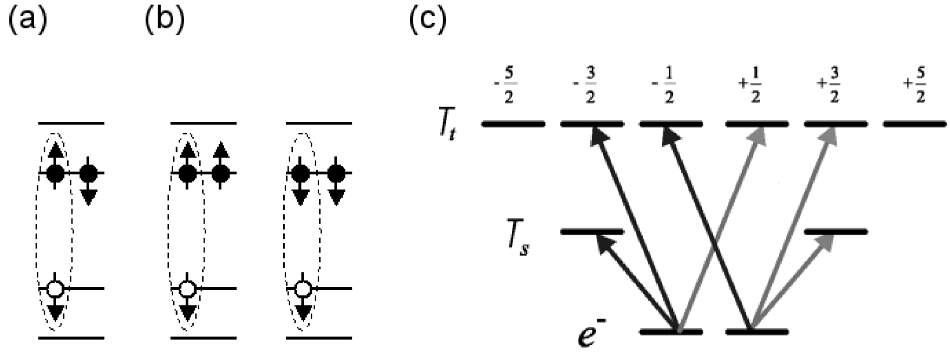

Figure 8.15: *Examples of spin configurations of negatively charged exciton states in the independent-particle picture: (a) negative trion singlet, (b) negative trion triplet. The dashed ellipsis indicates the possible recombination of an electron-hole pair, leaving final states behind. (c) Term scheme of electron (e^-), singlet trion (T_s) and triplet trion (T_t).*

[Shi95, Gov97]. The negative shift at low fields (at fields above a few tesla, the shift becomes positive) was explained by a magnetic-field-induced enhancement of the trion binding energy, due to the relatively large spatial extent of the trion at zero field and the significant effect of the magnetic cyclotron confinement. The cyclotron replica are related to shakeup processes, where after recombination of electron and hole the remaining electron is ejected into some high-energy state. At finite magnetic field, this energy state is a Landau level. The process gives rise to a fan of discrete lines, each associated with a Landau level as the final state of the electron, that move away from the main transition line to lower energy. In principle, in quantum dots the electron levels exhibit a quadratic dependence on the B-field at least at low field instead of the linear dependence of the laterally unconfined Landau levels. Therefore, in principle observation of negative diamagnetic coefficients could be expected.

Complete quantum confinement of trions has been observed by Tischler *et al.* [Tis02]. Schulhauser *et al.* studied magnetooptical spectra of trions in QDs in the strong and intermediate confinement regime [Sch02]. For the small QDs with strong confinement, a small reduction of the trion diamagnetic shift compared to the exciton diamagnetic shift was observed. For the QDs with intermediate confinement, a significantly stronger reduction, but still positive diamagnetic shift, was observed. Based on this observation of a paramagnetic contribution to the diamagnetic shift of charged excitons in quantum dots due to a confinement dependence of the few-body Coulomb interactions, it was suggested that in the weak confinement regime, the exciton diamagnetic shift should strongly depend on surplus charge. The possibility of negative diamagnetic shift coefficients for trion states in a weak lateral confinement potential was suggested [Sch02]. However, to the best of our knowledge this effect has not been reported to date.

A very interesting effect that possibly provides an explanation for the complex B-field patterns found in our data (Fig. 8.8), has been observed recently in an experiment on a coupled quantum dot structure in an electric field [Sti06]. A pair of vertically coupled InAs quantum dots in an asymmetric layer structure was studied (Fig. 8.16). Figure 8.16(A) shows a section through the band edge diagram of the asymmetric coupled layer structure. The applied external electric field ($\boldsymbol{F}$) could be used to tune the lowest electron and hole states in the InAs quantum dots relative to each other. The observed rich patterns of level anticrossings and crossings in electric-field-dependent spectra were interpreted as evidence for a superposition of charge and spin configurations of the two dots. Figure 8.16(B) zooms into the band diagrams of the asymmetric coupled QD structure at different bias voltages.

When the direct and indirect transition energies of an asymmetric coupled QD approach each other, either the electron or hole levels in the two dots become resonant, the wave functions become delocalized over both dots, and the transitions show anticrossing behavior (Fig. 8.16). Away from these anticrossings the wave functions retain their single dot character [Sti06]. It was observed that introduction of a single charge into the coupled QD dramatically enriched the spectrum. Depending on the detuning level, an intricate crossing pattern with several anticrossings at slightly different detuning was found (Fig. 8.17). The dominant feature was explained to arise from a strong indirect transition that anticrosses two direct transitions. Finally, the Coulomb energy shift between two charged exciton states was identified as the essential origin of the X-shape in the PL spectra (Fig. 8.17).

We suggest that a similar effect – only with magnetic-field induced detuning due to the magnetic shift instead of the electric-field induced detuning due to the Stark shift – is responsible for the crossing and anticrossing behavior observed in Fig. 8.8. The negative diamagnetic coefficients observed in Fig. 8.9 might also be related to charged exciton transitions in coupled quantum dots, possibly at a different detuning level. The detailed clarification of their origin is, however, definitely beyond the scope of this study. It remains as a task for future magnetooptical studies of coupled quantum dot structures, possibly also with attention to disorder effects, that have just been commenced.

8.3 Conclusions

The first clear-cut observation of excitonic transitions with negative diamagnetic coefficients in a semiconductor heterostructure has been presented. The observation of the negative diamagnetic coefficients simultaneously with signatures of strong disorder in the GaAs/AlAs DQW raised the question if the negative curvature may be a pure disorder effect – or, more precisely, if it may be explained by the negative contribution to the exciton diamagnetic shift in presence of disorder. This so-called center-of-mass shift has been discovered in a recent theoretical study [Gro05]. Theoretical investigations that were stimulated by our experimental observation of negative curvature have very recently excluded this possibility [Mul06]. At present, it is assumed that the negative diamagnetic coefficients as well as simultaneously observed complex shifts – including crossings and anticrossings – are related to charged exciton transitions in coupled quantum dots.

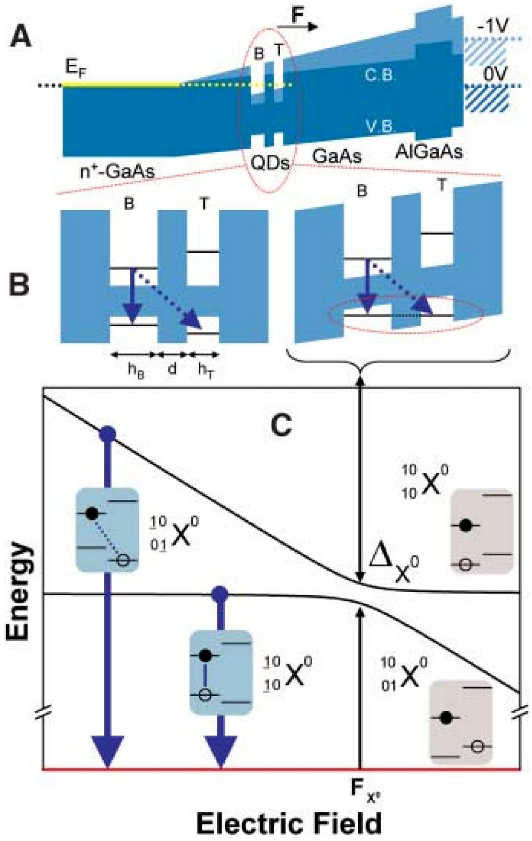

Figure 8.16: *[Sti06] (a) Band edge diagram of the device layer structure. The two dots are labeled bottom (B) and top (T). (b) Schematic of the coupled QD region at flat-band condition and at the electric where where hole resonance occurs. The direct (solid arrow) and indirect (dashed arrow) transitions are indicated. (c) Diagram of the* X^0 *initial state (black lins) and final state (erd line) for dot B. The direct and indirect recombinations are indicated.*

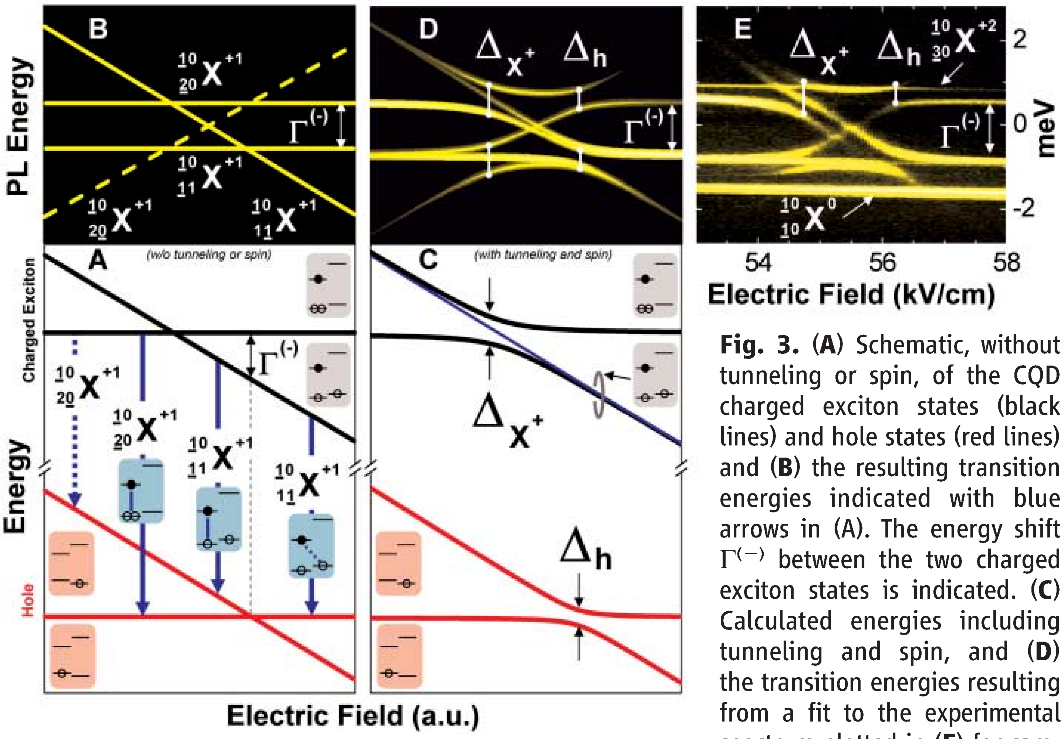

Fig. 3. (**A**) Schematic, without tunneling or spin, of the CQD charged exciton states (black lines) and hole states (red lines) and (**B**) the resulting transition energies indicated with blue arrows in (A). The energy shift $\Gamma^{(-)}$ between the two charged exciton states is indicated. (**C**) Calculated energies including tunneling and spin, and (**D**) the transition energies resulting from a fit to the experimental spectrum plotted in (**E**) for sample ($h_B/d/h_T$) = (4/4/2.5). With the introduction of tunneling and spin effects, we can see the two anticrossings events (Δ_h, Δ_{X^+}) which, along with $\Gamma^{(-)}$, give rise to the signature X-shape pattern. The parameters used to fit the data in (E) were $\Gamma^{(-)} = 1.27$ meV and $t = 1/2(\Delta_h) = 0.23$ meV. In (E), we note the two additional PL lines arising from the uncharged exciton ($^{10}_{\underline{1}0}X^0$) and the doubly positively charged exciton ($^{10}_{\underline{3}0}X^{+2}$). a.u., arbitrary units.

Figure 8.17: *[Sti06] Reproduced from Stinaff et al., Science 311, 636 (2006).*

References

[Ada94] S. Adachi, *GaAs and related materials*, World Scientific, 1994.

[And90] L. C. Andreani and A. Pasquarello, *Accurate theory of excitons in GaAs-*$Ga_{1-x}Al_xAs$ *quantum wells*, *Phys. Rev. B* 42, 8928 (1990).

[Bar05] I. Bar-Joseph, *Trions in GaAs quantum wells*, *Semicond. Sci. Tech.* 20, R29 (2005).

[Bay01] M. Bayer, P. Hawrylak, K. Hinzer, S. Fafard, M. Korkusinski, Z. R. Wasilewski, O. Stern, and A. Forchel, *Coupling and entangling of quantum states in quantum dot molecules*, *Science* 291, 451 (2001).

[Daw03] P. Dawson and M. J. Godfrey, *Recombination dynamics of spatially separated electron-hole plasmas in GaAs/AlAs mixed type-I/type-II quantum well structures*, *Phys. Rev. B* 68, (2003).

[Erd06] M. Erdmann, C. Ropers, M. Wenderoth, R. G. Ulbrich, S. Malzer, and G. H. Döhler, *Diamagnetic shift of disorder-localized excitons in narrow GaAs/AlGaAs quantum wells*, *Phys. Rev. B* 74, 125412 (2006).

[Fin96b] G. Finkelstein, H. Shtrikman, and I. Bar-Joseph, *Shakeup processes in the recombination spectra of negatively charged excitons*, *Phys. Rev. B* 53, 12593 (1996).

[Fin95] G. Finkelstein, H. Shtrikman, and I. Barjoseph, *Optical spectroscopy of a two-dimensional electron gas near the metal-insulator transition*, *Phys. Rev. Lett.* 74, 976 (1995).

[Fra04] S. Francoeur, J. F. Klem, and A. Mascarenhas, *Optical spectroscopy of single impurity centers in semiconductors*, *Phys. Rev. Lett.* 93, (2004).

[Gal89] I. Galbraith and G. Duggan, *Exciton binding energy and external-field-induced blue shift in double quantum wells*, *Phys. Rev. B* 40, 5515 (1989).

[Gam96] D. Gammon, E. S. Snow, and D. S. Katzer, *Naturally formed GaAs quantum dots*, *Surf. Sci.* 362, 814 (1996).

[Gov97] A. O. Govorov and A. V. Chaplik, *Multiply-charged magnetoexcitons in low-dimensional structures*, *JETP Lett.* 66, 454 (1997).

[Gro05] M. Grochol, F. Grosse, and R. Zimmermann, *Exciton wave function properties probed by diamagnetic shift in disordered quantum wells*, *Phys. Rev. B* 71, 125339 (2005).

[Hal92] V. Halonen, T. Chakraborty, and P. Pietilainen, *Excitons in a parabolic quantum dot in magnetic fields*, *Phys. Rev. B* 45, 5980 (1992).

[Kar94] V. A. Karasyuk, D. G. S. Beckett, M. K. Nissen, A. Villemaire, T. W. Steiner, and M. L. W. Thewalt, *Fourier-transform magnetophotoluminescence spectroscopy of donor-bound excitons in GaAs*, *Phys. Rev. B* 49, 16381 (1994).

[Khe93] K. Kheng, R. T. Cox, Y. M. Daubigne, F. Bassani, K. Saminadayar, and S. Tatarenko, *Observation of negatively charged excitons in semiconductor quantum wells*, *Phys. Rev. Lett.* 71, 1752 (1993).

[Kre05] H. J. Krenner, M. Sabathil, E. C. Clark, A. Kress, D. Schuh, M. Bichler, G. Abstreiter, and J. J. Finley, *Direct observation of controlled coupling in an individual quantum dot molecule*, *Phys. Rev. Lett.* 94, 57402 (2005).

[Lam58] M. A. Lampert, *Mobile and immobile effective-mass particle complexes in nonmetallic solids*, *Phys. Rev. Lett.* 1, 450 (1958).

[Moo88] K. J. Moore, P. Dawson, and C. T. Foxon, *Effects of electronic coupling on the band alignment of thin GaAs/AlAs quantum well structures*, *Phys. Rev. B* 38, 3368 (1988).

[Mul06] E. Muljarov and R. Zimmermann, unpublished result. Private communication (2006).

[Ort05] G. Ortner, M. Bayer, Y. Lyanda-Geller, T. L. Reinecke, A. Kress, J. P. Reithmaier, and A. Forchel, *Control of vertically coupled InGaAs/GaAs quantum dots with electric fields*, *Phys. Rev. Lett.* 94, 157401.

[Phi03] R. T. Phillips, A. G. Steffan, S. R. Newton, T. L. Reinecke, and R. Kotlyar, *Exciton fine structure in interfacial quantum dots*, *phys. stat. sol. b* 238, 601 (2003).

[Rog86] D. C. Rogers, J. Singleton, R. J. Nicholas, C. T. Foxon, and K. Woodbridge, *Magnetooptics in GaAs-*$Ga_{1-x}Al_xAs$ *quantum wells*, *Phys. Rev. B* 34, 4002 (1986).

[Sch97] G. Schedelbeck, W. Wegscheider, M. Bichler, and G. Abstreiter, *Coupled quantum dots fabricated by cleaved edge overgrowth: From artificial atoms to molecules*, *Science* 278, 1792 (1997).

[Sch02] C. Schulhauser, D. Haft, R. J. Warburton, K. Karrai, A. O. Govorov, A. V. Kalameitsev, A. C. andW. Schoenfeld, J. M. Garcia, and P. M. Petroff, *Magneto-optical properties of charged excitons in quantum dots*, *Phys. Rev. B* 66, (2002).

[Shi95] A. J. Shields, M. Pepper, M. Y. Simmons, and D. A. Ritchie, *Spin-triplet negatively charged excitons in GaAs quantum wells*, *Phys. Rev. B* 52, 7841 (1995).

[Sne92] M. J. Snelling, E. Blackwood, C. J. Mcdonagh, R. T. Harley, and C. T. B. Foxon, *Exciton, heavy-hole, and electron g-factors in type-I GaAs/*$Al_xGa_{1-x}As$ *quantum wells*, *Phys. Rev. B* 45, 3922 (1992).

[Som95] T. Someya, H. Akiyama, and H. Sakaki, *Laterally squeezed excitonic wavefunction in quantum wires*, *Phys. Rev. Lett.* 74, 3664 (1995).

[Sti06] E. A. Stinaff, M. Scheibner, A. S. Bracker, I. V. Ponomarev, V. L. Korenev, M. E. Ware, M. F.Doty, T. L. Reinecke, and D. Gammon, *Optical signatures of coupled quantum dots*, *Science* 311, 636 (2006).

[Tar84] S. Tarucha, H. Okamoto, Y. Iwasa, and N. Miura, *Exciton binding energy in GaAs quantum wells deduced from magnetooptical absorption measurement*, *Solid State Commun.* 52, 815 (1984).

[Tho90] D. B. T. Thoai, R. Zimmermann, M. Grundmann, and D. Bimberg, *Image charges in semiconductor quantum wells - Effect on exciton binding energy*, *Phys. Rev. B* 42, 5906 (1990).

[Tho62] D. G. Thomas and J. J. Hopfield, *Optical properties of bound exciton complexes in Cadmium Sulfide*, *Phys. Rev.* 128, 2135 (1962).

[Tis02] J. G. Tischler, A. S. Bracker, D. Gammon, and D. Park, *Fine structure of trions and excitons in single GaAs quantum dots*, *Phys. Rev. B* 66, (2002).

[Zim97] R. Zimmermann, F. Grosse, and E. Runge, *Excitons in semiconductor nanostructures with disorder*, *Pure Appl. Chem.* 69, 1179 (1997).

Chapter 9

Summary

The structural and optical properties of GaAs/Al$_x$Ga$_{1-x}$As quantum wells have been investigated in this thesis by a combination of optical (μPL) and magnetooptical (magneto-μPL) methods with the analysis of structural (XSTM) data. Central results of the research presented in this thesis are summarized in the following.

Short-range disorder on the atomic scale in GaAs/Al$_x$Ga$_{1-x}$As quantum wells, resulting from composition fluctuations in the Al$_x$Ga$_{1-x}$As barriers, has often been thought to be irrelevant for exciton localization [Wei81], or at least of secondary importance [War92]. This work demonstrates that short-range correlations in the Al distribution in the Al$_{0.3}$Ga$_{0.7}$As barriers are fundamental to the inhomogeneous broadening of optical spectra of narrow GaAs/Al$_{0.3}$Ga$_{0.7}$As quantum wells grown without growth interruption.

Several findings support this conclusion:

1. XSTM on a (110) cleavage surface on the 4-nm GaAs/Al$_{0.3}$Ga$_{0.7}$As QW in sample QW$_1$ demonstrated that Al atoms in the Al$_{0.3}$Ga$_{0.7}$As barriers show the tendency of short-range ordering on neighbouring lattice sites along the $[1\bar{1}0]$ direction, and that modulations of the Al concentration occur on a length scale of $5 - 10$ nm. Direct inspection of the XSTM images shows that also correlations between Al atoms in [001] direction are present.

2. The linearly polarized fine-structure components of low-energy tail states in μPL spectra of the 4-nm GaAs/Al$_{0.3}$Ga$_{0.7}$As quantum well showed no clear preferential polarization direction with respect to the crystal axes. This is in contrast to growth-interrupted samples, where a preferential orientation along the $[1\bar{1}0]$ direction has been reported [Gam96], caused by exciton localization in large anisotropic islands aligned along the $[1\bar{1}0]$ direction. Our observation therefore indicates that such large anisotropic islands aligned along the $[1\bar{1}0]$ direction are not responsible for exciton localization in the investigated non-growth interrupted quantum well. Rather, it indicates exciton localization by short-range correlated disorder.

3. Optical spectra of the 4-nm GaAs/Al$_{0.3}$Ga$_{0.7}$As QW were simulated on the basis of the XSTM data. Assuming in-plane disorder with isotropic exponential correlations with 0.4 nm correlation length, and assuming the disorder strength determined from the XSTM data, very good agreement is observed between inhomogeneous broadening

and temperature-dependent lineshapes of experimental and simulated μPL spectra.

4. In the low-energy tail of magneto-μPL spectra of the narrow GaAs/Al$_{0.3}$Ga$_{0.7}$As QWs, positive slope has been observed in the diamagnetic shift distribution as a function of transition energy. The positive slope is the consequence of exciton localization by short-range correlated interface disorder. Two-particle calculations on the basis of XSTM data have shown good agreement between theoretical and experimental shift coefficients. Including that the enhanced in-plane electron mass in the narrow QW significantly influences the exciton diamagnetic shift, the size of diamagnetic coefficients and the slope in the shift distribution were well reproduced by theoretical calculations based on in-plane disorder with isotropic exponential correlations with 0.4 nm correlation length, and assuming the disorder strength determined from the XSTM data.

The significance of magneto-μPL spectroscopy lies in the fact that it gives access to the in-plane band edge fluctuations in buried semiconductor quantum wells on a nm scale. This is achieved using a far-field optical technique, by employing the exciton as an extended particle as a probe of lateral confinement. Concerning the interpretation of the magneto-μPL experiments, a detailed qualitative picture of the relation between the underlying interface disorder and the diamagnetic shift distribution in the low-energy tail of magneto-μPL spectra has been developed. The limits of this approach have also been discussed: Due to the complexity of the problem of exciton disorder-localization, the introduced simple models do not allow a quantitative prediction of the slope in the diamagnetic shift distribution. Numerical two-particle calculations in the framework of the theory of exciton disorder-localization provide the only way of an accurate prediction of the diamagnetic shift distribution. Experimentally, the study of the diamagnetic shift distribution in the low-energy tail of magneto-μPL spectra is limited by the averaging over the Zeeman doublet and the limited number of exciton tail states for which both Zeeman components can be realiably resolved over a sufficient range of the magnetic field.

The influence of a variation of the correlation length or of an additional length scale, e.g., the presence of longer-range correlations, on the diamagnetic shift distribution has to be further investigated. Experimentally, it could be interesting to study the diamagnetic shift distribution in monolayer-split samples. Here, a region between the ML peaks should show negative slope, if the commonly accepted picture of well width fluctuations in growth-interrupted samples should be correct. Also the observation of a transition of magnetic-field dependent spectra from a single-peak to a double-peak structure, which has not been discussed in detail here because of the focus on single-dot experimentss, could be of interest in this respect.

Concerning the theory of the exciton diamagnetic shift in general, the first clear-cut observation of transitions with negative diamagnetic coefficients in optical spectra of a semiconductor heterostructure has been presented. This observation raised the question if negative curvature (as a function of magnetic field) can occur for disorder-localized exciton ground states. Theoretical investigations that were stimulated by our experimental observation of negative curvature have recently excluded this possibility [Mul06]. In addition to transitions with negative curvature, transitions exhibiting complex shifts including crossings and anticrossings have been observed. At present, it is assumed that as well the complex shifts as the negative diamagnetic coefficients are related to charged exciton transitions in coupled quantum dots.

References

[Gam96] D. Gammon, E. S. Snow, and D. S. Katzer, *Naturally formed GaAs quantum dots*, *Surf. Sci.* 362, 814 (1996).

[Mul06] E. Muljarov and R. Zimmermann, unpublished result. Private communication (2006).

[War92] C. A. Warwick and R. F. Kopf, *Microscopic thickness variation of macroscopically uniform quantum wells*, *Appl. Phys. Lett.* 60, 386 (1992).

[Wei81] C. Weisbuch, R. Dingle, A. C. Gossard, and W. Wiegmann, *Optical characterization of interface disorder in* $GaAs/Ga_{1-x}Al_xAs$ *multi-quantum well structures*, *Solid State Commun.* 38, 709 (1981).

Appendix A

Numerical algorithms

This chapter describes the numerical methods that have been used in this thesis to solve several problems related to electron and hole confinement in ideal and nonideal quantum structures.

A.1 Single-particle Schrödinger equation in 1D

Numerical methods to solve the time-independent Schrödinger equation for a single particle with mass m in a one-dimensional square well potential abound. Energies of eigenstates in a square well with finite barriers are conveniently calculated using shooting method or transfer matrix method (described in detail in [Har99]). Here, we use a finite-difference method to approximate the Schrödinger equation for a single particle with mass m by a finite-difference equation. Writing the set of linear finite-difference equations in matrix form, powerful matrix diagonalization methods can be applied to determine eigenvalues and eigenfunctions of the problem. The finite-difference approach has the advantage to be easily extensible to include the mass mismatch between well and barrier. The extension to two dimensions is also straightforward.

This paragraph describes a finite-difference method to solve the time-independent Schrödinger equation for a single particle with mass m in a potential $V(x)$ on a finite interval, $x \in [0, a]$, $a > 0$,

$$-\frac{\hbar^2}{2m}\frac{d^2}{dx^2}u(x) + V(x)u(x) = E\,u(x)\,. \tag{A.1}$$

The choice of periodic boundary conditions is convenient to avoid artefacts due to hard boundary conditions (infinite potential). Therefore, we assume $u(x + a) = u(x)$ in the following.

Finite-difference methods rely on replacing differential quotients by difference quotients [Pre02]. The wave function $u(x)$ is discretized on the n-component grid (vector) $x = (0, a/(n-1), \ldots, a)$, i.e., the map

$$u(x) \to (u_i)_i, \text{ where } u_i = u(x_i),\ i \in \{1, \ldots, n\} \tag{A.2}$$

is used. The second derivative $\frac{d^2}{dx^2}$ is replaced by a difference quotient according to the rule

$$\frac{d^2}{dx^2}u(x) \to \frac{u_{i+1} - 2u_i + u_{i-1}}{\delta x^2}\,, \tag{A.3}$$

where $\delta x := a/(n{-}1)$. Consequently, the discretized version of the Schrödinger equation (Eq. A.1) consists of the set of n linear equations for the u_i

$$-\frac{\hbar^2}{2m}\big(u_{i+1} + u_{i-1} - 2u_i\big)/\delta x^2 + V_i u_i = E\,u_i\,. \tag{A.4}$$

The matrix representation of this set of linear equations reads

$$Hu = Eu, \quad H = T + V\,, \tag{A.5}$$

where the n×n matrices T and V have been defined by

$$T := -\frac{\hbar^2}{2m}/\delta x^2 \begin{pmatrix} -2 & 1 & & & & 1 \\ 1 & -2 & 1 & & & \\ & 1 & . & . & & \\ & & . & . & . & \\ & & & . & . & 1 \\ 1 & & & & 1 & -2 \end{pmatrix}, \; V = \begin{pmatrix} V_1 & & & & & \\ & V_2 & & & & \\ & & . & & & \\ & & & . & & \\ & & & & . & \\ & & & & & V_n \end{pmatrix}. \tag{A.6}$$

The potential matrix V is diagonal with the values $V_i = V(x_i)$, $i \in \{1, \ldots, n\}$. The kinetic energy matrix T has the three terms corresponding to the discretized second derivative centered around the diagonal. The ones in the lower left and upper right corner of the kinetic energy matrix T correspond to the choice of periodic boundary conditions. The application of matrix diagonalization methods to Eq. (A.13) is now straightforward.

Figure A.1 shows electron ground state wave functions in a 4-nm square well with abrupt interfaces (solid line) and with exponentially smoothed interfaces (dashed line), calculated using the finite-difference method described above. The band offset Δ_e = 292 meV of GaAs/$\mathrm{Al_{0.3}Ga_{0.7}As}$ QW has been used, and the effective mass m_e=0.067 $\mathrm{m_0}$ has been assumed constant througout the structure. The shape of the wave functions is nearly identical; the lowest eigenstate in the well with smoothed profile is shifted upwards by $\sim$ 5 meV compared to the lowest eigenstate in the square well. There is a simple explanation for this upward shift: The effective width of the well in the energy range up to the ground state energy is smaller than of the square well.

Extension to variable quantization mass

In the Schrödinger equation Eq. (A.1), the same value for the mass parameter m has been assumed in well and barrier material. Since in a not too shallow quantum well, the largest portion of the electron (hole) wave function is localized in the well, the effective electron (hole) mass of the well material is usually chosen for this mass parameter. However, for accurate calculations the effective mass mismatch between well and barrier material has to be included. This can be done by solving the Schrödinger equation piecewise in regions of constant effective mass. The piecewise solutions are

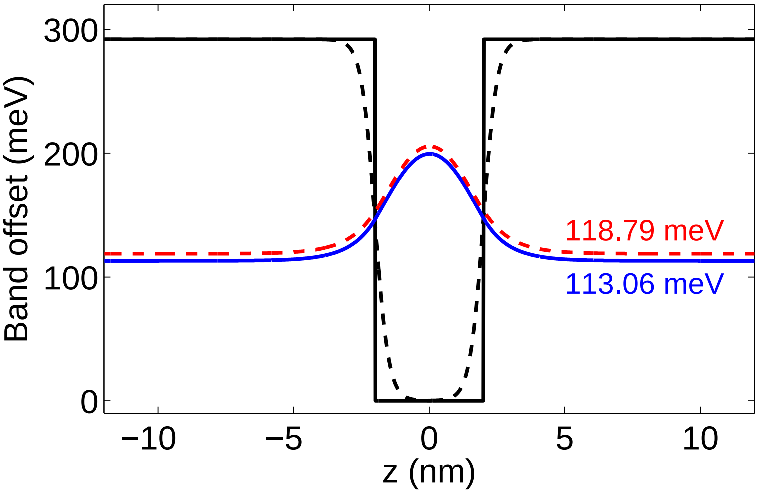

Figure A.1: *Electron ground state wave functions* ($|u_e(z)|^2$) *in a 4-nm GaAs/Al$_{0.3}$Ga$_{0.7}$As QW, assuming square potential (solid line) and exponentially smoothed profile (dashed line). The constant effective mass* m_e=0.067 m_0 *has been used.*

then connected by appropriate boundary conditions. Usually the condition is used that electron transport through a heterojunction requires continuity of the wave function $u(z)$ and of the electron current $1/m^* \, u'(z)$ [Ben66].

A more convenient approach retains a single Schrödinger equation for the whole heterostructure while including the mass mismatch: This approach is based on replacing the kinetic energy operator in Eq. (A.1) by a variable-mass term. The appropriate (Hermitean) operator that accounts for varying effective mass in a heterostructure is [Har99]

$$T = -\frac{\hbar^2}{2} \frac{d}{dx} \frac{1}{m(x)} \frac{d}{dx} \, . \tag{A.7}$$

Straightforward application of the chain rule shows that the variable-mass differential operator T is a sum of two terms, $T = T_1 + T_2$. Explicitly doing the differentiation,

$$\frac{d}{dx}\left(\frac{1}{m(x)} \frac{d}{dx} u(x)\right) = \frac{1}{m(x)} u''(x) - \frac{m'(x)}{m(x)^2} u'(x) \, , \tag{A.8}$$

it is found that the first term is the curvature term $u''(x)$ multiplied with the inverse mass, $1/m(x)$. Obviously, the discretized version of this term is

$$\frac{1}{m_i} \left(u_{i+1} + u_{i-1} - 2u_i\right) / \delta x^2 \, , \tag{A.9}$$

and the corresponding operator T_1 is the matrix product of the diagonal inverse mass

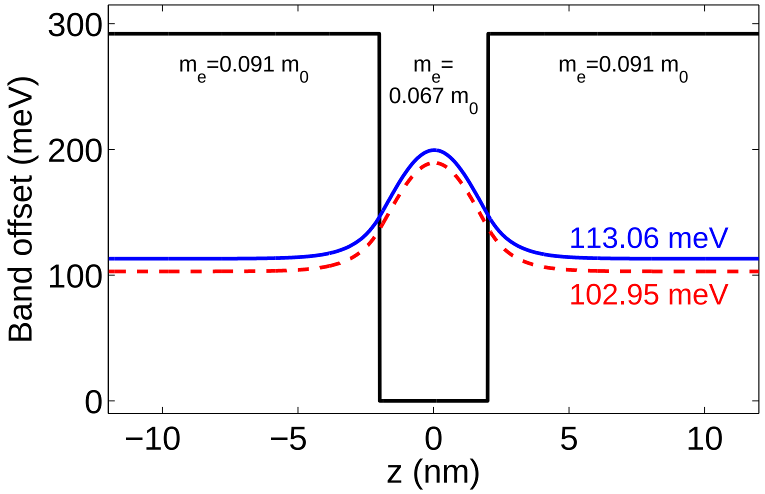

Figure A.2: *Electron ground state wave functions ($|u_e(z)|^2$) in a 4-nm GaAs/Al$_{0.3}$Ga$_{0.7}$As square well, calculated using constant mass ($m_{e,w}$=0.067 m_0, solid line) and variable masses ($m_{e,w}$=0.067 m_0, $m_{e,b}$=0.091 m_0) in well and barrier.*

matrix with the discretized curvature matrix:

$$T_1 = -\frac{\hbar^2}{2}/\delta x^2 \begin{pmatrix} \frac{1}{m_1} & & & & & \\ & \frac{1}{m_2} & & & & \\ & & \cdot & & & \\ & & & \cdot & & \\ & & & & \cdot & \\ & & & & & \frac{1}{m_n} \end{pmatrix} \cdot \begin{pmatrix} -2 & 1 & & & & 1 \\ 1 & -2 & \cdot & & & \\ & \cdot & \cdot & \cdot & & \\ & & \cdot & \cdot & \cdot & \\ & & & \cdot & \cdot & 1 \\ 1 & & & & 1 & -2 \end{pmatrix} . \tag{A.10}$$

It is easy to see that the discretized version of the second term is given by

$$\frac{1}{m_i^2}(m_{i+1} - m_i)(u_{i+1} - u_i)/\delta x^2 . \tag{A.11}$$

Defining the mass gradient vector by $m_i' = m_{i+1} - m_i$, the corresponding matrix is written

$$T_2 = -\frac{\hbar^2}{2}/\delta x^2 \begin{pmatrix} \frac{m_1'}{m_1^2} & & & & & \\ & \frac{m_2'}{m_2^2} & & & & \\ & & \cdot & & & \\ & & & \cdot & & \\ & & & & \cdot & \\ & & & & & \frac{m_n'}{m_n^2} \end{pmatrix} \cdot \begin{pmatrix} -1 & 1 & & & & 1 \\ & -1 & 1 & & & \\ & \cdot & \cdot & \cdot & & \\ & & \cdot & \cdot & \cdot & \\ & & & \cdot & \cdot & 1 \\ 1 & & & & 1 & -1 \end{pmatrix} . \tag{A.12}$$

The complete matrix equation is now written

$$Hu = Eu, \quad H = T_1 + T_2 + V , \tag{A.13}$$

where the position-dependent mass enters both kinetic-energy terms T_1 [Eq. (A.10)] and T_2 [Eq. (A.12)].

Figure A.2 shows electron ground state wave functions in a 4-nm square well calculated using the constant-mass (solid line) and variable-mass (dashed line) Schrödinger equation. The band offset $\Delta_e = 292$ meV of GaAs/Al$_{0.3}$Ga$_{0.7}$As QW has been used. For the effective electron mass, m$_{e,w}$=0.067 m$_0$ has been assumed in the GaAs well and m$_{e,w}$=0.091 m$_0$ in the Al$_{0.3}$Ga$_{0.7}$As barrier. Including the mass mismatch leads to an eigenenergy of the lowest electron eigenstate more then 10 meV lower than in the constant-mass model. The wave function is practically unaffected.

A.2 Single-particle Schrödinger equation in 2D

The constant-mass finite-difference method that has been applied to the solution of the single-particle Schrödinger equation in one dimension (described in the first paragraph) can be easily extended to two dimensions. The eigenvalue problem defined by the stationary, two-dimensional Schrödinger equation on the rectangular area $I = [0, a] \times [0, b] \ni (x, y)$,

$$-\frac{\hbar^2}{2m}\left(\frac{\partial^2}{\partial x^2} + \frac{\partial^2}{\partial y^2}\right) u(x,y) + V(x,y)u(x,y) = E\,u(x,y)\,, \tag{A.14}$$

can be written in matrix form by discretizing $u(x, y)$ on a *quadratic* lattice $(x_i, y_j)_{ij}$, $i, j \in \{1, \ldots, n\}$, i.e., using the map

$$u(x,y) \to (u_{ij})_{ij}\,, \text{ where } u_{ij} = u(x_i, y_j),\ i,j \in \{1,\ldots,n\}\,. \tag{A.15}$$

The discretized version of the curvature $(\frac{\partial^2 u}{\partial x^2} + \frac{\partial^2 u}{\partial y^2})$ is

$$\frac{u_{i+1,j} + u_{i-1,j} - 2u_{i,j}}{\delta x^2} + \frac{u_{i,j-1} + u_{i,j+1} - 2u_{i,j}}{\delta y^2}\,, \tag{A.16}$$

where $\delta x = a/(n-1)$, $\delta y = a/(n-1)$. By putting $\delta x = \delta y$, i.e., assuming the same grid point distance in x- and y-direction, we obtain

$$\frac{u_{i+1,j} + u_{i-1,j} + u_{i,j-1} + u_{i,j+1} - 4u_{i,j}}{\delta x^2}\,. \tag{A.17}$$

The resulting system of n^2 coupled linear equations for the u_{ij} is conveniently written in matrix form by concatenating the columns of $(u_{i,j})_{ij}$ in an n^2-component column vector, i.e., defining the map

$$u_{i,j} \to v_{i+n(j-1)}\,,\ i,j \in \{1,\ldots,n\}\,. \tag{A.18}$$

Defining the $n \times n$ matrices

$$A := \begin{pmatrix} -4 & 1 & & & & 1 \\ 1 & -4 & 1 & & & \\ & 1 & \ddots & \ddots & & \\ & & \ddots & \ddots & \ddots & \\ & & & \ddots & \ddots & 1 \\ 1 & & & & 1 & -4 \end{pmatrix}, \; I := I_n = \begin{pmatrix} 1 & & & & & \\ & 1 & & & & \\ & & \ddots & & & \\ & & & \ddots & & \\ & & & & \ddots & \\ & & & & & 1 \end{pmatrix}, \tag{A.19}$$

the $n^2 \times n^2$ Hamiltonian matrix H can be written as a sum of a block matrix composed of $n \times n$ sub-blocks, and of a diagonal potential matrix:

$$H = -\frac{\hbar^2}{2m} \begin{pmatrix} A & I & & & & I \\ I & A & \ddots & & & \\ & \ddots & \ddots & \ddots & & \\ & & \ddots & \ddots & \ddots & \\ & & & \ddots & \ddots & I \\ I & & & & I & A \end{pmatrix} + \begin{pmatrix} U_1 & & & & & \\ & U_2 & & & & \\ & & \ddots & & & \\ & & & \ddots & & \\ & & & & \ddots & \\ & & & & & U_{n^2} \end{pmatrix} \tag{A.20}$$

As before, the eigenvalue problem can be written as matrix equation

$$Hu = Eu\,, \tag{A.21}$$

where H now is a tridiagonal $n^2 \times n^2$ matrix with “fringes”. The choice of periodic boundary conditions reflects in the identities in the upper right and lower left corners in the matrix A, and in the identity matrices in the corners of the first term in Eq. (A.20). Leaving out these elements in the matrix corners would result in hard boundary conditions.

Eigenvalues and eigenvectors of the sparse $n^2 \times n^2$ matrix H are conveniently determined using a block Lanczos method [Und75]. For the actual numerical calculations, a Lanczos method from the `ARPACK` package, which is included in `MATLAB`, has been used. This method determines the k lowest eigenvalues and eigenvectors of the sparse matrix H by diagonalization in a k-dimensional subspace.

References

[Ben66] D. J. BenDaniel and C. B. Duke, *Space-charge effects on electron tunneling*, *Phys. Rev.* 152, 683 (1966).

[Har99] P. Harrison, *Quantum wells, wires and dots*, Kluwer Academic, 1999.

[Pre02] W. H. Press, S. A. Teukolsky, W. T. Vetterling, and B. P. Flannery, *Numerical Recipes in C++*, Cambridge University Press, 2002.

[Und75] R. R. Underwood, *An iterative block Lanczos method for the solution of large sparse symmetric eigenproblems*, Ph.D. thesis, available from NetLIB at AT&T and ORNL (1975).

Appendix B

Simulation source code

This section documents the MATLAB [Mat05] code that has been used in this thesis to solve 1D and 2D single-particle Schrödinger equation numerically using finite-difference methods.

B.1 Single-particle Schrödinger equation in 1D

The MATLAB routine `wf.m` listed below uses the finite-difference method described in the last chapter to solve the single-particle Schrödinger equation in an arbitrary one-dimensional real potential $V(z)$ defined by the vector z, assuming periodic boundary conditions. It calculates energies and wave functions of the lowest j eigenstates in this potential. The following parameters have to be specified (units are specified in brackets):

- `z`: z-axis (nm)
- `potential`: potential $V(z)$ (eV),
- `mass`: mass vector $m(z)$ (position-dependent effective mass),
- `j`: number of eigenstates

The routine yields as output the vector of eigenenergies `E` of the `j` lowest eigenstates, and the matrix `Psi` of the normalized eigenfunctions. The second index of `Psi` is the state index, i.e., `Psi`(:,1) is the wave function of the lowest eigenstate.

```
function [EmeV,Psi] = wf(z,potential,mass,j)

% physical constants and units [SI]
hbar=1.0546e−34
eV=1.602e−19;
meV=1e−3*eV;
m0=9.1094e−31;
nm=1e−9;

% number of grid points
n=length(z);
```

```
%% global definition of spatial grid
z_size=size(z);
if ( z_size(1) == 1 ) % vectors are internally handled as row vectors
     z=z';            % and transposed if specified otherwise
end

global dz
dz=(z(2)-z(1))*nm;

% building blocks of Laplace matrix (tridiagonal with fringes)
a=ones(n,1);
b=spdiags([a -2*a a],-1:1,n,n);

mass=mass*m0;
m_size=size(mass);
if ( m_size(1) == 1 )
     mass=mass';
end

m_inv=1./mass;
d_dz=spdiags([-a a],0:1,n,n);
d_dz(n,1)=1; % periodic boundary conditions

% kinetic energy including position-dependent mass
T=-hbar^2/2/dz^2 * d_dz * m_inv * d_dz;

% potential energy
potential=potential*eV;
p_size=size(potential);
if ( p_size(1) == 1 )
     potential=potential';
end

V=spdiags([potential],0,n,n);

% Hamiltonian
H=T+V;

% matrix diagonalization
% the matrix Psi contains the eigenfunctions
% the vector E the contains eigenenergies
[Psi,E]=eigs(H,j,'sm');
EmeV=diag(E)/meV
Psi=reshape(Psi,[j n]);

% normalization of wave functions
nr=size(Psi);
nr(2)=[];
for i=1:nr
  Psi(:,i)=Psi(:,i)./norm(Psi(:,i));
end
```

The following routine `wf_qw.m` calculates the lowest electron and hole eigenstates in a GaAs/$Al_xGa_{1-x}As$ single quantum well in the envelope function approximation, using the virtual crystal approximation for the $Al_xGa_{1-x}As$ barriers. It requires the following input parameters:

- `p`: particle type (`e` = electron, `h` = heavy hole)
- `xx`: Aluminum concentration in the barrier
- `well`: quantum well width (nm)
- `barr`: barrier width (nm)
- `j`: number of eigenstates

```
function [EmeV,Psi] = wf_qw(p,xx,well,barr,j)

% physical constants and units [SI]
hbar=1.0546e-34
eV=1.602e-19;
meV=1e-3*eV;
m0=9.1094e-31;
nm=1e-9;

global dz
dz=0.02*nm;

% definition of the heterostructure
% width of barriers and wells in nm
layers=[barr well barr];
N=length(layers);

structure=ones(1,round(nm/dz*layers(1)));

% alternating barriers and wells
for n=2:N
    if rem(n,2)==1
        structure=[structure ones(1,round(nm/dz*layers(n)))];
    elseif rem(n,2)==0
        structure=[structure zeros(1,round(nm/dz*layers(n)))];
    end
end

% number of grid points
n=length(structure);

% position-dependent alloy concentration
alloy=xx*structure;

% band edges
cb_offset=(1.36*alloy+0.22*alloy.^2)*0.65*eV;
vb_offset=(1.36*alloy+0.22*alloy.^2)*0.35*eV;

% position-dependent mass
m_e=(0.067+alloy*0.083)*m0;
m_h=(0.33+alloy*0.18)*m0;

% electron (e) or heavy-hole (h)
switch p
    case 'e'
        potential=cb_offset;
```

```
        mass=m_e;
    case 'h'
        potential=vb_offset;
        mass=m_h;
end

% building blocks of Laplace matrix (tridiagonal with fringes)
a=ones(n,1);
b=spdiags([a -2*a a], -1:1,n,n);

m_size=size(mass);
if ( m_size(1) == 1 )
     mass=mass';
end

m_inv=1./mass;
d_dz=spdiags([-a a], 0:1,n,n);
d_dz(n,1)=1; % periodic boundary conditions

% kinetic energy including position-dependent mass
T=-hbar^2/2/dz^2 * d_dz * m_inv * d_dz;

% potential matrix (diagonal)
p_size=size(potential);
if ( p_size(1) == 1 )
     potential=potential';
end

V=spdiags([potential], 0,n,n);

% Hamilton matrix
H=T+V;

% matrix diagonalization
% the matrix Psi contains the eigenfunctions
% the vector E the contains eigenenergies
[Psi,E]=eigs(H,j,'sm');
EmeV=diag(E)/meV
Psi=reshape(Psi,[j n]);

% normalization of wave functions
nr=size(Psi);
nr(2)=[];
for i=1:nr
  Psi(:,i)=Psi(:,i)./norm(Psi(:,i));
end
```

The routine `wf_qw.m` uses the following material parameters of the GaAs/Al$_x$Ga$_{1-x}$As system: The Al$_x$Ga$_{1-x}$As/GaAs band offset $\Delta(x) = 1.45\,x$ eV [Ont74], and the band offset ratio $f_e/f_h = 0.65/0.35$ [Dug85, Wol86, Kop92]. Effective electron and heavy-hole [001] masses in the Al$_x$Ga$_{1-x}$As alloy are obtained by linear interpolation between GaAs and AlAs masses [Ada94]:

$$m_e/m_0 = 0.067 + 0.083x\,, \quad m_{hh}/m_0 = 0.33 + 0.18x \tag{B.1}$$

B.2 Single-particle Schrödinger equation in 2D

The routine listed in this paragraph

- creates uncorrelated, Gaussian-distributed 2d disorder potentials $V_e(x,y)$, $V_h(x,y)$ on a 160×160 nm^2 square grid with 0.4 nm grid step; the standard deviation (disorder strength) of the electron potential is $\sigma_e = 33$ meV, and the disorder strength of the hole potential $\sigma_h = 9$ meV;
- calculates an effective potential $V_{\text{eff}}(x,y)$ for the exciton center-of-mass, assuming a fixed Bohr radius $a_B = 8$ nm, by convolution with scaled 1s wave functions according to Eq. (3.5),
- and calculates eigenvalues and eigenfunctions of the lowest k (default: $k = 100$) center-of-mass eigenstates by solving the single-particle Schrödinger equation [Eq. 3.4] in the effective potential $V_{\text{eff}}(x,y)$.

The ratio of disorder strengths σ_e/σ_h is chosen larger than the band offset ratio $f_e/f_h = 2/1$, because disorder resulting from alloy fluctuations in a GaAs/AlGaAs quantum well is considered: As shown in chapter 3, in a GaAs/AlGaAs quantum well the penetration depth of the electron wave function into the AlGaAs barrier is larger than that of the hole wave function. Consequently, the effect of alloy fluctuations is larger for the electron than for the hole.

```
%% physical constants (SI)
eV=1.6021773e−19;
meV=1e−3*eV;
m0=9.109390e−31;
nm=1e−9;

%% number of grid points
N=100;

%% Gaussian−distributed disorder realization, sigma = standard deviation
sigma=33*meV;
pot2d=randn(2*N+1,2*N+1)*sigma;

%% electron and hole potentials
pot2d_e = pot2d;
pot2d_h = pot2d/2;

%% scaled 1s wave functions for electron and hole
%% with different decay constants

% coordinate system with 0.4 nm grid step
scale=(−N:N)*0.4*nm;
[x,y]=meshgrid(scale,scale);

%% exciton Bohr radius and effective in−plane masses
%% for 4 nm GaAs/AlGaAs quantum well (x=0.3)
aB=8*nm;
m_e=0.078*m0;
m_h=0.23*m0;
```

```
M=m_e+m_h;
beta_e=M/m_h;
beta_h=M/m_e;

phi2d_e=exp(-beta_e*sqrt(x.^2+y.^2)/aB);
phi2d_e=phi2d_e/sqrt(sum(sum(phi2d_e.^2)));

phi2d_h=exp(-beta_h*sqrt(x.^2+y.^2)/aB);
phi2d_h=phi2d_h/sqrt(sum(sum(phi2d_h.^2)));

% wave function squares
phi2d_e=phi2d_e.^2;
phi2d_h=phi2d_h.^2;

%% convolution of electron and hole potentials with 1s wave functions

pot_com=conv2(pot2d_e,phi2d_e) + conv2(pot2d_h,phi2d_h);
pot_com=pot_com(N+1:3*N,N+1:3*N);
pot=pot_com;

potmin=min(min(pot))-meV;
pot=pot+abs(potmin);

%% total Hamiltonian matrix

m0=9.109390e-31;
m=(0.078+0.23)*m0;

hbar=1.054573e-34;
eps0=8.8542e-12;

dx=0.4*nm;
dy=0.4*nm;

% number of grid points
n=2*N;

% Laplace matrix (tridiagonal with "fringes")
a = ones(n,1);
b = spdiags([a/dy^2 a/dy^2 -2*a*(1/dx^2+1/dy^2) a/dy^2 a/dy^2], [-n+1,-1:1,n-1] ,n,n);
u=b;

for t=1:n-1
    u=blkdiagsp(u,b);
end

o=ones(n^2,1);
o=[o o];
per=ones(n,1);
u = spdiags(o/dx^2,[-n n],u);

per=ones(n^2,1);
per=[per per];
u = spdiags(per/dx^2,[-n*(n-1) n*(n-1)],u);

% kinetic energy
u=-u*hbar^2/2/m;

% potential energy
```

```
potential=reshape(pot,[nˆ2 1]);
dia = spdiags([potential], 0,nˆ2,nˆ2);

% total energy
hamilton=u+dia;

% save this disorder realization and clear variables to save memory
save disorder_realization potmin pot hamilton n meV
clear

%% matrix diagonalization

load disorder_realization
j=100;

% MATLAB routine ``eigs'' with parameter ``sm'' = smallest magnitude
% used to determine the lowest j eigenstates
[Psi,D]=eigs(hamilton,j,'sm');
Psi=reshape(Psi,[n n j]);
EmeV=(diag(D)−abs(potmin))/meV;

% order of eigenstates: first eigenstate = ground state
psiSize=size(Psi);
Phi=zeros(psiSize);
for i=1:j
  Phi(:,:,i)=Psi(:,:,j+1−i);
end
Psi=Phi;

%% row vector of eigenenergies (in meV)
EmeV=flipud(EmeV);

%% image wave function of eigenstate j:
%% imagesc(abs(Psi(:,:,j)))
```

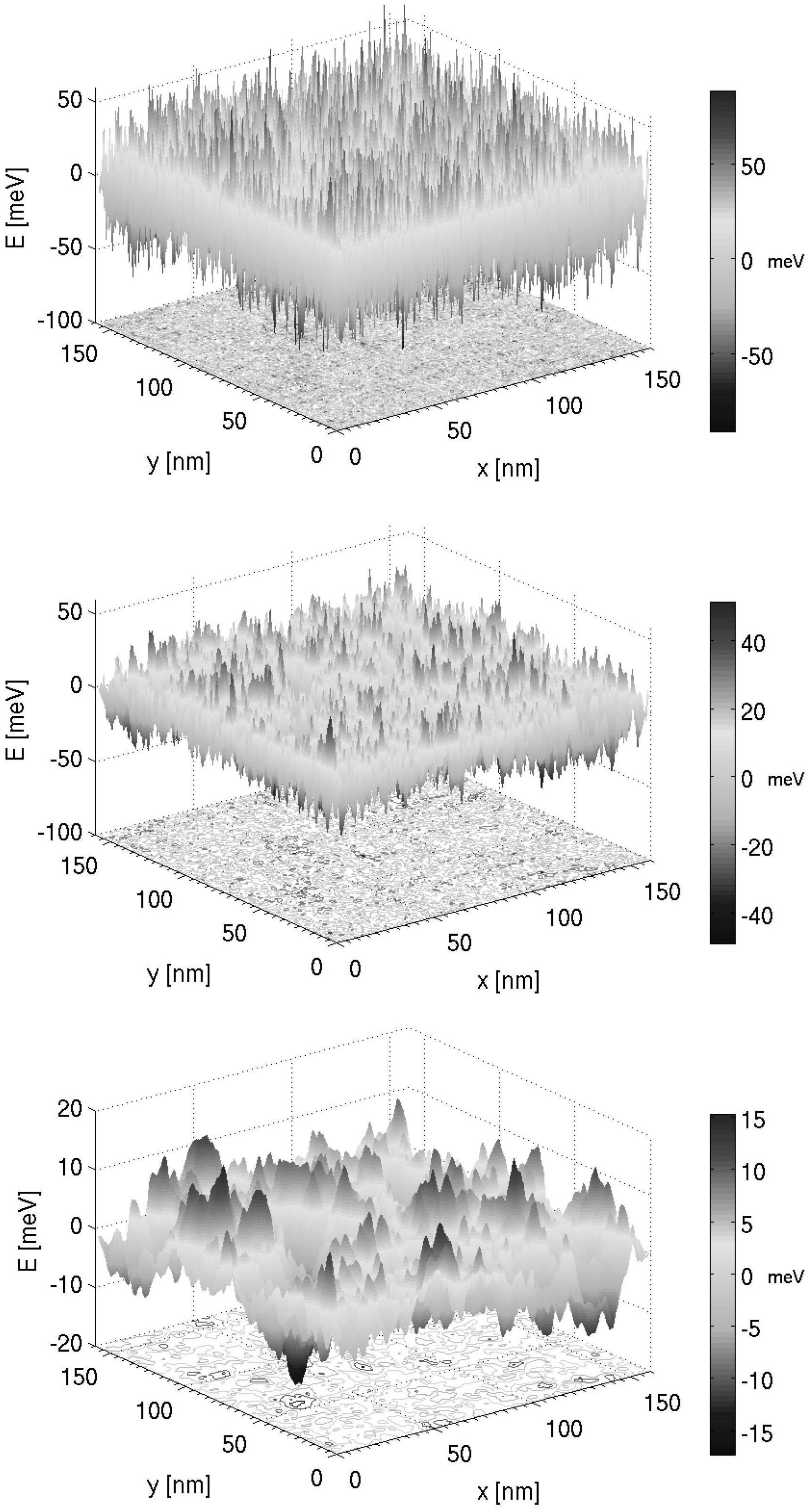

Figure B.1: *The disorder potentials shown in (a)-(c) have been obtained from uncorrelated, Gaussian-distributed disorder potentials* $V_e(x,y)$, $V_h(x,y)$ *(*$\sigma_e = 33$ *meV,* $\sigma_h = 9$ *meV) on a* 160×160 *nm*^{2} *square grid (0.4 nm grid step) by convolution with 1s wave functions with different Bohr radii according to Eq. (3.5): (a)* $a_B = 0.1$ *nm, (b)* $a_B = 1$ *nm, (c)* $a_B = 8$ *nm.*

References

[Mat05] *MATLAB v7.1. Mathworks Inc., 2005.*

[Ada94] S. Adachi, *GaAs and related materials*, World Scientific, 1994.

[Dug85] G. Duggan, H. I. Ralph, and K. J. Moore, *Reappraisal of the band-edge discontinuities at the* $Al_xGa_{1-x}As$*-GaAs heterojunction*, *Phys. Rev. B* 32, 8395 (1985).

[Kop92] R. F. Kopf, M. H. Herman, M. L. Schnoes, A. P. Perley, G. Livescu, and M. Ohring, *Band offset determination in analog graded parabolic and triangular quantum wells of GaAs/AlGaAs and GaInAs/AlInAs*, *J. Appl. Phys.* 71, 5004 (1992).

[Ont74] A. Onton, M. R. Lorenz, J. M. Woddall, and R. J. Chicotka, *Optical characterization of compound semiconductor alloys*, *J. Cryst. Growth* 27, 166 (1974).

[Wol86] D. J. Wolford, T. F. Kuech, J. A. Bradley, M. A. Gell, D. Ninno, and M. Jaros, *Pressure dependence of GaAs/*$Al_xGa_{1-x}As$ *quantum well bound states - the determination of valence band offsets*, *J. Vac. Sci. Technol. B* 4, 1043 (1986).

Scientific contributions

Original papers

- 1. M. Erdmann, C. Ropers, M. Wenderoth, R.G. Ulbrich, S. Malzer, and G.H. Döhler, *Diamagnetic shift of disorder-localized excitons in narrow GaAs/AlGaAs quantum wells*, Phys. Rev. B 74, 125412 (2006).
- 2. C. Ropers, M. Wenderoth, L. Winking, T.C.G. Reusch, M. Erdmann, R.G. Ulbrich, M. Grochol, F. Grosse, R. Zimmermann, S. Malzer, and G.H. Döhler, *Atomic scale structure and optical emission of GaAs/AlGaAs quantum wells*, Phys. Rev. B 75, 115317 (2007).

Contributions to International Conferences

- 1. M. Wenderoth, C. Ropers, L. Winking, T.C.G. Reusch, M. Erdmann, S. Malzer, G.H. Döhler, and R.G. Ulbrich, *Comparison of the optical properties with the atomic scale structure of AlGaAs/GaAs quantum wells*, 1st German-Japanese Symposium on Nanooptics, Berlin 2003.
- 2. M. Grochol, F. Grosse, R. Zimmermann, C. Ropers, M. Erdmann, M. Wenderoth, R.G. Ulbrich, S. Malzer, and G.H. Döhler, *Exciton diamagnetic shift in realistic quantum wells*, EXCON 7, Wake Forest 2006.
- 3. M. Erdmann, M. Wenderoth, R.G. Ulbrich, S. Malzer, and G.H. Döhler, *Disorder-induced exciton magnetic shifts in semiconductor nanostructures*, Poster, ICPS 28, Wien 2006.

Further contributions

- 1. M. Erdmann, C. Ropers, M. Wenderoth, R.G. Ulbrich, S. Malzer, and G.H. Döhler, *Polarisationsverhalten der Emission aus lokalisierten Exzitonzuständen in GaAs/AlGaAs-Quantenfilmen*, Poster, DPG Spring Meeting, Dresden 2003.
- 2. C. Ropers, M. Wenderoth, L. Winking, T.C.G. Reusch, M. Erdmann, S. Malzer, G.H. Döhler, and R.G. Ulbrich, *XSTM vs. μPL: Ein direkter Vergleich der strukturellen und optischen Eigenschaften von GaAs/AlGaAs-Quantenfilmen*, Poster, DPG Spring Meeting, Dresden 2003.

- 3. C. Ropers, M. Erdmann, M. Wenderoth, L. Winking, T.C.G. Reusch, R.G. Ulbrich, S. Malzer, and G.H. Döhler, *The correlation between emission spectra and atomic scale structure of GaAs/AlGaAs quantum wells*, Poster, DPG Spring Meeting, Regensburg 2004.
- 4. M. Erdmann, C. Ropers, M. Wenderoth, R.G. Ulbrich, S. Malzer, and G.H. Döhler, *Diamagnetic shift of localized excitons in GaAs/AlGaAs quantum wells*, Poster, DPG Spring Meeting, Berlin 2005.
- 5. M. Erdmann, M. Wenderoth, R.G. Ulbrich, S. Malzer, and G.H. Döhler, *Diamagnetic shift of disorder-localized excitons in narrow quantum wells*, Talk, DPG Spring Meeting, Dresden 2006.

Danksagung

Zum Schluss möchte ich einigen Menschen danken, die zum Gelingen dieser Arbeit beigetragen haben.

An oberster Stelle danke ich Herrn Prof. Dr. Rainer G. Ulbrich für die Möglichkeit, diese spannende Arbeit durchzuführen. Trotz seiner Belastung als Dekan der Fakultät für Physik in den letzten zwei Jahren hat er sich immer wieder die Zeit für wissenschaftliche Diskussionen genommen. Seine Fähigkeit, komplizierte physikalische Probleme aus allen Bereichen auf die grundlegenden Konzepte "abzukochen", hat jedesmal zu einer Vielzahl neuer Einsichten und zur Klärung wesentlicher Fragen geführt.

Herrn Prof. Dr. Thomas Pruschke danke ich für die Übernahme des Zweitgutachtens.

Claus Ropers und Ilya Mingareev waren in der Anfangszeit dieser Arbeit unersetzliche Labormitstreiter, ohne die der Umstieg von der "theoretischen Seite" so nicht möglich gewesen wäre. Claus Ropers danke ich für die gute und produktive Zusammenarbeit im ersten Jahr dieser Arbeit, und für interessante Diskussionen auch nach seiner Göttinger Zeit.

Lars Winking und Thilo Reusch danke ich für die ausgezeichneten XSTM-Messungen.

Ein großer Dank geht an Dr. Martin Wenderoth. Mit seiner unzerstörbar-freundlichen Art gelingt es ihm, ein Klima des Umgangs miteinander zu schaffen, in dem man alle Durststrecken übersteht. Seine Unterstützung hat diese Arbeit von Anfang an immer wieder vorangebracht.

Dr. Michal Grochol, Dr. Frank Grosse und Prof. Dr. Roland Zimmermann von der AG Halbleitertheorie an der Humboldt-Universität Berlin danke ich für fruchtbare Diskussionen und einen wissenschaftlichen Austausch, von dem beide Seiten profitiert haben. Prof. Dr. Erich Runge, der inzwischen einen eigenen Lehrstuhl an der TU Ilmenau übernommen hat, danke ich ebenfalls für einige anregende Diskussionen.

Dr. Stefan Malzer (Max-Planck Research Group, Institute for Optics, Information, and Photonics, Universität Erlangen-Nürnberg) danke ich für die Unterstützung dieser Arbeit durch sein bereitwilliges Eingehen auf Probenwünsche, und für eine Reihe interessanter Diskussionen.

M.Sc. Daniel Quinlan danke ich für die kompetente muttersprachliche Unterstützung bei der Formulierung der Veröffentlichungen wie auch dieser Arbeit.

Den Mitgliedern der "Tunnlergruppe", Sebastian Loth, Lars Winking, Jan Homoth, Alexander Weismann, Thomas Druga und Karen Teichmann danke ich für interessante physikalische und nicht-physikalische Kaffeerunden.

Dipl.-Ing. Bernhard Spicher war in allen technischen Fragen immer außergewöhnlich hilfsbereit. In der Zeit des Umzugs von der “alten” in die “neue” Physik und bei der Einrichtung des neuen Labors war er eine unschätzbare Unterstützung.

Für die gute Unterstützung in technischen Dingen danke ich Klaus Langohr und Rasit Kösker (Elektronik-Werkstatt), Thomas Lehmann und Andreas Juretzko (feinmechanische Werkstatt) sowie Uwe Frenzel (Zentralwerkstatt). Dr. Hans-D. Schulte und Dr. Karl Ahlborn möchte ich für die zuverlässige Unterstützung in administrativen und netzwerktechnischen Fragen danken.

Dr. Jens Garleff danke ich für freundschaftliche Begleitung von Beginn des Studiums an. Unsere ausdauernden mittäglichen Diskussionen haben mit dazu beigetragen, dass ich mein Arbeitsgebiet noch einmal komplett gewechselt habe. In seinem - nach eigener Aussage - manchmal grenzwertigen Humor ließ sich immer auch ein Körnchen inspirierende Kritik finden.

Viel zu verdanken habe ich den Freundinnen und Freunden aus der Jongliergruppe im Hochschulsport der Uni Göttingen. Danke für die unzähligen schönen Samstagnachmittage im IFL, im Cheltenhampark und auf den Schillerwiesen!

Hedda, Karsten und Regula wissen, was ich ihnen verdanke. Ohne Euch wäre ich nicht der Mensch geworden, der ich heute bin.

Thomas und Julika danke ich für ihre Gastfreundschaft vor allem in der letzten Phase der Doktorarbeit, in der die letzten Kontakte zur Aussenwelt tatsächlich eine besondere Bedeutung bekommen.

Meinem Physiklehrer Dr. Wolfgang Speller (Heriburg-Gymnasium, Coesfeld) danke ich für zwei sehr intensive Jahre Physikunterricht. Seine fachlichen und menschlichen Qualitäten haben wesentlich zu meiner Entscheidung beigetragen, Physik zu studieren.

Der größte Dank gilt meinen Eltern und meiner Schwester, die mich immer darin bestärkt haben, meinen eigenen Weg zu gehen.

Lebenslauf

Matthias Erdmann
geboren am 09.03.1975 in Unna
Staatsangehörigkeit: deutsch

1981-1985	Laurentius-Grundschule in Coesfeld (Westf.)
1985-1994	Gymnasium Nepomucenum in Coesfeld
5/1994	Abitur
7/1994 - 9/1995	Zivildienst in der NABU-Naturschutzstation, Kranenburg (Niederrhein)
9/1995-9/1997	Grundstudium Physik (Diplom) in Göttingen
10/1997	Vordiplom
10/1997-3/1998	Hauptstudium Physik (Diplom) in Oldenburg
4/1998-6/2001	Hauptstudium Physik (Diplom) in Göttingen
7/2001	Diplom
	Thema der Diplomarbeit: Thermische Nichtgleichgewichtszustände in einem Modell der Quantenfeldtheorie
9/2001-12/2001	Wissenschaftlicher Angestellter Hahn-Meitner-Institut GmbH, Berlin
1/2002-3/2002	Wissenschaftliche Hilfskraft am IV. Physikalischen Institut der Universität Göttingen
4/2002-04/2007	Wissenschaftlicher Angestellter am IV. Physikalischen Institut der Universität Göttingen mit Gelegenheit zur Promotion